Quantum fluctuations of the charge in single electron and single Cooper pair devices

Fluctuations quantiques de la charge dans les circuits à un électron et à une paire de Cooper

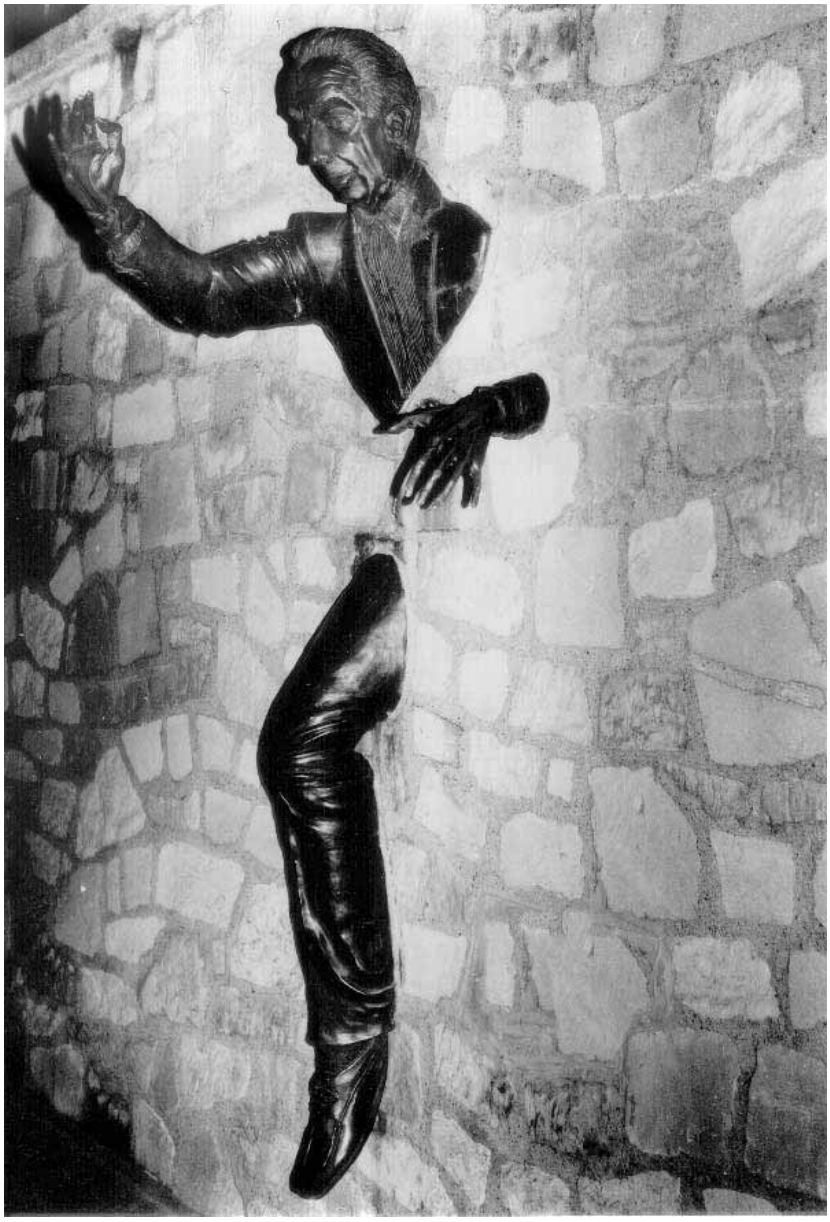

Vincent BOUCHIAT

THÈSE DE DOCTORAT DE L'UNIVERSITÉ PARIS 6

Fluctuations quantiques de la charge dans les circuits à un électron et à une paire de Cooper

spécialité :
Physique des solides

présentée par:

Vincent BOUCHIAT
pour obtenir le grade de DOCTEUR de l'UNIVERSITE PARIS 6

Soutenue le 21 Février 1997
Amphithéâtre Claude BLOCH,
Orme des merisiers,
CEA-Saclay.

devant le Jury :

Président :	J. Bok
Rapporteurs:	H. Grabert
	L. Lévy
Examinateurs:	M. Devoret
	D. Mailly
	P. Monod

à mes parents.

Remerciements

Le travail de cette thèse a été réalisé entre Juillet 1993 et Février 1997 dans le service de Physique de l'état condensé à l'Orme des Merisiers (CEA-Saclay), au sein du groupe de quantronique et sous la direction de Michel Devoret. Je voudrais ici témoigner de ma gratitude envers tous ceux qui m'ont permis d'effectuer ce travail dans les meilleures conditions possibles.

Arrivé de façon impromptue dans le groupe, j'ai très vite bénéficié de la confiance de Michel Devoret et Daniel Estève, qui ont passé de longs moments à m'expliquer et à me faire partager les richesses des effets de charges et de la supraconductivité.

Il m'a fallu ensuite maîtriser les techniques de fabrication des nanostructures. Pour connaître des chances raisonnables de succès, un tel savoir-faire doit s'appuyer sur une tradition "orale", car il s'accommode mal d'un apprentissage académique ou procédurier. Philippe Lafarge et Philippe Joyez ont ainsi bien voulu m'initier à "l'alchimie" de la nanofabrication. Je les en remercie très chaleureusement. J'ai également bénéficié par la suite de l'aide bienveillante de Hugues Pothier.

Lorsque je suis devenu à mon tour autonome, Daniel Estève m'a ensuite donné la stimulation nécessaire pour que je puisse m'attaquer au développement de nouvelles techniques. Son expertise, son extraordinaire dynamisme et sa disponibilité ont été déterminants pour la réalisation de tout ce travail. J'ai été également extrêmement sensible à l'aide de Cristiàn Urbina durant cette période délicate : ses conseils et ses encouragements m'ont été d'un grand soutien moral.

Les expériences proprement dites sur ces nanostructures obtenues, ont été réalisées en compagnie de Denis Vion dont la gentillesse, l'énergie, et surtout la compétence ont une part prépondérante dans leur succès.

L'aide technique et les conseils précieux de Pief Orfila ont été cruciaux pour bien des aspects de cette thèse. Les réalisations expérimentales ont également bénéficié de l'aide extérieure de Josepha de la société Balzers, ainsi que des conseils avisés de Mr. Smuteck de la société Plassys. Par ailleurs ce travail a bénéficié en partie du soutien financier du Bureau National de la Métrologie.

Ce manuscrit doit beaucoup à l'aide constante du groupe tout au long de sa rédaction :

Daniel Estève a passé de longs moments à mes côtés pour sa mise en forme; l'intervention de Philippe Joyez a également été cruciale pour le chapitre 1; Michel Devoret, Cristian Urbina, Denis Vion et Laurent Lévy ont permis, par leur lecture attentive, sa mise au point. Enfin, Sophie Guéron m'a sauvé de mon anglais parfois bien déficient.

Je suis très reconnaissant à Hermann Grabert et Laurent Lévy d'avoir accepté d'être les rapporteurs de cette thèse ainsi qu'à Julien Bok, Dominique Mailly, Philippe Monod de bien vouloir faire partie du Jury.

Je remercie Daniel Beysens et Francis Williams de m'avoir accueilli dans le laboratoire et de m'avoir fait bénéficier d'un contrat CEA, ainsi que Jacques Hammann qui m'a permis de terminer ma thèse un peu après les délais impartis. A cette occasion, l'intervention efficace de Raymonde Marciano a permis de dénouer plus d'un imbroglio administratif.

Je n'oublie pas Corinne Miramond pour son aide durant le tirage de cette thèse et les multiples heures passées ensemble en salle blanche.

Je voudrais aussi remercier tous les chercheurs avec qui j'ai pu discuter durant ma thèse, et tout particulièrement : Norman Birge, Gabriel Chardin, Giancarlo Faini, Antoine Georges, Christian Glattli, Hermann Grabert, Gert Ingold, François Ladieu, Gwenaëlle Lebras, Yasunobu Nakamura, Bernard Pannetier, Jan van Ruitenbeek, Marc Sanquer et Sacha Zorin.

Enfin, j'ai une pensée toute particulière pour mes parents, Geneviève, Hélène, et Behnaz pour leur soutien constant durant toutes ces années.

Table of Contents

Chapter 3

Chapter 4

Notice

The first part of this manuscript, composed of an introduction followed by an extended abstract, is written in french. English readers should go directly to page 37.

Avertissement

La partie rédigée en français de ce manuscrit est organisée de la façon suivante : dans un court préambule, est exposée une présentation générale du domaine dans laquelle s'inscrit cette thèse: les effets de charges dans les nanostructures métalliques et leur principaux développements. Les problèmes spécifiques considérés dans le corps du manuscrit, à savoir la mise en évidence des fluctuations quantiques de la charge dans ces circuits, sont ensuite abordés dans l'introduction. Cette introduction est suivie d'une présentation synthétique des principaux résultats obtenus, qui font chacun l'objet d'un chapitre distinct dans le corps du manuscrit rédigé en anglais.

encadré 1

L'effet tunnel dans les nanostructures métalliques

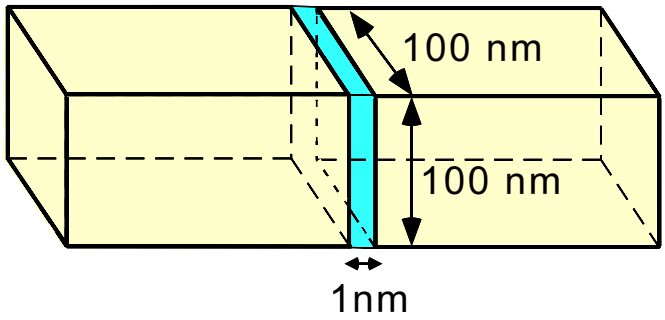

Les jonctions tunnel considérées dans cette thèse sont du type métal/isolant/métal. Les surfaces caractéristiques S des jonctions sont de l'ordre de 0.1x0.1 μm^2. La fine barrière isolante séparant les deux électrodes est constituée d'une couche d'oxyde d'environ 1 nm d'épaisseur.

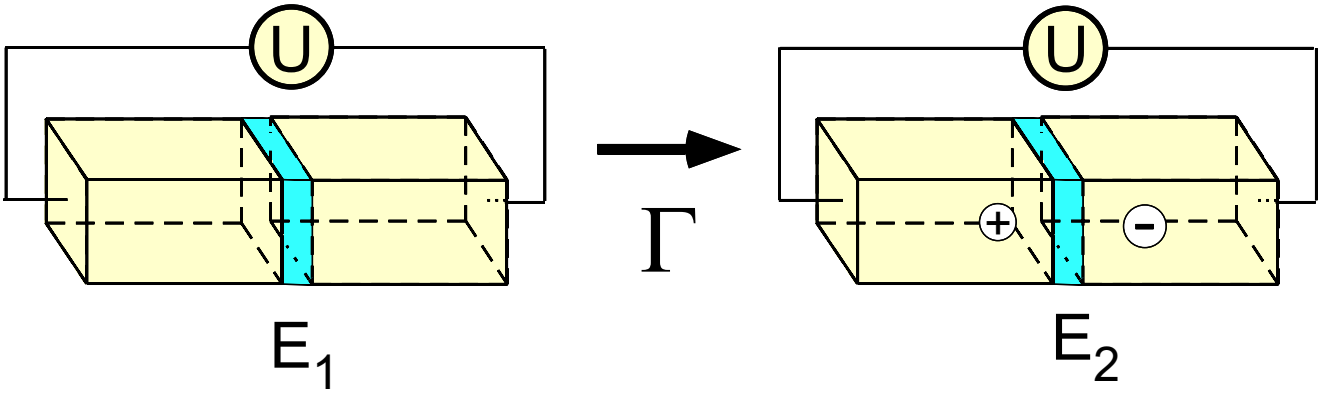

Les deux électrodes sont ici connectées à une source de tension U. Un évenement tunnel se traduit par la création d'une paire électron-trou de part et d'autre de la jonction. Le travail de la source vaut E_2-E_1=eU. Le taux de transition tunnel par unité de temps Γ est donné par:

$$\Gamma = g_t \frac{E_1 - E_2}{e^2} = g_t \frac{U}{e}$$

où g_t est la conductance tunnel de la jonction. Cette conductance s'écrit comme:

$$g_t = 2\ e^2/h\ N\ \overline{T}$$

Le nombre N correspond au nombre de canaux ouverts, il est donné par le rapport entre la surface S et l'extension latérale caractéristique λ_F^2 d'une fonction d'onde électronique soit environ 10^6 pour la jonction considérée; $\overline{T}$ est la transmission moyenne d'un canal.

Les conductances tunnel fabriquées étant petites ou du même ordre de grandeur que le quantum de conductance e^2/h, le produit $N\overline{T}$ est d'ordre unité, soit $\overline{T} \ll 1$. Les jonctions tunnel considérées par la suite sont donc constituées d'un grand nombre de canaux électroniques très peu transmis. La situation est donc très différente de celle rencontrée dans les boîtes quantiques contruites à partir de gaz bidimensionnels d'électrons, pour lesquelles les jonctions tunnel sont caractérisées par un petit nombre de canaux dont la transmission peut être rendue proche de l'unité.

Préambule

L'électronique à un électron

Quantification de la charge d'une électrode

Au cours d'une expérience restée célèbre [1], Millikan a montré, en mesurant la déviation de la trajectoire dans un champ électrique de gouttelettes d'huile chargées, que la charge électrique de ces gouttelettes était quantifiée en multiples du quantum de charge $e \approx 1.6 \times 10^{-19} C$. Cette expérience, réalisée en 1911, marque un des débuts de la mécanique quantique. De façon plus directe, elle montre que la charge d'une électrode isolée est quantifiée. Cette expérience reste cependant limitée puisque Millikan ne pouvait contrôler la charge de ces gouttelettes parfaitement isolées.

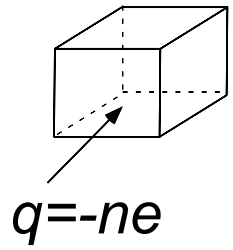

Représentation schématique d'une électrode isolée: sa charge est un multiple de la charge électronique e.

Par ailleurs, il n'aurait pu observer la quantification de la charge sur une armature de condensateur non isolée, non pas à cause du nombre plus important d'électrons mis en jeu mais parce que la quantification même de la charge en multiples de e n'aurait plus été dans ce cas assurée: la charge d'un condensateur connecté à une source de tension est une quantité continue, correspondant à un déplacement (pouvant être rendu infinitésimal) du fluide électronique par rapport au réseau ionique. La quantification de la charge apparait donc *a priori* comme antagoniste avec la possibilité de son contrôle par une source.

Transfert de la charge par effet tunnel

L'effet tunnel permet de réconcilier ces deux propriétés. Supposons que l'on rapproche une petite électrode métallique, appelée par la suite "île", d'un réservoir de charge tout en les gardant séparés par une fine paroi isolante (voir figure ci-dessous).

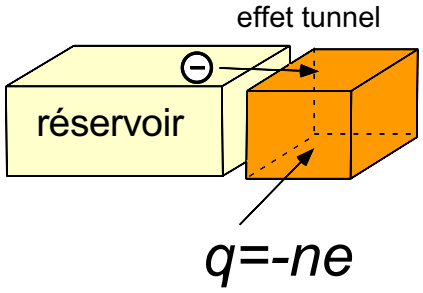

Ile couplée à un réservoir de charge par l'intermédiaire d'une jonction tunnel.

Les électrons vont alors pouvoir passer par effet tunnel entre l'îlot et le réservoir. Si la jonction tunnel est suffisament opaque, l'extension des fonctions d'onde électroniques à travers la jonction sera négligeable, si bien que la quantification de la charge de l'île en multiple de e est assurée à un instant donné, mais reste néanmoins susceptible de fluctuer dans le temps suite aux fluctuations thermiques. La quantité physique caractérisant l'opacité de la barrière tunnel est la résistance tunnel R_T (voir encadré 1), dont la valeur doit être comparée au quantum de résistance $R_K = h/e^2 \approx 26\ k\Omega$. La localisation de la charge dans l'île sera ainsi obtenue pour des résistances tunnel grandes devant le quantum de résistance:

$$R_T \gg R_{K.} \tag{1}$$

Notons que cette relation est analogue au critère de localisation de la charge dans une couche métallique désordonnée pour laquelle la transition métal-isolant intervient lorsque la résistance par carré excède $R_{K.}$.

Blocage de la charge par effet capacitif

L'énergie électrostatique associée à l'entrée d'un électron dans l'île est donnée par $e^2/2C$, où C est la capacité totale de l'île. Si cette énergie est rendue grande devant l'énergie caractéristiques des fluctuations thermiques k_BT soit :

$$e^2/2C \gg k_BT, \tag{2}$$

seule la configuration électrostatique d'énergie minimale est sélectionnée. Le nombre d'électrons dans l'île est alors bien défini lorsque les inégalités (1) et (2) sont simultanément satisfaites. Cette dernière inégalité est la plus restrictive: elle relie la surface d'une jonction tunnel qui détermine la capacité de la jonction, à la température d'apparition des effets de charge.

La capacité associée à une jonction tunnel de dimensions latérales typique 0.1×0.1 μm^2, vaut 1 fF, ce qui équivaut à une température de 1 K. L'observation des effets de charge demande donc un effort technologique simultané dans des domaines aussi différents tels que la fabrication de nanostructures et les techniques cryogéniques. Une telle exigence explique le développement tardif de ce champ de recherche dont les premiers développements ont tout juste dix ans.

Contrôle de la charge par polarisation électrostatique

La charge de l'île étant fixée par l'énergie électrostatique, celle-ci doit pouvoir être modifiée pour permettre le transfert contrôlé de la charge du réservoir vers l'île. Ce contrôle est obtenu en couplant capacitivement l'île à une source de tension (voir figure ci-dessous).

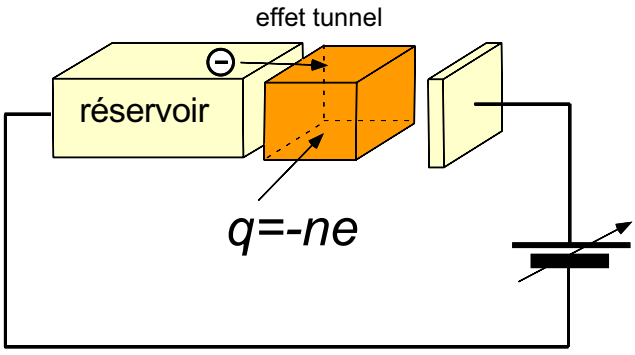

Représentation du circuit dit de la "boite à électrons" pour laquelle la charge de l'île est contrôlée par la source de tension variable.

Cette tension de polarisation électrostatique, dite tension de grille, permet d'ajuster les valeurs relatives des énergies électrostatiques associées à des nombres d'électrons dans l'île différents: elle modifie ainsi la configuration de charge pour laquelle l'énergie du système est minimale. Un tel contrôle est à l'origine de "l'électronique à un électron" dont les deux circuits de base sont décrits dans la suite.

encadré 2

La boîte à électrons

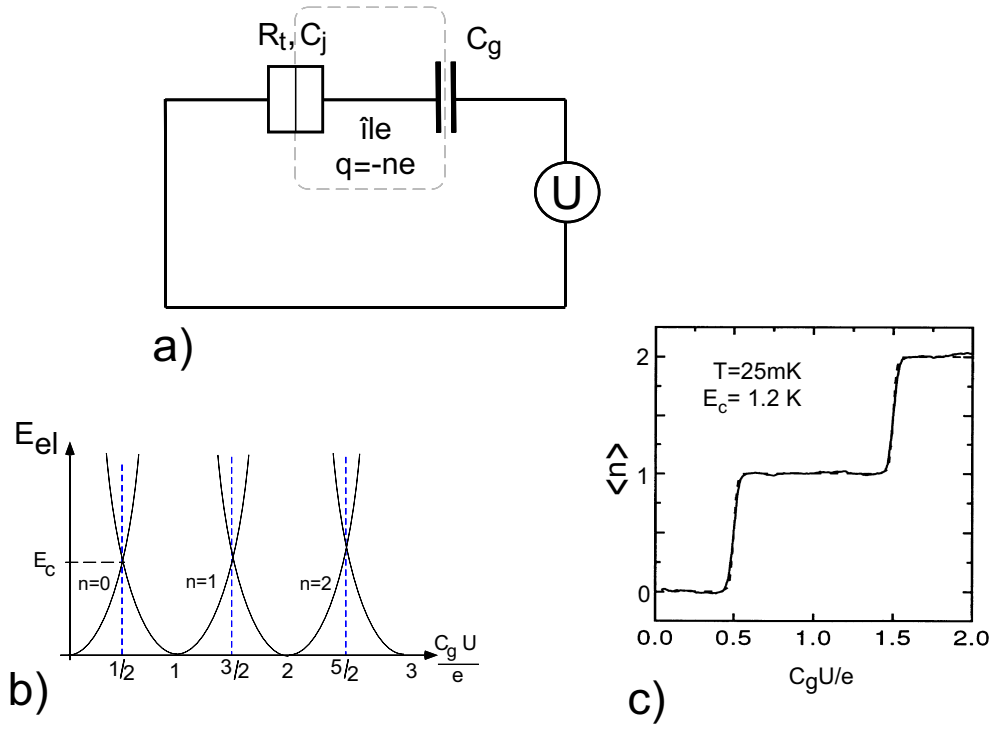

a) Représentation schématique de la boîte à électrons, b) Courbes représentatives de l'énergie électrostatique du circuit pour différents états de charge c) Mesure expérimentale de l'escalier de Coulomb, en pointillés: prédiction théorique.

encadré 3

Le transistor à un électron

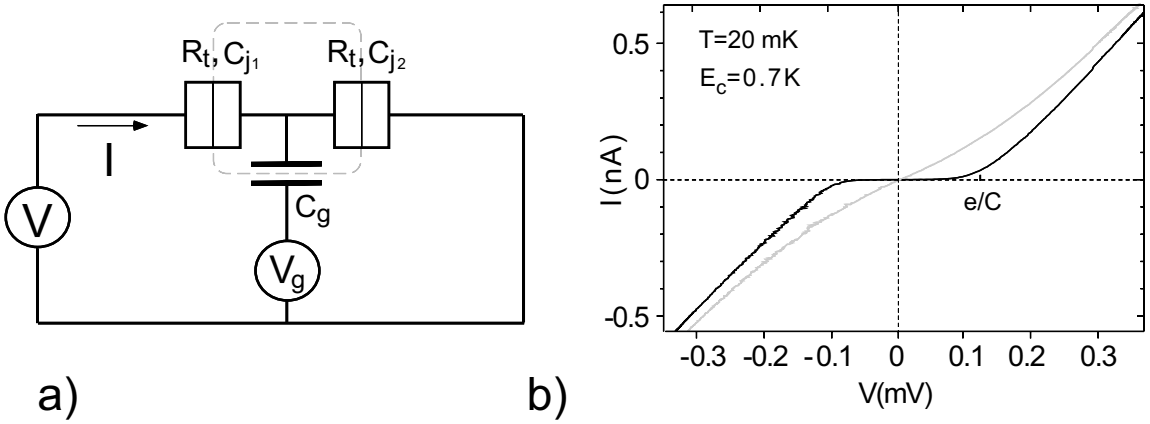

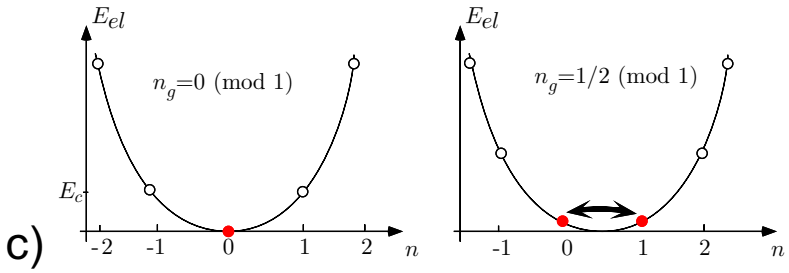

a) Représentation schématique du transistor à un électron. b) Caractéristiques courant-tension du circuit pour des nombre entiers (courbe noire) et demi-entier (courbe grise) de nombre de charge de grille $n_g=C_gV_g/e$. c) Energie électrostatique du circuit pour les deux cas limites.

La boîte à électrons

L'expérience de la boîte à électron est conceptuellement la plus simple de l'électronique à un électron [4]. Il s'agit exactement du circuit introduit dans le paragraphe précédent.

Le circuit est constitué d'une jonction tunnel placée en série avec un condensateur et une source de tension U (voir encadré 2, figure a). La petite électrode métallique située entre la jonction et la capacité est une île pouvant recevoir ou donner des électrons à travers la jonction tunnel. L'expérience consiste à mesurer la charge moyenne de l'île $\langle Q \rangle$ en fonction de la tension U. La boîte est caractérisée par l'énergie de charge $E_c = e^2/2(C_j + C_g)$ qui correspond à l'énergie électrostatique nécéssaire pour ajouter un électron sur l'île. L'énergie électrostatique totale du circuit pour un nombre n d'électrons en excès dans l'île est une fonction quadratique de la tension de grille U:

$$E_{el} = E_c(n - C_g U/e)^2 \ . \tag{3}$$

Chaque état de charge n est ainsi représenté par une parabole (voir encadré 2, figure b). Les transitions vers un état de charge voisin s'effectuent pour les paramètres correspondant aux points d'intersection des paraboles, qui intervient pour les valeurs demi-entières de la charge de polarisation réduite $C_g U/e$. Lorsque l'énergie caractéristique des fluctuations thermiques $k_B T$ est petite devant l'énergie de charge E_c nécessaire pour ajouter un électron à l'île, le nombre moyen d'électrons en excès dans l'île $\langle n \rangle$ varie avec la tension de commande U en décrivant une série de marches régulières, communément appelée "escalier de Coulomb" (encadré 2, figure c). Chaque palier correspond au nombre d'électrons qui minimise l'énergie électrostatique du circuit. L'escalier de Coulomb constitue la preuve directe de la quantification de la charge dans l'île. C'est en quelque sorte une expérience de Millikan effectuée dans l'état solide.

Le transistor à un électron

Le transistor à un électron est constitué de deux jonctions tunnel en série. l'île centrale est donc connectée à des réservoirs amont et aval (encadré 3, figure a). Il s'agit du premier circuit d'électronique à un électron réalisé il y a 10 ans [2]. Contrairement à la boîte à électrons où on réalise une expérience à l'équilibre, on mesure dans le transistor des propriétés de transport. Le système transistor+source est caractérisé par deux degrés de liberté : Le nombre n d'électrons en excès dans l'île et le nombre p d'électrons ayant traversé le circuit. L'expression de l'énergie électrostatique du circuit est la somme d'un terme analogue à celle

de la boîte à électrons (équation (3)) à laquelle il faut ajouter le travail de la source : $-peV$. Comme pour la boîte à électrons, la charge n de l'île à basse température correspond à un nombre entier d'électrons.

On s'intéresse tout d'abord aux propriétés de transport du dispositif aux faibles tensions, ceci afin d'estimer la conductance à l'origine de la caractéristique courant-tension

Deux cas limites peuvent être considérés, suivant les valeurs de la charge de polarisation réduite $n_g = C_g U/e$ (encadré 3, figure c).

• Lorsque n_g est un entier, seule la charge $n = 0$ minimise l'énergie électrostatique du circuit. Le transfert de charge à travers le transistor est donc bloqué pour les faibles tensions, puisqu'un transfert de charge nécessite un passage par l'état $n = 1$, que les fluctuations thermiques ne permettent d'atteindre lorsque la condition (2) est satisfaite. Ce phénomène générique aux nanostructures est couramment appelé "blocage de Coulomb".

• Lorsque n_g est demi-entier, les états $n = 0$ et $n = 1$ sont dégénérés (voir encadré 3, figure c). Il en résulte un effet tunnel séquentiel d'électrons individuels à travers les deux jonctions, intervenant suivant une statistique Poissonienne : l'état de charge de l'île passe successivement à travers les états $n = 1$ et $n = 0$ par suite d'évènements tunnel consécutifs à travers la jonction amont puis à travers la jonction aval. Le transistor est donc "passant", chaque évènement tunnel intervenant à un taux dont la valeur dépend de la différence d'énergie électrostatique qu'induit le transfert de charge (cf. encadré 1). Cette différence étant fonction de la tension de grille (cf. équation (3)), la conductance du transitor est ainsi modulée par cette tension. La modulation en courant est maximale pour des tensions de V de l'ordre de e/C. La période de cette modulation est égale à un électron induit sur l'île: **polarisé à tension finie, une différence de polarisation électrostatique d'un demi-électron sur la grille permet de contrôler un courant d'environ 10^9 électrons par seconde**. Une telle propriété justifie le nom de "transistor à un électron" donné à ce dispositif, qui constitue également un électromètre avec une sensibilité inégalée. C'est d'ailleurs ce circuit qui permet de mesurer la charge de l'île avec une sensibilité sub-électronique, dans l'expérience de la boîte à électrons décrite dans le paragraphe précédent.

Introduction
Les effets de charge, dix ans après

Une décennie s'est écoulée depuis la réalisation par Fulton et Dolan d'un transistor à un électron [2]. Dans ce dispositif, décrit dans le préambule, le courant est modulé par la charge induite sur une capacité de couplage avec une période égale à la charge électronique. Depuis cette expérience qui marque le début de l'électronique à un électron, de nombreux circuits ont été développés, tant pour comprendre ce nouveau domaine que pour réaliser de nouvelles fonctions [3]. Comme précisé dans le préambule, tous ces dispositifs à un électron sont constitués de petites électrodes conductrices couplées entre elles ou au reste du circuit par des jonctions tunnel ou des capacités. Leur fonctionnement repose sur la quantification de la charge de ces électrodes intermédiaires, appelées îles, lorsque les jonctions sont opaques c'est-à-dire lorsque leur résistance tunnel est grande devant le quantum de résistance. Dans ce régime, les électrons sont presque localisés dans les îles, et l'énergie du circuit est simplement l'énergie électrostatique de la configuration de charges calculée en remplaçant chaque jonction par un condensateur donné par la capacité effective de la jonction. Le passage par effet tunnel d'un électron à travers une jonction conduit à une nouvelle configuration. A très basse température, sont uniquement possibles les transitions conduisant à une configuration dont l'énergie électrostatique est inférieure. Ce processus de sélection des configurations de charge des îles est exploité dans les circuits à un électron. Dans le circuit élémentaire de la boîte à électrons [4] (cf. encadré 2), une configuration d'énergie minimale existe et est donc sélectionnée aux basses températures vérifiant $k_B T \ll E_c = e^2/2C$, où C est la capacité de l'île. Dans le transistor à un électron, qui est une île connectée à deux réservoirs, nous avons vu dans le préambule qu'il n'y a pas toujours de configuration stable vis à vis des transitions tunnel sur les deux jonctions. La configuration évolue dans ce cas selon une cascade continue et aléatoire de transitions à travers les deux jonctions, et un courant non nul traverse le circuit. C'est la dépendance du taux de transition avec la tension de polarisation de l'île qui est à l'origine de la modulation du courant. D'autres dispositifs mettent à profit les règles d'évolution pour transférer la charge électron par électron : dans l'écluse à électrons [5] et la pompe à électrons [6], un signal externe répété à la fréquence f cadence ainsi le passage des électrons un par un. Le courant à travers le circuit est alors donné par la relation $I = ef$. Ces derniers

circuits ont déjà été adoptés par les laboratoires de métrologie en vue de la mesure de la constante de structure fine et de la réalisation d'un étalon de l'ampère. Une pompe à 7 jonctions tunnel en série [7] a ainsi récemment atteint une précision relative égale à 10^{-8} pour une cadence de transfert de 5 MHz. Parallèlement à ces développements, plusieurs équipes [8] ont abordé le problème de l'extension de l'électronique à un électron aux circuits supraconducteurs. Elles ont montré qu'il était possible de construire une électronique dite "à une paire de Cooper" combinant les effets de charges aux propriétés intrinsèques à la supraconductivité. Il s'agissait tout d'abord de s'assurer de la robustesse du quantum de charge $2e$: les premières expériences [9] ont ainsi montré que la charge d'une île supraconductrice est un multiple de $2e$ si l'énergie nécessaire à la création d'une quasiparticule est plus grande que l'énergie de charge E_c. La transposition des concepts de l'électronique à un électron à l'électronique à "une paire de Cooper" ne consiste pas toutefois à seulement doubler la charge des porteurs. La cohérence quantique du condensat supraconducteur est à l'origine d'un couplage cohérent entre deux électrodes supraconductrices couplées par une jonction tunnel. Nous lui donnerons le nom de couplage Josephson puisqu'il est à l'origine d'un effet quantique macroscopique, l'effet Josephson continu, prédit en 1962 par Brian Josephson. La situation rencontré dans ce cas est très différente de l'effet tunnel intervenant entre électrodes "normales" (*i.e.* non supraconductrices), pour lequel le transfert de charge est dissipatif et incohérent puisqu'il aboutit à la création d'excitations de paires électron-trou décorrélées les unes par rapport aux autres.

L'effet "Josephson" induit une délocalisation des paires de Cooper: il est antagoniste aux effets de charge qui tendent au contraire à localiser les paires de Cooper dans les îles. C'est cette compétition entre le couplage Josephson et les effets de charge qui explique notamment la modulation du courant critique (i.e. courant supraconducteur maximum) observée dans la version supraconductrice du transistor à un électron [10].

Les questions abordées dans cette thèse

Les succès obtenus ne doivent toutefois pas masquer le fait que les fondements mêmes de l'électronique à un électron ou à une paire de Cooper ne sont bien compris que dans la limite où l'effet tunnel apporte une perturbation faible aux interactions électrostatiques. Le thème principal de cette thèse porte sur les circuits de petites jonctions tunnel, normaux et supraconducteurs, dans le régime où le couplage par effet tunnel entre les différentes électrodes est assez important pour modifier les effets de charge de façon non perturbative. Tout d'abord, s'il est couramment admis que la quantification de la charge des îles nécessite des jonctions tunnel suffisamment opaques, la façon précise dont les effets à un électron s'effacent lorsque les jonctions deviennent très passantes n'est pas connue. Que devient dans ce régime le circuit le plus simple de la mono-électronique, à savoir le transistor à un électron ? Ce problème est abordé dans le premier chapitre de cette thèse, dans le but de dégager des résultats expérimentaux un scénario pour la disparition des effets de charge dans le régime d'effet tunnel fort.

L'électronique à une paire de Cooper, quant à elle, n'a pas été explorée au delà du transistor supraconducteur [10], où le phénomène essentiel qu'est la compétition entre effets de charge et couplage Josephson n'a été qu'indirectement observé. Peut-on mettre en évidence cette compétition en mesurant la charge d'une électrode supraconductrice fortement couplée à un réservoir supraconducteur par une jonction Josephson ? Qu'elle est l'analogue pour les electrodes supraconductrices de la limite des faibles résistances tunnel ($R \ll R_K$) ? Pour répondre à ces questions, nous avons réalisé l'expérience de la "boîte supraconductrice à une paire de Cooper" qui constitue la version entièrement supraconductrice de la boite à électrons. Ce nouveau circuit présente également un intérêt fondamental du point de vue de la mécanique quantique, puisqu'elle permet "d'intégrer", au sens de la microélectronique, un système quantique à deux niveaux : l'état quantique fondamental de l'île correspond en effet à une superposition cohérente de deux états de charge différant de $2e$. Ces développements font l'objet du chapitre 2 de cette thèse.

Cette expérience ne donne toutefois pas accès aux états excités. La spectroscopie des états quantiques d'un circuit à une paire de Cooper est-elle possible ? Nous avons imaginé dans ce but un circuit, plus complexe que la boîte supraconductrice, qui comporte deux îles fortement

couplées. Un signal de radio-fréquence irradiant une île induit des transitions vers les états excités. Ces états sont détectés par la variation du courant supraconducteur maximum pouvant circuler à travers le circuit. Les résultats préliminaires obtenu sur ce circuit sont présentés dans le troisième chapitre de cette thèse.

Il existe aussi une autre différence extrêmement importante entre l'électronique à un électron et l'électronique à une paire de Cooper concernant l'effet de l'environnement électromagnétique du circuit. Nous avons considéré jusqu'ici des circuits polarisés en tension. La théorie du blocage de Coulomb pour les circuits à un électron montre que cette approximation est excellente si l'impédance entre la source de tension et le circuit est faible devant R_K. Dans le cas opposé, -qui n'a pu être qu'imparfaitement réalisé expérimentalement-, la présence de cette impédance conduit à une réduction de la conductance aux faibles tensions même dans le cas d'une simple jonction. Ce comportement non linéaire est dû au partage, lors du passage d'un électron par effet tunnel, de l'énergie électrostatique disponible entre les modes électromagnétiques de l'impédance et les degrés de liberté électroniques des électrodes. L'effet de l'environnement sur les circuits à une paire de Cooper n'est connu quant à lui que dans la limite des faibles couplages Josephson. Lorsque le couplage Josephson est fort, la question qui se pose naturellement est de savoir si le courant critique qui peut traverser une jonction est affecté par l'environnement électromagnétique. Ce problème du blocage de Coulomb de l'effet Josephson est abordé théoriquement dans le chapitre 4 de cette thèse.

Comme signalé plus haut, les applications présentes de l'électronique à un électron sont la métrologie, avec l'écluse et la pompe à électrons, et l'électrométrie, avec le transistor à un électron. La sensibilité de ce dernier dispositif est d'ailleurs exploitée pour mesurer la charge de l'île dans toutes les expériences du type boîte à électrons. La précision sub-électronique obtenue mérite à elle seule de l'interêt. De façon générale, quels sont les mécanismes qui limitent la détection de charge ? Comment se comparent des transistors fabriqués de différentes façons ? Peut-on utiliser un transistor à un électron pour détecter sans les perturber des particules chargées ? Ces questions sont discutées dans le chapitre 5.

Les expériences réalisées pour cette thèse utilisent des circuits de petites jonctions tunnel fabriqués au laboratoire pour la plupart par lithographie électronique. Plus généralement, toutes les considérations sur l'électronique à un électron ou l'électronique à une paire de Cooper n'ont d'intérêt que si l'on parvient à fabriquer les circuits imaginés. La complexité croissante

de ces circuits nécessite notamment des techniques de fabrication plus souples autorisant plus de fonctionalités. Peut-on intégrer dans le même circuit des jonctions, des condensateurs et des résistances ? Existe-t-il d'autres méthodes générales de nanofabrication outre la lithographie électronique ? Les procédés de fabrication que nous avons développés pour répondre à ces questions sont décrits dans le chapitre 6.

Les principaux résultats obtenus sur les questions abordées dans cette thèse sont résumés dans les paragraphes qui suivent.

Le transistor à un électron dans le régime passant $R_T < R_K$

De façon surprenante, le comportement du simple transistor à un électron dans le régime "passant" $R_T < R_K$ n'est qu'en partie élucidé du point de vue théorique, et les résultats expérimentaux publiés se limitent à constater l'affaiblissement des effets de charge. La relative absence de résultats expérimentaux s'explique notamment par la difficulté de déterminer les paramètres du transistor de façon indépendante, en particulier l'énergie de charge de l'île $E_c^0 = e^2/2C$ où C est la capacité de l'île en absence d'effet tunnel. Nous avons résolu cette difficulté en mesurant, pour le même transistor rendu supraconducteur par la suppression du champ magnétique, la position dans le plan $U - V_g$ de résonances en courant récemment identifiées. Nous avons mesuré la conductance G de plusieurs transistors d'énergies de charge E_c^0 voisines mais de résistances tunnel R_T différentes variant dans la gamme $5-100$ kΩ donc s'étallant de part et d'autre du seuil $R = R_K$.

Les variations de G avec la charge de polarisation réduite $n_g = C_g V_g/e$ et la température sont portées sur la figure 1 pour des valeurs de résistance tunnel respectivement grandes et de l'ordre du quantum de résistance. Les différences entre les deux réseaux de courbes sont particulièrement notables à basse température. Pour le transistor "peu passant", les pics de conductance sont fins et ont une valeur maximale proche de la moitié de la conductance asymptotique à haute température. Ce comportement est bien celui prévu par le modèle de transfert séquentiel de la charge par les deux jonctions brièvement décrit dans le préambule. Les pics correspondent aux valeurs de n_g pour lesquelles deux états de charge de l'île ont la même énergie. Pour le transistor "passant", les pics restent larges et continuent de diminuer jusqu'aux plus basses températures explorées. Cet effet, récemment étudié théoriquement, est semblable à l'effet Kondo : l'état quantique de l'île restreint à deux états de charge voisins est

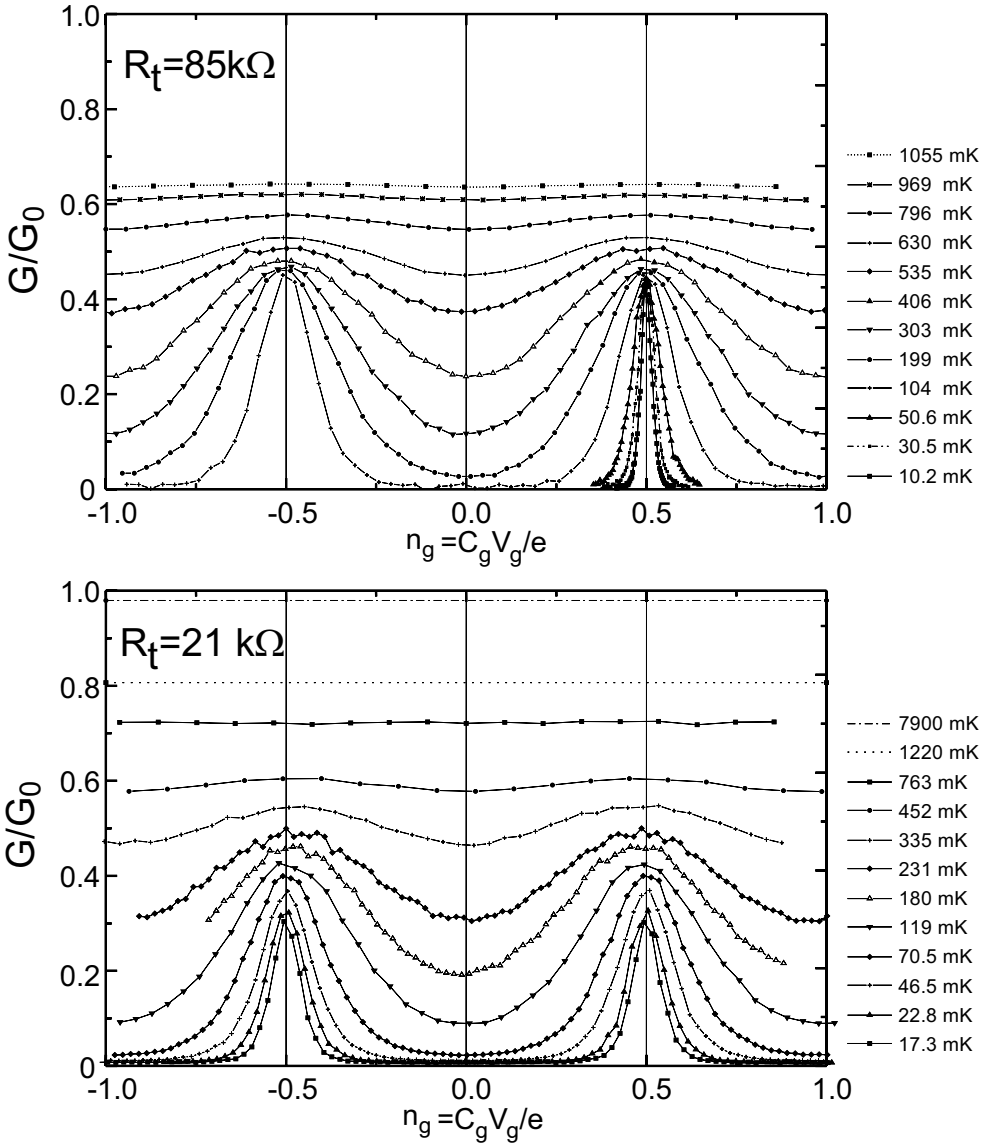

Figure 1. Mesures de la conductance réduite de transistors à un électron en fonction de la charge de grille n_g à diverses températures. Les deux régimes sont ici présentés. En haut, le transistor aux jonctions résistives ($R_t \approx 85$ kΩ), présente des pics de conductance à $n_g = 1/2$ étroits à basse température dont le maximum atteint la moitié de la conductance asymptotique G_0, (valeur prédite par la théorie de l'effet tunnel séquentiel). En bas, le transistor possède des jonctions passantes ($R_t \approx 21$ kΩ $\sim R_K$) et les pics de conductance restent larges à $n_g = 1/2$, leur maximum continuant à décroitre à basse température.

l'analogue du spin, et les excitations tunnel sont les analogues des excitations électroniques. Le scénario suivant se dégage de l'ensemble des résultats expérimentaux : A haute température, la conductance d'un transistor "passant" se comporte comme celle d'un transistor peu passant mais avec une énergie de charge renormalisée $E_c^{eff} < E_c^0$, l'effet étant d'autant plus important que la résistance tunnel est petite devant R_K. Cette description reste valable jusqu'à des températures inférieures à E_c^0/k_B. A plus basse température, la modulation de la conductance par les effets de charge diminue progressivement. La comparaison avec les prédictions théoriques prenant en compte l'effet tunnel à tous les ordres en perturbation reste délicate car ces théories font intervenir des paramètres renormalisés non déductibles de l'expérience. Nous présentons également les résultats d'un calcul très récent où le hamiltonien tunnel est développé au deuxième ordre en perturbation qui rend bien compte des résultats expérimentaux tant que la résistance n'est pas trop petite devant le quantum de résistance.

L'effet Josephson à une paire de Cooper dans la boîte supraconductrice

L'expérience de la boîte à une paire de Cooper constitue l'analogue supraconducteur de la boîte à électrons présentée dans le préambule : Le circuit est constitué d'une petite jonction Josephson en série avec un condensateur et une source de tension U (voir cartouche figure 2). La petite électrode supraconductrice entre la jonction et la capacité est une île pouvant échanger des paires de Cooper à travers la jonction avec un réservoir supraconducteur. L'énergie électrostatique de cette île peut être modifiée en variant la tension de polarisation U. L'expérience consiste à mesurer la charge moyenne en excès dans l'île en fonction de U. Cette mesure s'effectue en couplant capacitivement l'île à un électromètre de sensibilité sub-électronique qui n'est autre qu'un transistor à un électron décrit dans le préambule.

Dans la boîte à électrons, les effets de charge, qui tendent à quantifier le nombre de charges en excès dans l'île, sont uniquement en compétition avec les fluctuations thermiques. Dans la boîte à paires de Cooper, le couplage Josephson qui tend à délocaliser les paires de Cooper doit de plus être pris en compte.

Le circuit est conçu pour que l'énergie de couplage Josephson notée E_J soit légèrement inférieure à l'énergie electrostatique de l'île: $E_c = e^2/2C$, où C est la capacité totale de l'île.

Dans l'expérience que nous avons réalisée, le nombre moyen de paires de Cooper en excès $\langle n \rangle$ est une fonction de la tension U en forme d'escalier, indépendante de la température pour

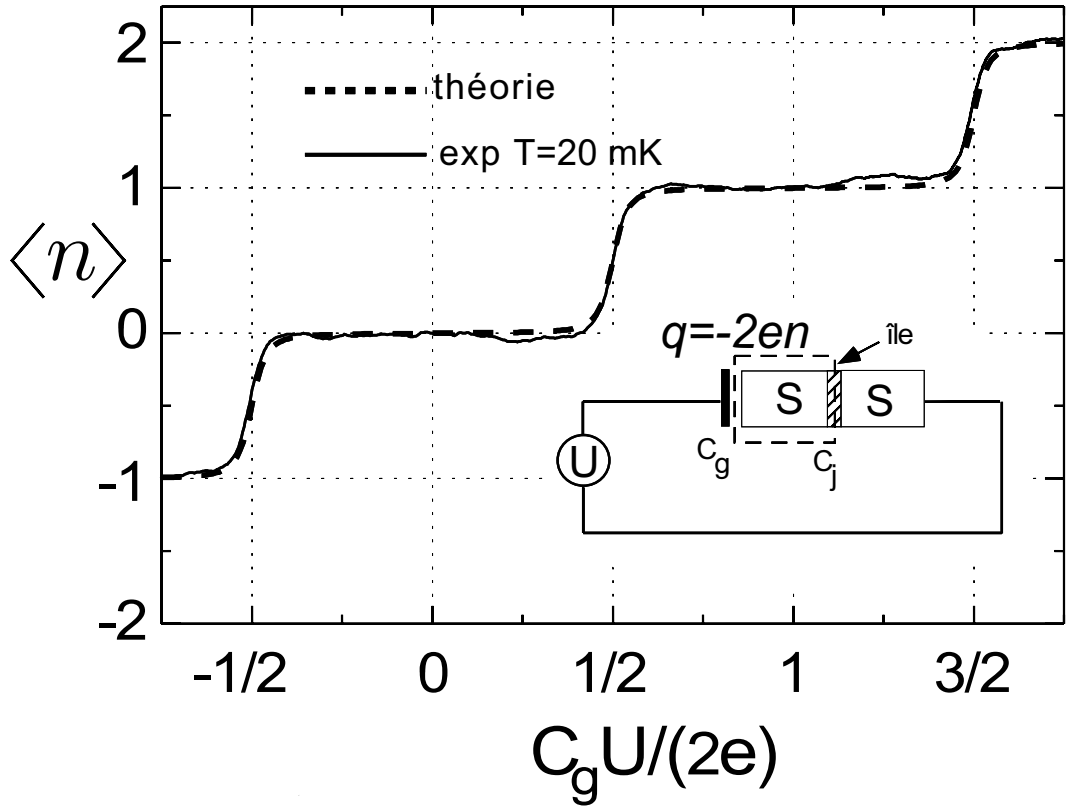

Figure 2. Variations de la nombre moyen de paires de Cooper en excès $\langle n \rangle$ dans la boite à paires de Cooper en fonction de la tension de commande réduite $C_g U/(2e)$. La courbe expérimentale obtenue à 20 mK (trait plein) est comparée à la prédiction théorique (en pointillés).

$T < 80$ mK, et dont la hauteur de chaque marche est égale à paire de Cooper (voir figure ci-contre). Chaque palier correspond au nombre de paires de Cooper qui minimise l'énergie électrostatique du circuit. Sur un palier, le circuit se trouve dans un état quantique où le nombre de paires dans l'île est bien défini. Par contre la transition entre deux paliers successifs garde une largeur finie à basse température en raison du couplage Josephson qui induit des fluctuations quantiques lorsque l'énergie séparant deux configurations de charge voisines est inférieure à E_J. Dans la plage de transition, l'état quantique du circuit est une superposition cohérente des deux états de charge voisins $|n\rangle$ et $|n+1\rangle$. Au milieu de la marche, le circuit est ainsi dans l'état $\frac{1}{\sqrt{2}}(|n\rangle + |n+1\rangle)$, la pente de la courbe en ce point est égale au rapport de l'énergie électrostatique d'une paire de Cooper $4E_c$ sur l'énergie Josephson E_J, énergies qui peuvent être évaluées indépendamment. La courbe théorique tracée pour ces valeurs est en bon accord avec la courbe expérimentale. Cette expérience, qui constitue l'observation directe de l'effet Josephson mettant en jeu une unique paire de Cooper, réalise un état de cohérence quantique pour un système macroscopique.

Le blocage de Coulomb de l'effet Josephson

Le système que nous avons étudié est formé d'une jonction Josephson de courant critique I_0 en série avec une impédance supraconductrice arbitraire. On impose une phase δ aux bornes du système. Une telle polarisation peut s'effectuer en refermant le circuit sur lui-même et en appliquant un flux magnétique à travers la boucle ainsi formée (voir figure 3).

Le hamiltonien de ce système est la somme du hamiltonien Josephson et du hamiltonien de l'environnement. L'état fondamental correspond à un courant non nul $I(\delta)$ dont l'expression en l'absence d'impédance est donnée par la relation de Josephson $I(\delta) = I_0 \sin\delta$. Nous avons tout d'abord effectué un calcul champ moyen de ce courant et trouvé que le courant supraconducteur maximum I_c est d'autant plus diminué par rapport à I_0 que l'impédance est grande. Ce phénomène peut être considéré comme un blocage de Coulomb de l'effet Josephson. Nous avons comparé les prédictions de ce calcul au résultat exact obtenu numériquement pour un environnement comportant un seul mode (cas où l'impédance en série est une pure inductance). Par analogie avec le système spin-boson, nous avons modifié le calcul champ moyen pour incorporer les effets de renormalisation des modes de basse énergie de l'environnement. Dans l'état fondamental, ces modes sont en effet éliminés car la modification de leur état ne coûte pas d'énergie. Nous avons ainsi obtenu le facteur de renormalisation du courant critique

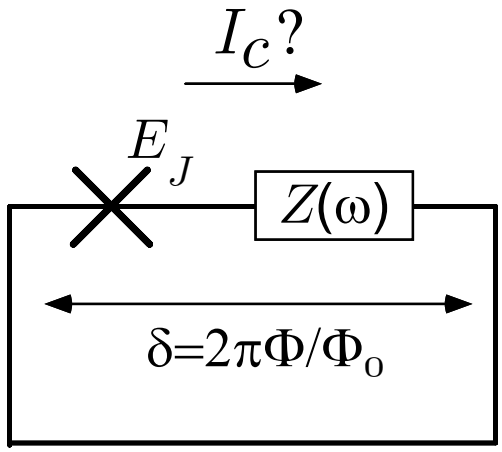

Figure 3. Représentation schématique du circuit : une jonction Josephson caractérisée par l'énergie de couplage Josephson E_J est mise en série avec une impédance $Z(\omega)$. Le dipôle ainsi formé est polarisé en phase par une boucle coupant un flux magnétique Φ. Il s'agit de trouver le courant supraconducteur maximum de la jonction pour une impédance Z donnée.

pour une impédance arbitraire. Cette expression généralise le résultat récemment obtenu par d'autres auteurs dans un cas particulier d'environnement. Nous avons ensuite repris le calcul en ne supposant pas l'existence du hamiltonien Josephson mais en partant du hamiltonien tunnel. Nous avons combiné des résultats précédemment obtenus sur la modification du hamiltonien Josephson par une impédance avec nos résultats pour déterminer l'expression générale du courant critique en fonction de la résistance tunnel de la jonction et de l'impédance du circuit.

Application à l'électrométrie du transistor à un électron

Nous avons évalué les performances des transistors à un électron en mesurant leur bruit. A basse fréquence, ce bruit est d'origine extrinsèque : le déplacement des charges environnantes modifient la charge induite sur l'île et par suite le courant mesuré. Nous avons mis en évidence l'importance des fluctuateurs chargés, sources de bruit télégraphique au voisinage immédiat ou dans la barrière des jonctions tunnels. Nous avons comparé les bruits de transistors fabriqués sur différents substrats et ayant des îles de différentes tailles. Ces mesures nous permetent notamment de conclure que le niveau moyen du bruit en charge (voir figure 4) ne dépend pas de la nature chimique du substrat.

La compréhension du couplage électrostatique de charges extérieures ponctuelles à un électromètre nous a permis d'envisager l'utilisation d'un transistor à un électron pour détecter le

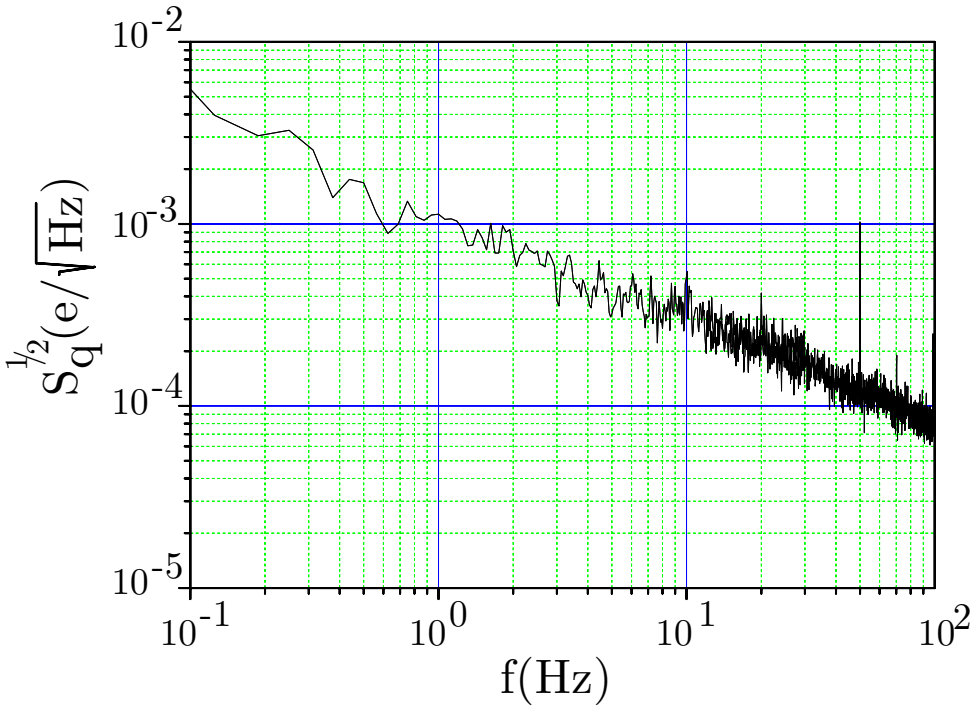

Figure 4. Densité spectrale du bruit en charge typique d'un transistor à un électron mesurée à 20 mK. Le bruit en 1/f observé est attribué à la superposition des bruits télégraphiques émis par des dipôles fluctuants au voisinage de l'île du transistor. Le niveau de bruit de référence est de 3×10^{-4} *e.Hz*$^{-1/2}$ *à 10 Hz.*

mouvement de particules chargées (voir figure 5).

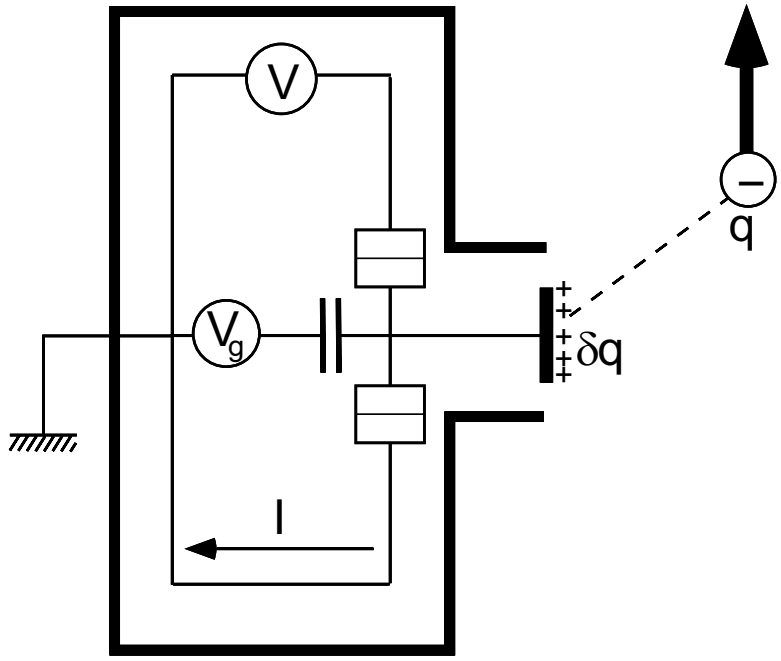

Figure 5. Schéma d'un dispositif utilisant un transistor à un électron polarisé en tension pour détecter la position d'une particule chargée. La charge q induit une charge δq sur l'île du transistor. Les déplacements de la charge sont mesurées par la variations du courant dans le transistor.

Un tel dispositif pourrait en effet s'avérer utile pour une mesure délicate de physique des particules : Nous avons montré que la sensibilité d'un transistor à un électron rend concevable la mesure de la masse gravitationnelle d'antiprotons effectuant un mouvement unidimensionnel le long de l'axe d'un tube équipotentiel. Nous avons estimé que le transistor à un électron possède un niveau de bruit suffisant bas pour de telles mesures. En outre il apporte une perturbation electromagnétique en retour sur la particule qui ne masque pas l'effet de la gravitation.

Techniques de fabrication

Les circuits à un électron, qui comportent des détails de taille inférieure à 100 nm, sont obtenus par lithographie électronique. Cette technique est universellement utilisée pour fabriquer des nanostructures dont les dimensions sont bien contrôlées : le faisceau d'électrons accéléré dans une colonne de microscope à balayage vient altérer localement une résine électrosensible conduisant à la réalisation d'un masque. D'autres techniques de lithographie mettant à profit les microscopes à sonde de proximité (STM, AFM, etc.) ont été proposées mais elles sont trop spécifiques pour s'appliquer à la fabrication de circuits à un électron.

Nous avons développé une technique générale de lithographie basée sur le microscope à force atomique (AFM). Dans ce nouveau procédé, la pointe effilée du microscope vient creuser un sillon étroit dans une couche molle de polyimide (figure 6). Ce sillon est ensuite transféré dans une couche mince de germanium qui sert de masque pour l'évaporation des couches constituant la nanostructure. Nous avons fabriqué à l'aide de cette technique un transistor à un électron de performances équivalentes à celles de transistors fabriqués selon les techniques conventionnelles.

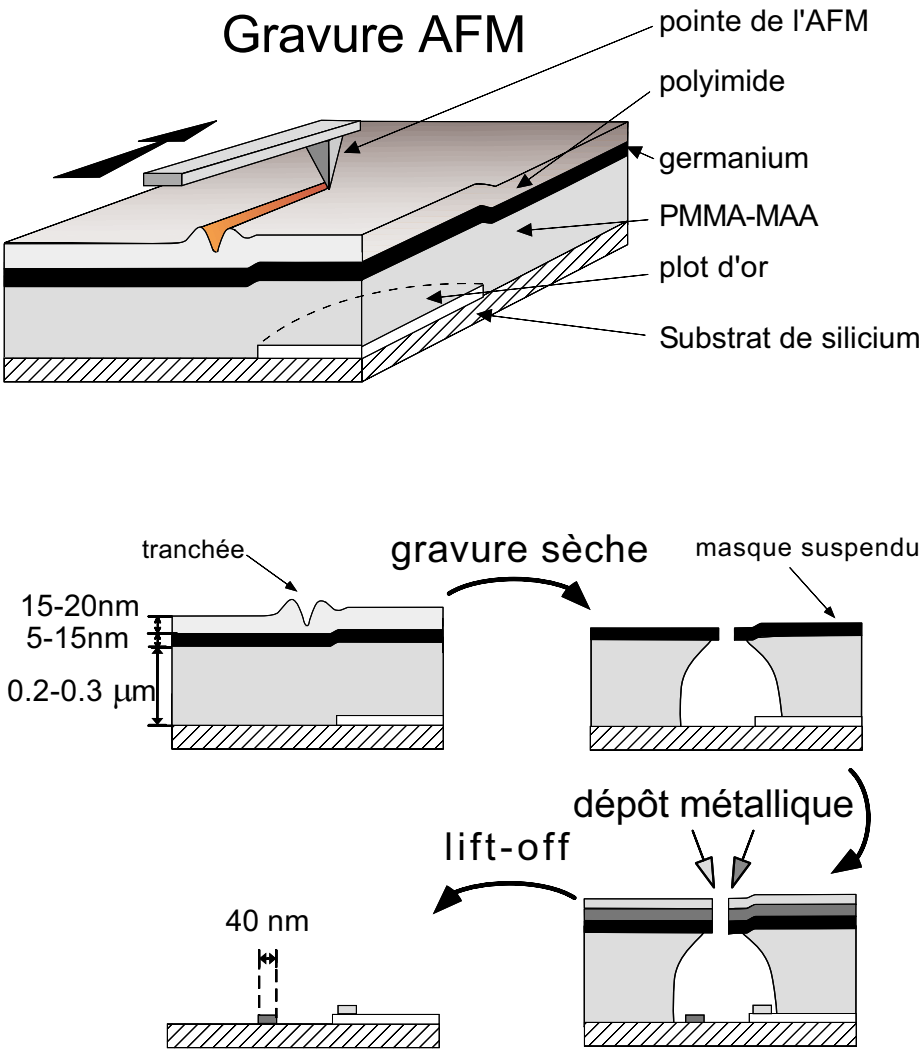

Figure 6. Procédé de fabrication de nanostructures à l'aide d'un microscope à force atomique (AFM). La pointe du microscope, appliquée en fort contact (force $\sim \mu N$) sur la couche molle de polyimide y creuse un sillon (haut). La couche de polyimide, amincie sous le sillon, ne protège plus le masque sous-jacent de germanium lors de l'attaque par gravure sèche, ce qui aboutit au percement du masque sous le sillon. La nanostructure est obtenue par évaporation à travers le masque de couches métalliques, masque qui est finalement retiré, dégageant les structures évaporées dont la taille latérale est de l'ordre de 40 nm.

Par ailleurs, les développements de l'électronique à un électron conduisent à imaginer des circuits de plus en plus complexes. Ceux-ci nécessitent l'intégration croissante de fonctionalités impossibles à réaliser sur une seule couche conductrice. Nous avons donc développé une technique de fabrication en multicouches qui offre comme nouvelles fonctions de pouvoir établir des connexions ou des couplages capacitifs avec un circuit préalablement fabriqué, "enterré" sous une couche séparatrice isolante et percée aux points de connexions (voir figure 7). Cette technique permet ainsi le contrôle de l'environnement électromagnétique de circuits à une paire de Cooper et la réalisation de lignes blindées pour l'injection de signaux radio-fréquence.

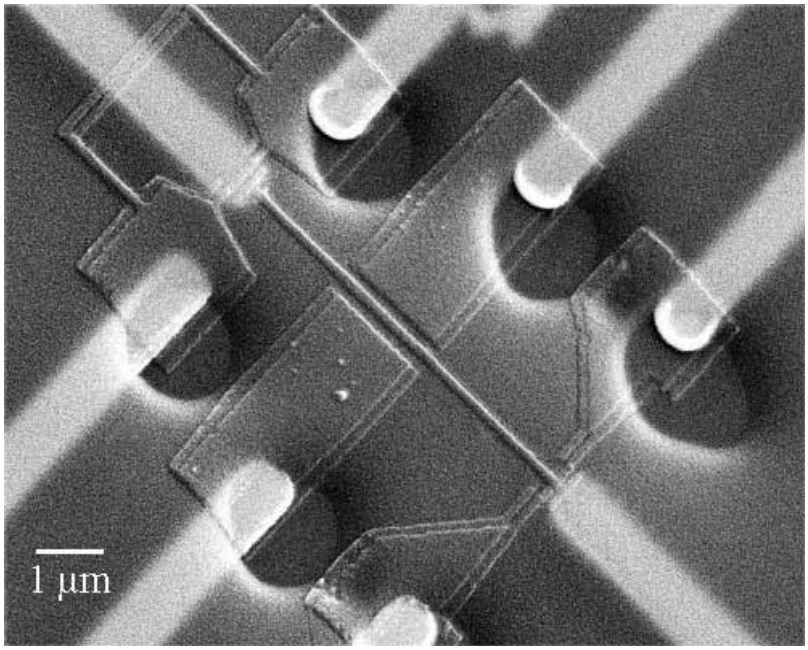

Figure 7. Micrographie prise au microscope electronique à balayage d'un circuit multicouche composé d'une boite à paires de Cooper (en haut à gauche) couplée à un électromètre (en bas à droite). La nanostructure a été déposée sur une couche isolante de polyimide percée en 6 points (cercles sombres) pour contacter des fils d'or sous-jacents. La polarisation électrostatique des îles s'effectue grâce à des capacités enterrées dont les armatures inférieures sont les extrémités des deux fils non découverts.

Références

[1] R.A. Millikan, Phys. Rev. **32,** 349, (1911).

[2] T. A. Fulton and G. J. Dolan, Phys. Rev. Lett. **59**, 109 (1987).

[3] M. H. Devoret, D. Esteve and C. Urbina, Nature **360,** 547 (1992); pour une revue du sujet plus développée : *Single Charge Tunneling*, NATO ASI series, eds. H. Grabert and M. H. Devoret (Plenum, New York, 1992).

[4] P. Lafarge, H. Pothier, E.R. Williams, D. Esteve, C. Urbina, and M. H. Devoret, Z. Phys. **B 85**, 327 (1991).

[5] L.J. Geerligs, V.F. Anderegg, P.A. M. Holweg, J.E. Mooij, H. Pothier, D. Esteve, C. Urbina and M.H. Devoret, Phys. Rev. Lett. **64**, 2691, (1990)

[6] H. Pothier, P. Lafarge, D. Esteve, C. Urbina, and M. H. Devoret, Europhys. Lett., **67**, 1626, 1991

[7] J.M. Martinis, proceeding of CPEM'96, see also J.M. Martinis, M. Nahum, and H.J. Jensen, Phys. Rev. Lett. **72**, 904 (1994).

[8] M.T. Tuominen, J.M. Hergenrother, T.S. Tighe and M. Tinkham, Phys. Rev. Lett. **69**, 1997, (1992).

[9] P. Lafarge, P. Joyez, D. Esteve, C. Urbina, and M. H. Devoret, Nature **365**, 422, (1993).

[10] P. Joyez, P. Lafarge, A. Filipe, D. Esteve, C. Urbina, and M.H. Devoret, **72**,15, (1994)

[11] L.J. Geerligs, Ph. D. Thesis, Delft University of Technology, 1990.

[12] P. Lafarge, P. Joyez, D. Esteve, C. Urbina, and M.H. Devoret, Phys. Rev. Lett. **70**, 994 (1993).

Introduction
Single charge effects : ten years after

Ten years have passed since the realization by Fulton & Dolan of the first single electron transistor (SET) [2]. In this device, the current is modulated by the charge induced on a coupling capacitor, with a period equals to the electronic charge (see frame). This experiment marked the beginning of single electronics. Many other devices have since been realized, with the aim of understanding this new emerging field and exploring new electronic functions [3] . All these single electron devices are made of small conducting electrodes coupled to each other and to the rest of the circuit by tunnel junctions or capacitors. Their operating principle is based on the quantization of charge in intermediate electrodes, nicknamed islands, when the tunnel junctions are sufficiently opaque. More precisely, when the tunnel junction resistances R_T far exceed the resistance quantum $R_K = h/e^2 \approx 26\ k\Omega$, the charge of each island corresponds to an integer number of electrons. Electrons are localized in the islands and the energy of the system is given by the electrostatic energy for which tunnel junctions are replaced by equivalent capacitances. When an electron tunnels through a junction, a new energy configuration is generally obtained. At very low temperature, only transitions towards configurations with lower electrostatic energies are possible. Single electron devices exploit these selection processes. In the single electron box [4] (see inset), a unique minimum configuration is selected when $k_B T \ll E_c = e^2/2C$, where C is the total island capacitance and E_c the associated charging energy. In the single electron transistor composed of an island connected to two reservoirs, there is not always a stable configuration with respect to tunnel transitions through each junction. In such a case, the circuit state evolves in a continuous cascade of random transitions through both junctions and a finite current flows through the whole circuit. The dependence of transition rates on the island polarization voltage induces the current modulation. Other devices exploit evolution rules and enable the transfer of charges one by one: in the "turnstile" [5] and the "pump" devices [6], an external signal at a frequency f clocks the transfer of electrons. The current through the circuit is then given by the fundamental relation $I = ef$. This last device has been chosen by metrologists to realize a current standard and to provide a precise measurement of the fine structure constant α. A 7-junctions pump operated at 5 MHz has already reached a relative precision of 10^{-8} [7].

The single electron box

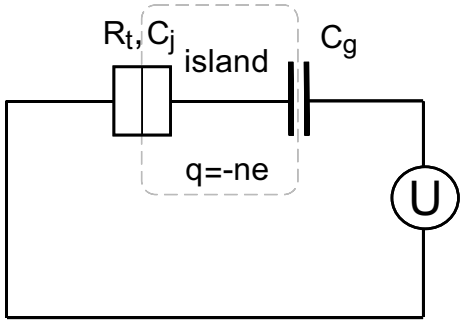

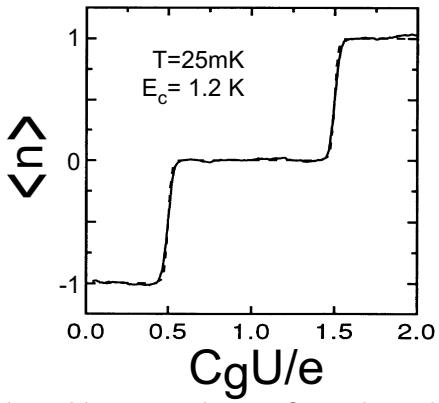

The electron box consists of a tunnel junction in series with a capacitance C_g and a voltage source U. The small metallic electrode between the junction and the capacitance is an island exchanging electrons through the junction. When the characteristic energy of thermal fluctuations k_BT is small compared to the charging energy $E_C=e^2/2(C_j+C_g)$ corresponding to the cost for adding an extra electron to the island, the average number <n> of electrons in the island is a step-like function of the voltage U so-called "Coulomb staircase". Each plateau corresponds to the number of electrons which minimize the electrostatic energy of the circuit. Transitions to the next step occur when the electrostatic energy of the two neighboring charges states are equal. This is obtained for half-integer values of the reduced polarization charge C_gU/e.

The single electron transistor (SET)

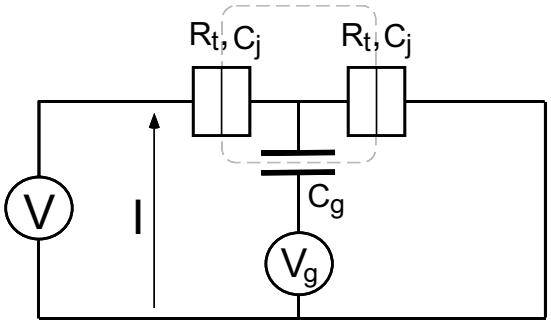

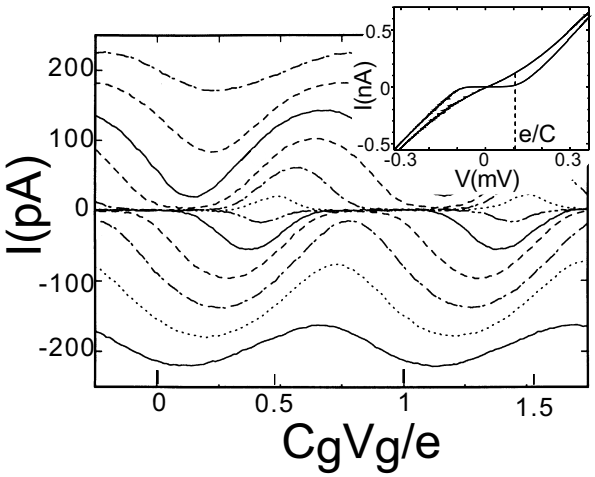

The single electron transistor consist of two ultrasmall tunnel junction in series. The intermediate electrode (island) is capacitively coupled to a voltage Vg. As for the electron box, the island charge at low temperature is equal to an integer number of electrons. The current results from sequential tunnel effect of single electrons through both junctions. Each tunnel event occurs at a rate which depend of the change in electrostatic energy that it induces. Since the electrostatic energy of the island depends on the gate voltage, the current through the whole device is periodically modulated by the gate voltage. In a voltage biased SET, the current modulation is maximum for bias of the order of e/C (see curves). This modulated period is equal to one induced electron on the island. electrostatically coupled to a measurement, this device is an electrometer with a sub-electronic charge sensitivity. It has been used to measure the charge of the electron box described above.

Meanwhile, several groups [8] have investigated the extension of single electronics to superconducting circuits. The first experiments [9] have shown that the charge of a superconducting island is a multiple of $2e$, if the energy necessary to create a quasi-particle is larger than the charging energy. The adaptation of single electron concepts to a newly developed "single Cooper pair electronics" does not merely consist in doubling the carrier charges. The quantum coherence of the superconducting condensate leads to a strong coupling between two superconducting electrodes separated by a tunnel junction (*i.e.* a Josephson junction). This tends to delocalize Cooper pairs and therefore counteracts charging effects which tend to spatially localize charges in islands. The modulation of the critical current (*i.e.* maximum supercurrent) in the superconducting version of the SET originates from this competition between charging effects and the Josephson effect [10].

The questions addressed in this work

The achievements previously mentioned should not hide the fact that the foundations of single charge tunneling are still not well settled: A good understanding is only provided in the limit of a perturbational tunnel effect with respect to electrostatic interactions. The main subject of this thesis concerns normal and superconducting circuits composed of small tunnel junctions in which the tunnel coupling is strong enough to alter significantly charging effects. First of all, if it is currently agreed upon that charge quantization in islands necessitates sufficiently opaque tunnel junctions, the way these single charge effects are washed out when tunnel junctions become transparent is not known. How does the single electron transistor behave in this regime? This issue is reviewed in the first chapter of this thesis, in which experimental results suggest a scenario for the vanishing of charging effects in the strong coupling regime.

On the other hand, single Cooper pair electronics has not been investigated beyond the superconducting transistor where competition between charging effects and the Josephson effect is only indirectly observed. Is it possible to show directly this competition by measuring the charge of a superconducting electrode strongly coupled to a superconducting reservoir of charges? For this purpose, we have realized the experiment called "the single Cooper pair superconducting box", described in the second chapter of this thesis.

This experiment is also of fundamental interest regarding quantum mechanics since the ground state of the island, which is a coherent superposition of two charge states differing by $2e$, can be directly probed. However, this experiment gives no information on excited quantum states.

Is the spectroscopy of the quantum states in a single Cooper pair circuit possible? We have considered a novel circuit, more complex than the superconducting box, in which two islands very strongly coupled to each other are placed in a superconducting transistor. A radio-frequency signal irradiating one island induces transitions to excited states. These states are probed by the change of the critical current flowing through the whole circuit.

Very preliminary results on this system are presented in the third chapter of this thesis.

Another essential difference between single electronics and single Cooper pair electronics regards the action of the electromagnetic environment. Up to now, we have only considered voltage biased circuits. The Coulomb blockade theory for single electron circuits shows that this approximation is excellent if the impedance between the voltage source and the circuit is much lower than the resistance quantum R_K. In the opposite case, which has been only imperfectly realized experimentally, the impedance in series reduces the conductance at low voltages even if it is connected to a single junction. This reduction can be explained by the excitation of electromagnetic degrees of freedom of the impedance due to the tunneling of a single electron.

On the other hand, Coulomb blockade theory for Single Cooper pairs circuits is only known in the limit of low Josephson coupling. In the case of strong Josephson coupling, one can wonder whether the maximum supercurrent that can flow through a single junction is reduced by the electromagnetic environment. The problem of Coulomb blockade of Josephson tunneling is theoretically treated in the chapter 4.

Recent applications of single electronics can be found in metrology with the development of the turnstile and the electron pump and in charge detection with the single electron transistor. We take advantage of the sensitivity of this latter device to measure the island charge in the electron box experiment. What mechanisms set the detection limit? Can we compare SETs fabricated with different methods? Can these devices be used to monitor the position of charged particles? We try to provide answers to these questions in chapter 5.

All experiments described in this thesis are based on circuits with small tunnel junctions

and metallic islands fabricated in the laboratory using electron beam lithography. In the same way, any consideration regarding single electronics are of interest only if one can fabricate the envisioned circuits. The increasing complexity of these circuits necessitate more versatile techniques which implement new features. Can one succeed in integrating on one chip ultrasmall junctions, capacitors with overlap and resistances? Are there other general-purpose techniques that allow us to fabricate nanostructures? Novel fabrication methods developed during this thesis are described in chapter 6.

The main results obtained in this thesis for the different fields mentioned above are summarized in the following paragraphs.

The single electron transistor in the high transparency limit $R_T < R_K$

Surprisingly, the behavior of a simple single electron transistor is only partly solved theoretically in the high transparency limit $R_T < R_K$. On the other hand, experimental results are limited to observing the weakening of charging effects. The relative lack of experimental results can be explained by the difficulty to determine independently the transistor parameters, in particular the charging energy $E_c^0 = e^2/2C$ where C is the island capacitance without tunneling. We have solved this problem by obtaining an independent determination of E_c . This was done by measuring resonance positions in the $U - V_g$ space for the same transistor but in the superconducting state, obtained by suppressing the applied magnetic field. We have measured the conductance G of several transistors with similar charging energies E_c^0 but with different tunnel resistances R_T in the interval $5 - 100$ kΩ.

The measured dependence of the reduced conductance G/G_0 with the reduced polarization charge $n_g = C_g V_g/e$ and with temperature are plotted on figure 1 for values of R_T respectively much larger and a bit smaller than the resistance quantum. Differences between the two sets of curves are especially clear at low temperatures. For the "low transparency" transistor, conductance peaks are sharp and reach a maximum value close to half the high-temperature asymptotic conductance. This behavior is well predicted by a model based on the sequential transfer of charge through both junctions. Peaks occur for gate charges n_g for which two charge states have the same energy.

In a transparent transistor, conductance peaks stay broad but with a decreasing width which still decrease at the lowest explored temperatures. This effect, recently investigated theoretically, is similar to the Kondo effect: the two neighboring island states is analog to

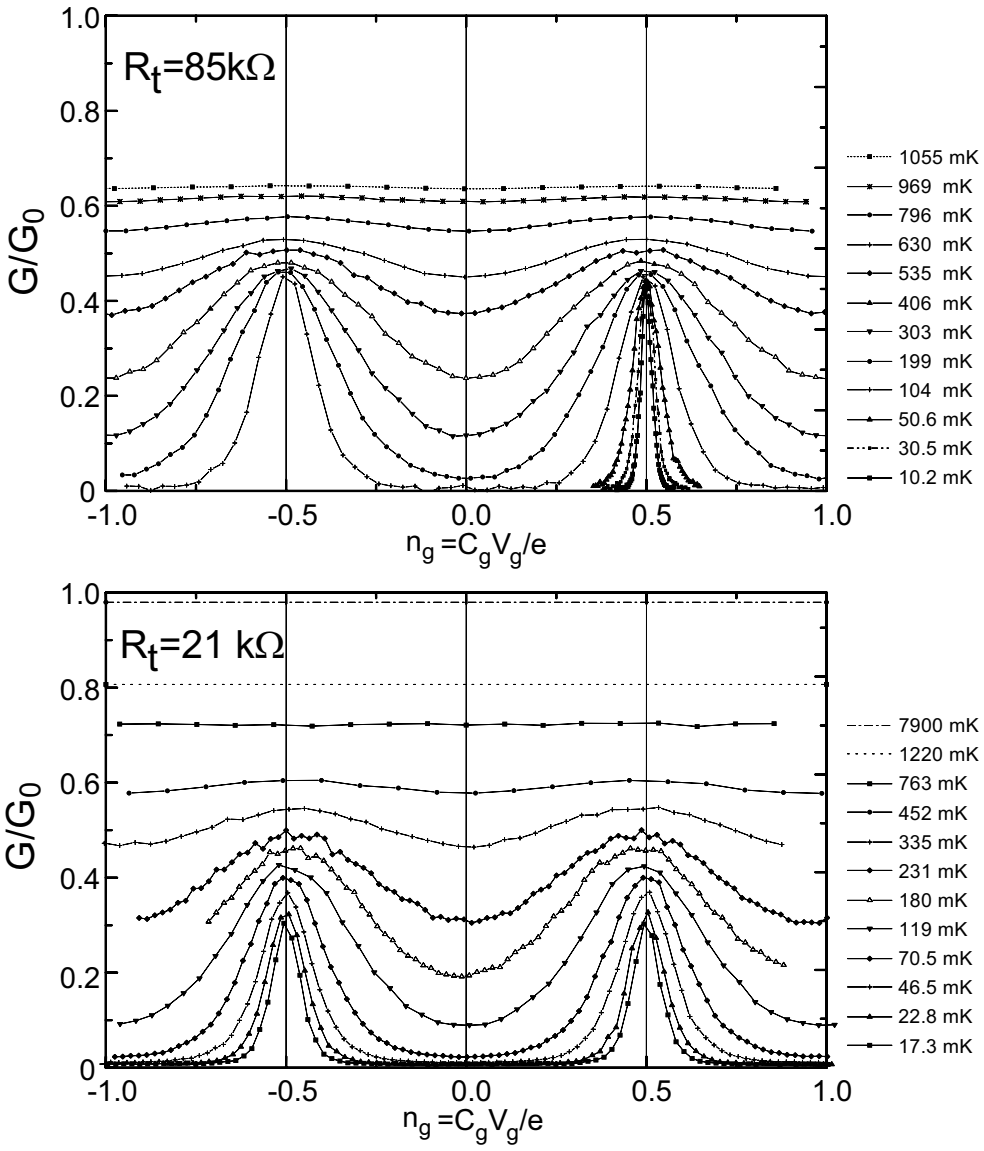

Figure 1. Normalized conductance of the SET as a function of the gate charge n_g for respectively large junction resistances (top : $R_t \approx 85$ kΩ) and for junction resistances of the order of the resistance quantum (bottom: $R_s \approx 21$ kΩ $\sim R_K$) measured at increasing temperatures. Note that at low temperature the conductance at $n_g = 1/2$ decreases continuously down to zero for the weak junction SET whereas it stabilizes near the classical value $G/G_0 = 0.5$ for the most resistive SET.

the spin, and tunnel excitations are equivalent to electronic excitations. Experimental results suggest the following scenario: at high temperature, the transparent transistor conductance behaves like a low transparency transistor but with a renormalized charging energy $E_c^{eff} < E_c^0$ with a stronger renormalization for lower tunnel resistances R_T. This description remains valid for temperatures down to E_c^0/k_B. For the lowest temperatures, the conductance modulation steadily decreases as predicted by the Kondo model. A quantitative comparison with theory has not however been possible because the model uses an effective Hamiltonian which renormalized parameters have not yet been theoretically calculated.

Quantum fluctuations in the single Cooper pair box

The experiment of the superconducting box is the superconducting analog of the electron box presented in inset. The circuit consists of an ultrasmall Josephson junction in series with a capacitance C_g and a voltage source U (see figure 2). The metallic superconducting electrode between the junction and the capacitance is an "island" which can exchange Cooper pairs with a superconducting reservoir through the Josephson junction. The electrostatic energy of this island is controlled by the voltage U on the gate capacitance C_g. The experiment consists in measuring the average excess charge of the island as a function of U. As in the electron box experiment, this measurement is obtained by electrostatically coupling the island to an electrometer with sub-electronic sensitivity which is a single electron transistor. In the electron box, the charging effects that led to the quantization of the charge in the island were in competition only with thermal fluctuations. In this Cooper pair box, the Josephson coupling, which tends to induce quantum fluctuations of the number of Cooper pairs must also be considered.

The circuit is designed so that the Josephson coupling energy E_J is a bit smaller than the characteristic charging energy of the circuit $E_c = e^2/2C$ where C is the total capacitance of the island. In the realized experiment, the average number of excess electrons $\langle n \rangle$ is a step-like function of the voltage U, which is temperature independent below 100 mK. The step height is equal to one Cooper pair (see figure 2) and each plateau corresponds to the number of Cooper pairs which minimizes the electrostatic energy of the circuit. On such plateaus, the circuit is in a quantum state for which the number of charges in the island is well defined. On the other hand, due to the Josephson coupling which induces large quantum fluctuations of the island charge when the energy difference between two neighboring charge states is

lower than E_J, the transition width between two successive plateaus remains finite at low temperature. In this domain, the quantum state of the circuit is in a coherent superposition of the two neighboring charge states $|n\rangle$ and $|n+1\rangle$. At the middle of the transition, the quantum state of the circuit is $\frac{1}{\sqrt{2}}(|n\rangle + |n+1\rangle)$. The slope of the step at this point directly reflects the competition between the Josephson effect and charging effects since it is equal to the ratio of the superconducting charging energy $4E_c$, over the Josephson energy E_J, these two energies being measured separately. The theoretical prediction plotted for these values with no adjustable parameters is in good agreement with the experimental data.

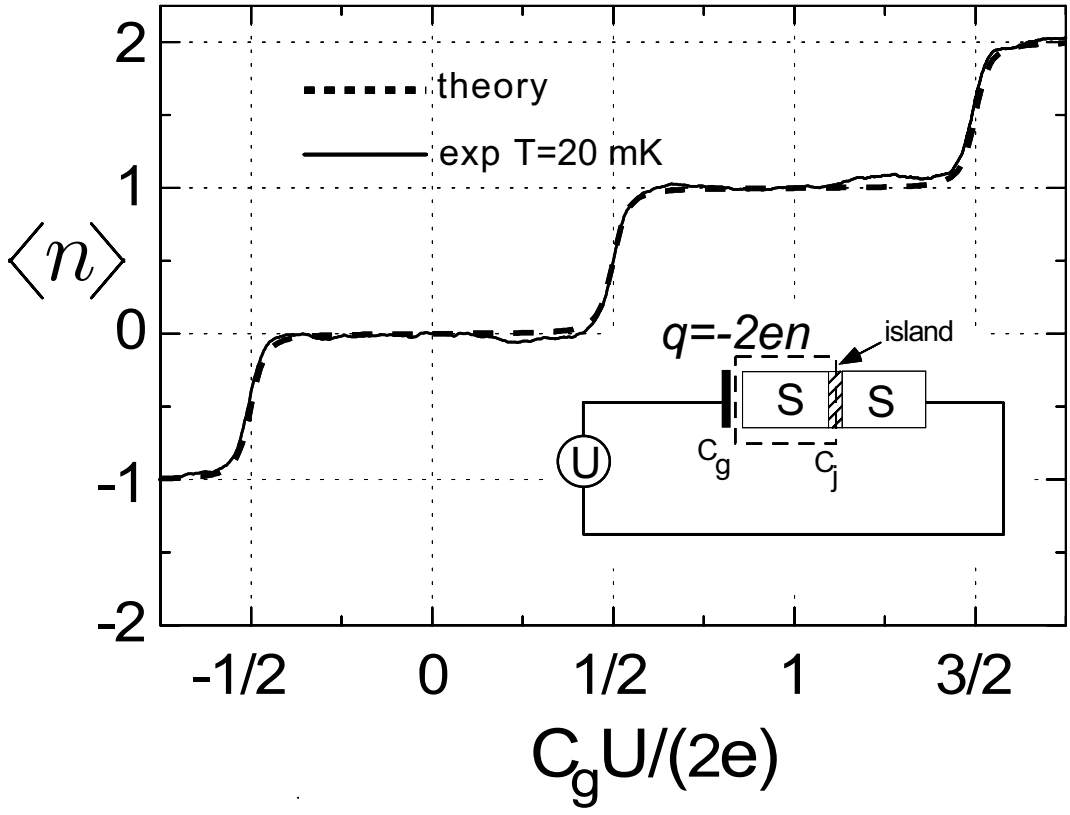

Figure 2. Average number of excess Cooper pairs $\langle n \rangle$ in the superconducting box as a function of the reduced gate voltage $C_gU/(2e)$. The experimental curve obtained at 20 mK (solid line) is compared to the theoretical prediction (dashed curve).

This experiment provides the direct observation of the Josephson effect which involves a single Cooper pair. It is also the realization of a quantum coherent state for a macroscopic system.

The Coulomb blockade of the Josephson effect

The system we have considered consists of a Josephson junction with critical current I_0 in series with an arbitrary superconducting impedance. A phase δ is imposed across the system. Such a bias can be performed by closing the circuit and applying a magnetic flux through the loop that is formed (see figure 3).

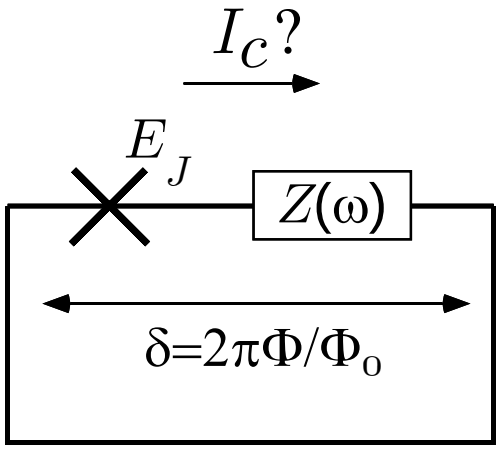

Figure 3. Schematic diagram of the circuit. A Josephson junction characterized by its Josephson energy E_J is placed in series with a impedance $Z(\omega)$. The obtained dipole is phase-biased by applying magnetic flux Φ in the loop. The issue consists in obtaining the maximum supercurrent that can flow through the junction for a given impedance Z.

The Hamiltonian describing this system is the sum of the Josephson Hamiltonian and the Hamiltonian of the electromagnetic environment. The fundamental state is associated with a finite current $I(\delta)$ flowing through the loop which expression without environment is given by the Josephson relation: $I(\delta) = I_0 \sin\delta$. We first performed a calculation based on the mean-field approximation and found that the maximum superconducting current I_c is all the more reduced with respect to I_0 that the environment impedance is high compared to R_K. This phenomenon can be considered as a Coulomb blockade of the Josephson effect. We have compared these predictions with the exact computation in the simple case for which the environment is a single-mode oscillator (the serial impedance is then reduced to a pure inductance). By analogy with the spin-boson system, we have modified the mean-field calculation in order to take into account the renormalization of low-energy modes. In the ground state, these modes are eliminated because their modification does not lead to an energy cost. We then calculated the renormalization factor for an arbitrary impedance. This expression provides a general re-

sult, obtained by other authors only in the case of a specific environment. In a second step, we resumed the calculation ignoring the Josephson Hamiltonian and beginning directly from the tunnel Hamiltonian. We have finally used the previous results on the modification of the Josephson Hamiltonian to determine a general expression of the critical current as a function of the tunnel resistance of the junction, for an arbitrary environment impedance.

Charge detection using the single electron transistor

We have characterized single electron transistors by measuring their noise levels.

In the low-frequency range, the noise originates from an external cause: random motion of charges in the vicinity of the SET induces a fluctuating polarized charge on the island and leads to a noisy current in the device. We have compared the so-called "charge-noise" of transistors with islands of different size, fabricated on different substrates (see figure 4).

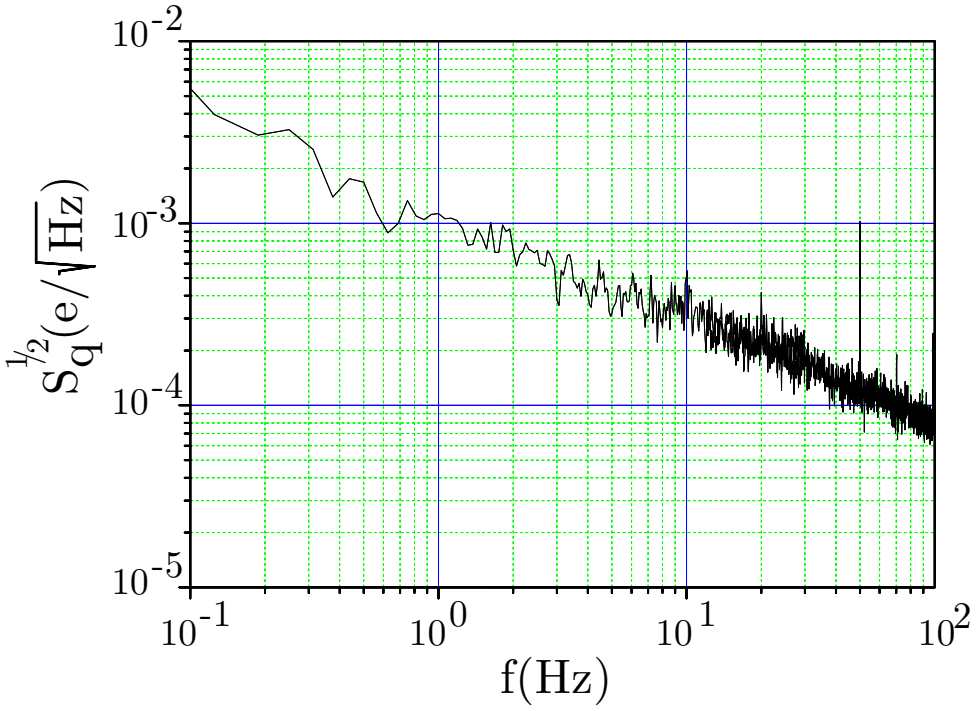

Figure 4. Typical noise spectral density of a SET transistor measured at 20 mK. The 1/f noise observed is attributed to the superposition of uncorrelated telegraphic noises emited by fluctuating dipoles in the vicinity of the transistor island. The noise level reference is 3×10^{-4} $e.\mathrm{Hz}^{-1/2}$ *at 10 Hz.*

These measurements indicates that the average charge noise level does not seem to dramatically depend on the chemical nature of the substrate nor on the island size, since the noise

appears to be dominated by a small number of charged fluctuators.

Considering the electrostatic coupling between an external charge and the SET island is also of some interest in electrometry. For that purpose we have considered the position monitoring of individual charged particles by single electron transistors. Such a method might be useful for critical measurements in particle physics. We have shown that the very high charge-sensitivity of the SET makes possible the measurement of the gravitational mass of antiprotons moving back and forth along the axis of a drift tube. We have estimated that a SET with a high-frequency bandwidth has a sufficiently low noise level to allow such a detection. Our calculation suggests that back-action noise of the SET on the particle would not wash out the tiny gravitation effect.

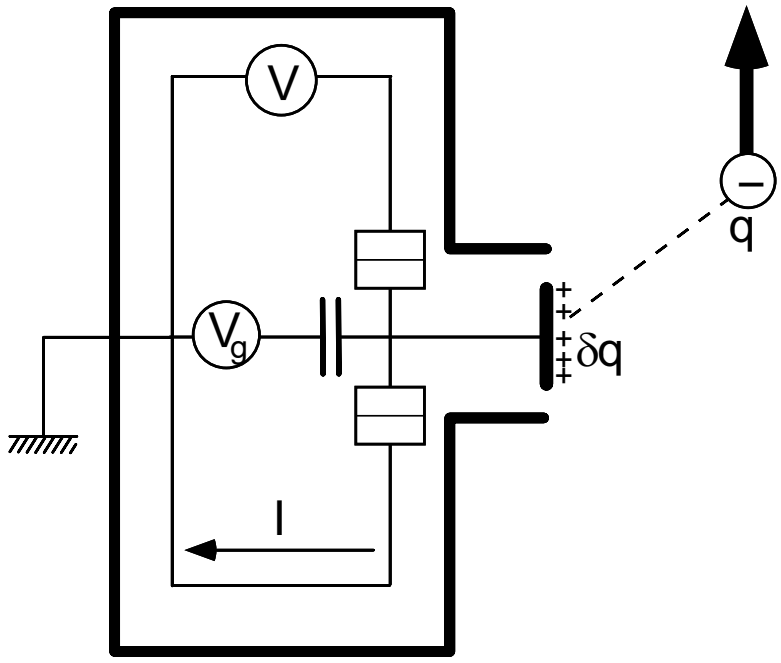

Figure 5. Schematic of a voltage biased single electron transistor used to monitor the trajectory of a charged particle. The charge q induces a time dependent δq on the transistor island which is measured by detecting the current I through the device.

Fabrication techniques

Single electron devices, which contain details with lateral dimensions below 100 nm are now routinely obtained using electron beam lithography. This technique is widely used to fabricate nanostructures with well-controlled geometries: an electron beam accelerated in an electron microscope locally expose a specific resist, leading to the realization of a mask.

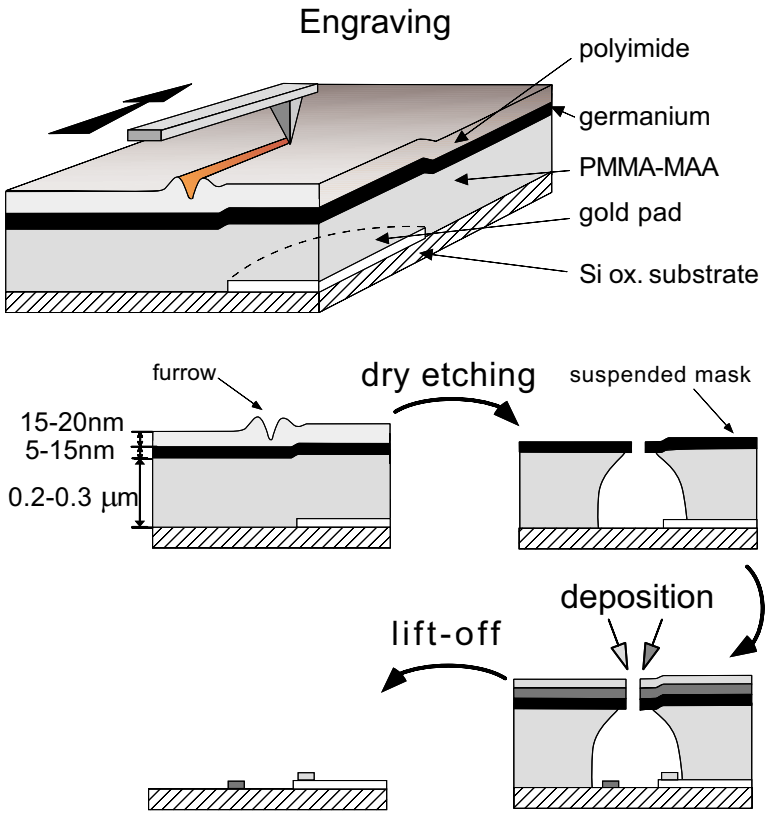

Figure 6. Sketches depicting the AFM-based nanolithography process. A sharp AFM tip engraves a furrow in a soft polyimide layer (top). The resulting scratch is transferred using dry etching into a solid mask of germanium. This is finally used to evaporate metallic layers through the obtained slit. Typical tip-dependent resolution lie around 40nm.

Other nanolithography techniques using recently developed proximal probe microscopy (AFM, STM) have been proposed but they were by far too specific to apply for the fabrication of single electron devices.

We have developed a general lithography technique based on the atomic force microscope (AFM). In this new process, the sharp tip of an atomic force microscope engraves a narrow "furrow" in a soft layer of "freshly baked" polyimide (figure 6).

This furrow is then transferred to a thin germanium layer which forms a mask for the deposition of layers constituting the nanostructure. Using this technique, we have fabricated single electron transistors with characteristics similar to those fabricated using conventional electron beam lithography.

New developments in single electronics lead to imagine more complex circuits. These require an increased integration of features which is impossible to obtain using a single conducting

layer. For that purpose, we have developed a fabrication technique leading to multilayered circuits. (see figure 7).

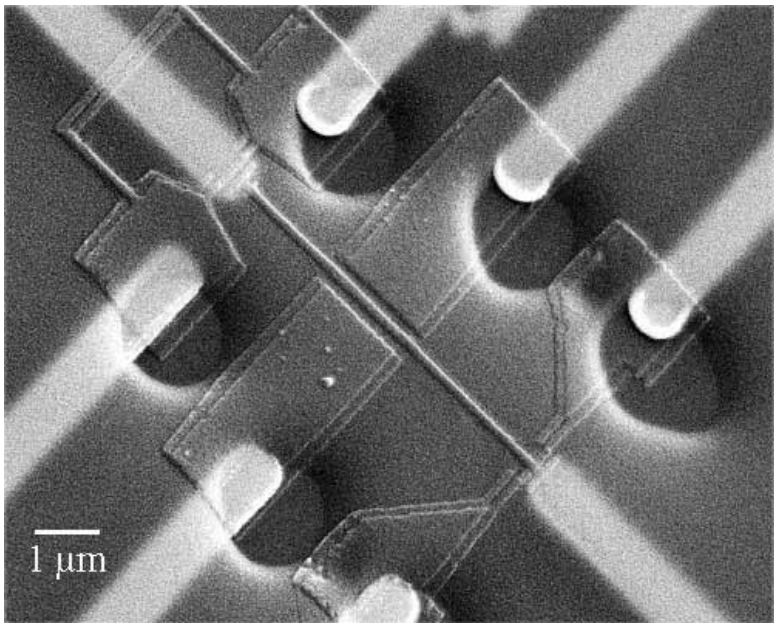

Figure 7. Scanning electron micrograph of a multilayer device: It consists of a single Cooper pair box (top left) coupled to an electrometer (bottom right). The nanostructure has been deposited onto an insulating polyimide layer (dark circles) for contacting the gold fingers underneath. Electrostatic polarization is performed using the two burried leads.

Such a technique offers new possibilities such as interlayer connections, capacitive coupling between layers. It also enables the control the electromagnetic environment of single Cooper pair devices, and the realization of shielded gates for microwave radiations.

References

[1] R.A. Millikan, Phys. Rev. **32,** 349, (1911).

[2] T. A. Fulton and G. J. Dolan, Phys. Rev. Lett. **59**, 109 (1987).

[3] M. H. Devoret, D. Esteve and C. Urbina, Nature **360,** 547 (1992); For a review of this field, see *Single Charge Tunneling*, NATO ASI series, eds. H. Grabert and M. H. Devoret (Plenum, New York, 1992).

[4] P. Lafarge, H. Pothier, E.R. Williams, D. Esteve, C. Urbina, and M. H. Devoret, Z. Phys. **B 85**, 327 (1991).

[5] L.J. Geerligs, V.F. Anderegg, P.A. M. Holweg, J.E. Mooij, H. Pothier, D. Esteve, C. Urbina and M.H. Devoret, Phys. Rev. Lett. **64**, 2691, (1990).

[6] H. Pothier, P. Lafarge, D. Esteve, C. Urbina, and M. H. Devoret, Europhys. Lett., **67**, 1626, (1991).

[7] J.M. Martinis, proceeding of CPEM'96, see also J.M. Martinis, M. Nahum, and H.J. Jensen, Phys. Rev. Lett. **72**, 904 (1994).

[8] M.T. Tuominen, J.M. Hergenrother, T.S. Tighe and M. Tinkham, Phys. Rev. Lett. **69**, 1997, (1992).

[9] P. Lafarge, P. Joyez, D. Esteve, C. Urbina, and M. H. Devoret, Nature **365**, 422, (1993).

[10] P. Joyez, P. Lafarge, A. Filipe, D. Esteve, C. Urbina, and M.H. Devoret, Phys. Rev. Lett. **72**, 15, (1994).

[11] L.J. Geerligs, Ph. D. Thesis, Delft University of Technology, 1990.

[12] P. Lafarge, P. Joyez, D. Esteve, C. Urbina, and M.H. Devoret, Phys. Rev. Lett. **70**, 994 (1993).

Chapter 1

The single electron transistor in the strong tunneling regime $R_T < R_K$

Introduction

Single electronics is based on the quasi-perfect quantization in units of e of the charge of small islands only coupled between them or to charge reservoirs through large resistance tunnel junctions. This phenomenon of charge quantization in single electron devices strongly resembles electron localization in disordered materials. Not surprisingly, charge quantization holds when the tunnel junction resistances R_T are larger than the resistance quantum $R_K = h/e^2$. This condition defines the weak tunneling regime in which single electron devices are usually operated. The question of the robustness of charge quantization with respect to quantum fluctuations in the strong tunneling regime $R_T \leq R_K$ is obviously fundamental in the field of single electronics. In this regime one expects qualitatively that virtual electron hole tunneling at the barriers will somewhat screen the island charges and suppress charge quantization. One should notice that this problem is not only important for the basic understanding of single electronics, but has also practical implications for device optimization. From the theoretical point of view, there is presently no comprehensive theory of single electron devices in the strong tunneling regime. The problem belongs in fact to the class of difficult many-body

problems, and the theoretical effort has focussed on the simplest circuits, namely the single electron box and the SET. Apart from perturbational expansions, the methods used are based on the functional integral and on the renormalization group. In the case of the single electron box, these theories have also been completed by quantum Monte Carlo numerical calculations.

From the experimental point of view, the strong tunneling regime has only been observed in electron gas junctions by taking advantage of the junction modulation using gates. One should note that tunnel junctions between bidimensional electron gases have a small number of transmission channels with transmissions that can reach unity, whereas metallic tunnel junctions have a large number of channels with always small transmissions. We report in this chapter our investigation of the strong tunneling regime in metallic single electron transistors. We have chosen the SET rather than the single electron box mainly because the measurement of the conductance is far more accurate than the measurement of the box Coulomb staircase and because the SET parameters can be independently determined whereas the box parameters can only be estimated. As it will soon appear, the determination of the parameters and in particular of the island charging energy $E_c^0 = e^2/2C$ is indeed crucial to the quantitative analysis of the data.

1.1 Description of the Single Electron Transistor

As explained in the introduction, the single electron transistor consists of two ultrasmall tunnel junctions in series (see Fig. 1.1). The SET parameters are the tunnel resistances R_{T1} and R_{T2}, the capacitances C_1 and C_2, and the gate capacitance C_g, usually much smaller than the junction capacitances. The bare charging energy of the island is $E_c^0 = e^2/2C_\Sigma$, where $C_\Sigma = C_1 + C_2 + C_g$ is the total island capacitance. The circuit is biased with a voltage source V and the central island is polarized by a gate voltage V_g. The dimensionless polarization charge is $n_g = C_g V_g/e$.

The charge configuration of the device has two degrees of freedom which are respectively the number n of extra electrons on the island and the number p of electrons having passed through the whole circuit. The number of electrons n_1 and n_2 having passed through the first and the second junction are thus $p + n$ and $p - n$, respectively.

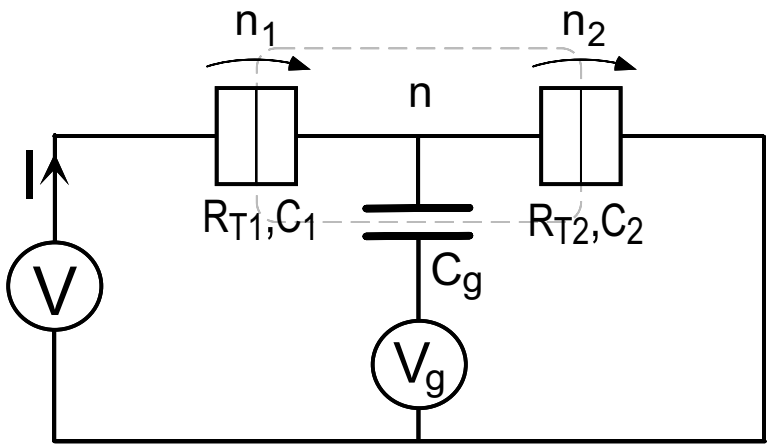

Figure 1.1. Schematics of a single electron transistor, and parameters of the system. The junctions are characterized by their capacitances C_i and their tunnel resistances R_{Ti}. The charge configuration of the system is specified by the number of electrons n_1 and n_2 having crossed the junctions.

1.1.1 Hamiltonian of the system

We use the set of states of the electrodes in the absence of tunneling as a basis for the quantum states of a SET. A state of this basis is fully described by the charge variables n and p, and by the occupation numbers of the quasiparticle states in the electrodes. In this basis, the electrostatic Hamiltonian H_{el} is diagonal and the electrostatic energy of a state is :

$$E(n,p) = (n - n_g)^2 E_c^0 - peV. \tag{1.1}$$

The quasiparticle states are the kinetic energy excitations of the electrodes. The quasiparticle Hamiltonian H_{qp}^i of the electrode i is :

$$H_{qp}^i = \sum_{l,\sigma} \epsilon_l c_{l\sigma}^\dagger c_{l\sigma}, \tag{1.2}$$

where the operators $c_{l\sigma}^\dagger$ and $c_{l\sigma}$ are the creation and annihilation operators for quasiparticles of spin σ in the eigenstate l in the electrode i.

Within the tunneling approximation, the tunnel effect occurring in each junction is treated by adding a tunneling term $H_t = h_{t_1} + h_{t_2}$ to the Hamiltonian of the system. This Hamiltonian H_t couples states which differ by one electron having passed through one junction, and by one quasiparticle in each electrode of the junction. The Hamiltonian h_{t_1} (or h_{t_2}) is a function both of electrostatic degrees of freedom operators and quasiparticle operators:

$$h_{t1} = \sum_{l,r,\sigma} t_{lr} \widehat{S}_{1lr} \left(c_{l\sigma}^\dagger c_{r\sigma} \right) + h.c. \tag{1.3}$$

where t_{lr} is the matrix element, and where the translation operator $\widehat{S}_{lr}$ increases the number of electrons having passed through the junction:

$$\widehat{S}_{1lr} \mid n_1, n_2; .. \rangle = \mid n_1 + 1, n_2; .. \rangle. \tag{1.4}$$

The tunnel resistance of a junction is related to the tunneling Hamiltonian parameters by the following relation:

$$R_T = \frac{R_K}{4\pi^2 \rho_L \rho_R \left\langle |t_{lr}^2| \right\rangle_{av}}, \tag{1.5}$$

where ρ_L and ρ_R denote respectively the electronic density of states at Fermi level in respectively left and right electrodes and $\left\langle |t_{lr}^2| \right\rangle_{av}$ is the average square modulus of the tunneling matrix elements.

The total Hamiltonian of the system H is then given by:

$$H = H_{el} + \sum_i H_{qp}^i + h_{t1} + h_{t2} \quad . \tag{1.6}$$

1.1.2 The weak tunneling regime

In the weak tunneling regime $R_T \gg R_K$, the tunneling Hamiltonian $h_{t1} + h_{t2}$ can be treated at the lowest order in perturbation theory. The energy shift of the eigenstates of the Hamiltonian $\left(H_{el} + \sum_i H_{qp}^i\right)$ are neglected and tunneling rates between charge states are calculated using the Fermi Golden Rule and linear response theory [2]. Assuming that the electrodes are in thermal equilibrium, the tunneling rate Γ_i at zero voltage through the tunnel junction number i is given by the following convolution product:

$$\Gamma_i(\Delta E) = \left(\frac{1}{e^2 R_{Ti}}\right) \int dE\, dE^{'}\, f(E) \left[1 - f(E^{'} + \Delta E)\right] \mathcal{P}(E - E^{'}) \quad , \tag{1.7}$$

where $f(E)$ is the Fermi density of states at energy E and $P(E - E^{'})$ is the probability of tunneling for an energy $E - E^{'}$ transferred to the electromagnetic environment modes. In the limit case of a tunnel junction totally decoupled from the environment (*i.e* in the low impedance limit), one can show that $\mathcal{P}(E)$ reduces to:

$$\mathcal{P}(E - E^{'}) = \delta(E - E^{'}) \quad . \tag{1.8}$$

In such a case, only elastic tunneling processes are possible and the single electron rate Γ_i is given by:

$$\Gamma_i(\Delta E) = \left(\frac{1}{e^2 R_{Ti}}\right) \frac{\Delta E}{1 - e^{-\frac{\Delta E}{kT}}} \quad , \tag{1.9}$$

The stochastic evolution of the charge configuration of a single electron device is governed by these transition rates.

1.1.3 The sequential model

The sequential tunneling model (SM) of the SET is based on the resolution of the Markov equations for the number n of extra electrons in the SET island using the transition rates on both junctions calculated from the above expression. The current results from the difference between the upward and downward rates. This method of calculation of the charge transport within the SET actually corresponds to a semi-classical treatment of the Hamiltonian. Indeed,

the tunnel effect has no incidence on the level positions, which only depends on the electrostatic energies.

Although these equations are easily solved, there is no closed formulation for the current or for the conductance. In particular, the zero-voltage conductance of a SET is given by the following expression:

$$G = \frac{G_0}{2} \sum_{n=-\infty}^{+\infty} P(n) \left[\frac{\beta \Delta E_n^+}{1 - e^{-\beta \Delta E_n^+}} + \frac{\beta \Delta E_n^-}{1 - e^{-\beta \Delta E_n^-}} \right] \quad , \tag{1.10}$$

where $\beta = 1/k_B T$ is the inverse temperature, $G_0 = 1/(R_{T1} + R_{T2})$ is the series tunnel conductance of the two junctions,

$$\Delta E_n^+ = E(n \pm 1) - E(n) = (\pm 2(n - n_g) - 1) E_c^0 \quad , \tag{1.11}$$

is the electrostatic energy change when n changes by $\pm$ 1 and

$$P(n) = \frac{e^{-\beta E(n)}}{\sum_{m=-\infty}^{+\infty} e^{-\beta E(m)}} \quad , \tag{1.12}$$

is the Boltzmann probability to have n excess electrons on the island. This zero-voltage conductance turns out to be a interesting quantity both experimentally and theoretically:

• Experimentally, it can be measured easily and accurately by a lock-in technique. Moreover, being measured at zero bias voltage, it is not affected by Joule heating effects.

• Theoretically, it is in principle most easily calculated since it is mere equilibrium property of the system. As an example, a derivation of Eq. (1.10), based on the fluctuation-dissipation theorem, is given in Appendix 1-A.

As pointed out by Pekola *et al.* [4], the measurement of the conductance in this weak tunneling regime provides a way to obtain to measure (in an absolute way) the temperature of the system.

1.2 The SET in the strong tunneling regime

We have investigated the effect of strong tunneling in the SET. Our work is reported in the manuscript "Strong tunneling in the single electron transistor" by P. Joyez, V. Bouchiat, D. Esteve, C. Urbina and M.H. Devoret, which is reproduced below. This manuscript has been accepted for publication in Physical Review Letters.

Strong Tunneling in the Single Electron Transistor

P. Joyez, V. Bouchiat, D. Esteve, C. Urbina and M. H. Devoret

Service de Physique de l'Etat Condensé,

CEA-Saclay

91191 Gif-sur-Yvette, France

(May 26, 1997)

Abstract

We have investigated the suppression of single electron charging effects in metallic single electron transistors when the conductance of the tunnel junctions becomes larger than the conductance quantum e^2/h . We find that the Coulomb blockade of the conductance is progressively shifted at lower temperatures. The experimental results agree quantitatively with the available $1/T$ expansion at high temperature, and qualitatively with the predictions of an effective two-state model at low temperature, which predicts at $T = 0$ a blockade of conductance for all gate voltages.

PACS numbers: 73.23.Hk, 73.20.Jc, 85.30.Wx, 73.40.Gk

Physical Review Letters **79**, 1349, (1997).

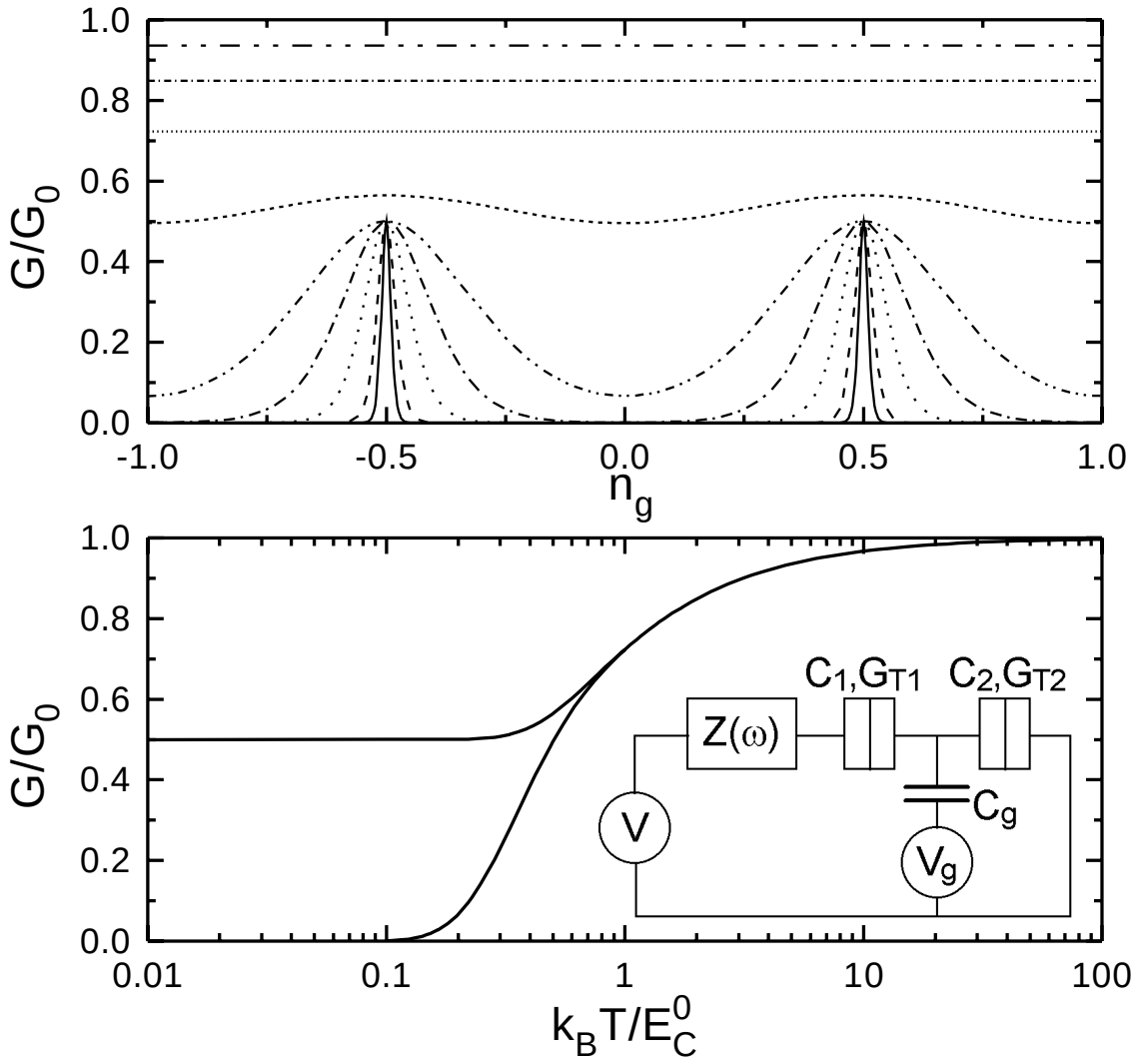

Figure 1. Schematics of a SET and predictions of the sequential tunneling model for its conductance in the case when $Z(\omega) = 0$. Top panel: conductance of the SET as a function of the gate charge $n_g = C_g V_g/e$, for various temperatures. From top to bottom $k_B T/E_c^0$ =5, 2, 1, 0.5, 0.2, 0.1, 0.05, 0.02 and 0.01. Bottom panel: temperature dependence of the maximum ($n_g = 1/2$ mod 1) and minimum (n_g =0 mod 1) conductance. At high temperature, the conductance depends on temperature but not on n_g. The value $G = G_0$ is reached only in the limit $T \to \infty$. Below a certain temperature roughly given by $k_B T \approx E_c^0$, gate-charge modulation sets in and the well-known conductance peaks appear at $n_g = 1/2$ mod 1, for which two adjacent island charge states have the same electrostatic energy. As temperature is reduced further, the conductance peaks sharpen. The maxima remain fixed at $G_0 = 2$ and the width of the conductance peaks becomes proportional to T.

Single electron devices consist of small "island" electrodes whose charge is nearly perfectly quantized in units of e, but which can exchange electrons through tunnel junctions. These two seemingly contradictory requirements can be met if the tunnel conductances of the tunnel junctions are much lower than the conductance quantum $G_K = e^2/h$. In the recent years, different single electron devices such as single electron transistors [1], turnstiles [2] and pumps [3,4], have been successfully operated and their behavior is now well understood [5]. However, little is known on single electron effects when the tunnel conductances are comparable or greater than G_K. In this strong tunneling regime, one expects that quantum fluctuations of the island charges will eventually suppress single electron effects. Indeed, such a suppression of Coulomb blockade with increasing tunneling strength has been observed in the particular case of tunnel junctions with only a few, well-transmitted channels [6, 7]. In this Letter, we investigate the effect of strong tunneling in the case of metallic tunnel junctions with a large number of low-transparency channels.

For this purpose, we have measured the zero-voltage conductance of metallic single electron transistors (SET) with moderate to large conductances. A SET consists of two series-connected tunnel junctions defining one island (see inset of Fig. 1) and of a gate electrode which electrostatically controls the current through the device. We first recall the predicted conductance within the sequential tunneling model (SM), on which our data analysis will be based. This model, relevant for weak tunneling, assumes that the number n of electrons in the island is a good quantum number. It only considers tunnel transitions $n \rightarrow n \pm 1$ at the lowest order in perturbation theory, level shifts being neglected [5,8]. The SM predictions for the conductance G of the SET can be expressed using a single function g of reduced parameters: $G = G_0\, g\left(n_g, E_c^0/k_BT\right)$, where $G_0 = 1/\left(G_{T1}^{-1} + G_{T2}^{-1}\right)$ is the series tunnel conductance of the two junctions, $n_g = C_gV_g/e$ is the dimensionless gate charge, T is the temperature and $E_c^0 = e^2/2C_\Sigma$ is the bare charging energy of one excess electron on the island, $C_\Sigma = C_1 + C_2 + C_g$ being the total geometric capacitance of the island. The predictions of the model are summarized in Fig. 1, in the case of a zero-impedance electromagnetic environment for the SET. Finite impedance effects can be evaluated within the

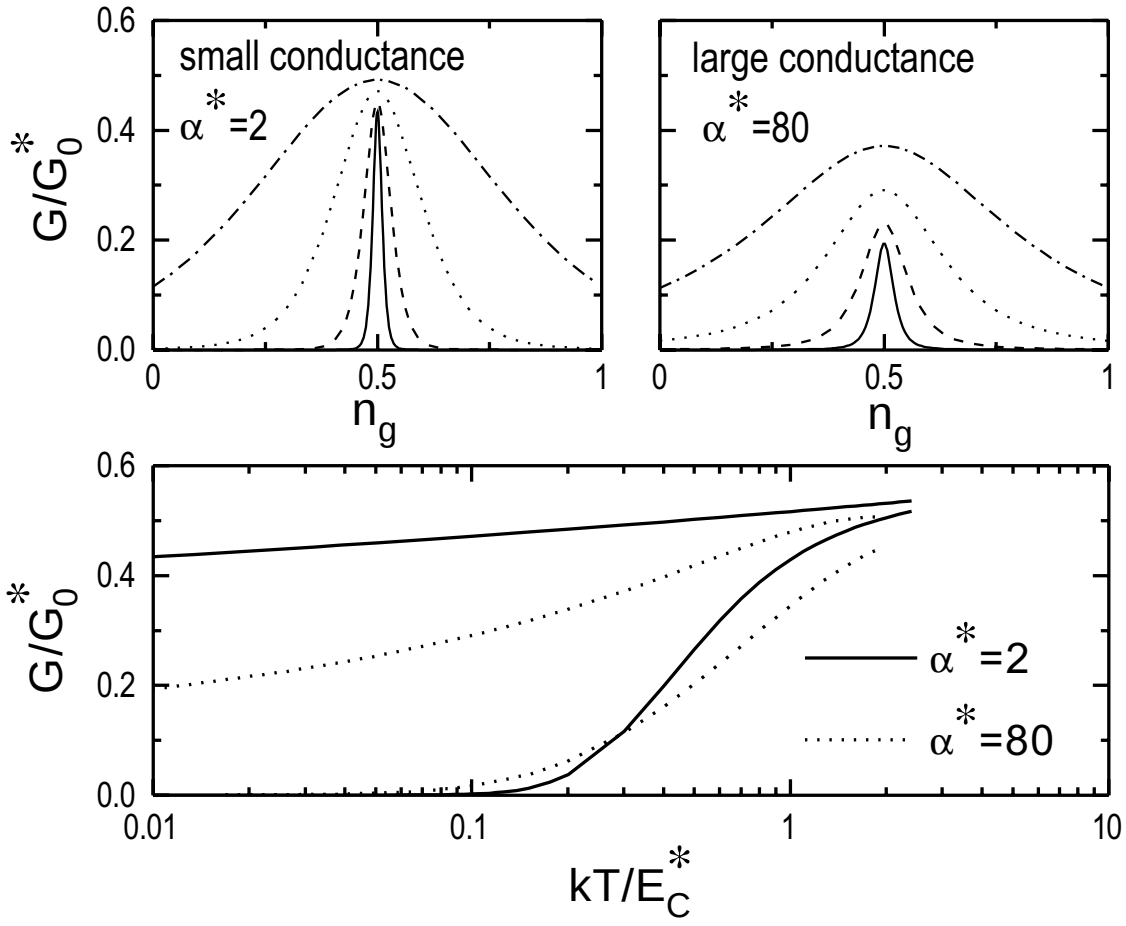

Figure 2. Predictions of the two-state model of Ref. 10 for the reduced conductance at low temperatures. Top panels: gate-charge modulation for k_BT/E_c^*= 0.3, 0.1, 0.03 and 0.01 from top to bottom, respectively. Bottom panel: temperature dependence of the maximum and minimum conductance. This model, which uses renormalized parameters E_c^*, G_0^* and α^*, predicts a broadening of the conductance peaks and a reduction of the peak value when the tunnel conductance is increased, in qualitative agreement with the experiments (see Fig. 3).

SM [9]. In our samples, they yield less than 1% conductance corrections which were taken into account in the data analysis.

We now present the theoretical predictions for strong tunneling in the SET. We define the tunneling strength parameter as $\alpha = G_{//}/G_K$, where $G_{//} = G_{T1} + G_{T2}$ is the parallel tunnel conductance of the two junctions. In the low temperature regime, the conductance of the SET has been calculated for arbitrary α [10] by mapping the system on an effective two-state model. This calculation, which only retains the lowest two electrostatic energy states of the island, is only valid near the conductance peaks and at temperatures for which the occupation of other charge states can be neglected. In the strong tunneling regime, this model predicts that the finite energy width of the island charge states prevents the conductance peaks to sharpen at low temperature, as shown in Fig. 2. Correlatively, the maximum conductance decays as $1/\ln T$ at low temperature. This suppression of conductance for all values of gate voltage is a new feature which is not predicted by weak tunneling theories. However, these predictions cannot be tested quantitatively because the model uses cutoff-dependent renormalized parameters E_c^*, G_0^* and α^* [11,12] whose relation to the bare parameters is unknown in the strong tunneling regime.

At high temperatures ($k_B T >> E_c^0$), the conductance is given by the expansion [13,14]:

$$\frac{G}{G_0} = 1 - \frac{1}{3}\tilde{E}_C/k_B T + O\left[\left(\tilde{E}_C/k_B T\right)^2\right] \tag{1}$$

where

$$\tilde{E}_C = E_c^0 \left\{1 - \frac{9\zeta(3)}{2\pi^4}\alpha\frac{E_c^0}{k_B T}\right\} \tag{2}$$

ζ being the Riemann Zeta function. Expansion (1) coincides with the one found within the SM, but with $\tilde{E}_C$ in place of the bare charging energy E_c^0. Hence, $\tilde{E}_C$ appears as a temperature-dependent effective charging energy which contains all the effects of strong tunneling in the high temperature limit. The model developed in Ref. 14, valid for arbitrary α, also covers the intermediate temperature range. This model is however not quantitative because it reproduces only part of the SM predictions and it incorporates an unknown cut-off parameter.

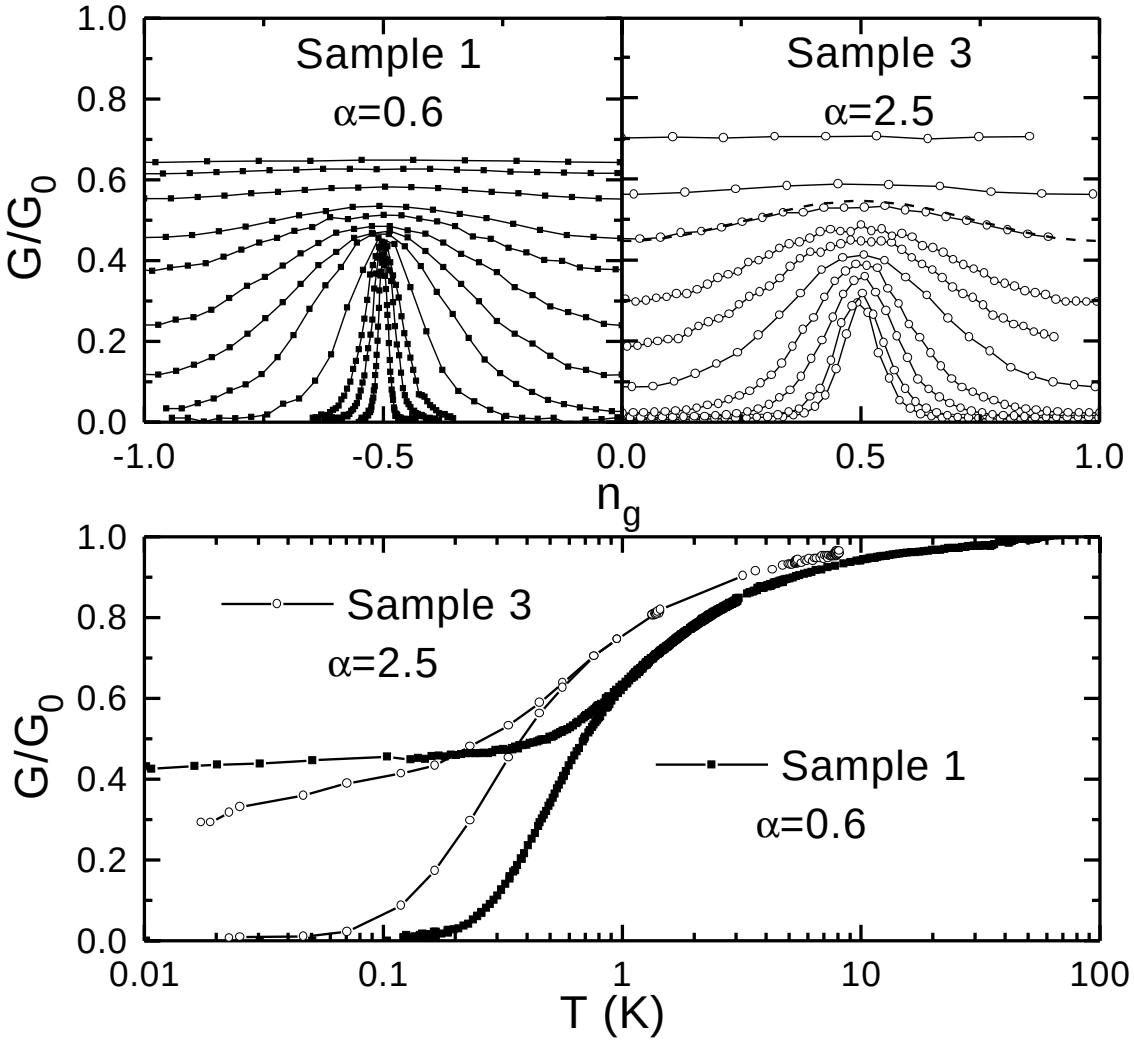

Figure 3. Reduced measured conductance of samples 1 and 3. Top panels: variations with gate charge at various temperatures. The temperatures of the curves are, from top to bottom : 1055, 969, 796, 630, 535, 406, 303, 199, 104, 50.6, 30.5 and 10.2 mK (top left panel) and 763, 452, 335, 231, 180, 119, 70.5, 46.5, 22.8 and 17.3 mK (top right panel). The dashed line is a fit using the SM with an effective charging energy (see Fig. 4). Bottom panel: temperature dependence of the maximum and minimum conductance.

The samples were prepared using standard e-beam lithography and 3-angle evaporation [15] through a shadow mask [16]. The SETs were embedded in a low-pass RC electromagnetic environment necessary to the determination of E_c^0 in the superconducting state. The resistances consisted of 1 μm-long resistive leads made of either Cu or AuCu alloy, and were connected to on-chip 100 pF planar capacitors with one plate connected to ground. The samples were placed inside a copper shield anchored to the mixing chamber of a dilution refrigerator. Most measurements were taken in the normal state of the Al electrodes, in a 0.5 T magnetic field. The electrical wiring between the sample and the measuring apparatus at room temperature was made through filtering coaxial lines, shielded twisted pairs and discrete miniature cryogenic filters [17]. We measured the zero-voltage conductance using a low-frequency (≈ 10 Hz) lock-in technique, at an excitation level adjusted to probe only the linear part of the current voltage characteristic. We have investigated 4 samples, labelled 1 to 4, with increasing conductances $G_0 = 5.82$ μS, 6.06 μS, 24.9 μS and 71 μS. Assuming $G_{//} = 4G_0$, since the two junctions of each sample are nominally identical, the values of α are 0.60, 0.62, 2.5 and 7.3, respectively. The junction size (typically 10^4 nm^2) results in a number of channels of the order of 10^6 and in a bare charging energy E_c^0 between 1.0 and 1.5 k_B K. For each sample, we measured the conductance as a function of the gate voltage V_g at various temperatures. Experimental data for samples 1 and 3 are shown in Fig. 3. For sample 1 (α =0.6), the data closely resemble the weak tunneling predictions of the SM (see Fig. 1), as expected. In particular, the width of the peaks at low temperature scales with temperature down to 10 mK, the lowest temperature we have reached. This good electron thermalization proves the efficiency of the filtering. Deviations from the SM predictions show up in the reduction of the peak height at low temperature. We interpret this effect as a finite tunneling strength correction (the environmental resistance of the AuCu leads of this sample, of the order of 200 Ω, results in a similar but much smaller effect). For sample 3 (α =2.5), the deviations from the SM are more pronounced: the conductance peaks are wider and the maximum conductance is more reduced at low temperature. Note that such deviations cannot be predicted by treating quantum fluctuations as an excess temperature

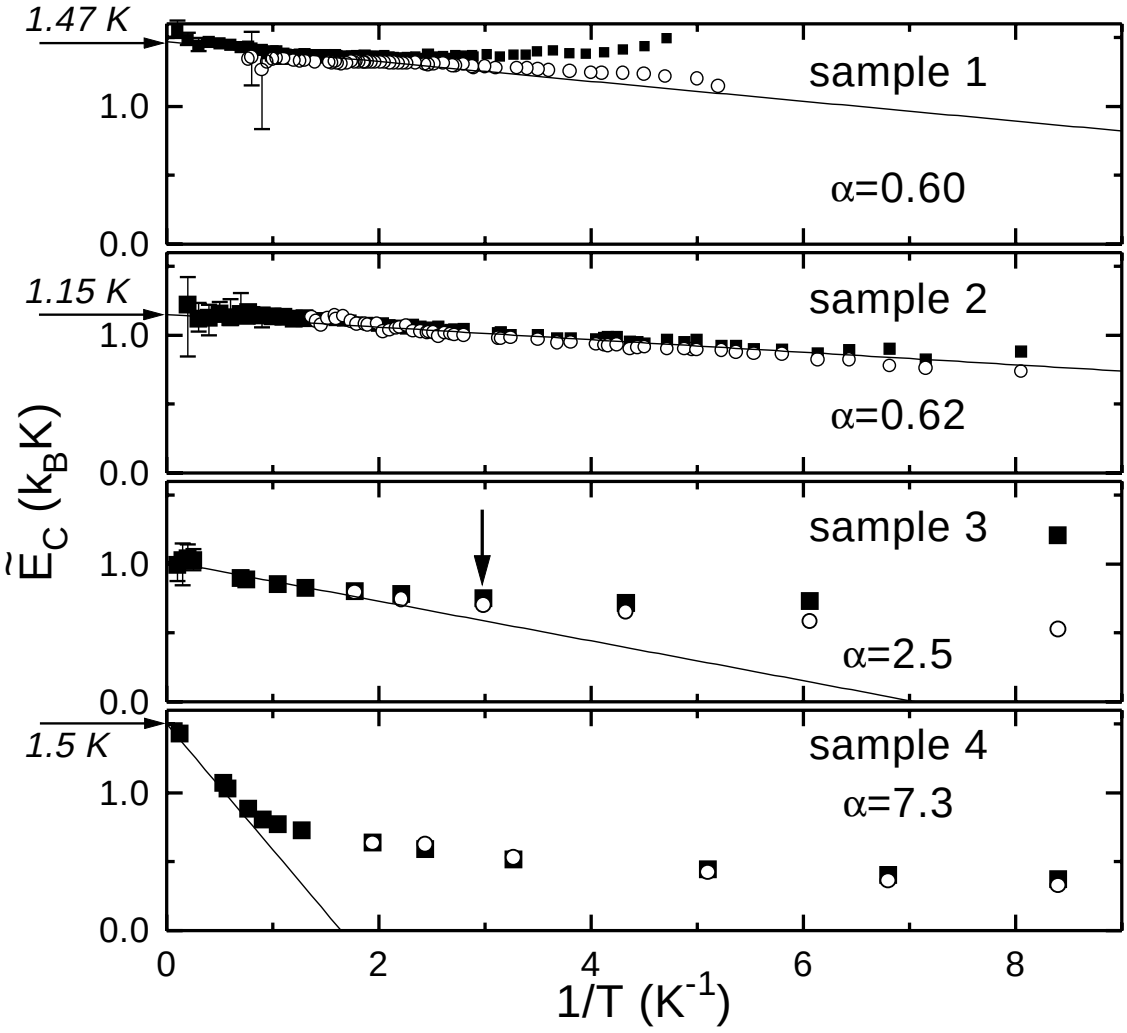

Figure 4. For each sample, effective charging energies $\tilde{E}_{c1}$ (solid squares) and $\tilde{E}_{c2}$ (open circles) obtained from the average conductance and from the aspect ratio of the modulation, respectively (see text), and predictions of Eq. (2) (straight lines), as a function of $1/T$. The points indicated by an arrow in sample 3 correspond to the dashed curve in the top right panel of Fig. 3. Values indicated by an arrow and italic text on the left axis are the bare charging energies E_c^0 obtained from resonances in the superconducting state (see text and inset of Fig. 5). The predictions of Eq. (2), are calculated using the above determined E_c^0 for sample 1, 2 and 4, and an extrapolation for sample 3 for which the resonances could not be measured.

within the SM. The experimental results are in qualitative agreement with the predictions of the two-state model of Ref. 10, for suitably chosen E_c^*, G_0^* and α^* (compare Figs. 2 and 3). Note also that the parameter α^* we have used is different from the bare α, as expected [11].

In the high temperature regime, we have analysed our data using the SM but with an effective charging energy as suggested by Eqs. (1-2). In the temperature range where there is no conductance modulation with the gate voltage, we define an effective charging energy $\tilde{E}_{C1}$ through the equation $G_{\rm exp}/G_0 = g\left(\tilde{E}_{C1}/k_BT\right)$, where $G_{\rm exp}$ is the measured conductance. In this regime, $\tilde{E}_{C1}$ is the only parameter needed to describe the data. This procedure can be generalized to the temperature range where the SET modulates, by using the n_g -averaged conductance, but fitting of the modulation is not guaranteed then. In this latter range, one can use a similar procedure to extract another effective energy $\tilde{E}_{C2}$ from the aspect ratio $(G_{\rm max} - G_{\rm min})\,/\,(G_{\rm max} + G_{\rm min})$ using the SM. If $\tilde{E}_{C2}$ and $\tilde{E}_{C1}$ coincide in the temperature regime where the conductance modulation is sinusoidal, the data can be well fitted using the SM with this effective charging energy. In Fig. 4, we show the values of $\tilde{E}_{C1}$ and $\tilde{E}_{C2}$ obtained following the above procedures. One finds that $\tilde{E}_{C1}$ and $\tilde{E}_{C2}$ indeed coincide in the temperature range where the modulation is sinusoidal, supporting the effective charging energy idea. The temperature dependence of the effective energies is more pronounced for increasing α. The reduction from the $T \to \infty$ extrapolation, already noticeable for α =0.6, reaches 70% for α =7.3. This reduction can be interpreted as an increase of the effective junction capacitance, which is expected to be infinite in the limit of infinite tunnel conductance. According to Eq. (2), the $T \to \infty$ extrapolation determines the bare charging energy E_c^0. In order to check this prediction, we have carried out an independent determination of the charging energy E_c^0. For this purpose, we took advantage of the subgap resonances in the I-V characteristic of the SET in the superconducting state. Clear observation of these resonances, due to the so-called resonant Cooper pair tunneling process [18, 19], necessitates an electromagnetic environment with a smooth frequency response and sufficient dissipation, as provided by our on-chip RC circuit. These resonances are gate-voltage dependent and

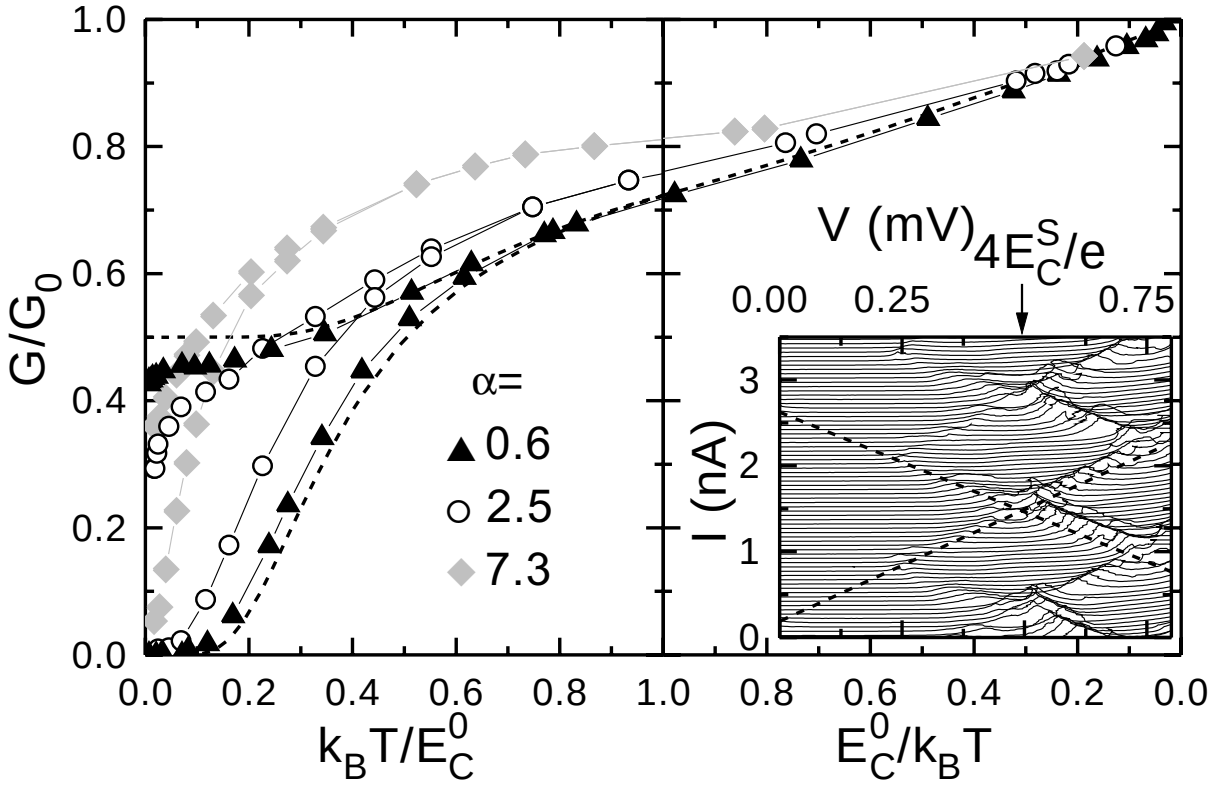

Figure 5. Reduced conductance as a function of the reduced temperature k_BT/E_c^0 for samples 1 (triangles, α =0.6), 3 (circles, α =2.5) and 4 (diamonds, α =7.3), and predictions of the SM (dashed lines). Single electron effects are progressively washed out as α increases. Inset: sub-gap current-voltage characteristics of sample 1 taken at different n_g and plotted with a vertical offset proportional to n_g. The checkered pattern yields a determination of the charging energy.

form a checkered pattern in a pseudo-3D I-V-V_g plot, as shown in the inset of Fig. 5. From the bias voltages at which resonance crossings occur, one obtains a charging energy E_c^S. This charging energy differs from E_c^0 due to virtual electron-hole excitations. Perturbation theory at the lowest order for $n_g = 0$, yields $E_c^S = E_c^0 \{1 - \alpha\, \Gamma\,(E_c^0/\Delta)\}$ where Δ =180 μeV is the gap of Al and $\Gamma\,(x) = \frac{x}{\pi} \int_0^{+\infty} u^2 K_{-1}^2\,(u)\, e^{-xu} \mathrm{d}u$, K_{-1} being a Bessel function [20]. Using this result, one finds that E_c^0 is 2% to 50% larger than E_c^S for our samples. The values of E_c^0 obtained this way are indicated by arrows on the left axes in Fig. 4. Using these values, we have plotted the predictions of Eq. (2) in Fig. 4. These predictions, with no adjustable parameter, are in quantitative agreement with the experimental data in the temperature range for which the first order expansion in α is sufficient.

The following scenario for the suppression of Coulomb blockade with increasing tunneling strength now emerges from the temperature dependence of the maximum and minimum conductances as a function of the reduced temperature $k_B T/E_c^0$ shown in Fig. 5, for samples 1, 3 and 4. At high temperatures, strong tunneling tends to suppress the reduction of the relative conductance due to Coulomb blockade, and to restore the bare conductance. The observed reduction of the effective charging energy with respect to the bare charging energy shifts the modulation regime below a temperature which decreases strongly as α increases. In the modulation regime, the conductance peaks are wide and their maximum continuously decays when the temperature decreases. Quantum fluctuations thus reduce not only the effective charging energy but also the modulation of the relative conductance with gate voltage. These effects, which impose a quantum limit to the performances of the SET, should be considered in electrometry applications. In conclusion, Coulomb blockade is washed out at large conductances, except at extremely low temperatures.

The authors are indebted to H. Grabert and H. Schoeller for useful discussions. This work was supported in part by the Bureau National de la Métrologie and EU ESPRIT project SETTRON.

REFERENCES

[1] T. A. Fulton and G. J. Dolan, Phys. Rev. Lett. 59, 109 (1987).

[2] L. J. Geerligs, V. F. Anderegg, P. A. M. Holweg, J. E. Mooij, H. Pothier, D. Esteve, C. Urbina and M. H. Devoret, Phys. Rev. Lett. 64, 2691 (1990).

[3] H. Pothier, P. Lafarge, D. Esteve, C. Urbina and M. H. Devoret, Europhys. Lett. 17, 249 (1992).

[4] J. M. Martinis, M. Nahum and H. D. Jensen, Phys. Rev. Lett. 72, 904 (1994); M. W. Keller, J. M. Martinis, N. M. Zimmerman, A. Steinbach, Appl. Phys. Lett. 69, 1804 (1996).

[5] Single Charge Tunneling, edited by H. Grabert and M. H. Devoret (Plenum, New York, 1992).

[6] C. Pasquier, U. Meirav, F. I. B. Williams, D. C. Glattli, Y. Jin and B. Etienne, Phys. Rev. Lett. 70, 69 (1993), C. Livermore, C. H. Crouch, R. M. Westerweld, K. L. Campman and A. C. Gossard, Science, 274, 1332 (1996) and references therein

[7] L. W. Molenkamp, K. Flensberg and M. Kemerink, Phys. Rev. Lett. 75, 4282 (1995).

[8] I. O. Kulik and R. I. Shekter, Zh. Eksp. Teor. Fiz. 68, 623 (1975) [Sov. Phys. JETP 41, 308 (1975)].

[9] P. Joyez and D. Esteve, submitted to Phys. Rev. B.

[10] J. König, H. Schoeller, and G. Schön, Europhys. Lett. 31, 31 (1995); H. Schoeller, and G. Schön, Phys. Rev. B 50, 18436 (1994).

[11] H. Grabert, H. Schoeller, private communications.

[12] Renormalization of charging energy has also been considered in Ref. 7 and in X. Wang, R. Egger and H. Grabert, submitted to Europhys. Lett., 1996.

[13] X. Wang, G. Göppert and H. Grabert, preprint, 1996.

[14] D. S. Golubev, and A. D. Zaikin, JETP Lett. 63, 1007 (1996).

[15] D. B. Haviland, L. S. Kuzmin, P. Delsing, K. K. Likharev, and T. Claeson, Z. Phys. B 85, 339 (1991).

[16] G. J. Dolan and J. H. Dunsmuir, Physica B 152, 7 (1988).

[17] D. Vion, P. F. Orfila, P. Joyez, D. Esteve and M. H. Devoret, J. Appl. Phys. 77 (6), 2519 (1995).

[18] D. B. Haviland, Y. Harada, P. Delsing, C. D. Chen, and T. Claeson, Phys. Rev. Lett. 73, 1541 (1994).

[19] A. Maassen van den Brink, L. J. Geerligs, and G. Schön, Phys. Rev. Lett. 67, 3030 (1991).

[20] Appendix 2-B in this thesis.

1.3 Comparison with a cotunneling theory

In a very recent paper [5], König, Schoeller and Schön were able to calculate the conductance of the SET without adjusting parameters by taking into account second order terms in the tunneling Hamiltonian. Their calculation has been compared with the experimental conductances G_{min} and G_{max} of the various SETs as a function of the temperature (see Fig. 1.2). One can notice that the agreement is good both for the temperature of appearance of modulation as for the $\ln T$ decay law of G_{max} at low temperatures. However their calculation does not hold for SETs with highly transparent junctions ($R_T \ll R_K$) for which a more complete calculation taking in account the tunneling Hamiltonian at all order is still needed.

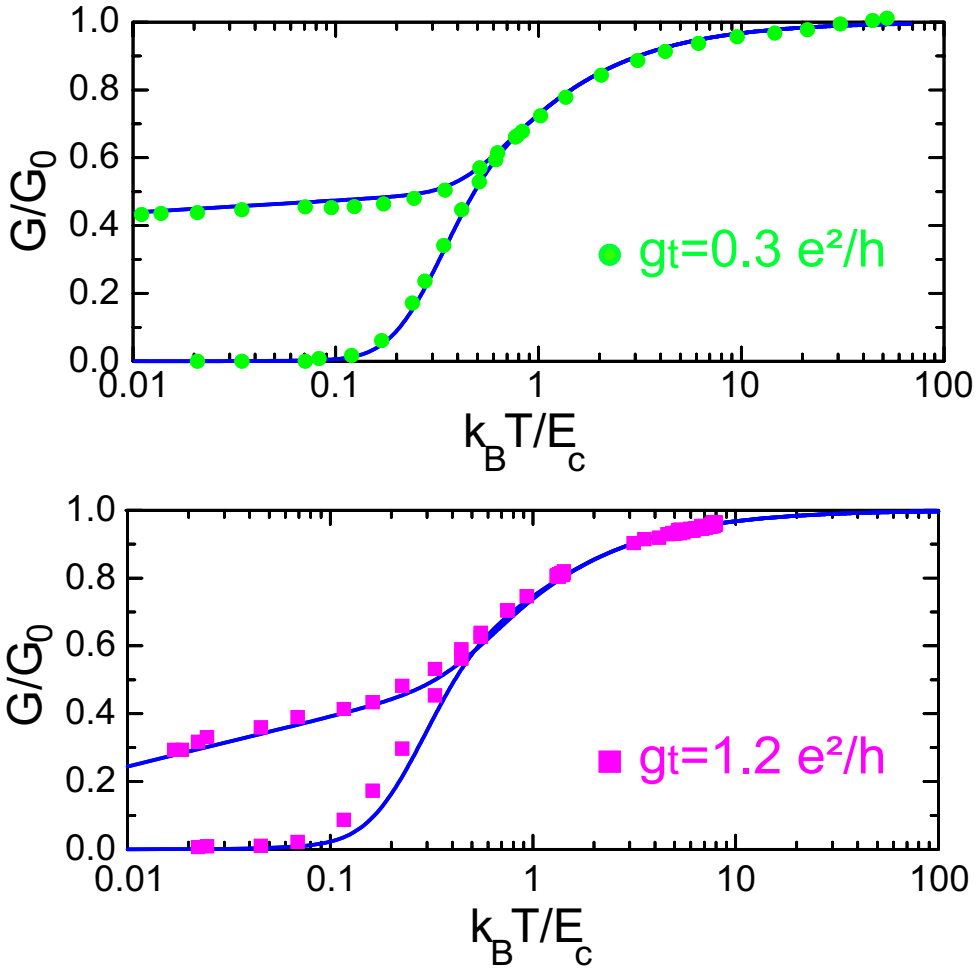

Figure 1.2. Reduced conductance as a function of the reduced temperature: sample 1 (top) and sample 3 (bottom). Comparison of the experimental results (dots) with the plot obtained from the calculation of König et al. (see Ref. [5]).

1.4 Analogy with the Kondo effect

As briefly mentioned above, an interesting analogy [6] is provided by comparing this problem with the Kondo problem.

The Kondo problem.

In its simplest form, the Kondo problem is concerned with a single magnetic impurity of spin $\frac{1}{2}$ which interacts via an exchange scattering potential with a band of free electrons. Such a description was first proposed by J. Kondo in 1964 [7] to interpret the minimum of resistivity-temperature curves in magnetic alloys. Kondo showed that the anomalous resistivity increase at low temperatures is a consequence of the enhanced scattering probability of the conduction electrons around diluted magnetic impurities. Consequently, the paramagnetism is screened by the interacting electrons which tends to "dress" such impurities.

Qualitative arguments

In our system, the virtual electron-hole pairs created on both sides of the tunnel junctions (an "elementary excitation" for the considered system) play the role of the conduction electrons in the Kondo problem; while the two neighboring charge states of the transistor island can be interpreted[1] as the "up" and "down" states of a spin $\frac{1}{2}$.

This analogy with the Kondo effect is helpful to picture what physically happens in the single electron transistor at low temperatures (see Fig. 1.3). Like in the Kondo effect, virtual electron-hole pairs dress the tunnel junctions and eventually lead to a screening of the island charge.

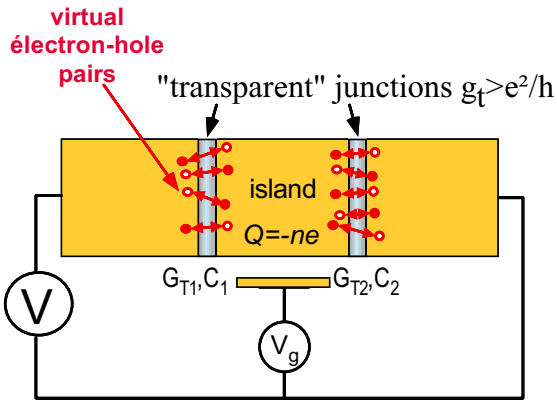

Figure 1.3. Schematics of a SET with virtuals electron-hole excitations dressing the junctions.

[1] Such a spin analogy to model neighboring charge states in single electron devices is further developed in section 2.1.2

Analogy in the Hamiltonian structure.

One can notice also that there exist a more formal analogy in the Hamiltonian structure of our system and the Kondo problem. Indeed, the Kondo model is described by a Kondo or $s-d$ Hamiltonian of following form:

$$H = \sum_{\overrightarrow{k},\sigma} \varepsilon\left(\overrightarrow{k}\right) c^{\dagger}_{\overrightarrow{k},\sigma} c_{\overrightarrow{k},\sigma} + J\,\overrightarrow{S}.\overrightarrow{s}\,(0)\,, \tag{1.13}$$

where the operators $c^{\dagger}_{\overrightarrow{k},\sigma}$ create conduction electrons of wave vector $\overrightarrow{k}$ and spin index $\sigma = \pm 1$. The impurity spin is $\overrightarrow{S}$, whereas $\overrightarrow{s}\,(0)$ denotes the effective spin resulting from the cumulative effect of the conduction electrons at the impurity site $\overrightarrow{r} = 0$. The exchange constant J is positive for an antiferromagnetic interaction, which is the usual situation in a real metal.

One can identify this last expression with the Hamiltonian for our system (Eq. 1.6). More precisely, the first and second terms of the Kondo Hamiltonian corresponds respectively to the quasiparticle Hamiltonians H^i_{qp} and the Hamiltonian $H_{el} + H_t$ described in section 1.1.1. The fact that this last term can be interpreted as an Hamiltonian describing a spin interacting with an effective field which can be written as: $J\,\overrightarrow{S}.\overrightarrow{s}\,(0)$, is further explained for an equivalent case in next chapter (section 2.1.2, Eq. 2.11).

1.5 SET optimization

Apart from their importance for the understanding of single electron charging effects, the above results have a direct implication on the optimization of SETs for electrometry applications. We show here that the disappearance of the Coulomb blockade in large conductance electrometers imposes a fundamental limit to the sensitivity of SET based electrometers.

The current noise in a SET is due to the discreteness of the charge transfer by the random tunneling events (see Chapter 5 for details). The current noise spectral density of the SET is given by the shot noise formula:

$$\delta I \simeq \sqrt{eI}\ \mathrm{A}/\sqrt{\mathrm{Hz}}. \tag{1.14}$$

The noise figure of a SET electrometer is defined as the input charge noise δq which would produce the same current noise. Assuming that the device is operated in the well developed

Coulomb blockade regime at the optimal current $I \simeq \alpha \tilde{E}_c e/h$, one readily obtains the following result:

$$\delta q \approx \sqrt{\frac{h}{\alpha \tilde{E}_c(\alpha)}}\, e/\sqrt{\text{Hz}}. \tag{1.15}$$

This expression shows that the SET sensitivity first improves on increasing α, reaches an optimum, and degrades afterwards when the effective charging energy decreases significantly. The operating temperature must however satisfy the inequality $k_B T \ll \tilde{E}_c(\alpha)$ for the SET to be in the Coulomb blockade regime. In practice, for given values of the bare charging energy and of the operating temperature, the optimal value of α is determined by minimizing the above expression while satisfying the inequality $k_B T \ll \tilde{E}_c(\alpha)$. Although we have not determined the best noise figure that can be achieved with a SET electrometer, our results indicate that the optimal value of α is much larger than unity : electrometers in the strong tunneling regime are more sensitive than electrometers in the weak tunneling regime because the increase in the current overcompensates the reduction of the Coulomb blockade.

Conclusion

Our experimental results confirm the intuitive knowledge that Coulomb blockade is suppressed when tunneling becomes too strong. They furthermore bring out a clear scenario for the transition from weak to strong tunneling. We have also shown that these results can be used to optimize the performance of single electron devices by operating them in the strong tunneling regime. Finally, our results provide a benchmark for testing future theoretical predictions on strong tunneling.

References of chapter 1

[1] see *e.g.* G.-L. Ingold and Yu. V. Nazarov, Chap. 2 in *Single Charge Tunneling* , edited by H. Grabert and M. H. Devoret (Plenum, New York, 1992).

[2] see pages 31-36 in ref. [1].

[3] H. Schoeller, and G. Schön, Phys. Rev. B **50**, 18436 (1994); J. König, H. Schoeller, and G. Schön, Europhys. Lett. **31**, 31 (1995).

[4] J. P. Pekola, K. P. Hirvi, J. P. Kauppinen, and M. A. Paalanen, Phys. Rev. Lett. **73**, 2903, (1994).

[5] J. König, H. Schoeller, and G. Schön, Phys. Rev. Lett. **78** ,4482, (1997).

[6] K.A. Matveev, Sov. Phys., JETP **72**, 892, (1991), L.I. Glazman and K.A. Matveev, Sov. Phys., JETP **71**, 1031, (1990).

[7] J. Kondo, Prog. Theo. Phys. **32**, 37 (1964).

[8] H. Schoeller and H. Grabert, private communications.

[9] H. Grabert, private communication.

[10] A. Maassen van den Brink, L. J. Geerligs, and G. Schön, Phys. Rev. Lett. **67**, 3030.

[11] A. Maassen van den Brink, A. A. Odintsov, P. A. Bobbert, and G. Schön, Z. Phys. **B 85**, 459 (1991).

[12] P. A. Bobbert and A. A. Odintsov, unpublished (1991).

[13] D. B. Haviland, Y. Harada, P. Delsing, C. D. Chen, and T. Claeson, Phys. Rev. Lett. **73**, 1541 (1994).

[14] P. Joyez, Chap. 3, Ph. D. Thesis, Université Paris 6, (1995).

Appendix 1-A
Fluctuation-dissipation derivation of the SET zero-voltage conductance within the sequential tunneling model

In the standard approach, Eq. 1.10 of the SET zero-voltage conductance in the weak tunneling regime is derived using the linear response theory, for small bias voltage V [1]. In this section, we propose another derivation of Eq. 1.10, making use of the fluctuation-dissipation theorem applied to the system *at equilibrium* ($V = 0$, see Fig. 1.4). For this purpose, we first need to identify the proper Brownian variable describing the charge transport in the system. Let us first note that since the island cannot charge excessively, the time average values of n_1 and n_2 tend to be equal. Thus, in principle, the charge q_t transferred through the SET can be defined as any linear combination:

$$q_t = e(\lambda_1 n_1 + \lambda_2 n_2) \quad , \tag{1.16}$$

where $\lambda_1 + \lambda_2 = 1$. However, if one wants q_t to be a Brownian variable it must fulfill the condition that successive events be uncorrelated, whatever the state of the system. In particular, suppose that the island is put in a high charge state, it will then tend to relax toward the ground state, expelling electrons one at a time through either junction. However, since the tunneling rate (1.9) through junction i is proportional to its tunnel conductance $G_{Ti} = R_{Ti}^{-1}$, electrons have a higher probability to cross the most transparent junction. In order for the variations Δq_t corresponding to each electron tunneling event to remain uncorrelated, one must weight n_1 and n_2 in order to compensate for the imbalance of the tunneling rates by choosing:

$$\lambda_1 = \frac{G_2}{G_1 + G_2} \quad ; \quad \lambda_2 = \frac{G_1}{G_1 + G_2} \quad , \tag{1.17}$$

With this choice, q_t is a proper Brownian variable. We now evaluate the diffusion constant D for q_t:

$$2D = \left\langle \frac{(\Delta q_t)^2}{\Delta t} \right\rangle \quad , \tag{1.18}$$

where $\left\langle \frac{(\Delta q_t)^2}{\Delta t} \right\rangle$ is evaluated by summing the different transitions weighed by their respective probabilities:

$$\begin{aligned} \left\langle \frac{(\Delta q_t)^2}{\Delta t} \right\rangle &= e^2 \left(\lambda_1^2 \left\langle \frac{(\Delta n_1)^2}{\Delta t} \right\rangle + \lambda_2^2 \left\langle \frac{(\Delta n_2)^2}{\Delta t} \right\rangle \right) \\ &= e^2 \sum_{n=-\infty}^{+\infty} P(n) \left[\lambda_1^2 \left(\Gamma_1(n,+) + \Gamma_1(n,-) \right) + \lambda_2^2 \left(\Gamma_2(n,+) + \Gamma_2(n,-) \right) \right] \end{aligned} \quad (1.19)$$

Here $P(n)$ is the Boltzmann probability to have the island in state n, given by Eq. (1.12) and $\Gamma_i(n,\pm)$ is the rate for the transition $n \rightarrow n \pm 1$ through junction i. Inserting expressions (1.17) and (1.9) for λ_i and $\Gamma_i(n,\pm)$, one obtains after elementary algebra:

$$D = \frac{1}{2} \frac{G_{T1} G_{T2}}{G_{T1} + G_{T2}} \sum_{n=-\infty}^{+\infty} P(n) \left[\frac{\Delta E_n^+}{1 - e^{-\beta \Delta E_n^+}} + \frac{\Delta E_n^-}{1 - e^{-\beta \Delta E_n^-}} \right]. \quad (1.20)$$

Finally, using Einstein's relation which relates the dissipative conductance G to the fluctuation parameter D :

$$k_B T G = D. \quad (1.21)$$

We then recover Eq. 1.10 for the SET conductance:

$$G = \frac{G_0}{2} \sum_{n=-\infty}^{+\infty} P(n) \left[\frac{\beta \Delta E_n^+}{1 - e^{-\beta \Delta E_n^+}} + \frac{\beta \Delta E_n^-}{1 - e^{-\beta \Delta E_n^-}} \right], \quad (1.22)$$

where $G_0 = 1/(R_{T1} + R_{T2})$ is the series tunnel conductance of the two junctions and $\Delta E_n^+ = E(n \pm 1) - E(n)$ is the electrostatic energy change when n changes by $\pm$ 1.

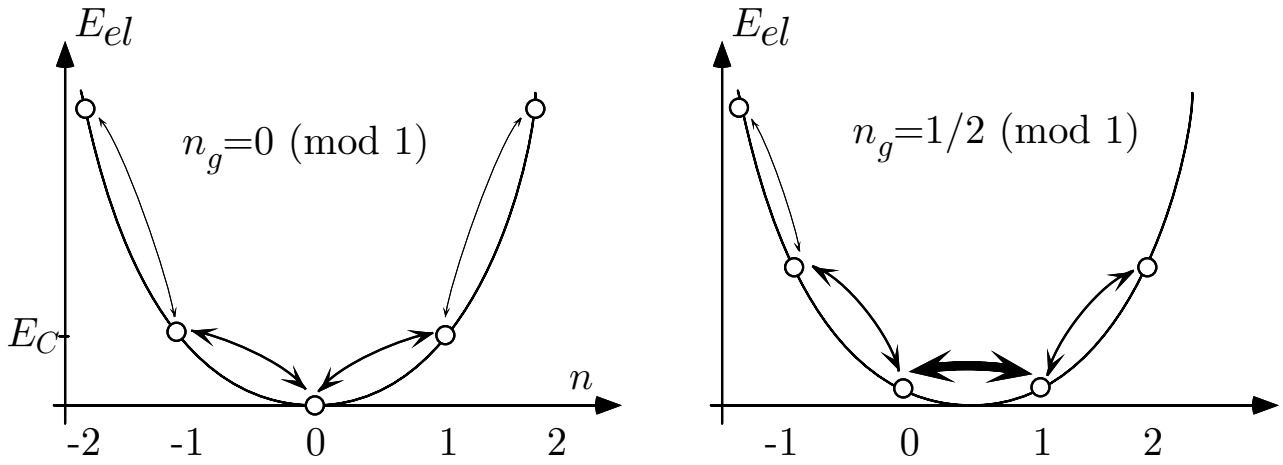

Figure 1.4. States of the SET at $V = 0$, corresponding to a minimum of conductance ($n_g = 0 \bmod 1$), and maximum conductance ($n_g = 0.5 \bmod 1$). The states are degenerate with respect to the number of electrons transferred through the device, and their energy only depends on n and n_g. At thermal equilibrium, stochastic transitions between the states obey detailed balance, and the different n states are populated according to Boltzmann's law. The random charge transfer in and out of the island through either junction causes a Brownian motion of the charge transferred through the SET. The conductance of the system is related to this diffusive behavior by the fluctuation-dissipation theorem.

Appendix 1-B
Renormalization group approach to the low temperature conductance of the SET

In Ref. [3], Schoeller and Schön derive non-perturbative expressions for the charge of the single electron box and for the conductance of the SET for an arbitrary tunneling strength. In this section we simply recall their results for the SET conductance which were used in the paper but could not be reproduced for lack of space. Their approach is based on the renormalization group technique, a powerful method which proved its efficiency in many problems. However, the method introduces an artificial cut-off energy which has the drawback of modifying the parameters of the system [8]. The link between the modified parameters and the measurable "bare" parameters must be determined by another method (*e.g.* high order perturbation theory). This has not yet been done for the present problem. In order to keep this essential point in mind, we will introduce below a "star" in the notation of these modified SET parameters. In their model, Schoeller and Schön only retain the two lowest charge states of the system, to simplify the calculations. Thus, their model can only capture correctly the behavior of the system when the other charge states play a negligible role. This is the case at temperatures $k_B T \ll E_c^0$ and in the vicinity of the conductance peaks.

Here, we consider only the peak at $n_g \approx 0.5$. The bare parameters of the model are :

- the energy gap between the two neighboring charge states :

$$E_g = E_c^0 \left| n_g - \frac{1}{2} \right| \tag{1.23}$$

- the tunneling strength parameter

$$\alpha = R_K G_{//} \tag{1.24}$$

where $G_{//} = \left(R_{T1}^{-1} + R_{T2}^{-1}\right)$ is the parallel conductance of both tunnel resistances, and

- the series tunnel conductance of the SET

$$G_0 = \frac{1}{(R_{T1} + R_{T2})}. \tag{1.25}$$

The renormalization process leads to the introduction of renormalized quantities which are

expressed using the following modified parameters:

$$\widetilde{E_g} = \frac{E_g^*}{1+\frac{\alpha^*}{2\pi^2}\ln\frac{E_c^*}{k_BT}}, \tag{1.26}$$

$$\tilde{\alpha} = \frac{\alpha^*}{1+\frac{\alpha^*}{2\pi^2}\ln\frac{E_C^*}{k_BT}}. \tag{1.27}$$

The conductance is then expressed in terms of the renormalized quantities :

$$G = \frac{G_0^*}{8\pi^2}\int_{-\infty}^{+\infty}\hbar\,\mathrm{d}\omega\frac{\hbar\omega}{k_BT}\,\mathrm{csch}\left(\frac{\hbar\omega}{k_BT}\right)\frac{\tilde{\alpha}\hbar\omega\coth\left(\frac{\hbar\omega}{2k_BT}\right)}{\left(\hbar\omega-\widetilde{E_g}\right)^2+\left(\frac{\hbar\omega\tilde{\alpha}}{4\pi}\coth\left(\frac{\hbar\omega}{2k_BT}\right)\right)^2} \tag{1.28}$$

The renormalization group method can be extended to include more charge states. It would then allow to cover all gate charges, and higher temperatures. However, this would not solve the main problem of this theory which is its lack of quantitative predictive power. Solving this problem amounts to finding the relationship between the modified parameters and the measurable quantities. As already mentioned, this can be done by calculating the perturbation theory at high orders and comparing the predictions of the two methods. In the strong tunneling single electron box, this comparison requires to evaluate *at least* the third order of the perturbation theory in a path integral representation, which involves summing the contributions of 136 diagrams [9].

Appendix 1-C
Determination of the charging energy from the subgap resonances of the superconducting transistor

In the absence of an applied magnetic field, the Al electrodes of the SET are in their superconducting state, and charge transport at bias voltages $0 < V < 2\Delta/e$, is mostly due to the Josephson tunneling of Cooper pairs. Josephson tunneling is however an essentially reversible process, and thus, no DC current can flow in the device unless some non-electronic degrees of freedom of the system can absorb the energy provided by the voltage source. This is why fully superconducting devices generally present a gap in their I-V characteristic. The current below the gap is however usually not strictly zero, because the electromagnetic environment of the device may always absorb some energy. In the case of the transistor, the energy provided by the voltage source can also promote the SET island to a higher charge state. Such an excitation of the island is unstable and decays, exciting the environment and returning the SET to its initial condition (see Fig. 1.5). This type of process is possible, when the voltage source fulfills a resonance condition with the discrete set of gate-voltage dependent levels in the island. Hence, one expects to see gate-voltage dependent resonances in the subgap I-V characteristics of superconducting SET transistors. This phenomenon, known as "resonant Cooper pair tunneling" was investigated in detail in Refs. [10–14] . When the Josephson coupling energy E_J is such that $E_J \ll E_c$, the authors have shown that the resonance conditions can be expressed as :

$$(2p+1)eV = 4E_c \left| q^2 - q(n_g \bmod 2) \right| \tag{1.29}$$

where p and q are integer numbers, V is the bias voltage, E_c is the charging energy, and n_g is the reduced gate charge. These resonances draw lines which form a checkered pattern in a 3-D I-V-Vg plot. This simple geometry enables a straightforward determination of the charging energy, using the above resonance condition.

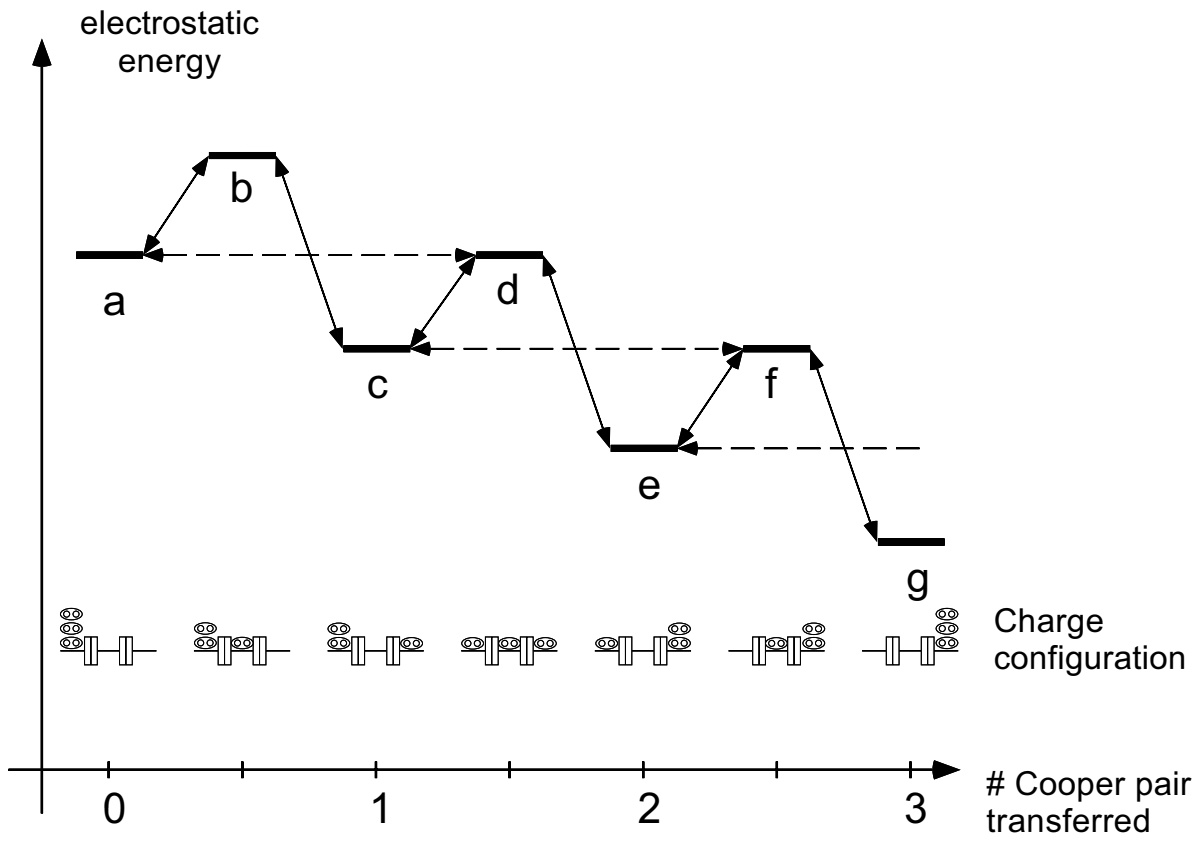

Figure 1.5. States of the superconducting SET at finite voltages, for $E_J \ll E_c$. Adjacent states $a, b, c, \ldots$ are coupled by Josephson coupling represented by the solid arrows. States $a, c, e, \ldots$ correspond to local minima of the electrostatic energy and are thus metastable. Their decay is usually slow, unless a resonant charge transfer can occur, as depicted here: states $a, c, e, \ldots$ are resonantly coupled to the states $d, f, \ldots$ by a high order Josephson coupling represented by dashed arrows (this resonance corresponds to $p = 1$ and $q = 1$ in Eq. (1.29)). Under such a resonance condition, starting from e.g. state a, the system coherently accesses to the unstable state d, and subsequently decays toward either state c or e, much faster than from the initial state a. The whole process (resonant transfer followed by an inelastic decay) then starts over again. These resonances, similar to a radiative cascade in atomic physics, manifest themselves by an increase in the current flowing through the SET (see Ref. [12] of Chapter 2).

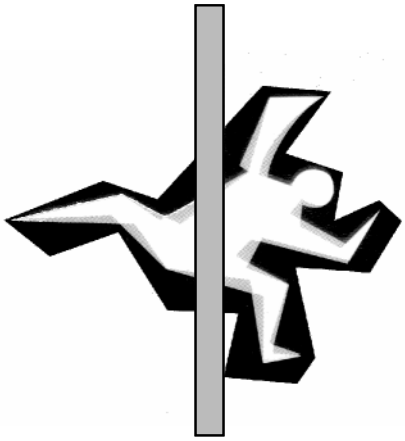

Chapter 2

Quantum fluctuations of charge in the single Cooper pair box

Introduction

The question of the behavior of single electron devices when the electrodes are superconducting arose at the very beginning of single electronics because the aluminum commonly used to fabricate most of the metallic-based single electron devices is superconducting at the typical sub-Kelvin operating temperatures (unless a sufficiently large magnetic field is applied). Such a situation is really different from the case of normal metal electrodes and the question arises whether the pairing of electrons in Cooper pairs interplays with charging effects. Do "single Cooper pair devices" exist ? At first, one naturally wonders if the charge of a small metallic superconducting electrode in a small tunnel junction circuit is still quantized, and if it is, with which charge quantum. A clear answer to this fundamental question was given by Lafarge *et al.* when they directly measured the charge of a superconducting island coupled to a *non-superconducting* metal reservoir of charges [1]. They found that the charge of a superconducting island is quantized in multiples of $2e$ at low temperature, provided that the charging energy of the island is kept smaller than the energy gap for the creation of a quasiparticle in the superconductor. The charge $2e$ is thus a charge quantum for single Cooper

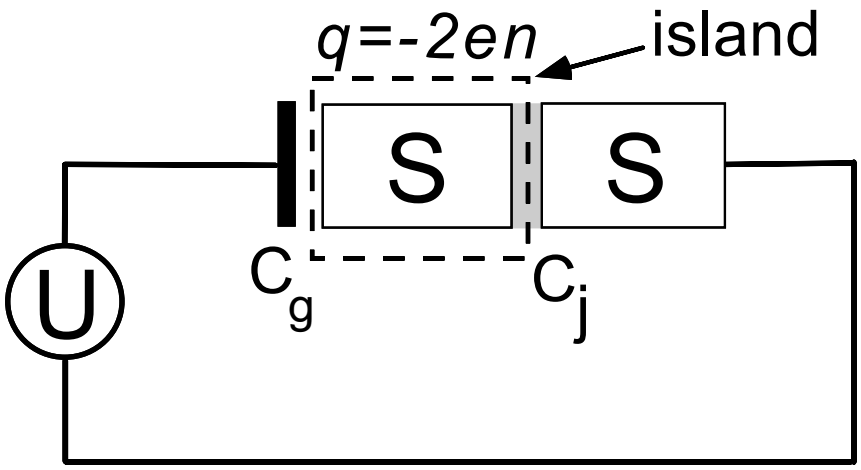

Figure 2.1 Schematic diagram of the single Cooper pair box. The state of the circuit is characterized by its number n of excess Cooper pairs that have entered the superconducting island (dashed frame) through the Josephson junction of capacitance C_j. The island can be electrostatically polarized by the voltage source U through the capacitance C_g .

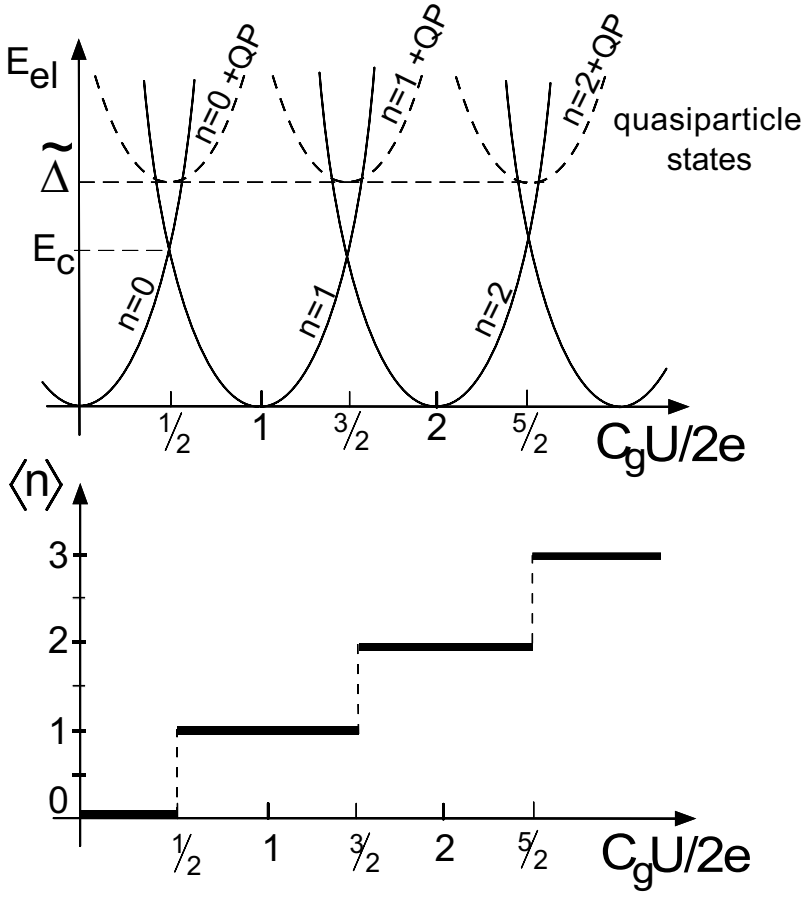

Figure 2.2 Top: Electrostatic energy of the box for given numbers n of Cooper pairs in excess in the island as a function of the reduced voltage CgU/2e. Energy curves associated to charge states with one extra quasiparticle in the island are shifted by the even-odd free energy $\tilde{\Delta}$.
Bottom: number of excess Cooper pairs in the island minimizing the electrostatic energy for $\tilde{\Delta}>E_C$ .It corresponds to an integer number of Cooper pairs in the island.

pair electronics, although it is not as robust as e for single electronics.

When the charge of a superconducting electrode corresponds to a given number of extra Cooper pairs, its superconducting phase is completely undetermined. The number of extra Cooper pairs in the island and the superconducting phase difference across the junction are in fact conjugated variables, which obey a Heisenberg uncertainty relation (note that the BCS theory makes use of the phase only, for the sake of calculation convenience).

Assuming that $2e$ is indeed the charge quantum in the superconducting state, one can then wonder how the coupling of a superconducting island to other *superconducting* electrodes through tunnel junctions affects the charge quantization in the island. What is for single Cooper pair devices the analog of the condition $R_T \geqslant R_K$ for single electron devices?

The tunnel junction permits the passage of Cooper pairs between the superconducting electrodes and tends to maintain the same superconducting phase on both sides of the junction, thus favoring quantum fluctuations of the conjugate variable, i.e. the number of Cooper pair transferred through the junction. As with single electrons, these quantum fluctuations of the island charge are in competition with charging effects which tend on the contrary to select the number of pairs in the island. However, there is an important difference: the tunneling of Cooper pairs is characterized by a coupling energy, called the Josephson energy E_J, which is a new energy scale which has to be compared directly to the charging energy and not by a resistance which has to be compared to the resistance quantum. The tunneling of Cooper pairs is a reversible process whereas the tunneling of single electrons is irreversible.

We report in this chapter an experiment on a single superconducting island coupled to a superconducting reservoir through a Josephson tunnel junction. This "fully-superconducting box" experiment is for single Cooper pair electronics the equivalent of the single electron box experiment for single electronics (see Introduction).

2.1 The superconducting box in the $2e$ quantization regime

The superconducting box circuit was first theoretically considered by Büttiker [2] It consists of a small superconducting electrode, nicknamed "island", connected to a superconducting lead, which acts as a "reservoir" of charges, through an ultrasmall Josephson junction (see

Fig. 2.1). The island is also capacitively coupled to a voltage source U through a gate capacitance C_g, thus providing a tunable electrostatic polarization. The principle of the box experiment consists in measuring the average charge of the island while sweeping the voltage U.

2.1.1 The Coulomb staircase in the absence of Josephson coupling

2.1.1.a Quantum description of the island states[1]

We assume here that the quasiparticle gap $\widetilde{\Delta}$ is large enough so that no quasiparticles are present in the electrodes at the temperature of the circuit. Under these conditions, the island charge q is quantized in units of $2e$, and the set of states $|n\rangle$ with n excess Cooper pairs in the island is a basis of the Hilbert space of the box. These states are eigenvectors of the operator $\widehat{n}$:

$$\widehat{n}\,|n\rangle = n\,|n\rangle \quad . \tag{2.1}$$

We will use in the following the basis of states $|n\rangle$ to express the Hamiltonian of the box.

As further developed in chapter 4, section 4.1.2, the phase δ across the Jospehson junction, defined by the eigenvalues of the operator $\widehat{\delta} = \frac{1}{i}\frac{\partial}{\partial n}$ is a conjugate variable of the Cooper pair number n.

2.1.1.b The electrostatic Hamiltonian

The total capacitance of the island $C_\Sigma = C_J + C_g$ determines the characteristic electrostatic charging energy E_c:

$$E_c = \frac{e^2}{2C_\Sigma} \quad . \tag{2.2}$$

The electrostatic Hamiltonian H_{el} is diagonal in the basis $|n\rangle$ and writes [3] :

$$H_{el} = 4E_c \sum_n (n - n_c)^2\,|n\rangle\,\langle n| \quad . \tag{2.3}$$

where $n_c = C_g U/(2e)$ is a dimensionless variable which corresponds to the effective number of excess Cooper pairs induced on the gate capacitance. In contrast with n, which can take only integer values, the reduced voltage n_c is a continuous parameter. As the gate voltage U varies, the electrostatic energies of the states $|n\rangle$ form a set of parabolas indexed by the number n of excess Cooper pairs. These parabolas are centered around voltages $U_n = n\,(2e/C_g)$ and cross

[1] A more detailed introduction to Hamiltonian mechanics applied to electrical circuits is provided in chapter 4.

at regularly spaced voltages $U_{n,c} = (2n+1)\,e/C_g$ (see Fig. 2.2, top panel). The electrostatic energy at crossing points between neighboring states is equal to the charging energy E_c. The pair quantization holds if, at these degeneracy voltages, the free energy $\widetilde{\Delta}$ of the states with one extra quasiparticle is large enough so that they are not thermally populated. Such a condition can be writen as:

$$k_B T \ll \widetilde{\Delta} - E_c \quad . \tag{2.4}$$

In an ideal sample and in the zero temperature and zero magnetic field limit, the energy $\widetilde{\Delta}$ equals the BCS gap Δ. The energy $\widetilde{\Delta}$ is reduced below Δ first the entropic contribution (see section 2.3.3.c) and, in most practical cases, by defects in the superconducting island. The Eq. 2.4 of course implies the relation $\Delta > E_c$. In the opposite case, a quasiparticle charge states can minimize the electrostatic energy around the voltages $U_{n,c}$, thus breaking the $2e-$quantization in the island.

2.1.1.c The Coulomb staircase at zero temperature

In the absence of Josephson coupling, the superconducting box is similar to the single box in the weak tunneling regime but with a double charge quantum. At zero temperature, the island adopts the number n of extra Cooper pairs which minimizes the electrostatic energy. Therefore Cooper pairs enter the island one by one at the degeneracy voltages as the voltage U is swept. The equilibrium value of n is quantized and follows a step-like function denoted as a "Coulomb staircase"[2] (see Figure 2.2, bottom panel), with a $2e$-periodicity with respect to the gate charge U/C_g. Like in the single electron box, the steps are infinitely sharp at zero temperature and are rounded by thermal fluctuations of the island charge at finite temperature.

2.1.2 The Coulomb staircase in presence of Josephson coupling

2.1.2.a. The Josephson Hamiltonian

The tunneling Hamiltonian between the electrodes of a tunnel junction with tunnel resistance R_T results in the superconducting case in a Josephson Hamiltonian which couples neighboring charge states (see section 4.1.2). The expression of the Josephson Hamiltonian in

[2] The "Coulomb staircase" term is also used for the periodic structure observed in the I-V curves of single electron transistors. Even if it manifests on different variables, such a staircase originates from the same physical reasons.

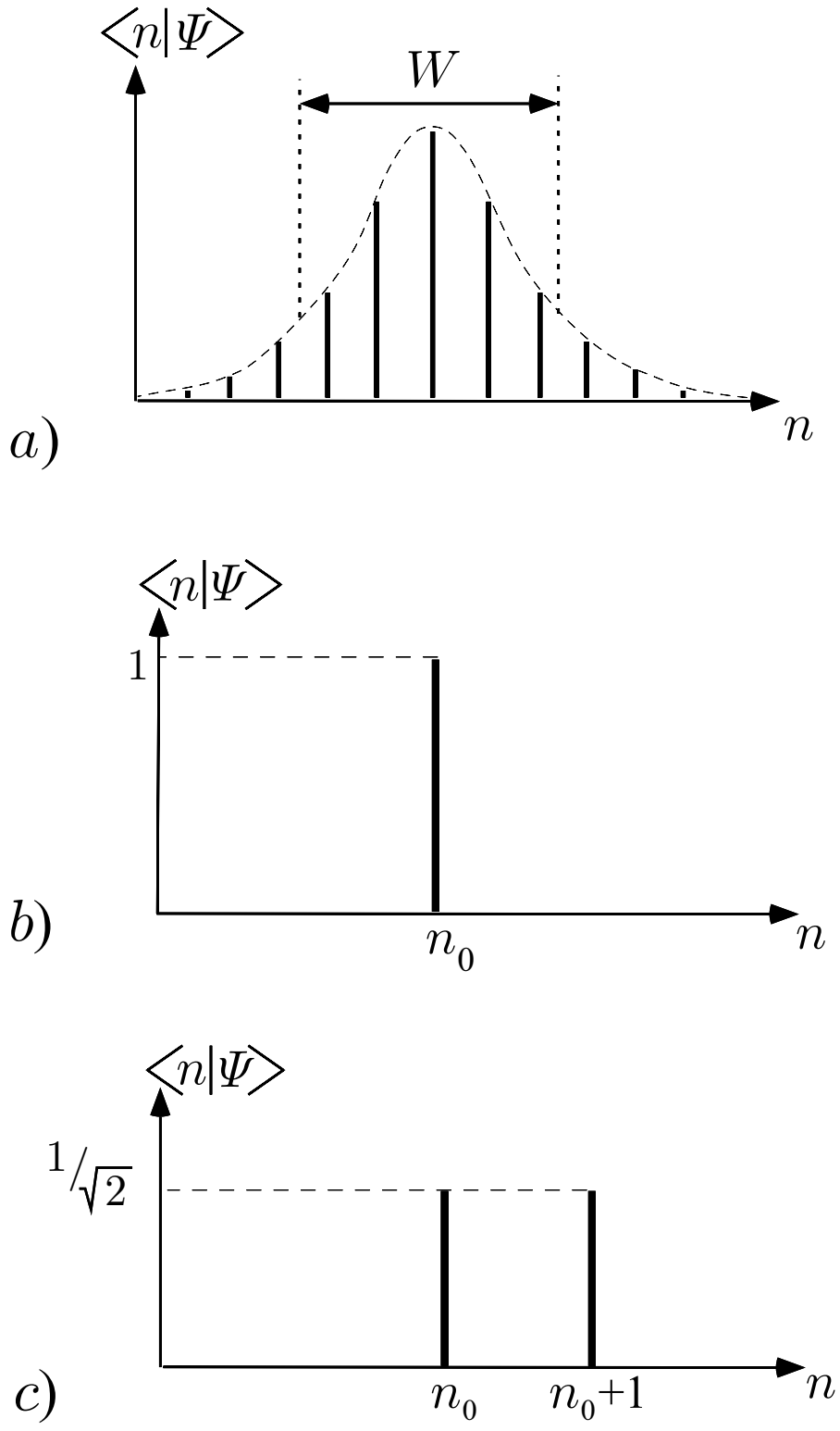

Figure 2.3 Box ground state amplitude in the charge state basis for respectively large capacitance Josephson junctions a) and for ultrasmall capacitance junctions b), c). These two latter amplitudes are represented respectively for voltages $U=2n_0e/C$ and $U=(2n_0+1)e/C$. For small junctions, the span of the ground state wave-function $|\Psi\rangle$ in the charge state basis is reduced, and quantum fluctuations occur only between two neighboring charge states.

the basis $|n\rangle$ writes:

$$H_J = -\frac{E_J}{2}\sum_n \left(|n+1\rangle\langle n| + |n\rangle\langle n+1|\right), \tag{2.5}$$

where the Josephson coupling energy E_J is assumed to follow the Ambegaokar-Baratoff relation:

$$E_J = \frac{h}{8}\frac{\Delta}{e^2 R_T}. \tag{2.6}$$

2.1.2.b. The total Hamiltonian

The total Hamiltonian H of the box is the sum of the Josephson and of the electrostatic Hamiltonian. Its expression in the $|n\rangle$ basis writes:

$$\begin{aligned} H &= H_{el} + H_J \\ &= \sum_n 4E_c\left(n-n_c\right)^2|n\rangle\langle n| - \frac{E_J}{2}\left(|n+1\rangle\langle n| + |n\rangle\langle n+1|\right) \quad . \end{aligned} \tag{2.7}$$

2.1.2.c. Squeezing of charge fluctuations in small capacitance junctions

Let us first examine the case when the charging energy E_c is small compared to the Josephson energy E_J. Such a situation is encountered in typical large capacitance Josephson junctions. In this regime, the Hamiltonian H_{el} can be treated as a perturbation and one can show that the ground state $|\Psi\rangle$ of the system is given by a coherent superposition of a large number of charge states:

$$\begin{aligned} |\Psi\rangle &= \sum_{k=-\infty}^{+\infty} e^{-\frac{k^2}{2W^2}}|n_0+k\rangle \quad , \\ \text{where } W &= \frac{1}{\sqrt{2}}\left(\frac{E_J}{E_c}\right)^{\frac{1}{4}}. \end{aligned} \tag{2.8}$$

The components of $|\Psi\rangle$ in the charge basis have a Gaussian envelope (see Fig. 2.3, left) with a width W which directly illustrates the competition between the Josephson energy and the charging energy. These large quantum fluctuations of the charge number n can be seen as a manifestation of the Heisenberg uncertainty principle. Indeed, as pointed out in the beginning of that chapter, the conjugate variable of n is the phase δ. For large Josephson couplings, the phase δ is a good quantum number, thus leading to important quantum fluctuations of its conjugate variable.

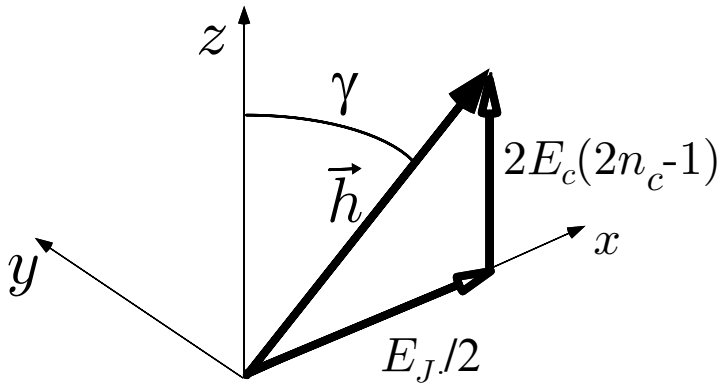

Figure 2.4. Effective spin representation for the superconducting island charge state. The Hamiltonian restricted to two neighboring charge states can be seen as a spin 1/2 interacting with a magnetic field which components are given by the box parameters.

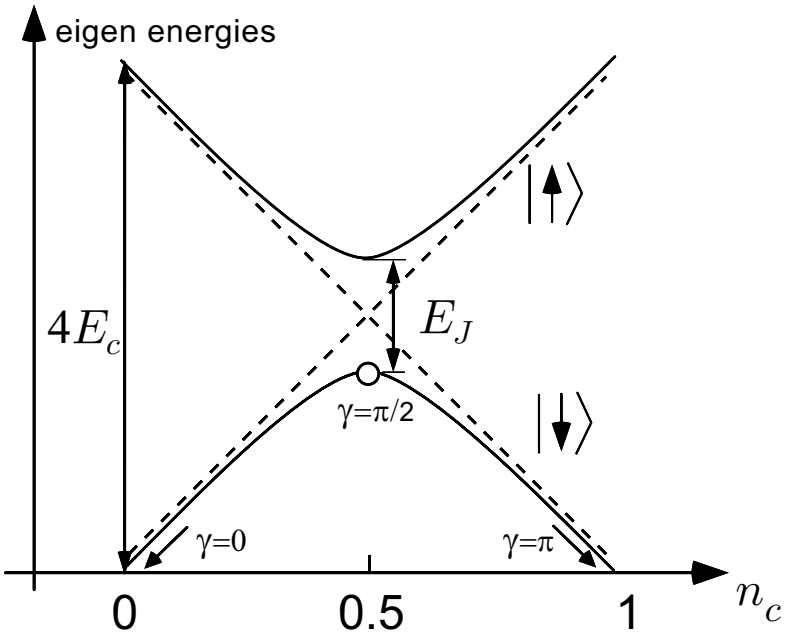

Figure 2.5. Energy bands of the superconducting box obtained in the framework of the spin representation. The box ground state correspond to the symmetric eigenstate which has an hyperbolic dependence upon the gate charge and asymptotaticaly reaches pure spin states.

The above result predicts that these quantum fluctuations ,characterized by the width W, are greatly reduced for an electrostatic energy comparable to the Josephson energy ($E_J/E_c \sim 1$). Coulomb charging limits the quantum delocalization of the charge which fluctuations are "squeezed" (see Fig. 2.3, right). In this intermediate regime where E_c and E_J are of the same order of magnitude, it is sufficient to take into account the Josephson coupling between a few lowest electrostatic energy states. When E_J is smaller than E_c, considering the two lowest energy states is in fact sufficient to determine the Coulomb staircase with great accuracy.

Since the superconducting box devices that we have fabricated precisely lie in this range of parameters, we calculate the Coulomb staircase in this approximation.

2.1.2.d. Effective two-level model of the superconducting box

We restrict the description to the gate charge interval $0 < n_c < 1$ so that the two neighboring charge states that need to be considered are $|0\rangle$ and $|1\rangle$.

For the sake of convenience, the reference level for the energy of the states is chosen to be:

$$E_0 = 4E_c \left(1 - C_g U/e\right)^2 . \tag{2.9}$$

The total Hamiltonian H (Eq. 2.7) expressed in the restricted Hilbert space ($|0\rangle , |1\rangle$) is represented by the following matrix :

$$H = \frac{1}{2} \begin{pmatrix} -E & -E_J \\ -E_J & +E \end{pmatrix} \quad , \tag{2.10}$$

where $E = 4E_c \left(1 - C_g U/e\right) = 4E_c \left(1 - 2n_c\right)$ has now a linear dependence upon the gate voltage. One can identify this expression with the Hamiltonian of a spin $\frac{1}{2}$ in a magnetic field by expressing H as a function of the following Pauli matrices:

$$\boldsymbol{\sigma}_x = \begin{pmatrix} 0 & 1 \\ 1 & 0 \end{pmatrix} \qquad \text{and} \qquad \boldsymbol{\sigma}_z = \begin{pmatrix} -1 & 0 \\ 0 & 1 \end{pmatrix}, \tag{2.11}$$

thus leading to:

$$H = -\frac{E}{2}\boldsymbol{\sigma}_z - \frac{E_J}{2}\boldsymbol{\sigma}_x = -\overrightarrow{s}.\overrightarrow{h} \quad , \tag{2.12}$$

where $\overrightarrow{s}$ is the spin operator of the effective spin $\frac{1}{2}$ and $\overrightarrow{h}$ the effective magnetic field (see Fig. 2.4) with components in the basis (x,y,z): $[E_J/2, 0, 2E_c\left(1 - 2n_c\right)]$.

Since we are looking at quasi-equilibrium properties of the system, the time of observation is supposed to be much larger than the relaxation time of the spin. In such a case, the

eigenstates of this Hamiltonian are given by the following combinations:

$$\left|\Psi_{s/a}\right\rangle = \cos\frac{\gamma}{2}\left|0\right\rangle \pm \sin\frac{\gamma}{2}\left|1\right\rangle \quad , \tag{2.13}$$

where γ =Arctan (E_J/E). At the degeneracy point $E = 0$, the eigenstates $|\Psi_s\rangle$ and $|\Psi_a\rangle$ are the symmetric and antisymmetric combinations of $|0\rangle$ and $|1\rangle$. The associated energy bands E_a and E_s have a hyperbolic gate voltage dependence (see Fig 2.5):

$$E_{a/s} = \pm E_c\sqrt{(1-2n_c)^2 + \left(\frac{E_J}{4E_c}\right)^2} \quad , \tag{2.14}$$

The Josephson Hamiltonian results in an anticrossing of the two levels with a gap E_J at $E = 0$ (see Fig. 2.5).

2.1.2.e. The zero temperature Coulomb staircase in the two-level approximation

Since the ground state is a superposition of two states with different numbers of Cooper pairs in the island, the mean value of n noted $\langle n\rangle$ is no longer quantized but varies continuously with the gate voltage U. At zero temperature, the number of excess pairs in the island is given by the projection of n on the symmetric eigenstate:

$$\begin{aligned}\langle n\rangle_{T=0} &= |\langle\Psi_s|\,\widehat{n}\,|\Psi_s\rangle|^2 = \sin^2\frac{\gamma}{2} \\ &= \frac{1}{2} + \frac{(C_gU/e-1)}{2\sqrt{(1-C_gU/e)^2 + (E_J/4E_c)^2}} \\ &= \frac{1}{2} + \frac{(2n_c-1)}{2\sqrt{(2n_c-1)^2 + (E_J/4E_c)^2}}.\end{aligned} \tag{2.15}$$

The competition between the Josephson coupling and the charging effects results in a rounding of the Coulomb staircase, as shown in Fig. 2.6. In particular, the maximum staircase slope is equal to $4E_c/E_J$ and directly reflects this competition. Taking advantage of the $2e$-periodicity, we can extend the obtained results to the whole Coulomb staircase. Compared to the staircase obtained in the absence of Josephson coupling, the steps are rounded at zero temperature due to quantum fluctuations of the charge, as shown in Fig. 2.7. The two-level approximation is valid as long as the slope at the center of the plateaus remains small.

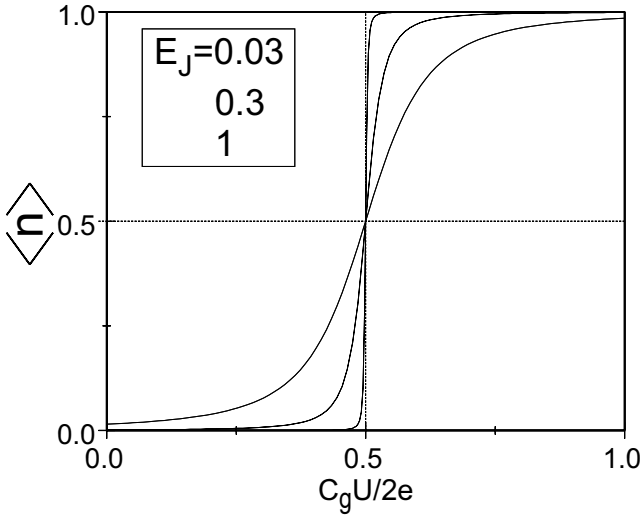

Figure 2.6: Average excess charge $\langle n \rangle$ at T=0 in the superconducting island as a function of the gate voltage $C_g U/2e$, for $E_J/E_c = 0.01, 0.3, 1$.

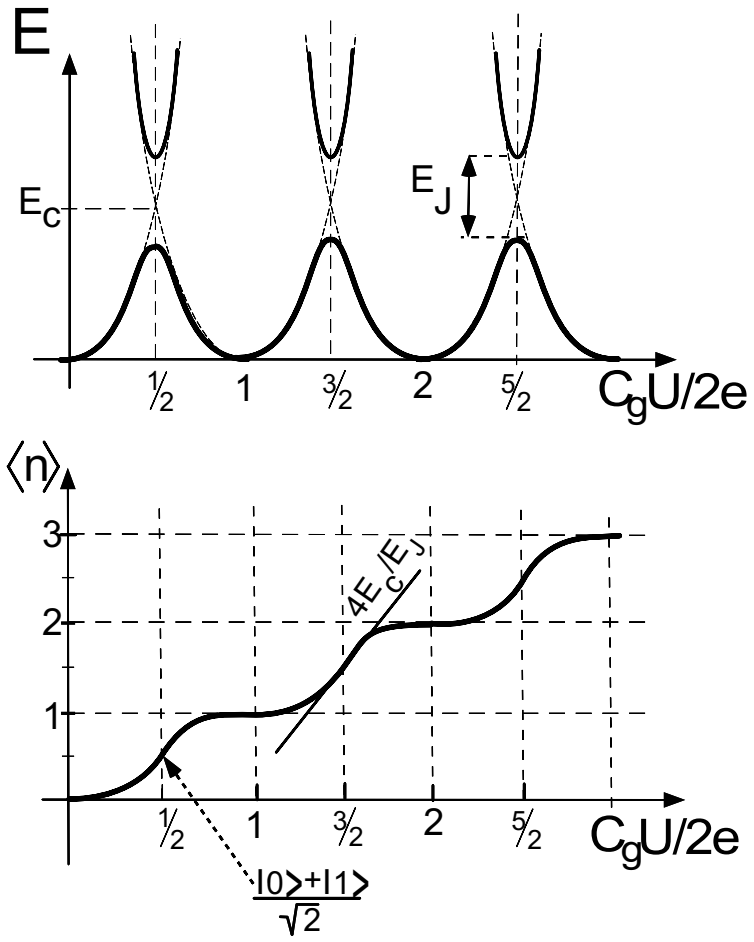

Figure 2.7 Top: *Energy bands of the superconducting box when both electrostatic and Josephson Hamiltonians are taken into account. The Josephson coupling forces electrostatic levels to anticross. The gap between the ground level and the first excited level is equal to the Josephson energy* E_J .

Bottom: Average excess charge of the island at T=0 obtained from the ground state energy. The "Coulomb staircase" is rounded due to quantum fluctuations of the charge. At transition voltages (n_C*=CgU/2e=half-integer), the box is in a macroscopic quantum superposition of two charge states difering by one Cooper pair. The slope of the curve at this point directly illustrates the interplay between charging and Josephson effects.*

2.2 Finite temperature calculation of the Coulomb staircase taking into account the quasiparticle states

We calculate in this section how the shape of the Coulomb staircase is modified by the finite temperature and magnetic field when island states with quasiparticles are taken into account. In addition to the charge states $q = 0$ and $q = 2e$ which contain an even number of quasiparticles in the island, we also consider the charge state $q = e$ which contains an odd number of quasiparticles in the island. The average charge in the island is obtained by weighing these three charge states according to their occupation function given from the partition function [1].

Refered to the energy E_0 given by Eq.(2.9), the electrostatic energy of the $q = e$ state writes:

$$E_1 = E_c \left[(1 - C_g U/e)^2 - 1 \right] . \tag{2.16}$$

The odd-even free energy difference $\widetilde{\Delta}(T, H)$ between odd and even charge states decreases when the temperature or the magnetic field increase [1] . At zero temperature and zero magnetic field, $\widetilde{\Delta}$ is the lowest quasiparticle energy. It coincides with the BCS superconducting gap Δ only if the sample is perfect. The thermal average $\langle n \rangle (T)$ of the island excess charge is obtained from the partition function and takes the following expression:

$$\langle n \rangle (T) = \frac{\left| \langle \Psi_s | \widehat{n} | \Psi_s \rangle \right|^2 e^{-\beta E_s} + \left| \langle \Psi_a | \widehat{n} | \Psi_a \rangle \right|^2 e^{-\beta E_a} + e^{-\beta \left(E_1 + \widetilde{\Delta}(T,H) \right)}}{e^{-\beta E_s} + e^{-\beta E_a} + e^{-\beta \left(E_1 + \widetilde{\Delta}(T,H) \right)}} \quad , \tag{2.17}$$

which can be related to the zero-temperature result $\langle n \rangle_{T=0}$:

$$\langle n \rangle = \frac{1}{2} + \left[\frac{\sinh \left(\frac{2E_c}{k_B T} \sqrt{(2n_c - 1)^2 + (E_J/4E_c)^2} \right)}{\cosh \left(\frac{2E_c}{k_B T} \sqrt{(2n_c - 1)^2 + (E_J/4E_c)^2} \right) + \frac{1}{2} e^{\frac{2(E_c - \widetilde{\Delta})}{k_B T}}} \right] \times \left(\langle n \rangle_{T=0} - \frac{1}{2} \right) . \tag{2.18}$$

This expression can be further simplified in the case when $\widetilde{\Delta} \gg E_c$, i.e. when odd charge states are not thermally populated:

$$\langle n \rangle = \frac{1}{2} + \left(\langle n \rangle_{T=0} - \frac{1}{2} \right) \times f(n_c, E_c/k_B T) \quad , \tag{2.19}$$

where the distortion factor $f(x, y)$ is given by : $\tanh \left[2y \sqrt{(2x - 1)^2 + (E_J/4E_c)^2} \right]$. (2.20)

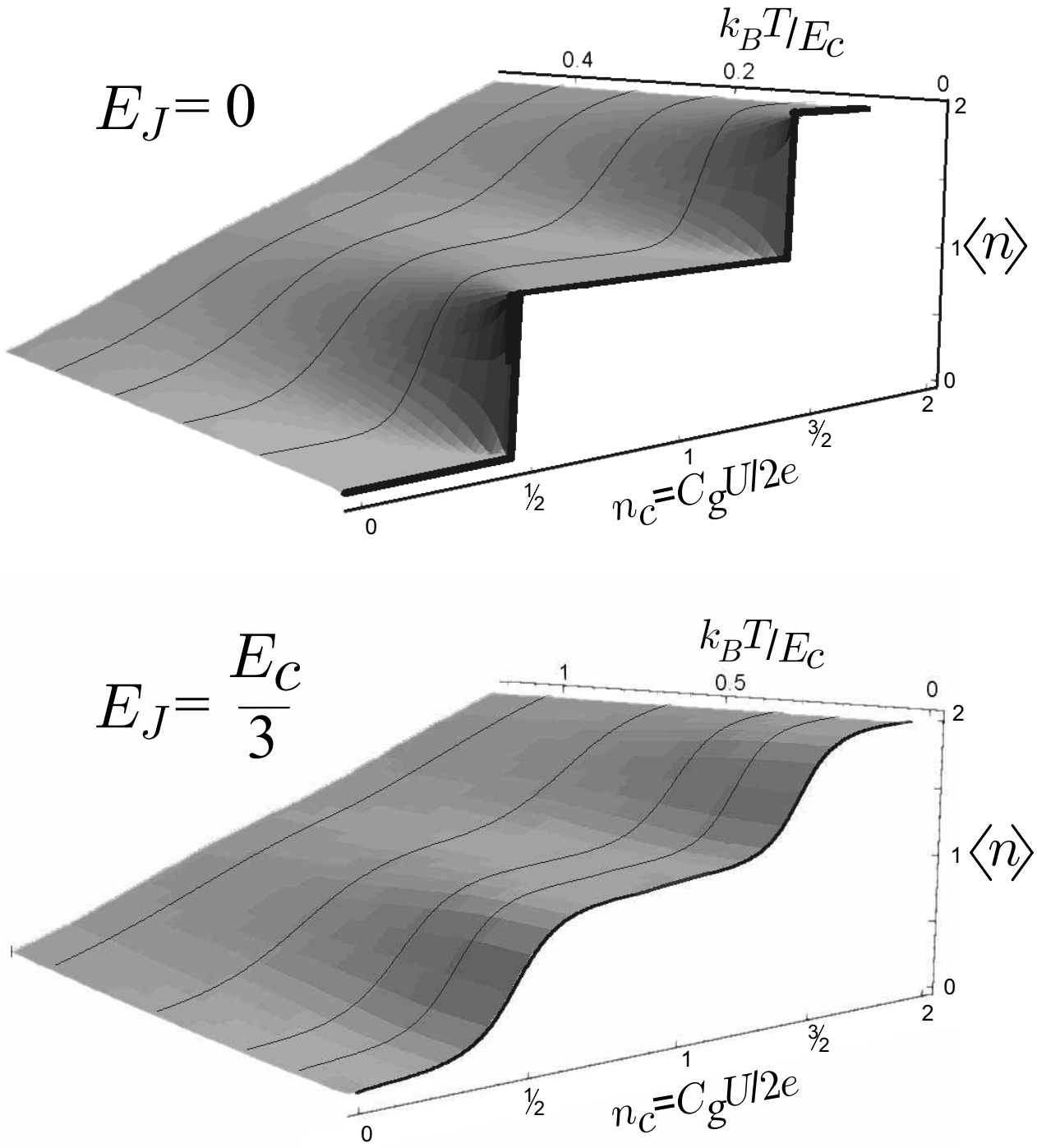

Figure 2.8. Three dimensionnal representations of the temperature dependence of the Coulomb staircase without Josephson coupling (top panel) and for a Josephson coupling energy equal to one third of the charging energy (bottom panel). In this last case, the Coulomb staircase becomes temperature-independent at low temperature ($kT \ll E_J$), due to the gap in the energy band diagram (see Fig. 2.7). This gap makes also the box ground state more robust with respect to thermal fluctuations, as illustrated by the staircase smearing which occurs at higher temperature compared to the case without Josephson coupling (top panel).

The corresponding thermal smearing of the Coulomb staircase is shown in Fig. 2.8 (bottom panel) in the particular case $E_J = E_c/3$. Below a temperature of the order of E_J, the Coulomb staircase becomes temperature independent and coincides with the zero-temperature result. This can be seen in Fig 2.9 which shows that the distorsion factor f is close to one at low temperature. This relative robustness of the Coulomb staircase with respect to thermal fluctuations is due to the gap E_J between the two eigenstates.

The disappearance at low temperature of the thermal contribution to the smearing of the staircase, and the persistence of rounded steps are then two signatures of the coherent superposition of charge states occurring in the superconducting box.

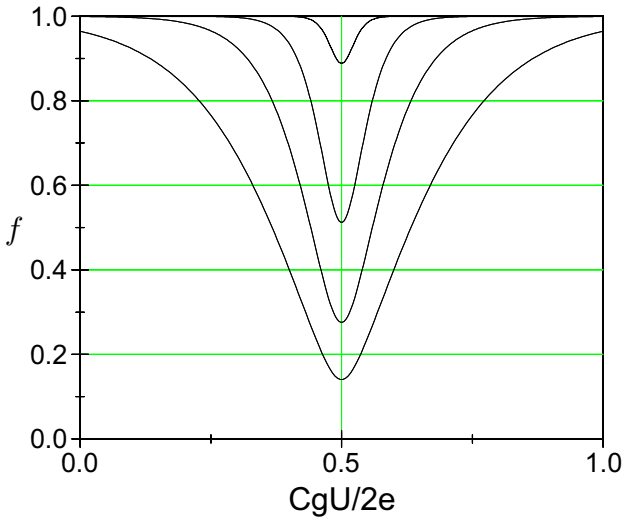

Figure 2.9. Distortion factor f (Eq. 2.18) of the superconducting Coulomb staircase as a function of the reduced gate voltage for typical parameters $E_J/E_c = 0.3$ and for reduced temperatures from bottom to top: $k_BT/E_c = 1, 0.25,\ 0.5, 0.1$. For temperatures such that $k_BT \ll E_J$, the distortion vanishes and the Coulomb staircase coincides with the zero-temperature result.

2.2.1 Effect of the electromagnetic environment

Can a coherent superposition of two different charge states be observed in "real-world" experiments, in which the charge degrees of freedom are coupled to a dissipative electromagnetic environment and to a measuring electrometer? The contribution to the decoherence of the measuring electrometer is in practice dominated by the effect of the circuit in which the box device is embedded. As explained in more details in chapter 4, in which the supercurrent through a single Josephson junction coupled to an arbitrary electromagnetic environment

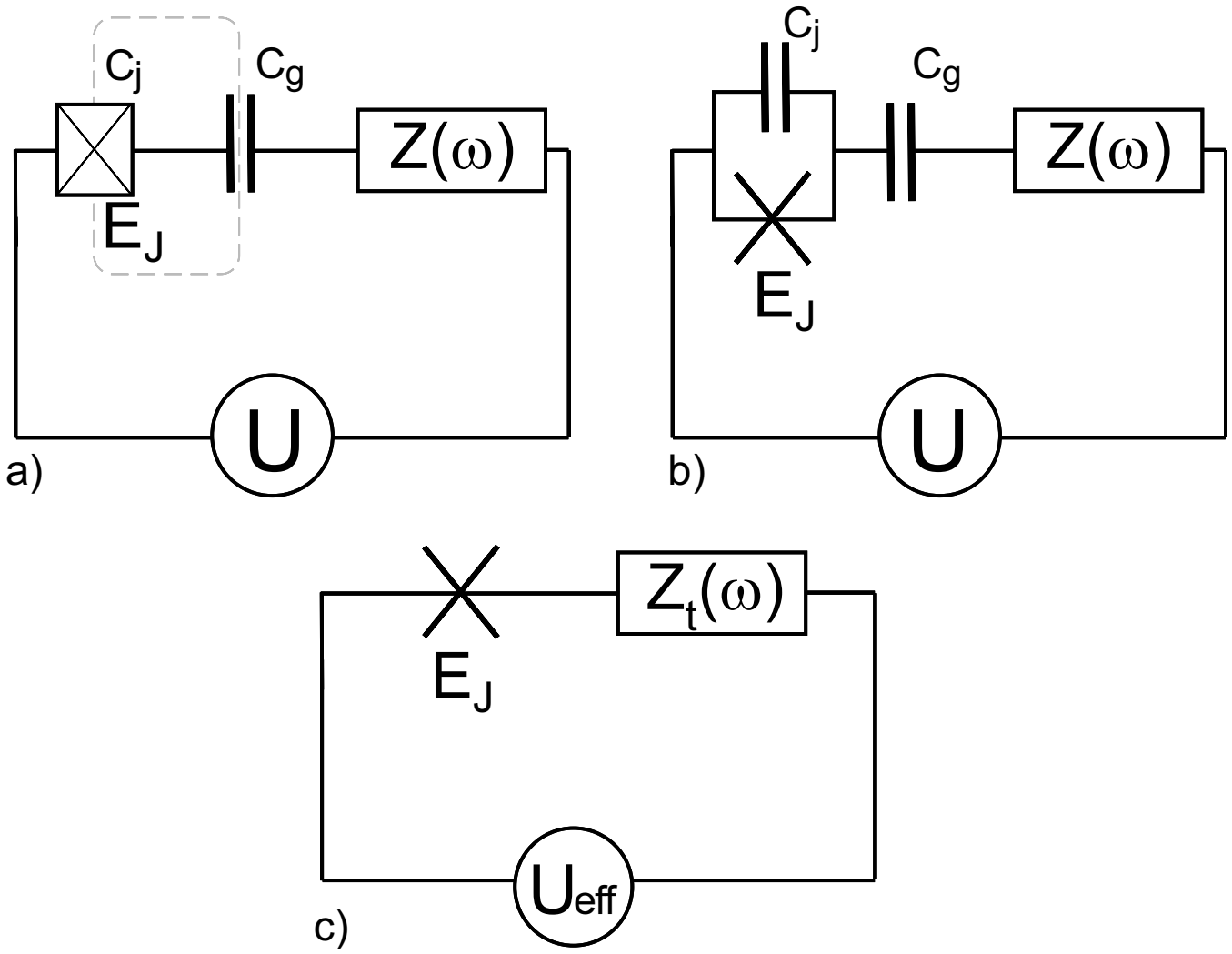

Figure 2.10. *a) Schematic of the superconducting box coupled to its electromagnetic environment, which has been modeled by an impedance* $Z(\omega)$ *in series with the voltage source. b) same circuit, in which the junction is represented by a capacitor Cj in parallel a pure Josephson element. c) Equivalent circuit seen by the Josephson element. All capacitances have been incorporated in the effective impedance* $Z_t(\omega)$.

calculated, dissipation strongly alters the quantum behavior of the system and tends to restore a classical regime. The influence of the electromagnetic environment in the particular case of the superconducting box has been done by Neumann *et al.* [4] and we present here their results which are relevant for our experiments.

The electromagnetic environment can be modeled as a series impedance $Z(\omega)$ placed between the voltage source and the gate capacitance (see Fig. 2.10, a). It can be shown [3] that the circuit is equivalent to a pure Josephson element in series with an effective impedance $Z_t(\omega)$ (see Fig. 2.10,c) given by:

$$Z_t(\omega) = \frac{\mathcal{K}^2}{i\mathcal{K}C_j\omega + Z^{-1}(\omega)} \quad \text{where} \quad \mathcal{K} = \frac{C_g}{C_g + C_j}. \tag{2.21}$$

In all our box experiments the factor $\mathcal{K}^2$ is smaller than 10^{-2} and the effective series impedance, of the order of the vacuum impedance 377 Ω, is much smaller than the resistance quantum R_K. The further attenuation of the effective impedance due to the "insulating" action of the gate capacitance makes the coupling between the charge states and the environment states extremely weak, so that a pertubational approach is sufficient.

2.2.1.a Effect of the environment on the ground state

By mapping the box Hamiltonian onto a spin-boson Hamiltonian, Neumann *et al.* [4] have shown that the effect of the environment on the ground state can be neglected when the following condition is fullfilled:

$$\int_{E_J}^{\infty} \frac{\mathrm{Re}\left(Z_t(\omega)\right)}{\omega} d\omega \ll \frac{R_K}{4}. \tag{2.22}$$

This condition, analysed in more detail in Chapter 4, is well satisfied in all our experiments. This ensures that the environment should not affect significantly the Coulomb staircase of the superconducting box in our experiments.

2.2.1.b Relaxation of the excited state

In presence of an electromagnetic environment, the excited state $|\Psi_a\rangle$ is no longer stable. It can decay to the ground state $|\Psi_s\rangle$ by creation of electromagnetic excitations [6]. In the low impedance limit, the perturbational calculation of the decay rate using the golden rule gives:

$$\Gamma = \frac{1}{2}\left(\frac{E_J}{\phi_0}\right)^2 \frac{\mathrm{Re}\left[Z_t(\omega = \epsilon/\hbar)\right]}{\epsilon} \tag{2.23}$$

where ϵ is the energy difference between both levels and $\phi_0 = h/2e$. In the case of a pure

ohmic series resistance R, the quality factor of the excited state is $Q = R_K/2R\mathcal{K}^2$ at the level crossing. This quality factor is above 10^3 in our experiments.

2.3 Experimental realization

2.3.1 Measurement of the island charge

In our experiment, we have measured the number of excess Cooper pairs in the island by coupling it electrostatically to a single electron transistor (SET) used as an electrometer (see appendix 2-C). The electrometer measures a time-averaged value $\overline{n}$ which is equal to the thermal average value $\langle n \rangle$. Since a SET electrometer has a relatively low cut-off frequency (around 100 Hz) and is also subject to $1/f$ noise (see Chapter 5 for the noise characterization of SETs), the charge detection was performed in the frequency range 0.1-100 Hz. In this domain, the detection precision is better of $10^{-2}e/\sqrt{\text{Hz}}$, which ensures a sub-electron accuracy for the island charge measurement even if the coupling capacitance between the box island and the SET island is small compared to the box island capacitance.

2.3.2 Experimental set-up

A micrograph of the sample used in the experiment reported below is shown in Fig. 2.11 together with its corresponding schematic diagram. The superconducting box circuit and the measuring electrometer can be seen at the top and at the bottom of the picture respectively. Both circuits are coupled by a small coupling capacitor placed at the end of the long T-shaped SET island. Box and SET circuits are simultaneously fabricated using a three-angle-evaporation of metallic layers through a nanofabricated trilayer mask on an oxidized silicon chip (see chapter 6 for fabrication techniques). Both devices consist of two identical Al/AlO_x/Al junctions in series which confers a symmetric structure to the whole circuit (Fig. 2.11, bottom panel). The fact that the box island is coupled to two reservoirs instead of one does not change its function nor the "topology" of the circuit. However, it enables the measurement of the serial resistance of the tunnel junctions at room-temperature, a crucial information that would be impossible to obtain with the box circuit initially proposed. The configuration of the superconducting box is recovered by connecting the two junctions to the same ground. This results in an effective junction with double capacitance and double

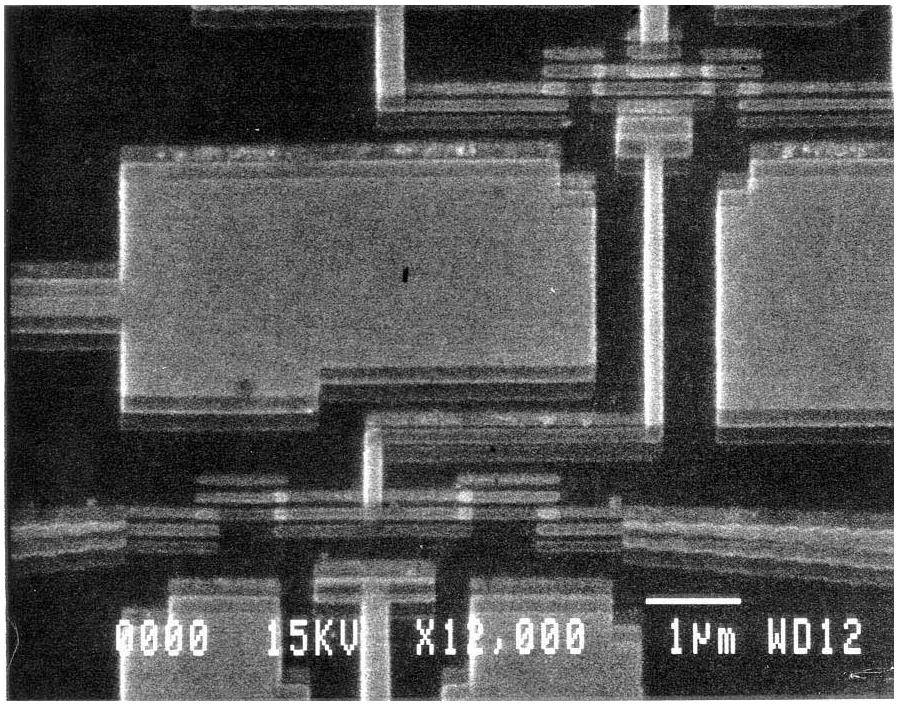

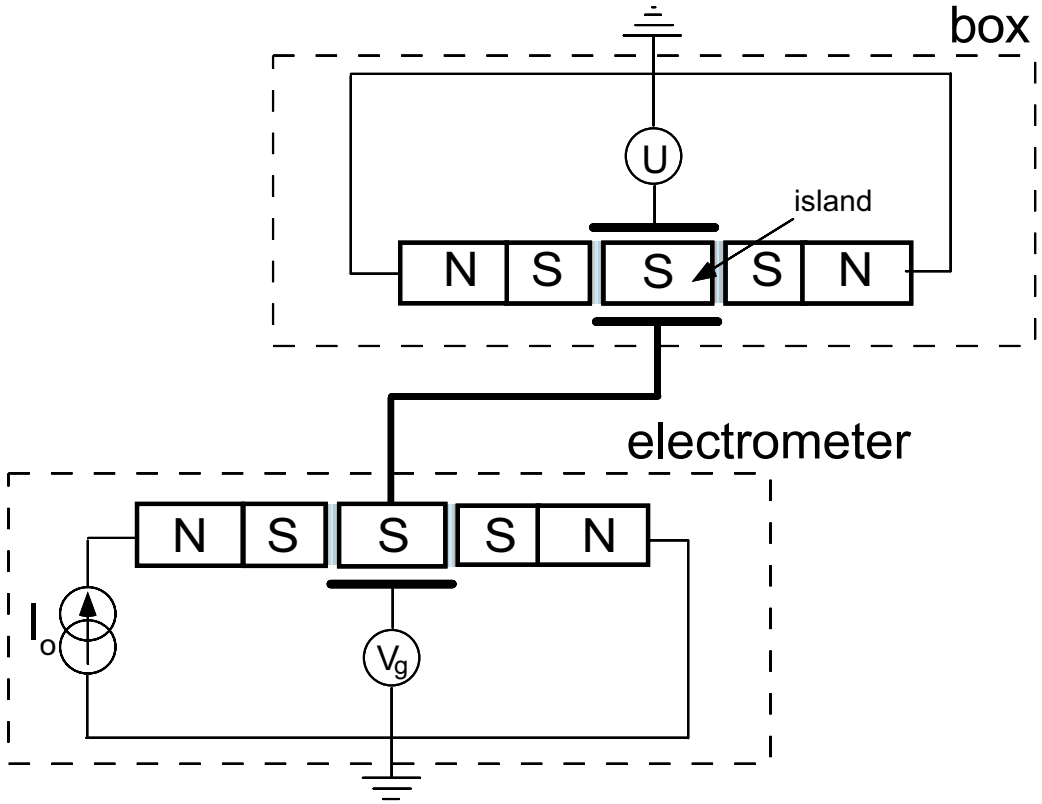

Figure 2.11. Top: *Scanning electron micrograph of the nanofabricated sample used in the box experiment. The superconducting box in the upper part is capacitively coupled to the electrometer (lower part). The sample was fabricated by electron beam lithography using a trilayer process (see fabrication techniques in chapter 6). Josephson junctions (bright dots) are obtained by overlap of oxidized aluminum layers. Large pads (center right and left) are grounded and act as shielded guards.*
Bottom: *Schematic diagram of the experimental setup, sketched with a geometry in correspondence with the top micrograph.*

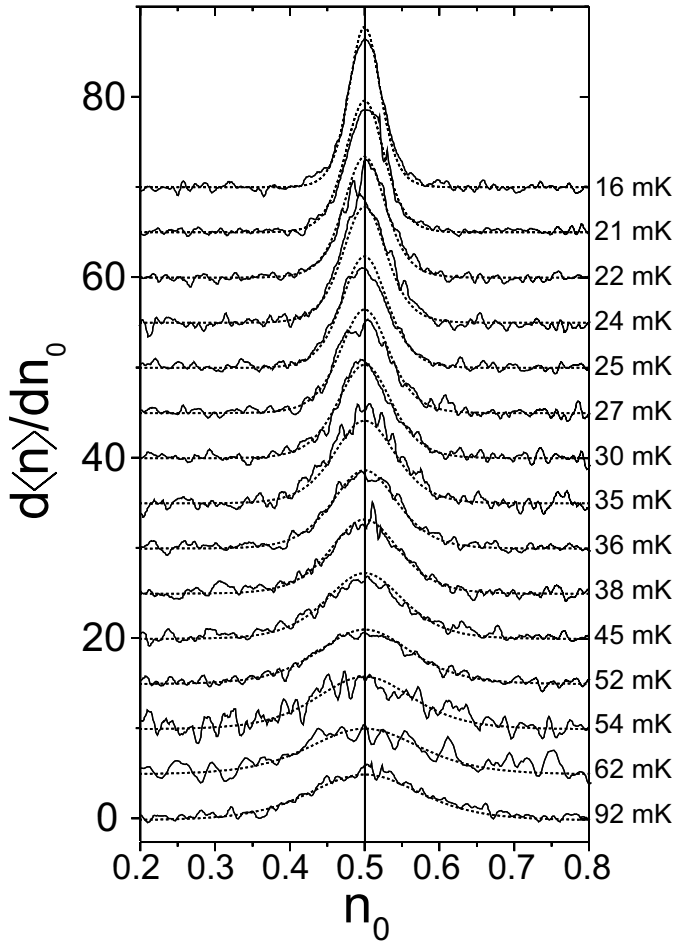

Figure 2.12. Derivative of the average charge of the box in the normal state as a function of the reduced gate voltage $n_0=C_gU/e$ for decreasing temperatures. Each curve has been normalized to area unity, and shifted for sake of clarity. Experimental curves (solid lines) are measured using the lock-in technique, under a magnetic field of 0.1T. Fitting curves (dashed lines) are obtained from the thermal smearing model described in Appendix 2-A.

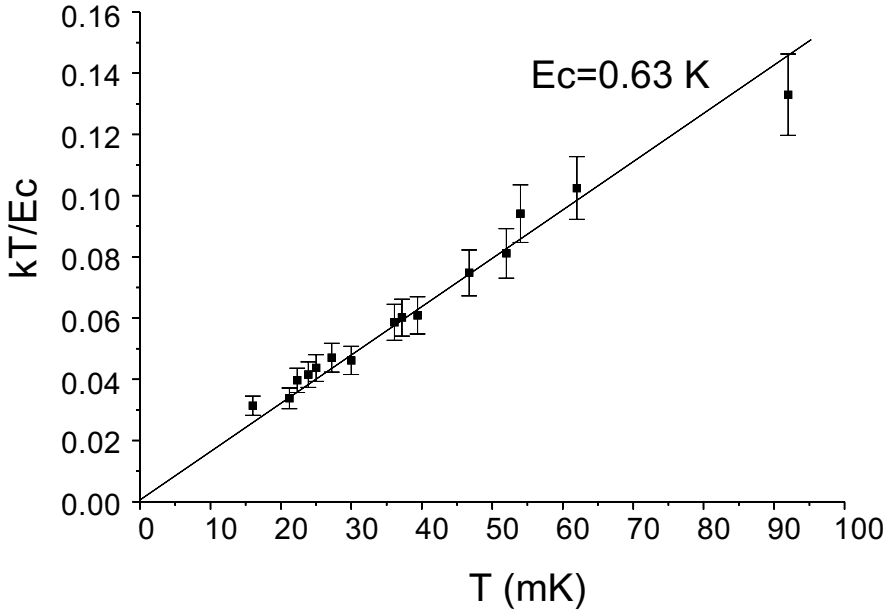

Figure 2.13. Fitting parameters of the normal Coulomb staircase as a function of the temperature, deduced from curves above. The average slope gives a charging energy of $E_C=0.63\,k_BK$.

Josephson energy. Implementing copper leads in series with the superconducting Al reservoirs proved to be useful to suppress spurious out-of-equilibrium quasiparticles. These normal-metal electrodes close to the device play the role of "filters" for quasiparticles. The measurement procedure of the box charge is presented in Appendix 2-C: a lock-in technique is used to measure the derivative of the Coulomb staircase $\frac{\partial\langle n\rangle}{\partial n_c}(U)$ with a good signal-to-noise ratio. The measured curve is then numerically integrated in order to obtain the "Coulomb staircase".

We first explain how we have determined the parameters of the experiment in order to make the comparison with the theoretical predictions. Since the effect of the Josephson coupling is to smear the Coulomb staircase, it is particularly important to check that spurious effects, such as extraneous electromagnetic noise, do not significantly contribute to a smearing of the Coulomb staircase. We thus discuss what evidence we have that the intrinsic Coulomb staircase of the superconducting box was indeed measured.

2.3.3 Experimental determination of the box parameters

Four relevant energies are involved:

- the island charging energy E_c
- the Josephson coupling energy E_J
- the odd-even free energy difference $\tilde{\Delta}(T, H)$
- the thermal fluctuation energy $k_B T$

The two energies E_c and E_J are determined during the fabrication by respectively choosing the tunnel junction areas at the electron-beam lithography stage, and transparencies at the oxidation stage (see Appendix 6−D). The third energy, $\tilde{\Delta}$, is sample dependent, but can also be continuously reduced down to zero during the measurement by applying a small magnetic field, as explained in Appendix 2-D. The lowest accessible value of the thermal energy $k_B T$ given by the base temperature is of the order of 20 mK. All these energies, necessary to the prediction (Eq. 2.18) of the Coulomb staircase, are successively obtained during the experiment from *independent measurements*.

2.3.3.a Determination of the electrostatic energy

Superconductivity in the aluminum electrodes is suppressed by applying a magnetic field of 0.1 Tesla. The device then becomes a single-electron box, the island charge is quantized in units of e and the Coulomb staircase is e-periodic. The reduced gate charge is $n_0 = n_c/2$. We

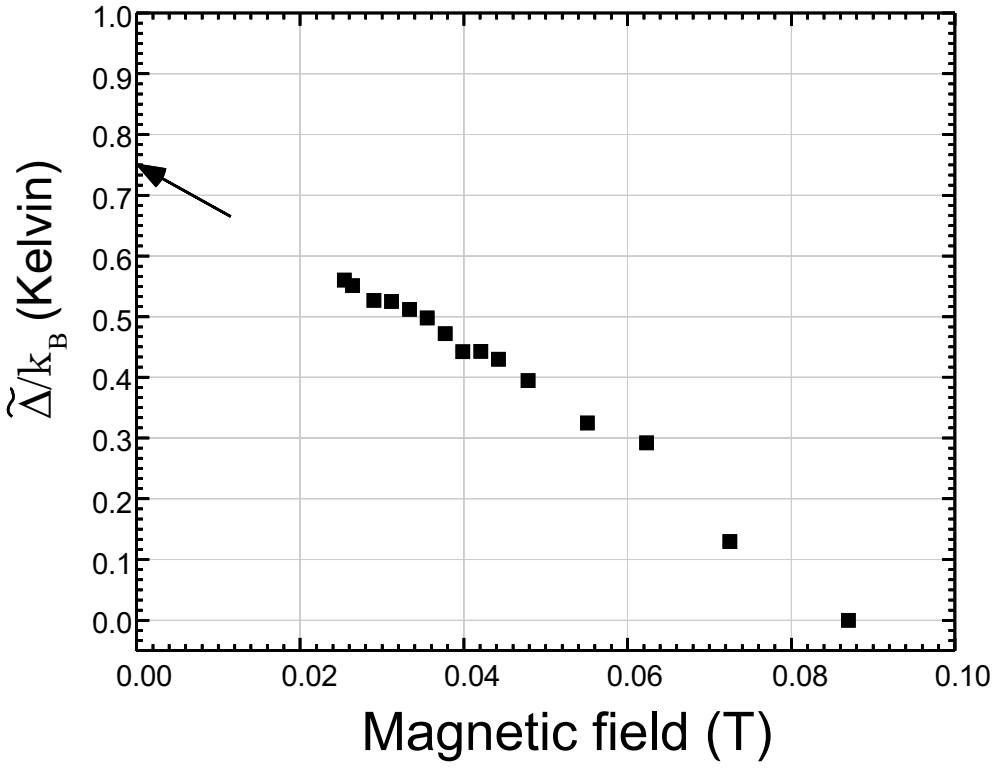

Figure 2.14 *Experimental determination of the even-odd free energy difference from the Coulomb staircase curve at increasing magnetic field* (*at* 20 *mK*). *The arrow shows the zero-field free energy* $\tilde{\Delta}(T,0)$ *deduced by extrapolating the curve.*

compare the measured derivative of the Coulomb staircase to the theoretical prediction (see appendix 2−A) in order to determine the charging energy E_c and to check that no spurious smearing is present. For each experimental curve $\frac{\partial \langle n \rangle}{\partial n_0}(n_0)$ (see Fig. 2.12), we determined the best fitting parameter $k_B T/E_c^N$, plotted as a function of the measured temperature in Fig. 2.13. The fitting parameter varies linearly with temperature down to the lowest temperatures, providing strong evidence that no extraneous noise source contributes to the smearing of the staircase. The charging energy of the box in the normal state, obtained from the slope of the best linear fit of the data points, is $E_c^N \approx 0.63\ k_B\mathrm{K}$. This value is in good agreement with our estimate of the tunnel junction capacitance.

However, one must take into account the renormalization factor of the capacitance due to virtual single electron tunneling. As shown in appendix 2-B, the bare charging energy is $E_c^0 = E_c^N/(1-4g)$, where g is the tunneling strength parameter $g = R_K/\left(4\pi^2 R_{T//}\right)$, where $R_{T//}$ is the resistance of the parallel combination of the two junctions. The superconducting state charging energy E_c is itself renormalized by virtual quasiparticle tunneling and is then given by:

$$E_c = E_c^0(1 - 4g\Gamma\left(\frac{E_c}{\Delta}\right)) = E_c^N \frac{(1 - 4g\Gamma\left(\frac{E_c}{\Delta}\right))}{(1-4g)}. \tag{2.24}$$

In our case ($\frac{E_c}{\Delta} \approx 0.3$ and $g \approx 0.02$), the renormalization factor E_c^S/E_c^N is about 1.05.

2.3.3.b Estimation of the Josephson energy E_J

The Josephson coupling energy E_J was estimated from the Ambegaokar-Baratoff formula: $E_J = h\Delta/(8e^2 R_{T//})$. The superconducting gap Δ, deduced from $I-V$ curves, is $\Delta = 2.33\ k_B\mathrm{K}$. The tunnel resistance of the two junctions in series measured in the normal state is $R_{T//} \approx$ 36.6 kΩ. Assuming that both junctions are identical, we obtain the value $E_J = 0.20\ k_B\mathrm{K}$.

2.3.3.c Estimation of the odd-even free energy difference $\tilde{\Delta}(T,H)$

This energy can be deduced from the Coulomb staircase measured at intermediate magnetic fields, in the regime when $\tilde{\Delta}(T,H)$ is reduced below E_c, thus leading to the appearance of intermediate steps in the Coulomb staircase. The analysis of the Coulomb staircase leads to a precise determination of $\tilde{\Delta}(H)$ [6]. The variations of the measured $\tilde{\Delta}(T \approx 0, H)$ with the magnetic field are shown in Fig. 2.14. The extrapolation of the curve to $H = 0$ provides $\lim_{H\to 0} \tilde{\Delta}(T \approx 0, H) \approx 0.74\ k_B\mathrm{K}$, which is smaller than the BCS gap: $\Delta = 2.33\ k_B\mathrm{K}$. We attribute this reduction to the existence of one or several *discrete quasiparticle states*. Such

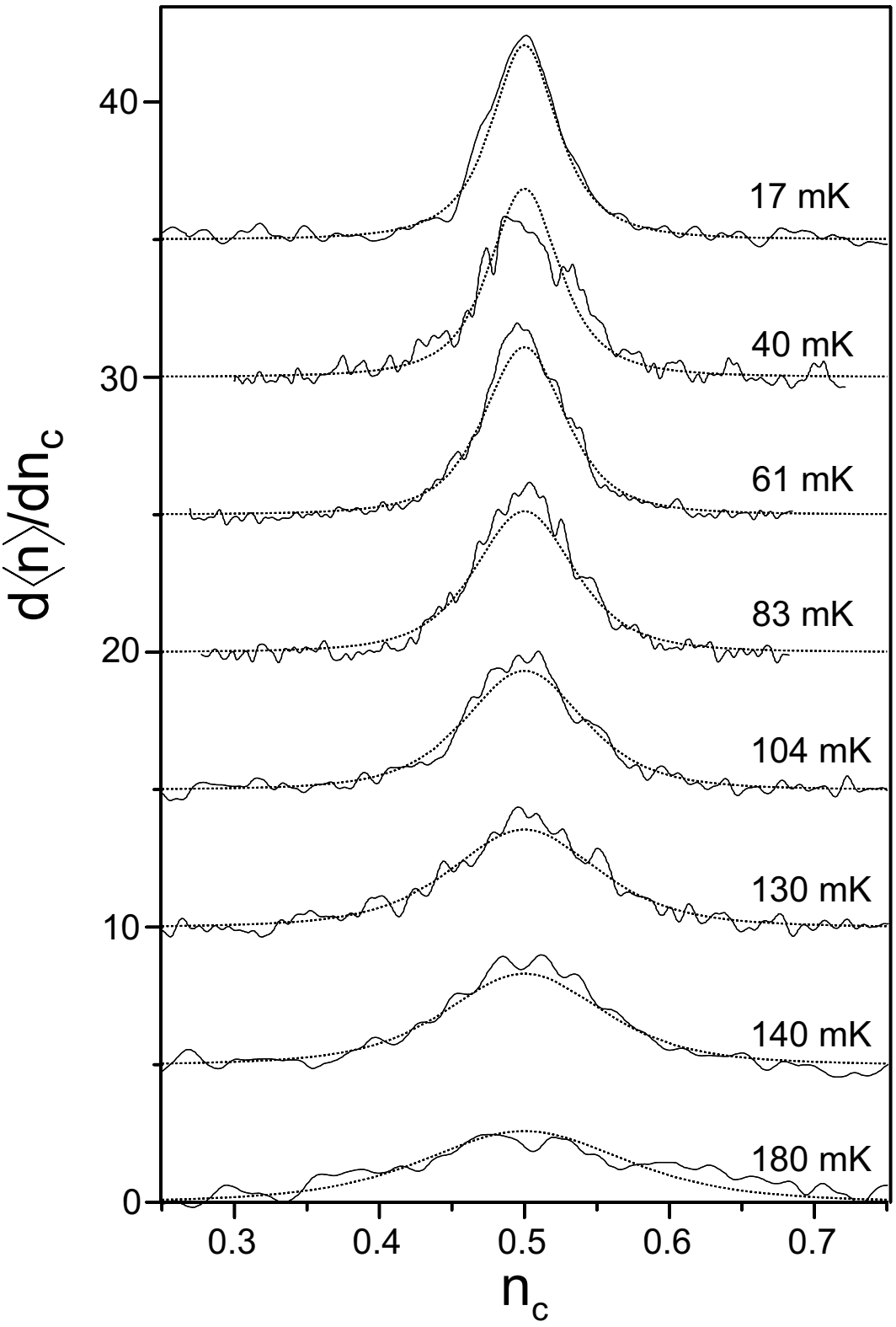

figure 2.15 Derivative of the average charge of the box in the superconducting case as a function of the gate charge ng for decreasing temperatures. Curves have been shifted for sake of clarity and thair area normalized. Experimental curves (solid lines) are measured using the lock-in technique. Dashed curves are theoretical predictions obtained using Equation 2.17 without any adjusted parameter.

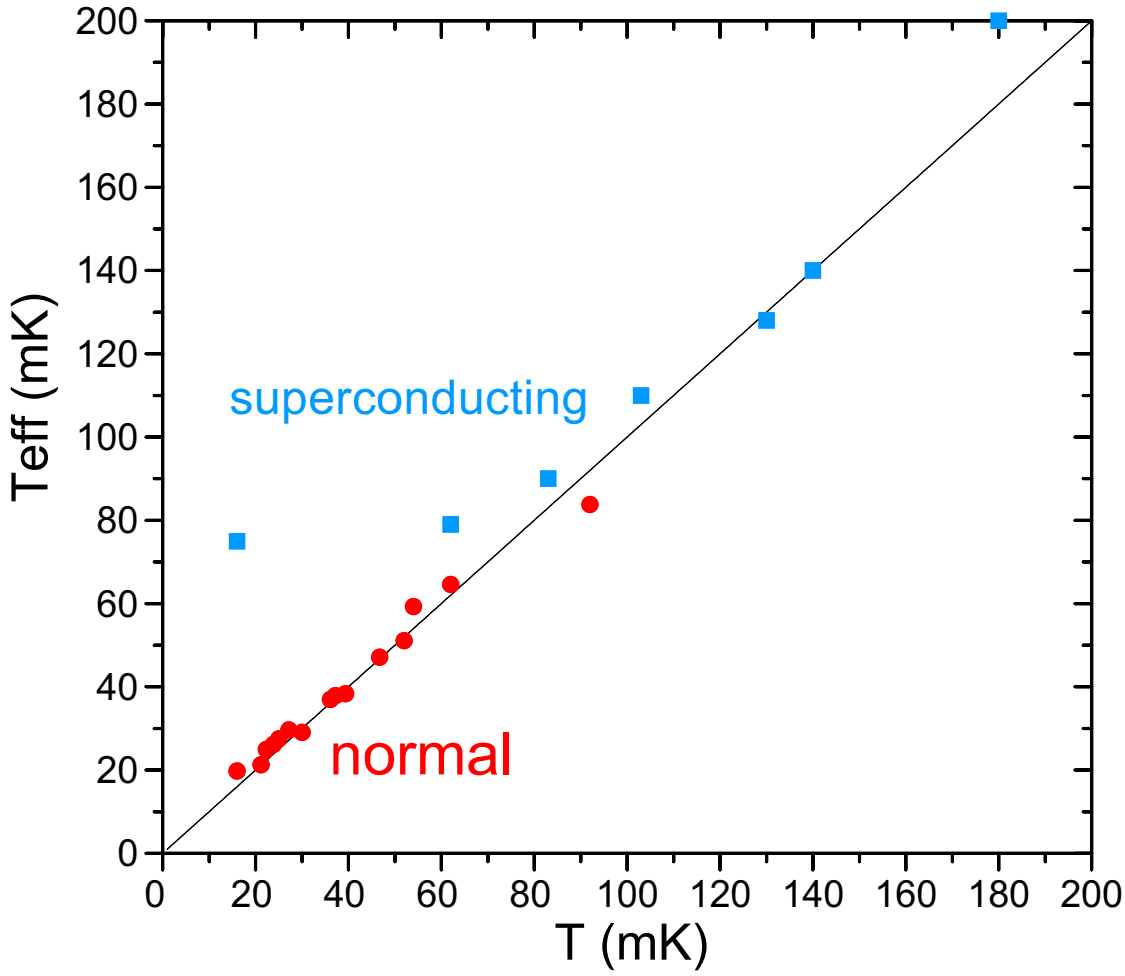

figure 2.16 Effective temperature deduced from fitting the box Coulomb staircase, as a function the temperature measured by the thermometer in both normal and superconducting cases. Quantum fluctuations are neglected in this last case. The normal box has a staircase smearing well described by a temperature effect whereas a discrepancy appears in the superconducting curve at temperatures below $80mK$*, proving that quantum effect must be taken into account.*

states, commonly observed in other similar samples, can even lead to the suppression of the $2e$-quantization. Their origin is not understood, but might arise from impurities in the aluminum island or in the oxide barrier of the junctions. It is important to notice that in the experiment performed by Lafarge et al. in a superconducting box connected to a normal reservoir of charges, a similar measurement gave the BCS gap. The odd-even free energy difference $\tilde{\Delta}(T, H = 0)$ is well described at finite temperature by the following law:

$$\tilde{\Delta}(T, H = 0) \approx \tilde{\Delta}(0, 0) - k_B T \ln m \tag{2.25}$$

where m is the degeneracy of the quasiparticule state. We have assumed that this degeneracy is small enough so that the entropic contribution to $\tilde{\Delta}(T, H = 0)$ is small compared to the energy contribution $\tilde{\Delta}(0, 0)$. We have thus used the zero-field-extrapolated low-temperature value $\lim_{H \to 0} \tilde{\Delta}(T \approx 0, H) \approx 0.74\ k_B\mathrm{K}$ (see Fig. 2.14), in the temperature range for which the contribution of the regular BCS quasiparticles can be neglected.

2.4 Temperature dependence of the superconducting Coulomb staircase

The variations of the Coulomb staircase derivative with temperature are shown in Fig. 2.15 together with the theoretical prediction (Expr. 2.18) calculated using the measured parameters. The theory reproduces well the shape and the width of the curves. In particular, the measurment at the lowest temperature is well fitted by the zero-temperature prediction which only depends on the ratio $E_J/E_C \simeq 0.3$. We have further checked that these results are not an artefact of the specific lock-in measurement technique by directly measuring the Coulomb staircase. The signal-noise ratio is then much worse but can be partially recovered by averaging curves obtained sweep after sweep. The Coulomb staircase obtained at 20 mK is also in good agreement with the theoretical prediction, as shown in Fig 2.17.

Finally, we have estimated the effective temperature T_{eff} needed to account for the observed smearing assuming no Josephson coupling. The variations of T_{eff} with temperature are shown in Fig. 2.16, together with the determination in the normal state given by the best fit obtained using Eq. 2.32 of appendix 2-A. Below 80 mK, the values measured in the superconducting state reaches a plateau clearly out of the error bars of the curve in the normal state.

Given all these control measurements, we attribute the smearing of the Coulomb staircase

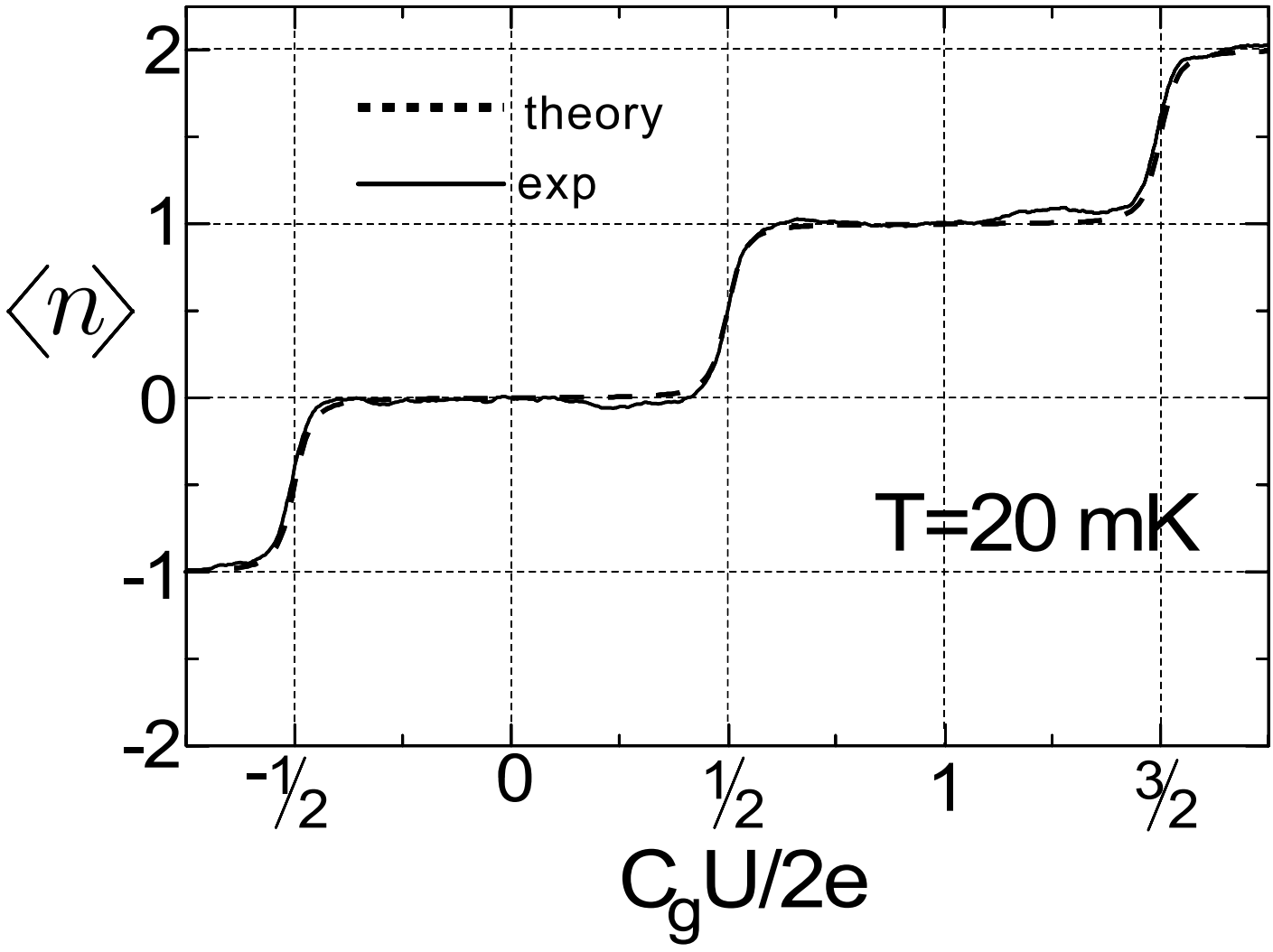

Figure 2.17: *Time averaged number of excess Cooper pairs in the island as a function of the reduced voltage C_gU/e. The experimental curve (solid line) is compared to the theoretical prediction (dotted line), ploted for the parameters deduced from the experiment : E_J/E_C=0.3 .*

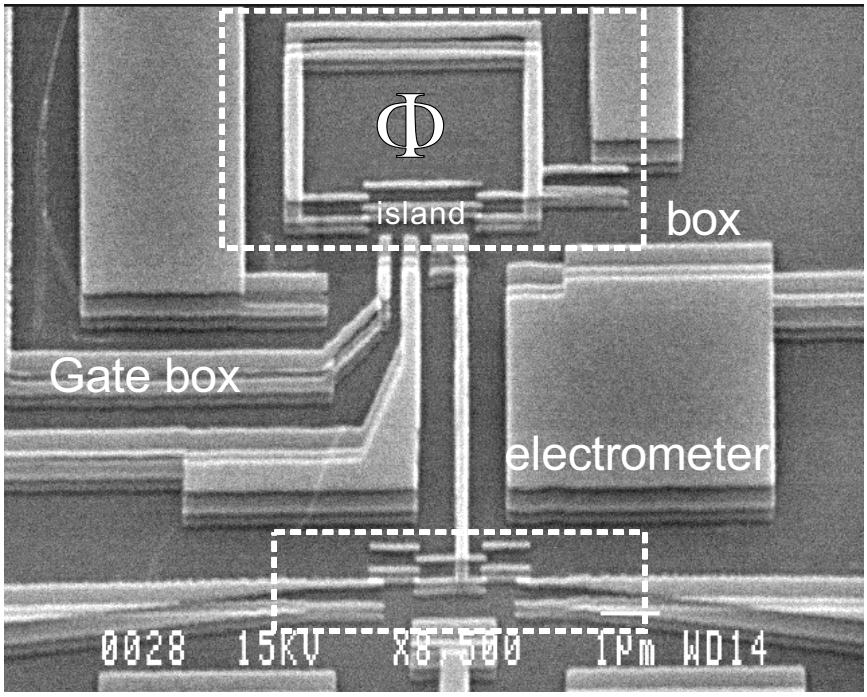

Figure 2.18. *Micrograph of the sample for the SQUID-Box experiment. Similarly as in the superconducting box presented in Fig. 2.11, an electrometer is coupled to the device. The island of the box is here embedded in a superconducting loop through which a magnetic flux* Φ *can be applied. This SQUID configuration should enable a flux-tunable Josephson coupling for the Superconducting box.*

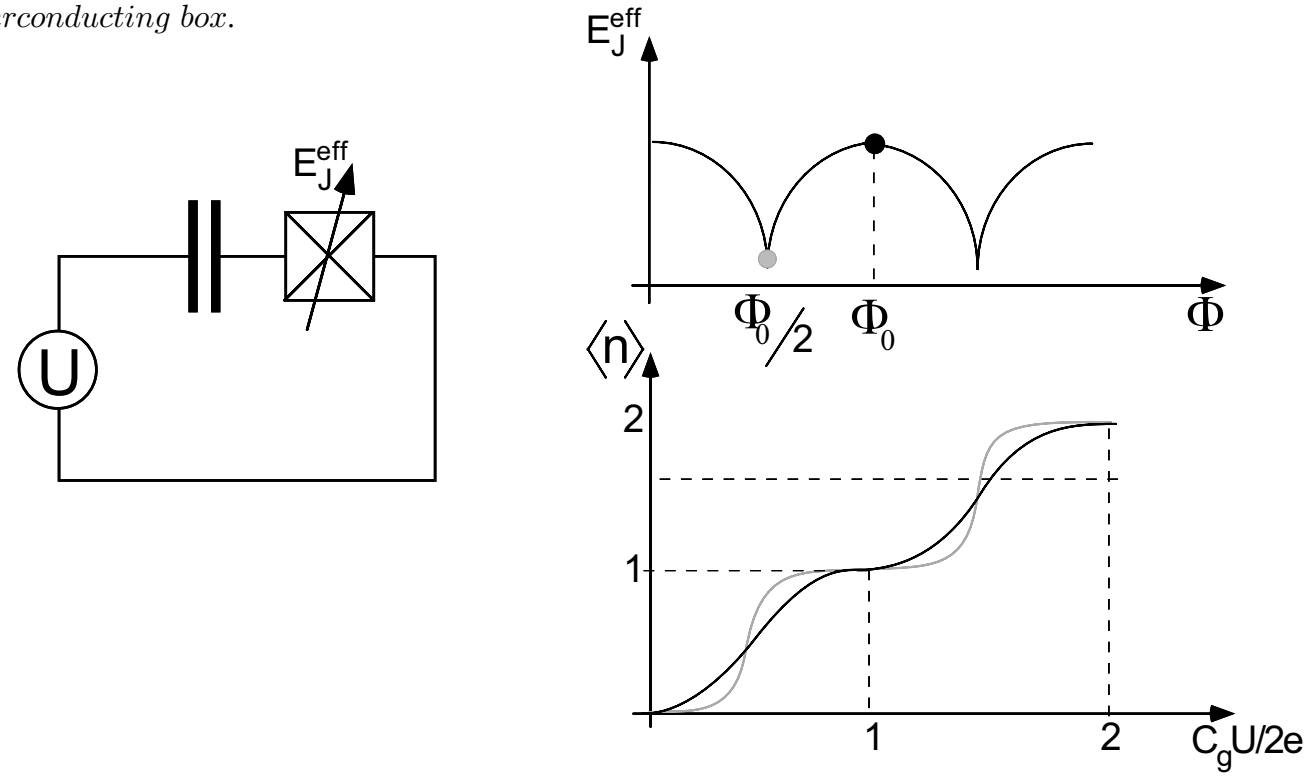

Figure 2.19. *Top left*: *Schematic diagram of the superconducting box with tunable Josephson coupling. Top right*: *Dependance of the effective Josephson coupling energy* E_J *with the flux* Φ *in the loop. Similarly as in a DC-SQUID, it is a function* Φ_0*–periodic of the magnetic flux. The contrast is determined by the Junction transparency unbalance.*
Bottom: *Resulting Coulomb staircase patterns for respectively maximum* (*black curve*) *and minimum* (*gray curve*) *values of the effective Josephson coupling energy* E_J. *The flux provides an "in-situ" modulation of the staircase pattern.*

observed at low temperature in the superconducting box to the effect of the Josephson coupling. This measurement provides the first direct evidence of a coherent superposition of two charge states in a single Cooper pair device.

2.5 Possible improvement : the SQUID-box experiment

The major drawback of the superconducting box experiment is that its parameters are determined at the fabrication stage. An important improvement of the experiment would be to enable an *in-situ* adjustment of the Josephson energy or of the charging energy. In a second series of box experiments, we have implemented the *in-situ* modulation of E_J by connecting the two junctions of the box island by a superconducting lead. The two junctions then form a DC SQUID which behaves as an effective junction whose Josephson energy can be periodically modulated by applying a small magnetic field (see Fig. 2.19). A micrograph of the sample realized for such a SQUID-BOX experiment is presented in Fig. 2.18. The circuit pattern reaches a complexity which necessitated the development of novel fabrication techniques such as multilayer fabrication, presented in chapter 6. Although we have tried different samples with different island and quasiparticle filter geometries, these experiments have not been successful because of the existence of finite quasiparticule states at energies below E_c.

2.6 Analogy with the superconducting transistor

The superconducting transistor (see Fig. 2.20) [12] which measures the island charge can also be used itself to prove that the ground state of its island is a coherent superposition of two charge states. The $I-V$ characteristic of the transistor is presented in Fig. 2.21. It shows a zero-voltage branch with a supercurrent, which switches as the current is increased to a finite voltage branch for which the conduction is due to quasiparticles. The switching occurs for a current I_s which fluctuates from sweep to sweep but whose average a marked gate dependence. Joyez *et al.* [10] have shown that the gate variations of the switching current well reproduce the variations of the maximum supercurrent that can be sustained in the ground state.

We have measured the variations of I_s as a function of the gate voltage (Fig. 2.22). The curve is $2e$-periodic with respect to the polarizing charge C_gU on the island. It has sharp

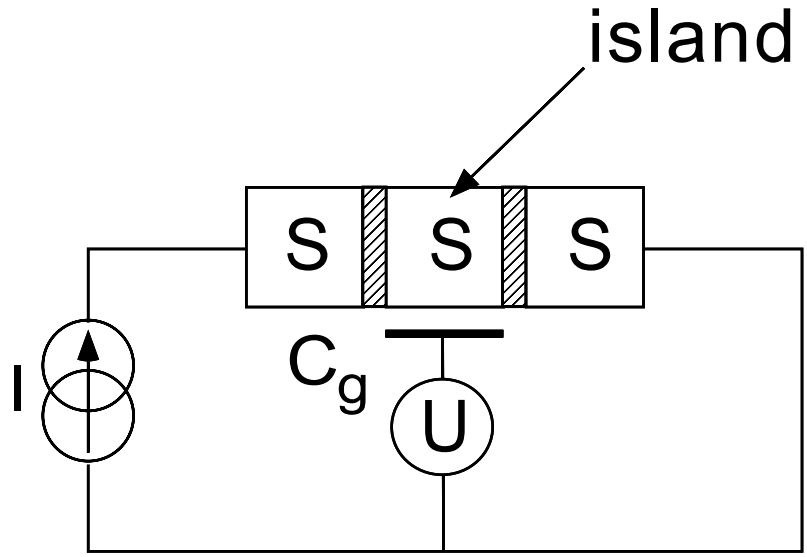

Figure 2.20. Schematic diagram of the superconducting transistor. The island is connected to two superconducting electrodes by Josephson junctions. The transistor is biased by a current source. Like the superconducting box, the island can be polarized by a capacitance connected to a voltage source U.

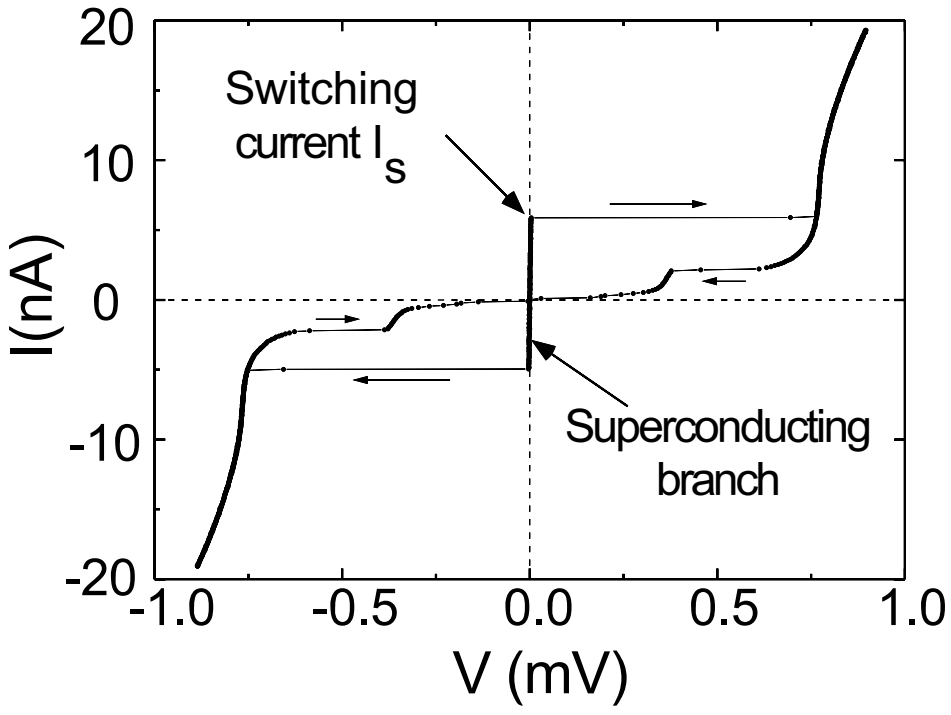

Figure 2.21. Experimental current-voltage characteristic of the superconducting transistor operated in a current-biased mode. The zero voltage branch corresponds to the superconducting state of the transistor. For a current equal to the switching current I_S, the transistor switches to the finite voltage branch for which both quasiparticles and Cooper pairs are transferred.

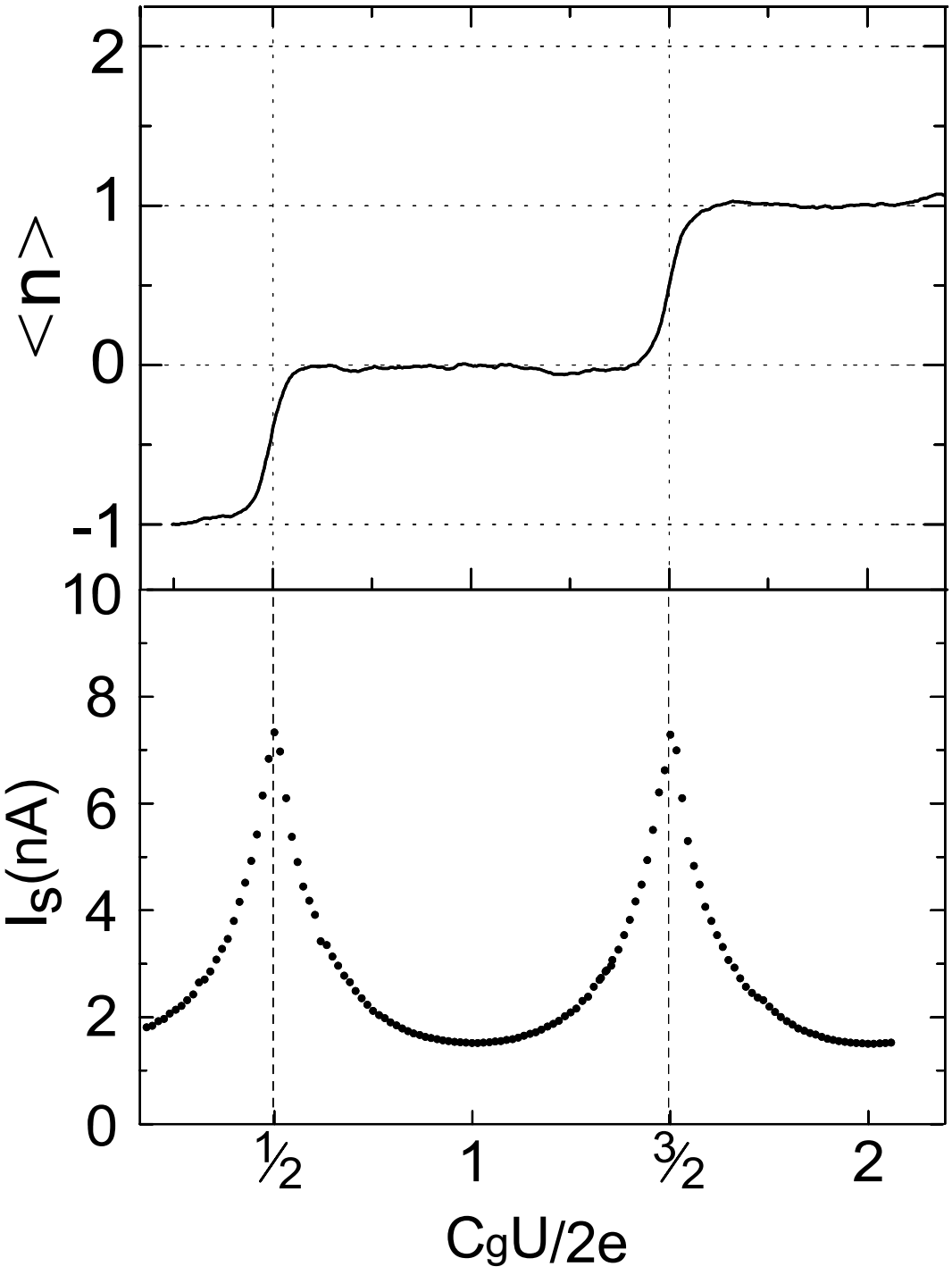

Figure 2.22. Comparison of the Coulomb staircase of the superconducting island with the gate dependence of the swiching current in the superconducting transistor. The switching current is maximum at voltages for which the island of the box show large quantum fluctuations. The cusp shape of this curve provides another of the coherent superposition of charges in a small superconducting island.

maxima which values are close to the maximum possible value $I_{\max} = e\,E_J/\hbar$ [13]. These maxima occur for voltages $U = (2n+1)e/C_g$ corresponding to level crossings in the superconducting box experiment, as depicted in Fig. 2.7. At the opposite of the conductance peaks in the normal state SET, The peaks in the switching current curve $I_s(U)$ curve are cusp-shaped. This particular feature is a signature of the coherent superposition of the two charge states for the island. The minima of $I_s(U)$ occur when the polarizing gate charge is an integer number of Cooper pairs. There, the quantum fluctuations of the number of excess Cooper pairs in the island is greatly reduced, and the supercurrent is of the order of :

$$I_{\min} \quad = I_{\max}(E_J/E_c) = (e/\hbar)\ E_J^2/E_c \tag{2.26}$$

The supercurrent modulation by the gate voltage is reminiscent of the current modulation in a field effect transistor (FET). However, unlike the FET whose principle is based on statistical variations of a macroscopic number of carriers, the modulation is due here to the control of the quantum state of the whole device.

2.7 Can the superconducting box provide a robust Q-bit for quantum computing ?

The possibility of using quantum mechanics for computing purpose is a rather old idea which presently attracts a renewed interest [14]. Indeed, it has been theoretically proven that quantum computing could solve complex computational problems, such as the factorization of large integers, which are beyond the reach of sequential Von Neuman computers whatever their speed. In some sense, a quantum computer with its entries in a coherent superposition of states, and which follows a unitary evolution, performs at the same time all the calculations for each entry state. The requirements for a quantum computer are drastic because the preservation of the coherent superposition requires an extreme decoupling from the environment. The amount of decoherence that can be tolerated is presently the subject of intense researchs. In particular, error-correcting codes which tolerate a *finite* amount of decoherence per bit have recently been proposed. Different quantum systems have been considered to implement quantum computing: the most serious candidates are ion lattices in optical molasses, coupled magnetic systems, nuclear spins and coupled quantum dot arrays. The main difficulty is the preservation of the coherence while maintaining the capacity of an external control. Not to

mention, none of the proposed systems is compatible with even low-scale integration, but some of them could be used to produce entangled quantum states with many-state quantum correlations. Using single Cooper pair devices for similar purposes is another interesting possibility. Although the problem of gate adjustment seems to limit the use of single Cooper pair devices for quantum computing purpose, we think that these devices are among the best candidates to fabricate entangled states. Another system suitable for implementing similar quantum states is presented in next chapter.

2.7.1 Coding a Q-bit

In quantum computing, the information can be coded by a two-state quantum system and its ground state is denoted as a "Q-bit", as a contraction of Quantum BInary digiT. Such a terminology was, of course, given by analogy with "classical bits" used in today's computers. As we have seen, the superconducting box provides a solid-state, readily integrated two-state quantum system. The two lowest energy states of a superconducting box can be thus used to code a single Q-bit. An array of superconducting boxes, controlled by gate voltages, and coupled to one another by Josephson junctions, could be used to implement a logic function. Such an array is equivalent to an array of coupled spins $\frac{1}{2}$ placed in a locally controllable magnetic field.

2.7.2 Estimation of the coherence time

Decoherence results in "fatal errors" in a quantum computer. We have shown in section 2.2.1 that the decoherence in the superconducting box is mainly due to the dissipation in the electromagnetic environment of the circuit. Using the expression of the decoherence rate already mentioned (Eq. 2.23), we estimate that the life-time of a Q-bit for typically encountered environment resistances, can be longer than 100 μs. This time is already sufficient to perform interesting manipulations on the quantum state of the whole system.

Conclusion

The experimental results presented in this chapter show that the "fully superconducting" box is more than a simple "sequel" of the single electron box. In this system, the interplay between charging effects and the Josephson coupling results in a coherent quantum superposition of two charge states for the ground state. A finite gap separates the ground state from the first excited state, which is discrete. Our experiment provides an experimental evidence of the Josephson effect with a single Cooper pair. Moreover, it opens the way to the realization of circuits which takes advantages of the coherence of superconductivity to show evidences of macroscopic quantum coherence. An example of a more complex device developped for that purpose is provided in next chapter.

References of chapter 2

[1] P. Lafarge, P. Joyez, D. Esteve, C. Urbina and M. H. Devoret, Nature **365**, 422 (1993).

[2] M. Büttiker, Phys. Rev. B, **36**, 3548, (1987).

[3] see chapter 3 in *Single Charge Tunneling*, edited by H. Grabert and M. H. Devoret (Plenum Press, New York, 1992).

[4] F. Neumann, G.L. Ingold, H. Grabert, Phys. Rev. B, **50**, 12811, (1994).

[5] P. Joyez, Ph. D. Thesis, Université Paris 6, (1995).

[6] see appendix 2-D and P.Lafarge, Ph. D. Thesis, Université Paris 6, (1993).

[7] P. Lafarge, H. Pothier, E. R. Williams, D. Esteve, C. Urbina and M. H. Devoret, Z. Phys. B **85**, 327 (1991).

[8] Abramovitz, special functions.

[9] D. Vion, P.F. Orfila, P. Joyez, D. Esteve, and M.H. Devoret, J. Appl. Phys. **77**, 2519 (1995).

[10] P. Joyez, P. Lafarge, A. Filipe, D. Esteve and M. H. Devoret, Phys. Rev. Lett. **72**, 2458, (1994).

[11] D. B. Haviland, L. S. Kuzmin, P. Delsing, K. K. Likharev, and T. Cleason, Z. Phys. B **85,** 339 (1991).

[12] T. A. Fulton, P. L. Gammel, D. J. Bishop, and L. N. Dunklerberger, Phys. Rev. Lett. **63**, 1307 (1989).

[13] D. Vion, M. Götz, P. Joyez, D. Esteve, and M. H. Devoret, Phys. Rev. Lett. **77**, 3435 (1996).

[14] A. Barenco, D. Deutsch, A. Ekert and R. Jozsa, Phys. Rev. Lett., **74**, 4083, (1995) and refs. therein.

Appendix 2−A
Thermal smearing of the Coulomb staircase in "normal-state" electron box

In the normal-metal (*i.e.* non superconducting) single electron box, the quantization of the charge is affected by thermal fluctuations. A direct determination of the resulting smearing of the "normal" Coulomb staircase can be obtained from the analytic expression of the partition function.

Analytic expression of the partition function

The partition function of the system writes :

$$\mathfrak{z} = \sum_{n=-\infty}^{+\infty} \exp\left(-E_n/k_BT\right), \tag{2.27}$$

where $E_n = E_c\left(n - n_0\right)^2$ is the electrostatic energy of the box in the normal state with n extra electrons, and n_0 is the number of electron polarized by the gate ($n_0 = C_gU/e$).

This series can be rewritten as:

$$\mathfrak{z} = \exp\left(-\frac{E_c}{k_BT}n_0^2\right)\left[1 + 2\sum_{n=1}^{+\infty}\exp\left(-\frac{E_c}{k_BT}n^2\right)\cosh\left(-\frac{E_cn_0}{k_BT}n\right)\right]. \tag{2.28}$$

One can identify the second factor with the expansion of the special elliptic function Θ_3 [8]:

$$\Theta_3\left(u,q\right) = 1 + 2\sum_{n=1}^{+\infty} q^{n^2}\cos(2nu). \tag{2.29}$$

the correspondence leads to the expression:

$$\mathfrak{z}\left[E_c, n_0, T\right] = \exp\left(-\frac{E_c}{k_BT}n_0^2\right) \times \Theta_3\left[u = i\frac{E_cn_0}{k_BT}, \quad q = e^{-E_c/k_BT}\right]. \tag{2.30}$$

Thermal average of excess electrons in the box

The thermal average number of excess electrons $\langle n\rangle$ in the island is related to the partition function by:

$$\langle n\rangle = \frac{k_BT}{2E_c}\left(\frac{\partial \ln \mathfrak{z}}{\partial n_0}\right), \tag{2.31}$$

which leads to the following analytic expression of $\langle n \rangle$:

$$\langle n \rangle (E_c, n_0, T) = \frac{k_B T}{2E_c} \left[\frac{\frac{\partial \Theta_3}{\partial n_0} \left(i\frac{E_c n_0}{k_B T}, e^{-E_c/k_B T} \right)}{\Theta_3 \left(i\frac{E_c n_0}{k_B T}, e^{-E_c/k_B T} \right)} \right] \tag{2.32}$$

We have checked that this formula matches the expressions obtained using the high temperature ($k_B T \gg E_c$) and low temperature ($k_B T \ll E_c$) expansions of the partition function in the appropriate limits. Our result is also well-suited to numerical calculations in the whole temperature range. Plots of $\langle n \rangle (n_0)$ at different temperatures are shown in Fig 2.23.

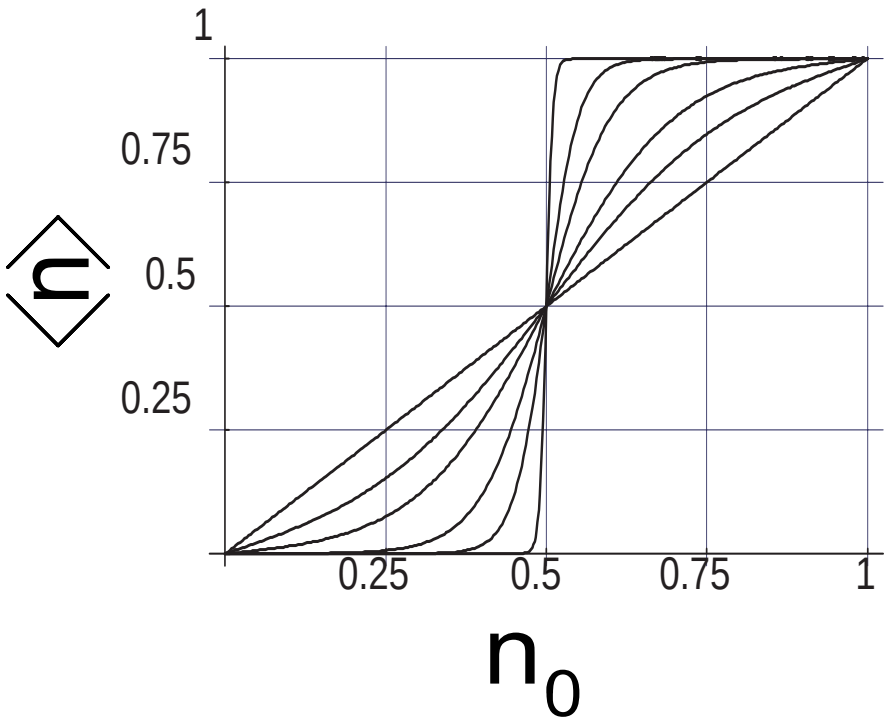

Figure 2.23: Average number of excess electrons $\langle n \rangle$ as a function of the reduced gate charge n_0, for the reduced temperatures $k_B T/E_c = 0.01, 0.05, 0.1, 0.2, 0.3$. As the temperature increases, the step is continuously smeared by thermal fluctuations.

Appendix 2−B
Renormalization of the charging energy by virtual quasiparticle tunneling

We have used in this chapter the standard Josephson Hamiltonian to describe the coupling between two superconducting electrodes in contact through a tunnel junction. This Hamiltonian is obtained by treating the tunnel Hamiltonian at the lowest order in perturbation theory. The matrix element between states $|n\rangle$and $|n \pm 1\rangle$ which differ by one Cooper pair in the island is:

$$\langle n \mid H_J \mid n \pm 1 \rangle = -E_J/2, \tag{2.33}$$

where E_J is given by the Ambegaokar-Baratoff formula. We calculate in this appendix the correction δE_n to the energy of a state $|n\rangle$ at the same order in perturbation. The tunnel Hamiltonian couples a state $|n\rangle$ to states which differ by one electron charge in the island. Assuming that all electrons in the superconducting electrodes are initially paired, such states contain one quasiparticle in each electrode. Their energy $\mathcal{E}_{\pm 1}$ referred to the electrostatic energy of state $|n\rangle$ is thus:

$$\mathcal{E}_{\pm 1} = \varepsilon + \varepsilon' + E_{\pm 1},$$

where ε and ε' are the energies of the quasiparticles which have been created and $E_{\pm 1}$ the change in the electrostatic energy. This electrostatic energy change writes:

$$E_{\pm 1} = 2E_c \left(n_g \pm \frac{1}{2} \right). \tag{2.34}$$

We assume here that the quasiparticle gap Δ is large enough so that both energies $\mathcal{E}_{\pm 1}$ are positive: the state $|n\rangle$ is stable respectively to single electron tunneling transitions. The energy of the state $|n\rangle$ is however slightly shifted by virtual single electron tunneling transitions. The standard perturbation theory leads to the following expression of the energy shift δE_n :

$$\delta E_n = t^2 \int_0^{+\infty} d\varepsilon \, f_L(\varepsilon) \int_0^{+\infty} d\varepsilon' \, f_R(\varepsilon') \left[\frac{1}{\mathcal{E}_{+1}} + \frac{1}{\mathcal{E}_{-1}} \right], \tag{2.35}$$

where t is the tunnel matrix element and $f_{L(R)}$ the quasiparticle density of states in the left (right) side of the Josephson junction. We assume here that the density of states follows the

BCS prediction:

$$f(\epsilon) = \rho \frac{\varepsilon/\Delta}{\sqrt{\frac{\varepsilon^2}{\Delta^2} - 1}}, \tag{2.36}$$

where ρ denotes the density-of-states of the normal metal at the Fermi level. The square of the matrix element t is related to the tunnel resistance R_T through the relation:

$$\rho_L \rho_R t^2 = R_K / \left(4\pi^2 R_T\right),$$

where ρ_L and ρ_R are respectively the density-of-states on both sides of the junction. We define the reduced tunneling strength parameter $g = R_K / \left(4\pi^2 R_T\right)$.

We now focus on the calculation of δE_n close to the center of the steps ($n_g = 0$) at the first order in n_g. Using Eq. (2.35), one finds:

$$\delta E_n^1 = \rho_L \rho_R t^2 \int_\Delta^{+\infty} d\varepsilon \int_\Delta^{+\infty} d\varepsilon' \frac{\varepsilon}{\sqrt{\varepsilon^2 - \Delta^2}} \frac{\varepsilon'}{\sqrt{\varepsilon'^2 - \Delta^2}} \frac{16\, E_c^2\, n_g}{\left(\varepsilon + \varepsilon' + E_c\right)^3} \tag{2.37}$$

$$= \rho_L \rho_R t^2 \int_\Delta^{+\infty} d\varepsilon \int_\Delta^{+\infty} d\varepsilon' \frac{\varepsilon/\Delta}{\sqrt{\frac{\varepsilon^2}{\Delta^2} - 1}} \frac{\varepsilon'/\Delta}{\sqrt{\frac{\varepsilon'^2}{\Delta^2} - 1}} \frac{16\, E_c^2\, n_g}{\left(\varepsilon + \varepsilon' + E_c\right)^3}, \tag{2.38}$$

These integrals can be rewritten using the Laplace transform:

$$\frac{1}{\left(\varepsilon + \varepsilon' + E_c\right)^3} = \frac{1}{2} \int_0^{+\infty} du\, u^2 \exp -u \left(E_c + \varepsilon + \varepsilon'\right).$$

One then obtains :

$$\delta E_n^1 = 8\, E_c^2\, t^2 n_g \int_0^{+\infty} du\, e^{-uE_c}\; u^2 \left[\int_1^{+\infty} dx \frac{x}{\sqrt{x^2 - 1}} \exp -u\Delta x\right]^2. \tag{2.39}$$

One recognizes in the inner integral the modified Bessel function of the second kind K_{-1}:

$$K_{-1}(\alpha) = \int_1^{+\infty} dx \frac{x}{\sqrt{x^2 - 1}} \exp -\alpha x, \tag{2.40}$$

which leads to:

$$\delta E_n^1 = 8\, E_c^2\, t^2 n_g \int_0^{+\infty} du\;\; e^{-u\frac{E_c}{\Delta}}\, u^2\, K_{-1}^2(u) = 8\, E_c^2\, t^2 n_g \Gamma\left(x\right). \tag{2.41}$$

The Laplace transform $\Gamma\left(x\right)$ of K_{-1}^2 can be expressed in terms of special functions:

$$\Gamma(x) = \int_0^{+\infty} du\; e^{-ux}\, u^2\, K_{-1}^2(u) = -\frac{2x}{3}\; {}_3F_2\left(1,2,3;\frac{3}{2},\frac{3}{2};\frac{x^2}{4}\right) + \frac{3}{32}\pi^2 H_{2F1}\left(\frac{3}{2},\frac{5}{2},2,\frac{x^2}{4}\right) \tag{2.42}$$

where ${}_3F_2$ and H_{2F1} are generalized hypergeometric functions.

Finally, the energy correction δE_n^1 given by Eq. (2.41) can be absorbed by a renormalization of the island charging energy E_c :

$$E_c^\star = E_c\,[1 - 4g\Gamma(E_c/\Delta)] \tag{2.43}$$

The graphic representation of the function $\Gamma(E_c/\Delta)$ is presented in Fig. 2.24:

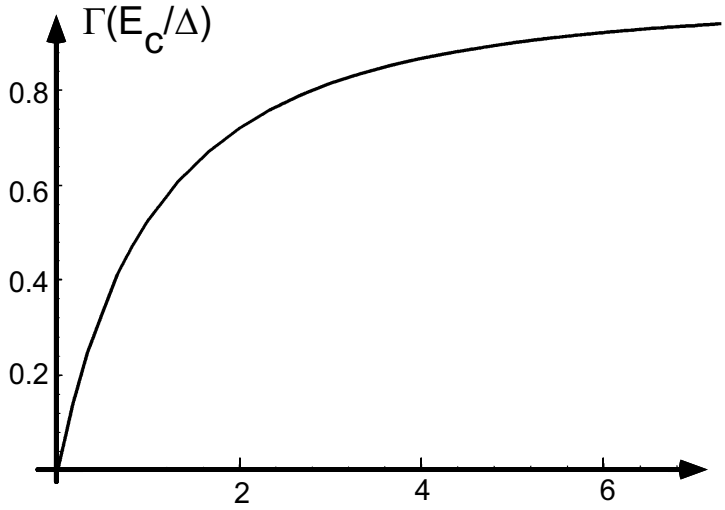

Figure 2.24. Plot of the function $\Gamma(E_c/\Delta)$.

This result is in agreement with the renormalization factor found in the normal case [6] which corresponds to the limit $\Delta \to 0$:

$$E_c^N = \lim_{\Delta\to 0} E_c^\star = E_c\left[1 - 4g \lim_{x\to+\infty} \Gamma(x)\right] = E_c\,(1 - 4g) \tag{2.44}$$

The results of this appendix have been also used in chapter 1 in order to determine the bare charging energy of the normal SET island using the phenomenon of resonant Cooper pair tunneling in the superconducting transistor.

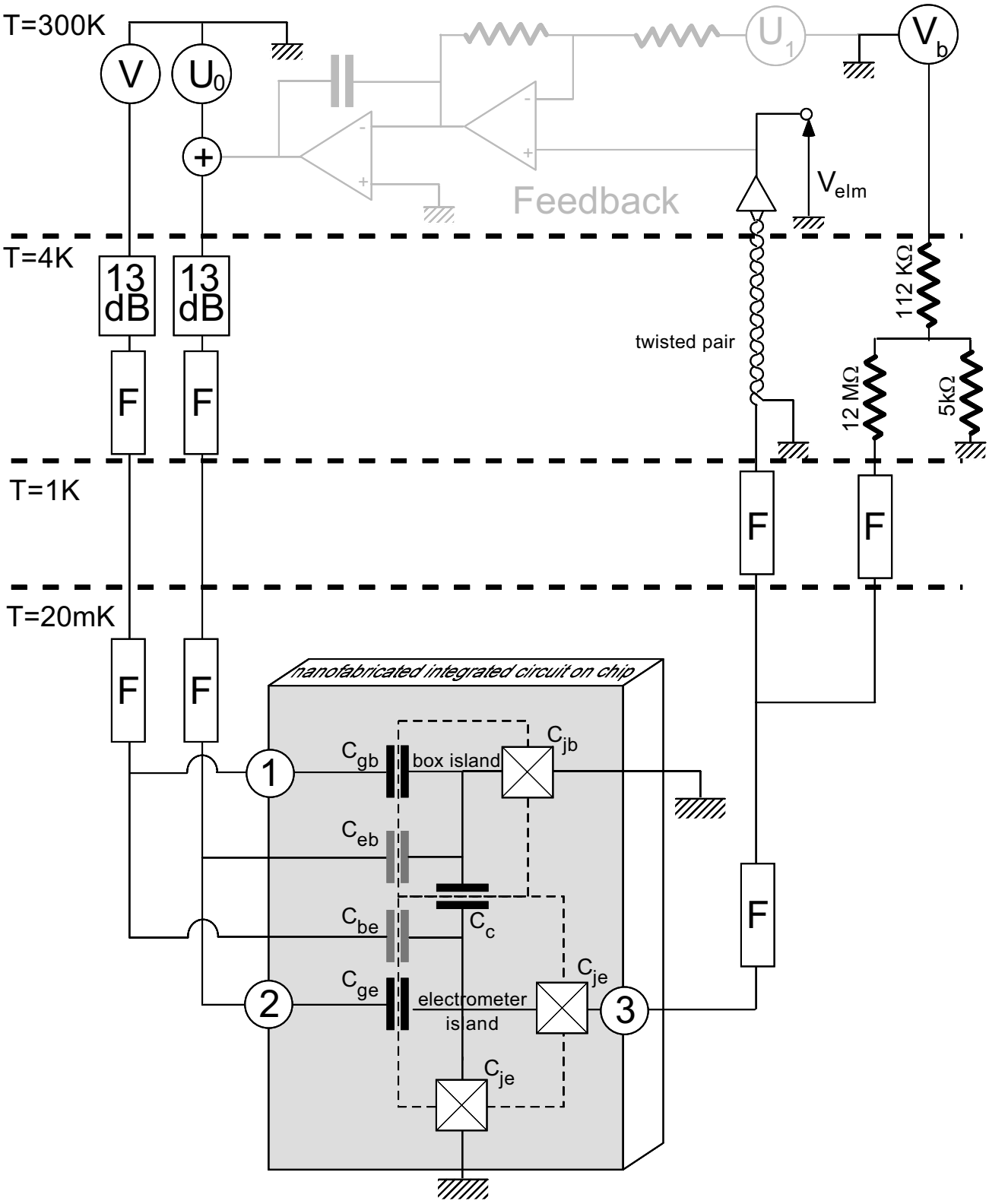

Figure 2.25. *Experimental wiring of the experiment placed inside the cryostat. We have indicated the typical operating temperatures for each stage. The sample (bottom gray area) is connected to the measurement apparatuses through carefuly filtered coaxial lines. The rectangular elements (marked F) are the miniature cryogenic filters mentioned in the text. The current bias is obtained by charging the voltage source V_b by a serial impedance of 12MΩ. The optional feedback loop (top) is represented in gray.*

Appendix 2−C
Techniques for the experimental measurement of the excess charge of the superconducting box

Experimental circuitry The schematics of the experimental set-up used in the experiments is presented in Fig. 2.25. The sample (gray zone) is thermally anchored to the mixing chamber of a ^{3}He−^{4}He dilution refrigerator, Which routinely ensures an operating temperature of 20 mK. Measuring and bias lines were carefuly filtered using miniature cryogenic low-pass filters, made of a RC meander lines [9] which provide a large attenuation in the GHz range. Such filters have proven to be useful to prevent single electronic devices from parasitic photon assisted tunneling due to the much higher noise temperature of the measuring and biasing apparatuses.

Charge detection

As pointed out in section 2.3.1, the charge detection is performed by a buit-in single electron transistor embedded on the same chip. The principles and limitations of charge detection using a normal metal single electron transistor (SET) as an electrometer are presented in chapter 5.

In this experiment, however, one has to notice that the detection of the excess island charge in the superconducting case is somewhat different since the electrometer is in the superconducting state as well. Nevertheless the supeconducting transistor provides almost the same charge detection accuracy. The voltage modulation which is induced by polarizing charges is then obtained by operating the superconducting SET near the superconducting voltage gaps $\pm 2\Delta/e$ for which quasiparticles are transferred. Biased near one of these two points, the voltage across the transistor V_{elm} is a $e-$periodic function of the island charge. Therefore the charge detection principles as well as the typical charge noise level are similar as for normal metal SETs.

Parasitic cross-talk capacitances

Typical values obtained for the capacitances are presented in the table 2.26.

C_{gb}	C_{ge}	C_c	C_{eb}	C_{be}	C_{jb}	C_{je}
85 aF	50 aF	150 aF	10 aF	30 aF	2.6 fF	1.3 fF

Table 2.26. Coupling and cross-talk capacitances in a typical sample.

In order to get a constant charge gain for the electrometer, one has to ensure that the single electron transistor is kept at a constant working point. For realizing such a condition, one has to compensate all external influences on the electrometer island charge with the electrometer gate voltage V. This is obtained by placing the electrometer circuit inside a feedback loop ensuring a constant charge for the electrometer island (grayed circuit in top of Fig. 2.25).

Principles of the feedback measurement

Changes of the electrometer island charge (due to a cumulated action of the variation of the box island charge and of the parasitic cross-talk charge $C_{be}U$) are detected by the electrometer output voltage V_{elm}. This voltage is locked on the constant reference voltage V_1 chosen to maximize the electrometer charge gain ($\partial V_{elm}/\partial q_{box}$). The error signal $V_{elm} - V_1$ is cancelled by applying a negative feedback on the voltage V. This feedback signal contains the information of the excess charge of the box charge that has to be extracted.

Determination of the box excess charge.

The box island staircase is obtained from the curve $V(U)$ by cancelling the parasitic influence caused by the cross-talk capacitance. In practice one has to subtract **a linear term** which equals $C_{be}U/C_{ge}$ (see Fig. 2.27) in order to get horizontal plateaus between steps in the Coulomb staircase**.**

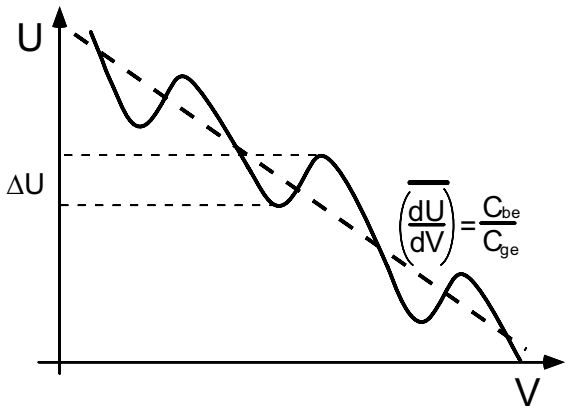

Figure 2.27. Typicals sawtooth-shaped error signal $U(V)$ obtained during feedback operation of the single Cooper pair box. The average slope is due to the cross-talk influence that need to be subtracted. A transition between two charge states for the island lead to a voltage shift ΔU.

Appendix 2−D
Determination of the even-odd free energy of the superconducting box

An estimate of the even-odd free energy $\widetilde{\Delta}(H,T)$ can be obtained by measuring the staircase assymetry, provided that $\widetilde{\Delta}(H,T)$ is reduced by the finite magnetic fied to a value below the charging energy E_c. In such a situation, the 2e steps splits into two steps corresponding of the sequential entrance of quasiparticles in the island. If one note L and S the respective lengths of long and short steps (see Fig 2.28 on next page) then, one has

$$\frac{\widetilde{\Delta}(H,T)}{E_c} = \frac{L-S}{L+S} \tag{2.45}$$

The method is explained with more details in [1].

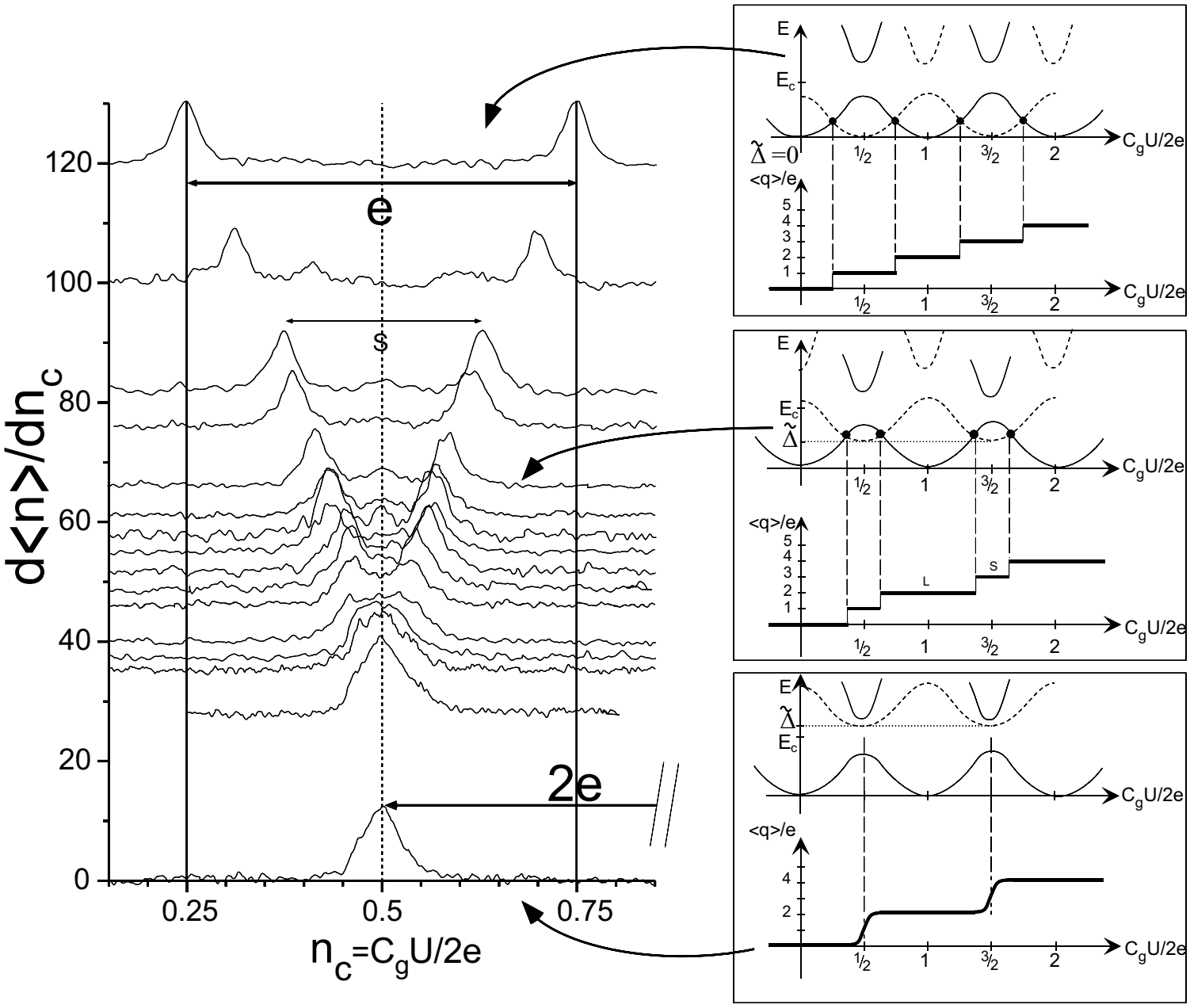

Figure 2.28. Left: *Derivative of the average excess charge in the superconducting box with respect to the gate charge number n_c for increasing magnetic field. Experimental curves have been shifted by an amount proportional to the applied field. The top curve corresponds to an applied field of* 0.1 T *for which the island is in the normal state.*
Right: *Schematics of the energy bands and corresponding Coulomb staircase for* 3 *typical cases* (*from bottom to top*: $\tilde{\Delta}>E_c$, $\tilde{\Delta}<E_c$ *and* $\tilde{\Delta}$=0). *Arrows show the curve for which the corresponding situation applies.*

Chapter 3

Quantum coherence in a small superconducting array

Introduction

The experiments reported in the previous chapter show that the ground state of the superconducting box circuit is a coherent superposition of two charge states. Since the measurement of the average charge in the island is performed at thermal equilibrium, it cannot lead to the determination of the energy and of the island charge of an individual given excited state. We have only shown that the average charge in the island is in agreement with the thermal average prediction. The aim of the experiment discussed in this chapter is to perform the full spectroscopy of the quantum states of a simple single Cooper pair device. Unlike the superconducting box, the proposed experiment follow a method that have been used to characterize the superconducting transistor [9]. It consists of measuring the maximum supercurrent that can flow through the circuit. Even though a transport property is now probed, it is still a characteristic of the quantum state of the circuit. We present preliminary experimental results on a circuit in which the energy and the level-width of the first excited state can be obtained from the resonant reduction of the critical current in presence of microwaves. The level-width of the first excited state provides in this system a direct measurement of the decoherence rate

of a pure charge state due to the coupling with the electromagnetic environment of the circuit.

3.1 The "self-dual" circuit

The simple Josephson array that we have considered consists of two superconducting transistors in parallel, with the two islands coupled by a junction (see Fig. 3.1). It has two islands, controlled by two gate voltages, and two superconducting loops, which can enclose same magnetic fluxes when a magnetic field is applied. It is called "self-dual circuit" because of this peculiar topology (two islands embedded in two loops) which provides a symmetric dependence upon charge and flux conjugate variables. Indeed, it is the simplest one in which the competition between $2e$ charge quantization and Φ_0 flux quantization effects can be investigated. Lafarge *et al.* [1] have first calculated the spectrum of this circuit and shown that the energy bands have a similar dependence with respect to both flux and gate charge variables.

3.1.1 Circuit parameters

We suppose that the four external Josephson junctions have the same Josephson coupling energy E_J and the same capacitance C. The junction parameters are adjusted such that E_J is smaller than the charging energy $E_c = e^2/2C$. The central Josephson junction can have a different area, and hence a different capacitance $C' = rC$. Since all the junctions of a given device have their insulating layers fabricated simultaneously, they have similar oxide layer thickness (see Chapter 6, Appendix 6-E). Therefore the Josephson coupling $E_J^{'}$ of the central junction is not an independent parameter, but is related to E_J and to the geometric area ratio r through the relation:

$$\frac{E_J^{'}}{E_J} = \frac{C'}{C} = r, \tag{3.1}$$

Both island charges and loop fluxes are independently controlled respectively by the two gate voltages U_1 and U_2, and by the applied magnetic flux Φ through the two symmetric loops. The three independently controlled parameters are therefore:

- the two gate charges (expressed in number of induced Cooper pairs) noted $n_{g1} = C_{g1}U_1/2e$ and $n_{g2} = C_{g2}U_2/2e$. It is convenient to introduce the sum $N_g = \frac{1}{2}(n_{g1} + n_{g2})$ and the difference $dn_g = \frac{1}{2}(n_{g1} - n_{g2})$ of these two variables.
- the magnetic flux Φ through each loop. Its dimensionless reduced value is $\alpha = \Phi/\Phi_0$.

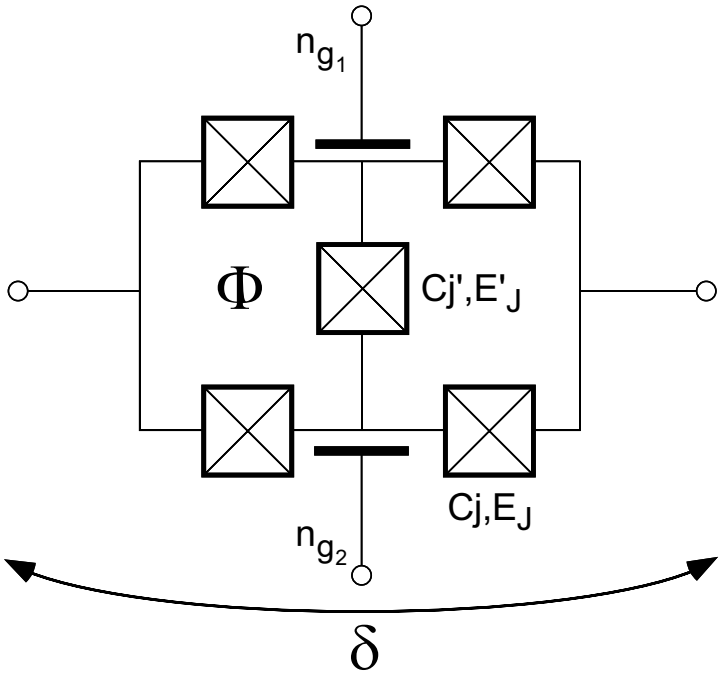

Figure 3.1. Schematic diagram of the self-dual circuit. Small Josephson junctions are represented by crossed boxes. The circuit has two loops through which a magnetic flux Φ *can be applied, two islands polarized by two gate charges* n_{g1} *and* n_{g2}*. Energy bands are calculated as a function of the global phase difference* δ*.*

The issue is to calculate the energy spectrum of the circuit as a function of the superconducting phase δ across the circuit.

3.1.2 Quantum description of the circuit

We perform a similar analysis as done for the superconducting box (section 2.1). Since our system is a two-island device, the relevant Hilbert space that act as the state basis is given by the tensorial product $|n_1, n_2\rangle = |n_1\rangle \otimes |n_2\rangle$ of each island charge states.

3.1.3 The electrostatic Hamiltonian H_{el}

The electrostatic Hamiltonian is diagonal in the charge basis and writes:

$$H_{el} = \sum_{n_1,n_2} E_{n_1,n_2} |n_1, n_2\rangle \langle n_1, n_2| , A \tag{3.2}$$

where E_{n_1,n_2} is the electrostatic energy of a charge configuration (n_1, n_2). The expression of this latter energy is obtained by inverting the capacitance matrix C_{ik} [2]. It is a quadratic function of the gate offset charges n_{g1} and n_{g2}:

$$E_{n_1,n_2} = E_c \left[\frac{r+2}{2(r+1)} \left[(n_1 - n_{g1})^2 + (n_2 - n_{g2})^2 \right] + \left(\frac{2r}{r+1} \right) (n_1 - n_{g1})(n_2 - n_{g2}) \right] . \tag{3.3}$$

3.1.4 The Josephson Hamiltonian

The Josephson Hamiltonian H_J couples charge states which differ by one Cooper pair passed through one of the junctions of the circuit. Its expression in absence of applied magnetic field writes:

$$\begin{aligned} H_J = -\frac{E_J}{2} \sum_{n_1,n_2} \Bigg[& \exp\left(\pm \frac{i\widehat{\delta}}{2} \right) |n_1 \pm 1, n_2\rangle \langle n_1, n_2| + \exp\left(\mp \frac{i\widehat{\delta}}{2} \right) |n_1, n_2 \pm 1\rangle \langle n_1, n_2| \\ & -r |n_1 - 1, n_2 + 1\rangle \langle n_1, n_2| + h.c. \Bigg] .A \end{aligned} \tag{3.4}$$

where $\widehat{\delta}$ is the operator associated to the superconducting phase difference across the circuit. In presence of a magnetic field, the different matrix elements acquire extra phase factors of the form $\exp(i\varphi_k)$, where φ_k is the phase of junction of index k such that the phase accumulated around each loop is equal to: $\alpha = \phi/\phi_0$

3.1.5 Effective Hamiltonian in a restricted charge state basis

As in the case of the superconducting box Hamiltonian, we restrict the gate charge numbers

n_{g1} and n_{g2} inside the interval $[0,1]$. In the case $E_J < E_c$, we have seen in previous chapter (Fig. 2.3), that quantum fluctuations are limited to two neighboring charge states. Therefore the restriction of the Hilbert space to the subspace spanned by the four charge states: $|0,0\rangle, |0,1\rangle, |1,0\rangle, |1,1\rangle$ is sufficient to determine the four lowest energy states.

We assume then that our experiment will provide a low impedance environment such that the phase difference δ is a good quantum number and becomes a simple parameter in the Hamiltonian. In this restricted basis, at zero magnetic field the total Hamiltonian $H = H_{el} + H_J$ has then the following matrix form:

$$H = \begin{pmatrix} E_{00} & -zE_J/2 & -\overline{z}E_J/2 & 0 \\ -\overline{z}E_J/2 & E_{01} & -rE_J/2 & -zE_J/2 \\ -zE_J/2 & -rE_J/2 & E_{10} & -\overline{z}E_J/2 \\ 0 & -\overline{z}E_J/2 & -zE_J/2 & E_{11} \end{pmatrix}, \tag{3.5}$$

where $z = \exp(i\delta/2)$. The eigenstates and the eigenenergies can be obtained by performing a direct numerical diagonalization. The supercurrent carried by a given eigenstate i is then obtained from the Hamilton equation:

$$I_i = \frac{1}{\phi_0}\frac{\partial E_i(\delta)}{\partial \delta}. \tag{3.6}$$

Although these numerical calculations do determine the supercurrent carried by the different eigenstates, they do not provide a satisfactory understanding of the parameters which control its amplitude. A better physical insight in the band structure is obtained from an analogy with a system of coupled spins.

3.1.6 Effective spin Hamiltonian

As in the case of the superconducting box, it is convenient to introduce fictitious spins 1/2. In the restricted charge state basis, we associate two pseudo-spins $\vec{s}_1$ and $\vec{s}_2$ to the islands 1 and 2 respectively (see Fig 3.2). The charge operators are obtained from the respective Pauli matrices $\boldsymbol{\sigma}_{z1}$ and $\boldsymbol{\sigma}_{z2}$ by a simple translation:

$$\begin{aligned} \widehat{n}_1 &= (\boldsymbol{\sigma}_{z1} + 1)/2 \\ \widehat{n}_2 &= (\boldsymbol{\sigma}_{z2} + 1)/2. \end{aligned} \tag{3.7}$$

We now introduce the total spin $\vec{S} = \vec{s}_1 + \vec{s}_2$. The expression of both Josephson and Hamiltonians can be expressed as a function of the spin operators:

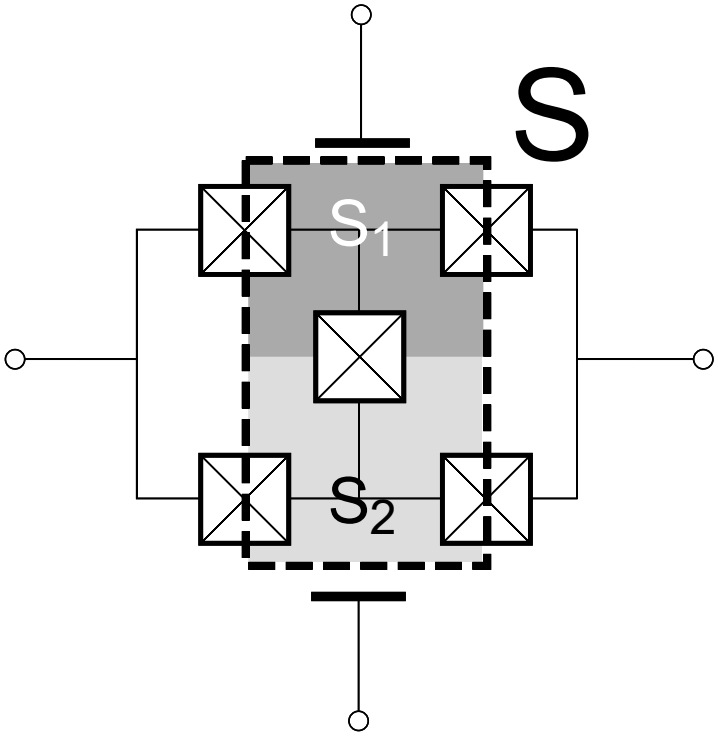

Figure 3.2: *Self-dual circuit in a restricted space. Each island* (*grayed areas*) *behaves as an effective spin* 1/2. *Eigenstates of the system will be indexed as a function of the quantum state of the sum* S *of the two spins which represents the state of the* "*macro-island*" (*dashed area*).

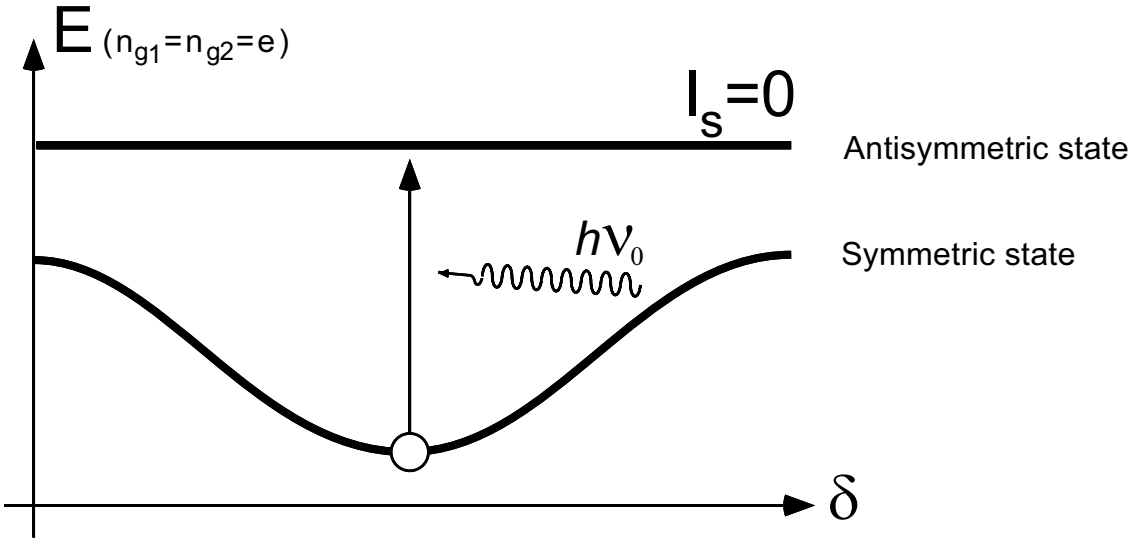

Figure 3.3. *Energy bands of the ground state and the first excited state for gate charges equal to e and zero magnetic field, as a function of the phase difference* δ. *The critical current of the circuit in a given state is proportional to the maximum slope of the associated energy band. The ground state correspond to a symetric state for the total spin* S *whereas the first excited state with zero critical current is antisymmetric. In the strong damping limit, the state can be modeled by a classical particle at the bottom of the washboard potential formed by the fundamental band. The energy difference* ΔE *to the first excited state is well defined and a photon of frequency* $\nu_0 = E_0/\hbar$ *can induce an interband transitions.*

$$H_{el} = 2E_c\,(1-2N_g)\,S_z + \frac{r}{1+r}E_c S_z^2 + \frac{4dn_g}{1+r}E_c\,(\boldsymbol{\sigma}_{2z} - \boldsymbol{\sigma}_{1z}) \quad (3.8)$$

$$H_J = -2E_J \cos\frac{\delta}{2} S_x - E_J\frac{r}{2}\left(\mathbf{S}^2 - \mathbf{1} - S_z^2\right). \quad (3.9)$$

The eigenstates of the total spin S provide a better basis to discuss the band structure.

3.1.6.a The totally symmetric case

The above expression has a simple form in the case of a symmetric polarization: $n_{g1} = n_{g2}$ (i.e. for $dn_g = 0$) and zero magnetic frustration (i.e. $\alpha = 0$). The total Hamiltonian can be expressed as a function of the total spin operators *only*. The total spin S becomes thus a good quantum number, and the diagonalization can be done separately in the sub-space $S = 0$, which contains the single state $|S = 0, S_z = 0\rangle$ and in the sub-space $S = 1$, spanned by the three states $|S = 1, S_z = 0, \pm 1\rangle$. The sub-matrix representing the Hamiltonian in each of these sub-spaces is obtained by applying the Wigner-Eckart theorem. This theorem states that all the operators which are transformed in the same way in a rotation are proportional in each subspace. In the particular subspace $S = 0$, all spin terms vanish. The state $|S = 0, 0\rangle$ is thus an eigenstate with an energy independent of the phase δ. *Therefore, this state* $|S = 0, 0\rangle$ *cannot sustain a supercurrent* (see Figs. 3.2 and 3.3). One can give a simple physical interpretation for that property: the effective Josephson coupling between the circuit electrodes is zero in this state because it is mediated through an antisymmetric combination $|S = 0, 0\rangle = \frac{1}{\sqrt{2}}\left(|1, 0\rangle - |0, 1\rangle\right)$ of the two equivalent macro-island states, which contribute with the same amplitude and therefore cancel. In the symmetric $S = 1$ subspace, the Hamiltonian reduces to the Hamiltonian of a spin in a magnetic field, lying in the xz plane, and subject to a quadrupolar perturbation proportional to S_z^2. The three corresponding energy bands are then obtained by solving analytically the eigenvalue equation.

3.1.6.b. Model of an Heisenberg Hamiltonian

If one now examines closely the spin analogy in the particular case of a symmetric charge and flux frustration, (*i.e.* : $N_g = \frac{1}{2}$, $dn_g = 0$, $\alpha = \pi$) then one can show that the total Hamiltonian rewrites:

$$\begin{aligned} H &= H_J + H_{el} \\ &= \frac{r}{1+r}E_c S_z^2 + E_J\frac{r}{2}\left(\mathbf{S}^2 - \mathbf{1} - S_z^2\right) \end{aligned} \quad (3.10)$$

If one chooses a particular set of parameters such that:

$$r = 1, \quad E_c = E_J, \tag{3.11}$$

one has the dramatic simplification :

$$H = \frac{E_c}{2}\left(\mathbf{S}^2 - \mathbf{1}\right) = E_c \overrightarrow{S_1}.\overrightarrow{S_2} \quad . \tag{3.12}$$

The total Hamiltonian takes then the form of an Heisenberg-like antiferromagnetic Hamiltonian for the two pseudo-spin 1/2.

3.1.6.c. Generalization to Josephson arrays

One can therefore easily see that the result obtained in the previous section, remains valid for more complex circuits such as Josephson arrays formed by a series of three-junction loops. Under the same set of "frustrating" parameters, such circuits are then good candidates for modelling Heisenberg triangular spin ladders [5] since by generalizing the previous result, we found that they obey to the following Hamiltonian:

$$H = E_c \sum_{\langle i,j \rangle} \overrightarrow{S_i}.\overrightarrow{S_j} \quad ,$$

where the symbol $\langle i, j \rangle$ denotes the indexes of neighboring islands linked by a Josephson junction.

3.2 Principle of the experiment

3.2.1 Measurement of the switching current

As introduced in previous chapter (page 111), such circuits behaves as an effective Josephson junction which parameters are tuned by the gate charges and optionally by the magnetic fluxes in the loops. Thus the dynamics of the circuit is similar as those of a single Josephson junction. We operate the circuit in a current-biased mode. The state of the effective Josephson junction as a function of the phase δ across the junction can be represented as a particle trapped in a dashboard potential [6]. The current forced through the junction is equivalent to an increase in the average slope (See fig. 3.4). When the current exceeds a certain value called "switching current", the particle runs away down the tilted potential. According to the

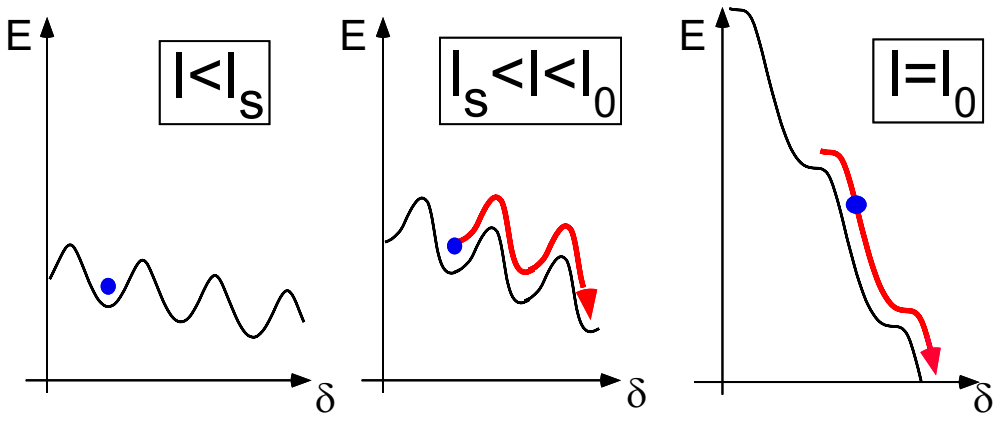

Figure 3.4: The dynamics of the current-biased circuit is analogous to a particle in a tilted washboard potential. The tilt is proportional to the bias current I. Left: For weak bias currents, the particle is trapped in the bottom of the well. Center : when the potential is tilted over a critical value corresponding to the so-called switching current I_s, thermal fluctuations make the particle escape from the well. A phase drift is then observed leading to a finite voltage across the circuit. Right: For a bias current equalling the critical current I_0, no metastable minimum is found. With an electromagnetic environment providing a large damping limit, fluctuations of phase are reduced and I_s is close to I_0.

Josephson equation: $\frac{\hbar}{2e}\partial\delta/\partial t = V$, a phase shift leads to a finite voltage across the circuit. In the high-damping limit, phase fluctuations of the particle in the bottom of the well are damped such that the switching current is close to the critical current (i.e. the highest current for which no metastable minima in the tilted potential are found).

3.2.2 Resonant suppression of the switching current

We have seen in 3.1.6.a that, for a given set of parameters, the first excited state has no phase dependence thus leading to a zero critical current. Actually the large difference between the critical current of the ground state and an excited state is a generic feature which persists for a wide range of values of N_g and dn_g. The operating principle of the experiment is to use this difference to probe the level spectrum. Applying a small radio-frequency component to one of the gate charges can indeed induce a transition from the ground state to an excited state (see Fig. 3.3). If this state cannot sustain a large enough supercurrent, such a transition results in a "switching event" to the quasiparticle branch unless the relaxation to the ground-state is too fast (see Fig. 3.5). The proposed experiment thus consists in finding a resonant suppression of the switching current. The Figure 3.6 shows the expected dependence of the

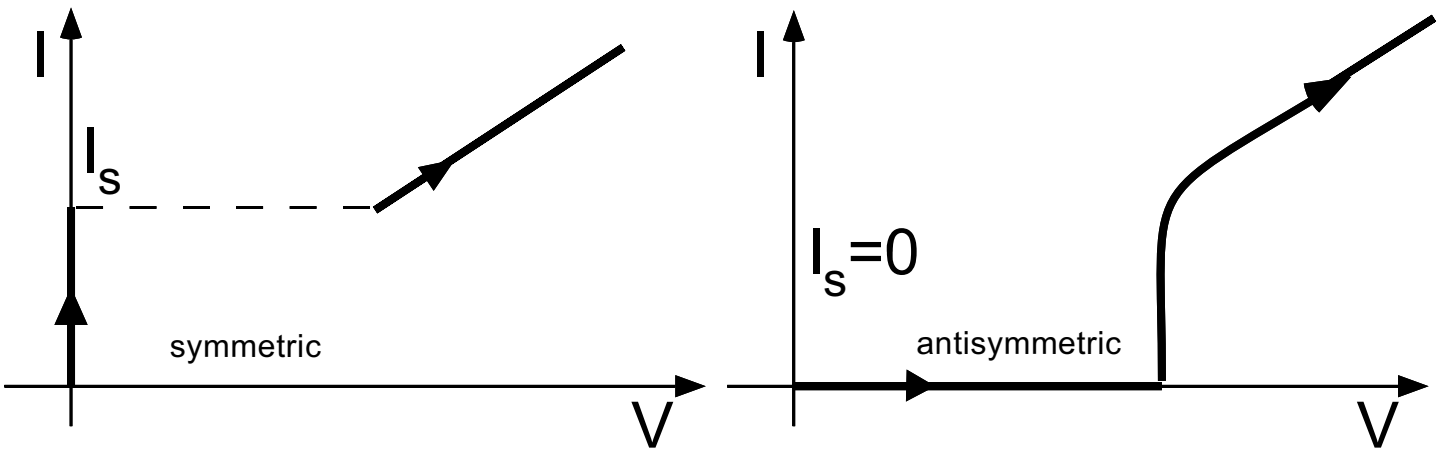

Figure 3.5. *Sketch of the expected I-V characteristics of the "self-dual" circuit.*
left: *in the symmetric ground state, a finite switching current is observed.*
right: *in the antisymmetric excited state, the energy band is phase independent and no supercurrent should therefore be observed.*

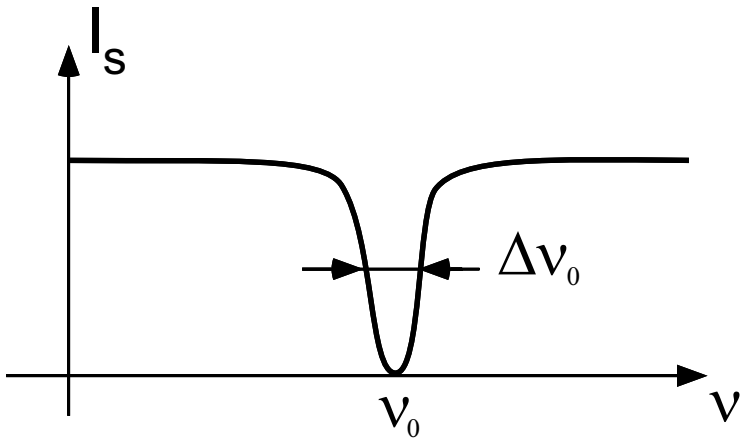

Figure 3.6. *Expected dependence of the switching current* I_s *for* $n_{g1}=n_{g2}=e$, $\phi=0$ *as a function of the microwave frequency* ν *applied on the gate electrode. The ground state corresponds to the symmetric state with a finite switching current. The switching current is suppressed when photons emitted by the gate induce a transition to the first excited state. The width* $\Delta\nu_0$ *of this resonance provides an estimate of the life-time of this excited state.*

switching current at the best working points defined by $N_g = 1/2 \pmod 1$, $dn_g = 0$ and α=0 (mod 1). The switching current is completely suppressed when the microwave signal on the gate induces a transition to the first excited state.

3.2.3 Resonance linewidth

Like in the superconducting box, the life-time of an excited state is limited by the coupling to the dissipative electromagnetic environment. The transition between the two states of the self-dual circuit that we consider, has however the peculiarity to be insensitive to the electromagnetic environment, provided that the four external junctions are exactly balanced. This decoupling effect is due to the fact that the transfer of a Cooper pair through the central junction does not result in a charge transfer in the external circuit. The transition is in some sense "orthogonal" to the environmental degrees of freedom. In other words the antisymmetric quantum state $\frac{1}{\sqrt{2}}(|1,0\rangle - |0,1\rangle)$ is expected to decay relatively slowly. In the case of imperfectly balanced circuits, the linewidth is of order of $(\Delta C/C)^2 E_J R/R_K$, where $\Delta C/C$ is the unbalance factor and R the effective environment impedance at the resonance frequency. Other effects could however contribute to the experimental linewidth. In particular, the fluctuations of the phase across the whole circuit due to the imperfect phase-bias could induce a broadening of the transition whose frequency depends on the phase (see Fig. 3.3).

3.3 Dependence of the critical current on the gate charges

The proposed experiment requires to place the circuit in the vicinity of the best working points (white dots in Fig. 3.8). The location of these points can be deduced from the analysis of the variations of the critical current $I_c(n_{g1}, n_{g2})$ with the gate charges. A plot of $I_c(n_{g1}, n_{g2})$is given in Fig. 3.9 for the set of parameters $E_J = E_c/10$. It displays sharp wedges that can be qualitatively understood by noticing that our circuit is equivalent, from the electrostatic point of view, to another well-known two-island circuit, the three junction "single electron pump" [3] (see Fig. 3.7). The electrostatic stability diagram of the pump configurations in the (n_{g1}, n_{g2}) plane consists of hexagonal cells whose boundaries correspond to the equality condition between the electrostatic energies of two neighboring charge states [4]. In the case where E_J and E'_J are smaller than E_c, the critical current is expected to be large only in the

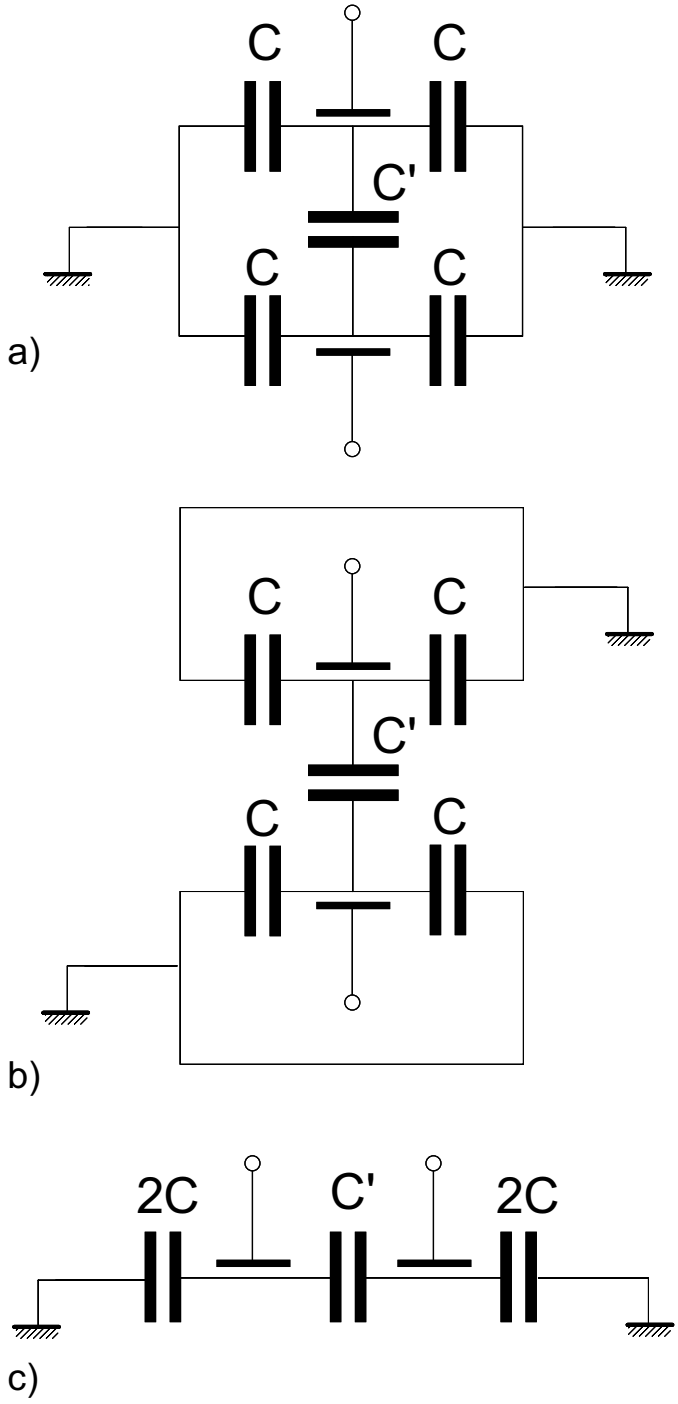

Figure 3.7. *Schematics of equivalent capacitance arrays for the electrostatic description of the self-dual circuit.*
Top: *Self-dual circuit for which all junctions have been replaced by their effective capacitances. Lead extremities are grounded.*
Middle: *equivalent representation of the circuit obtained by splitting the grounded leads.*
Bottom: *equivalent representation obtained by simplifying the above circuit. It corresponds to the electrostatic representation of a 3-junction pump.*

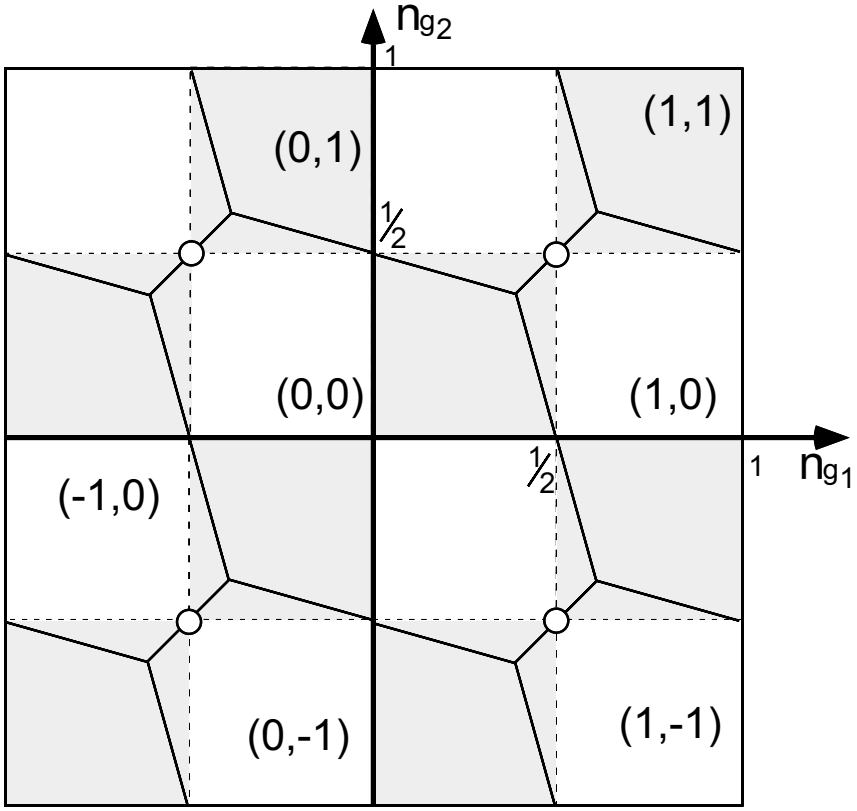

Figure 3.8. *Stability diagram of the island charge states* (n_1,n_2) *as a function of the gate charges, obtained by minimizing the electrostatic energy, for the specific case* C'=2C. *The hexagonal cell boundaries delimit two neighboring charge states with degenerate charging energies. The domain for which the critical current is appreciable forms a checkered pattern* (*gray zones*). *The resonance experiment is best performed in the vicinity of white dots.*

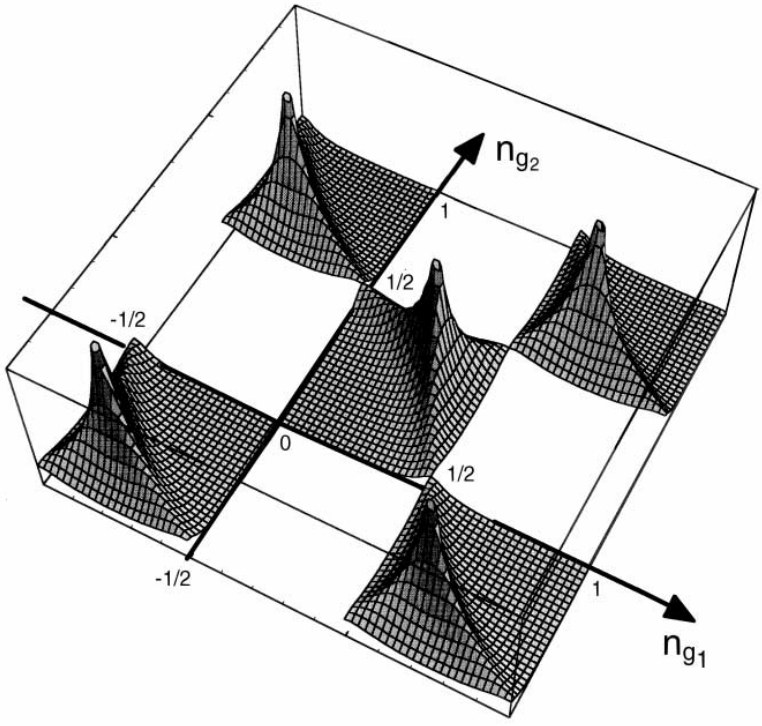

Figure 3.9. *Critical current of the self-dual circuit as a function of the two gate charges numbers* n_{g1} *and* n_{g2}. *It has been computed in the case of a small Josephson coupling equal to one tenth of the charging energy. The critical current is appreciable along the hexagonal cell boundaries and is maximum at the triple points.*

vicinity of the cell boundaries, and to be maximum at the triple points of the hexagonal tiling. This qualitative prediction is confirmed by the numerical calculations shown in Fig. 3.9.

3.4 Preliminary experimental results

The experimental set-up implementing the experiment is shown in Fig. 3.10, together with a micrograph of a typical sample (Fig. 3.11). The design of the RC electromagnetic environment has been optimized for the measurement of the switching current (see chapter 6, section 6.5.5). We have obtained with this high damping design a ratio between the measured switching current and the estimated maximum critical current higher than 80%, which proves that the phase-bias approximation is a good approximation [7]. In this regime, the variations of the switching current closely reproduce those of the critical current. However it remains a stochastic variable characterized by a switching probability. An example of $I-V$ characteristics with a large switching current is shown in Fig 3.12. Although we could not yet observe the predicted resonance, we were able to prove that the switching current measurement can be immune to residual quasiparticles.

3.4.1 "Odd/even" states

As mentioned in the previous chapter, many superconducting box experiments failed because of the "poisoning" by quasiparticles which give access to charge states with an odd number of extra electrons in the island. The box experiment is very sensitive to such "odd" charge states because it is a quasi-static experiment. The experiment discussed in this chapter is also sensitive to these "odd"-states, but unlike the box experiment, measuring the switching current is a dynamic measurement which allows to probe the circuit over a shorter and tunable time-scale.

3.4.2 Measurement of the life-time of the odd/even charge states

3.4.2.a. switching current statistics

We have measured the switching histograms of the circuit when the bias current is ramped at a constant ramp rate dI/dt. For a give gate charge number, we commonly observed a double bumped histogram, as shown in the top panel of Fig. 3.15, that we attribute to the separate switching of odd and even states. When we vary the gate charge number n_{g1}, we

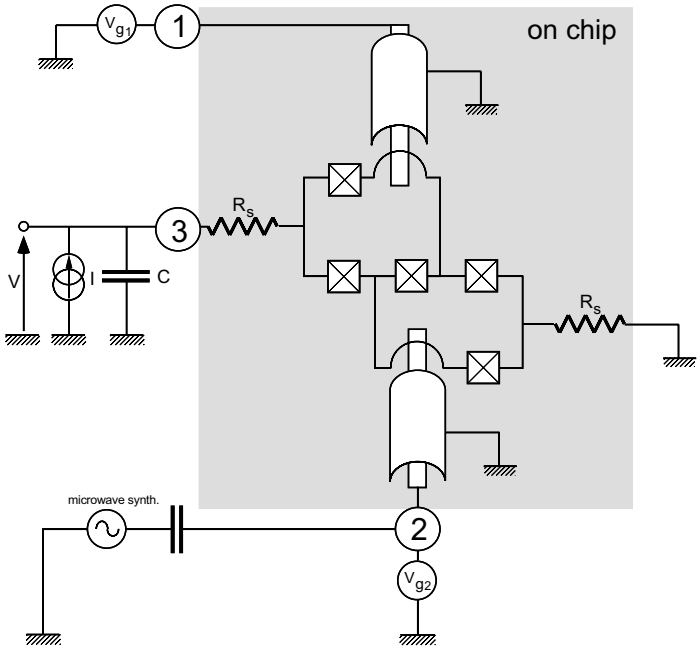

Figure 3.10. Schematics of the experimental set-up of a current biased self-dual circuit with a controlled electromagnetic environment. On-chip capacitances C and resistances R_S close to the Josephson junctions place the circuit in the high damping limit. Gate electrodes are buried under a shielding ground plane. One of them irradiates microwaves on the circuit in order to induce interband transitions. Numbered dots refer to the connection in the sample holder already shown in Fig. 2.25.

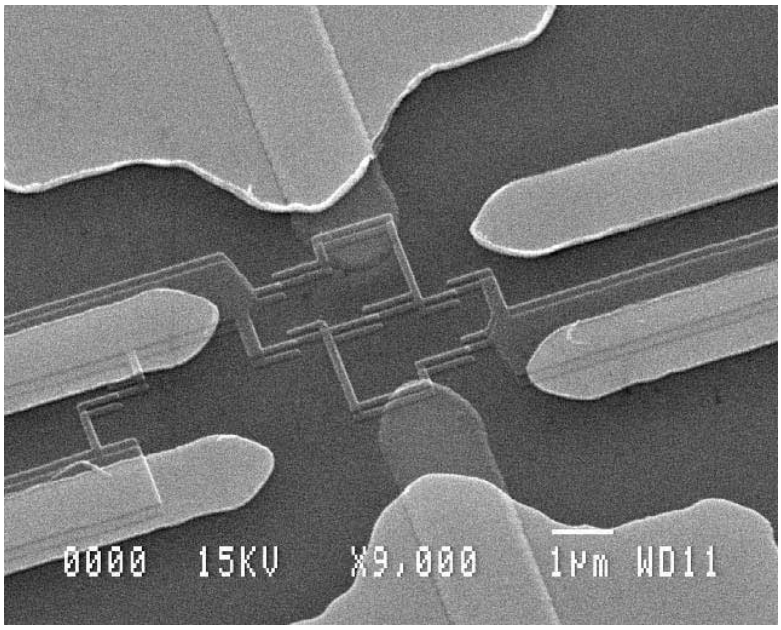

Figure 3.11. Scanning electron micrograph of a self-dual circuit fabricated using the multilayer technique described in part 6.5. It corresponds to the grayed frame in the set-up diagram shown above. It is composed of three conductive layers : the first gold layer implements the gate electrodes (dark fingers on top and bottom of the picture). The second gold circuitry layer separated from the bottom one by half-micron thick insulating silicon nitride layer acts for the bias serial resistances R_s (lateral fingers) for one part and shields the two gate lines (bright areas at top and bottom of the picture) for the other part. The top layer containing the Josephson junctions is fabricated by e-beam lithography and is directly connected on the second gold layer. It is aligned over the gate electrodes (see fabrication details in Chapter 6).

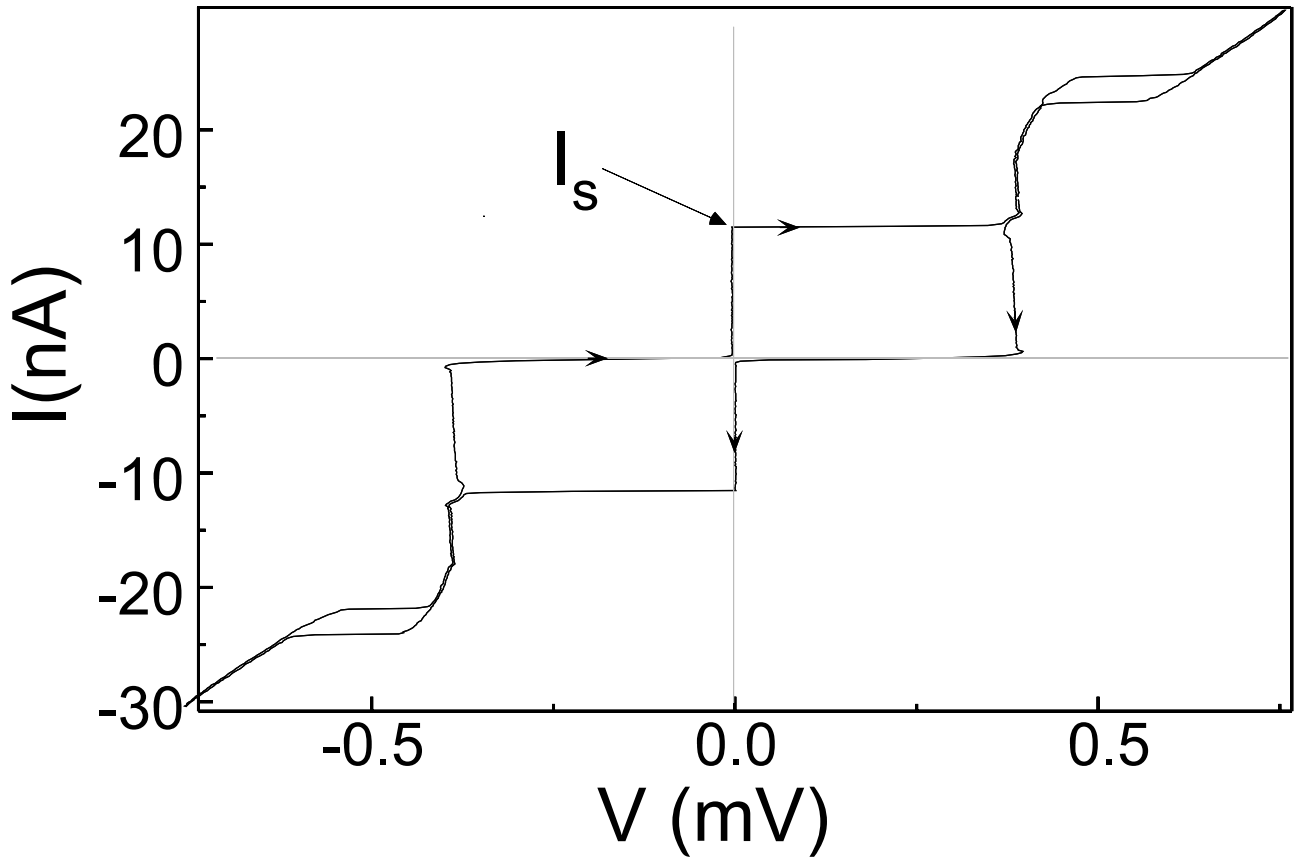

Figure 3.12. *Experimental I-V characteristic of the self-dual circuit, measured at 20 mK. The circuit switches to the finite voltage branch at the switching current* I_s*, which has an average value reaching* 80% *of the Ambegaokar-Baratoff prediction for the critical current.*

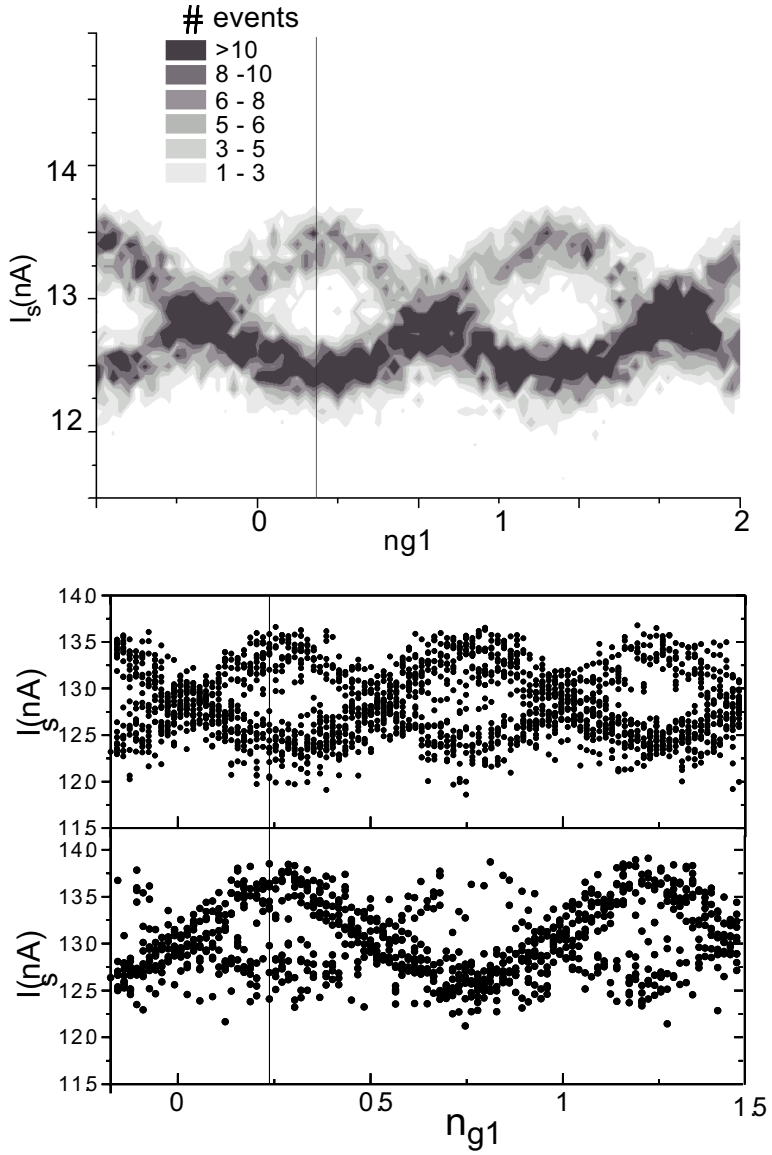

Figure 3.13. *Measured switching current distributions as a function of the gate charge number* n_{g1}, *for different ramp rates.*
Top panel show a density plot performed for the lowest ramp rate (di/dt=$10^{-7}A/s$), *dark areas correspond to the highest probability of switching. One observes two interlaced current bands which are both* 2e-*periodic. One is associated to charge states contaminated with a single quasiparticle while the other is free from contamination. For these low frequency sweeps, the circuit prefers to switch for the lowest current available whatever the band. As we increase the sweep frequency, the probability of switching continuously evolves* (*middle panel, medium rate* di/dt=$10^{-6}A/s$) *and finally favors one of the current bands, probably the even state band* (*bottom panel*).

could observe two interlaced $2e$-periodic current bands, each one being shifted by e (see Fig. 3.13). Lafarge *et al.* [8] have also observed such an even/odd dependence and double bumped histograms for the switching current in same circuits but its dependence on the ramp rate was not studied.

We now show how a simple dynamic model can reproduced the evolution of the switching histogram when the ramp rate dI/dt is varied.

3.4.2.b. interpretation using a phenomenological dynamic model

We assume that the island can be found in an even state a with probability p_a, and in an odd state b with probability p_b. These two states have different lifetimes τ_a and τ_b, and different switching rates Γ_a and Γ_b which depend on the bias-current I. The total switching rate is $\Gamma = \Gamma_a p_a + \Gamma_b p_b$.

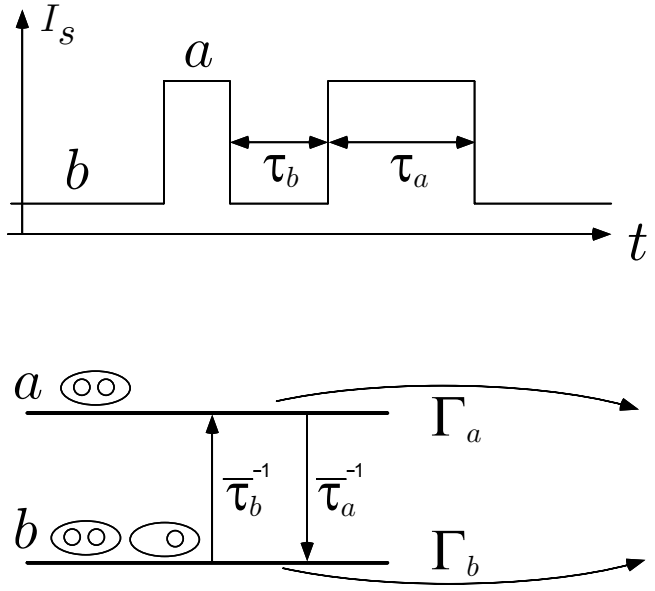

Figure 3.14. Top: time evolution of the island states. The system hops between state a and state b.
Bottom: Dynamic model for the switching. One state can decay in two ways: either by hopping to the other state, or by switching to the finite voltage branch.

In a given state, the system can evolve either by hopping to the other state or by switching. The evolution of the probabilities p_a and p_b during a bias-current sweep $I(t)$ is then governed

by the equations (see Fig. 3.14):

$$\begin{cases} \dfrac{dp_a}{dt} = \dfrac{p_b}{\tau_b} - \dfrac{p_a}{\tau_a} - \Gamma_a\left(I(t)\right) p_a \\ \dfrac{dp_b}{dt} = -\dfrac{p_b}{\tau_b} + \dfrac{p_a}{\tau_a} - \Gamma_b\left(I(t)\right) p_b \end{cases} \tag{3.13}$$

We choose for the switching rates an Arrhenius-like law:

$$\Gamma\left(E\right) = Ae^{B} \tag{3.14}$$

in which the exponent B increases with the bias-current. As a first order approximation, we assume that the exponent B depends linearly on the current I. Note that the switching process is an out-of-equilibrium process more complex than the thermally activated escape out of a potential well. Within this phenomenological approach, the switching rates in the two states a and b take the following form:

$$\begin{cases} \Gamma_a\left(I\right) = \Gamma_a^0 \exp\left[\frac{I}{\lambda_a}\right] \\ \Gamma_b\left(I\right) = \Gamma_b^0 \exp\left[\frac{I}{\lambda_b}\right] \end{cases} \tag{3.15}$$

Such an exponential dependence of the switching rate with the bias-current has been observed in small Josephson junctions [7]. We have solved these equations numerically using the above expressions. Switching histograms obtained by solving the differential equations (Eq. 3.13) are shown in the bottom panel of Fig. 3.15. The model reproduces well the evolution of the histogram shape with the ramp rate. At low ramp rate, the system has time to explore the two states during the current raise time: the switching occurs in the lowest switching current band, leading to a single bump histogram. The global pattern is then e-periodic At large ramp rates, the system does not have time to hop to another state during the current rise-time. Therefore the current probe sees a "frozen system"; the histograms becomes sharp (Fig. 3.15 top) and their relative weights reproduce the ratio of population p_a/p_b. This is further confirmed in the Fig. 3.13 bottom panel: the switching mainly occurs in the most populated band, which is expected to correspond to the even state. The overall agreement between the measured histograms and the calculated ones using our simple model gives confidence in the two state hypothesis. We can deduce from this comparison the average life-time τ_a which equal about 3 ms, and the population ratio $p_a/p_b \approx 1.3$. We attribute the global shift of the measured

histograms towards larger currents when the ramp rate is increased, to the finite bandwidth of the biasing and measuring circuitry. Although the present experiment is still plagued with quasiparticles, measuring the switching current with a large enough ramp rate allows to get rid of this spurious effect.

One has to notice that such a "quasiparticle poisoning" at low temperature has been also reported for the superconducting transistor as reported by Joyez *et al.* [9]. However they did not observe such two-bumped histograms, probably because of the large difference between odd and even state switching currents.

3.4.3 Effect of the microwave irradiation

We always have observed a reduction of the switching current when a sufficiently large microwave signal was applied onto one gate. At higher levels, we have observed Shapiro steps on the I-V characteristic. However, we could not observe a resonant suppression of the switching current because the transition frequency was higher than the microwave line cut-off frequency.

Since this work has been performed, a group at Stony Brook [10] has observed such interband transitions in the superconducting transistor. Using a similar technique based on the reduction of the critical current, they have measured the band gap for that system and found it in good agreement with the theoretical prediction.

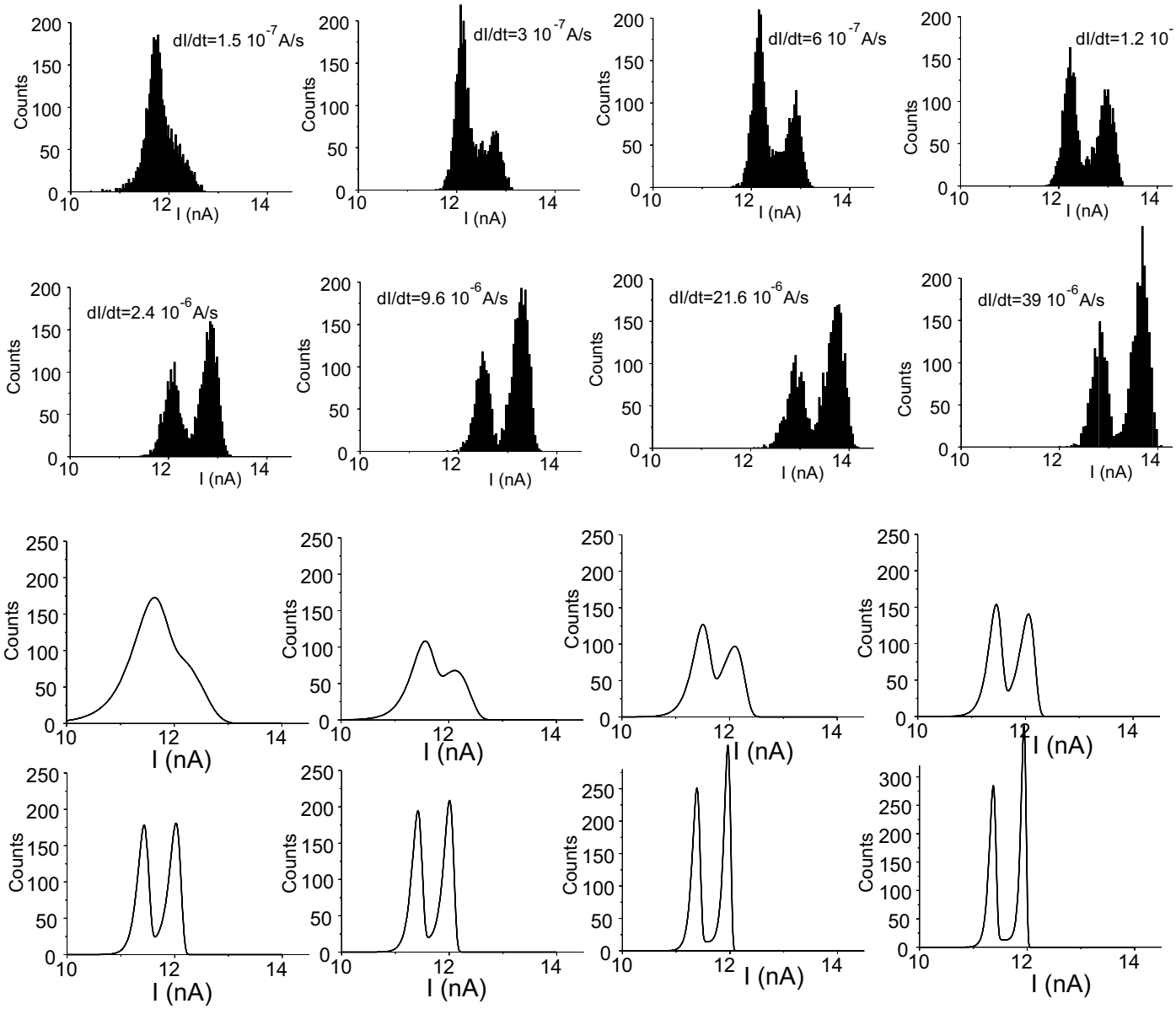

Figure 3.15. *Top*: *Experimental histograms of the switching current I_S measured at 20 mK for increasing ramp rates. the histograms were measured for the gate charge corresponding to the vertical line in fig.* 3.13.

Bottom: *Corresponding switching currents calculated with the phenomenological dynamic model discussed in the text.*

Conclusion

The self-dual circuit is a promising candidate for a macroscopic quantum coherence type experiment. In particular, we have found that the switching current measurement in this circuit is more immune to spurious quasiparticles than the island charge measurement in the superconducting box. By using samples with a suitable RC environment, and by applying large bias current ramp-rates, we could measure the switching current in the quasiparticle-free lowest energy band.

References of Chapter 3

[1] P. Lafarge, M. Matters, and J. E. Mooij, Phys. Rev. B, **54**, 10, (1996).

[2] P. Lafarge, Ph. D. Thesis, Université PARIS 6, (1993).

[3] H. Pothier, P. Lafarge, P.F. Orfila, C. Urbina, D. Esteve and M.H. Devoret, Physica B, **169**, 573 (1991). Europhys. Lett. **17**, 259, (1991).

[4] see chapter 3 in *Single Charge Tunneling*, eds. H. Grabert and M. H. Devoret, (Plenum Press, New York,1992).

[5] M. Devoret, private communication

[6] see chapter 6, p147, in *Physics and applications of the Josephson effect*, A. Barone and G. Paternò, (J. Wiley & sons, New York, 1982).

[7] D. Vion, M. Götz, P. Joyez, D. Estève, and M. H. Devoret, Phys. Rev. Lett. **77**, 3435, (1996).

[8] P. Lafarge, M. Matters, and J. E. Mooij, Proceedings of the International Conference on Quantum devices and Circuits, Alexandria, Egypt, June 1996.

[9] P. Joyez, P. Lafarge, A. Filipe, D. Esteve, C. Urbina, and M.H. Devoret, Phys. Rev. Lett. **72**, 2458, (1994).

[10] D.J. Flees, S. Han and J.E. Lukens, Phys. Rev Lett. **78**, 4817, (1997).

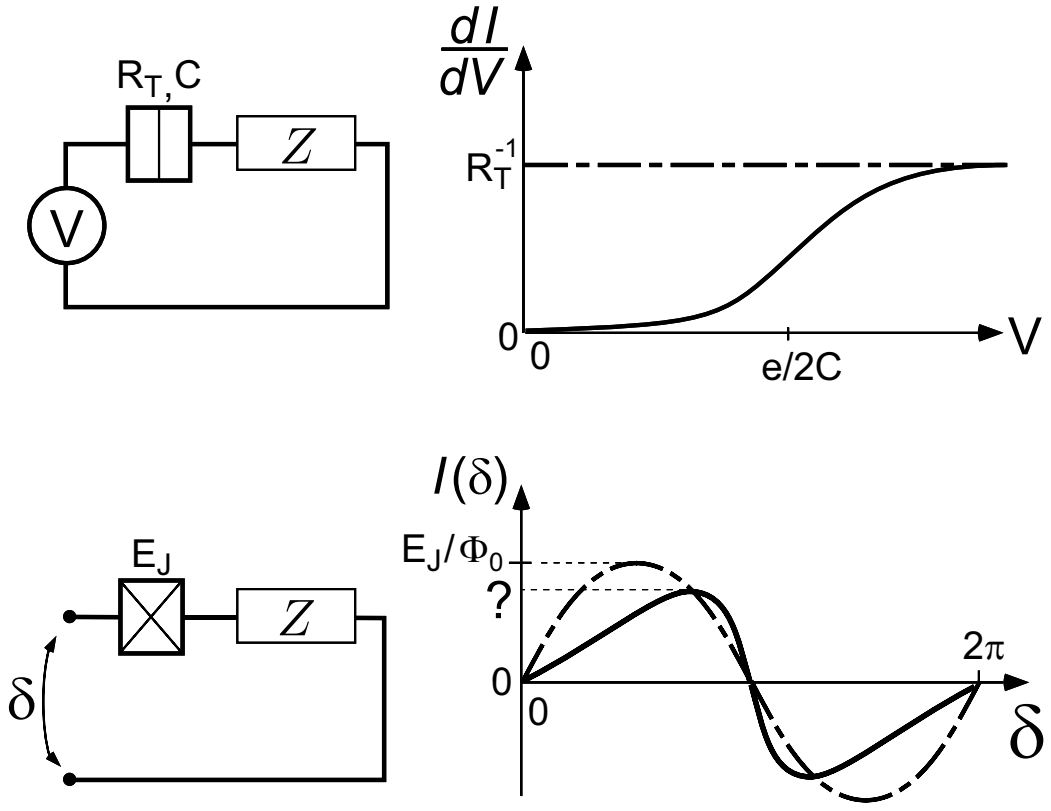

Figure 4.1. Top: schematics of a normal-metal tunnel junction in series with an impedance $Z(\omega)$. The whole circuit is voltage biased. In the high impedance regime, the conductance $\left(\frac{\partial I}{\partial V}\right)$ is reduced at low voltages compared to the normal tunnel conductance R_T^{-1}. This effect is known as the "environmental Coulomb blockade of tunneling".
Bottom: schematics of a Josephson junction in series with an impedance $Z(\omega)$. The whole circuit is phase-biased. The issue of this chapter is to determine how the current-phase relation of the supercurrent $I(\delta)$ is affected by $Z(\omega)$ compared to the bare junction dependence $(E_J/\Phi_0)\sin\delta$.

Chapter 4

Environmental Coulomb blockade of the Josephson effect

Introduction

The theory of single electron tunneling [1] shows that the conductance of a small normal-metal tunnel junction is not a property of the junction itself, but depends also on the electromagnetic environment in which the junction is embedded. In particular, if one considers an opaque tunnel junction (*i.e.* $R_T \gg h/e^2 = R_K$), a large reduction of the conductance at low voltages is observed for an electromagnetic environment whose impedance $Z(\omega)$ is large compared to the resistance quantum over a sufficiently wide frequency range. This phenomenon is known as the "environmental Coulomb blockade" of single electron tunneling (see Fig. 4.1, top panel). One can wonder in a similar way whether the properties of a small Josephson junction (*i.e.* a small junction with superconducting electrodes) are affected by the electromagnetic environment of the junction. More precisely, the issue is to calculate the supercurrent flow through a Josephson junction placed in an arbitrary electromagnetic environment: does an "environmental Coulomb blockade of the Josephson effect" exist?

To answer this question, one has to consider the whole electrical circuit, which consists of the Josephson junction and its electromagnetic environment, as a quantum system and

determine its eigenstates. The supercurrent that circulates through the junction and other measurable quantities will be then deduced from the eigenstate energies.

4.1 Quantum description of the circuit

We first explain how the Hamiltonian formalism can be applied to such circuits.

4.1.1 Quantum representation of a Josephson junction

The Josephson junction itself is modelled as a pure Josephson element (conventionally represented in diagrams by a cross, see Fig. 4.2, right panel) in parallel with the capacitance C formed by the electrodes facing each other at the junction.

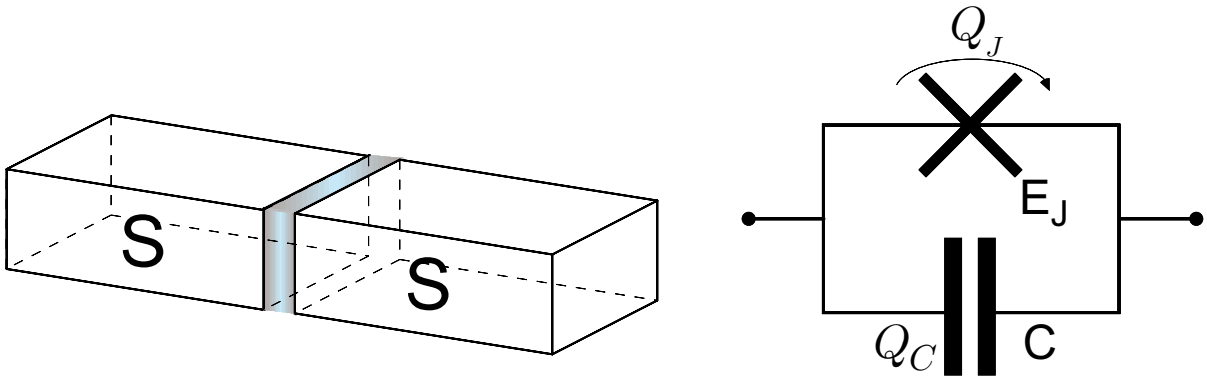

Figure 4.2. Left: sketch a Josephson junction. Two superconducting electrodes are separated by a thin insulating layer (~ 1 nm) through which Cooper pairs tunnel.
Right: equivalent dipole for the Josephson junction. It is modeled as a pure Josephson element (cross) in parallel with a capacitance C. Each component has it own degree of freedom (respectively referred as Q_J and Q_C).

The total charge having passed through the device is thus the sum of two charges:

- the electrostatic charge Q_C on the capacitor plates.
- the charge Q_J passed through the junction. This charge can be written as Q_J=-2en,

where n is the number of Cooper pairs that have tunneled through the junction.

There is a fundamental difference between these two charges. The charge Q_C is a continuous variable which is associated to the displacement of the electron fluid with respect to the ion lattice. The charge Q_J is, on the contrary, a discrete variable, because discrete number of charge can be positioned virtually inside the junction. One associates to the number of

transferred Cooper pairs n a quantum operator $\hat{N}$ whose eigenvectors $|n\rangle$ verifies:

$$\hat{N}\,|n\rangle = n\,|n\rangle\,. \tag{4.1}$$

4.1.2 The Josephson Hamiltonian

We suppose here that the charging energy of the junction capacitance $E_c = e^2/2C$ is much lower the superconducting gap Δ so that the Josephson Hamiltonian which couples states $|n\rangle$ differing by one Cooper pair (see Fig. 4.3), takes in the $|n\rangle$ basis the following form:

$$H_J = -\frac{E_J}{2}\sum_n \left(|n+1\rangle\langle n| + |n\rangle\langle n+1|\right), \tag{4.2}$$

where the characteristic Josephson coupling energy E_J is given by the Ambegaokar-Baratoff formula [2]:

$$E_J = \frac{h}{8}\frac{\Delta}{e^2 R_T}\,. \tag{4.3}$$

Here R_T denotes the normal state tunnel resistance of the junction. Note that this Hamiltonian is invariant under translations of $|n\rangle$.

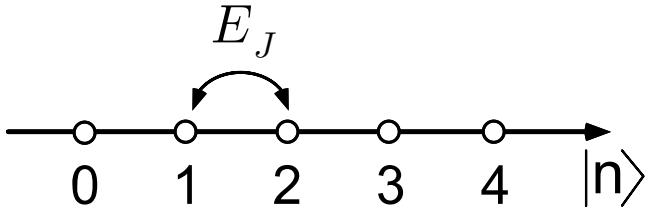

Figure 4.3. Diagram of the quantum states $|n\rangle$ corresponding to the number of Cooper pairs transfered through the junction. The Josephson Hamiltonian couples neighboring states.

Let us then introduce the set of states $|\delta\rangle$ defined by the Fourier series of the kets $|n\rangle$:

$$|\delta\rangle = \frac{1}{\sqrt{2\pi}}\sum_n e^{in\delta}\,|n\rangle\,. \tag{4.4}$$

We associate to the phase δ the operator $\hat{\delta} = \frac{1}{i}\frac{\partial}{\partial n}$ which verifies $\hat{\delta}\,|\delta\rangle = \delta\,|\delta\rangle$. The variables n and δ are thus conjugate variables in the sense of Hamiltonian mechanics [5]. The operators $\hat{n}$ and $\hat{\delta}$ obey to the commutation rule: $\left[\hat{n},\hat{\delta}\right] = i$.

Expressed in the $|\delta\rangle$ basis, the Josephson Hamiltonian is diagonal and takes its usual form:

$$H_J = -\int_0^{2\pi} d\delta\; E_J\cos\delta\,|\delta\rangle\langle\delta|\,. \tag{4.5}$$

This basis is well suited to calculate the evolution of the junction state when the voltage $V(t)$ across the junction is imposed externally. In this case, a state $|\delta\rangle$ evolves in time in the following way:

$$|\delta(t)\rangle = \left|\delta(0) + \frac{2e}{\hbar}\int_0^t V(t')dt'\right\rangle . \tag{4.6}$$

This latter expression actually provides a quantum generalization of the Josephson relation for the evolution of the phase:

$$V = \frac{\hbar}{2e}\dot{\delta}. \tag{4.7}$$

4.1.3 Modeling the electromagnetic environment

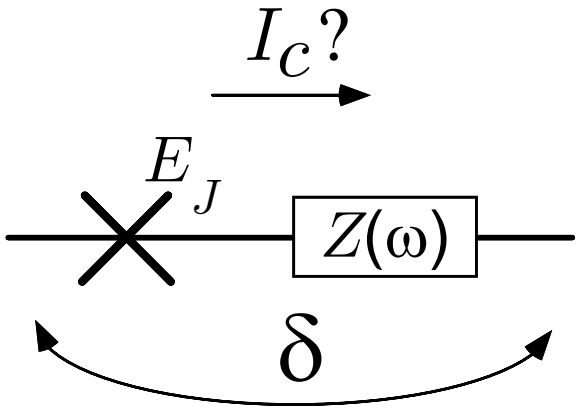

Figure 4.4. Schematic diagram of the circuit which is considered. It consists of a pure Josephson element in series with an impedance $Z(\omega)$ which models the electromagnetic environment seen from the Josephson junction.

The electromagnetic environment seen by the Josephson junction is entirely defined by the series impedance $Z(\omega)$ (Fig. 4.4). For sake of simplicity, we assume that the capacitance C of the Josephson junction has been incorporated in the impedance. We assume here that the impedance does not have any DC component, *i.e.* $\lim_{\omega\to 0} Z(\omega) = 0$, so that a supercurrent can flow through the whole circuit. Dissipation at finite frequency, described by the real part of the impedance is however allowed.

We use the quantum description of dissipative electrical circuits developed by Caldeira and Leggett [4]. The idea is to treat dissipation without corrupting Hamiltonian mechanics. For that purpose, the impedance is replaced by an infinite collection of harmonic oscillators.

Firstly, the real part of the impedance $\mathrm{Re}\, Z(\omega)$ is divided into a discrete series of infinitely thin frequency slices:

$$\begin{aligned} \mathrm{Re}\,(Z(\omega)) &= \sum_{m\geqslant 0} \mathrm{Re}(Z(m\times\Delta\omega))\delta\left(\frac{\omega}{\Delta\omega}-m\right), \\ \text{with } \Delta\omega &\rightarrow 0. \end{aligned} \tag{4.8}$$

We then associate to each slice a single harmonic oscillator with resonance frequency

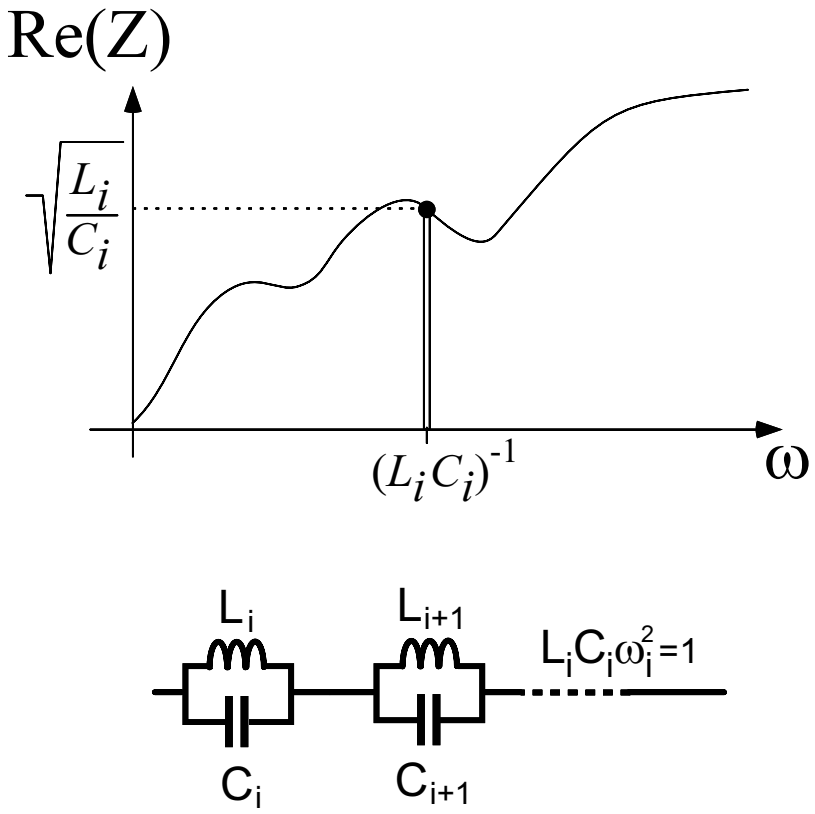

Figure 4.5. Top: frequency spectrum $Re[Z(\omega)]$ of the dissipative part of the electromagnetic environment. Each slice $[\omega_i, \omega_i + \Delta\omega]$ is associated to a single LC oscillator resonating at $\omega = \omega_i$, which real part $\frac{\pi}{2}\sqrt{\frac{L_i}{C_i}}$ matches the impedance $Re[Z(\omega_i)]$ at that frequency.
Bottom: equivalent circuit for a model of the electromagnetic environment. A quantum state for the environment is characterized by the number of photons in each LC oscillator.

$\omega_m = m\Delta\omega$ centered on the frequency slice (see Fig. 4.5, top panel). An oscillator consists of a parallel LC circuit with lumped elements L_m and C_m verifying:

$$\omega_m = m\Delta\omega = \frac{1}{\sqrt{L_m C_m}}. \tag{4.9}$$

The electromagnetic environment is therefore modeled by an infinite series of LC dipoles (see Fig. 4.5, bottom panel) and the impedance $Z(\omega)$ is the sum of all the oscillator impedances $Z_m(\omega)$:

$$Z(\omega) = \sum_m Z_m(\omega). \tag{4.10}$$

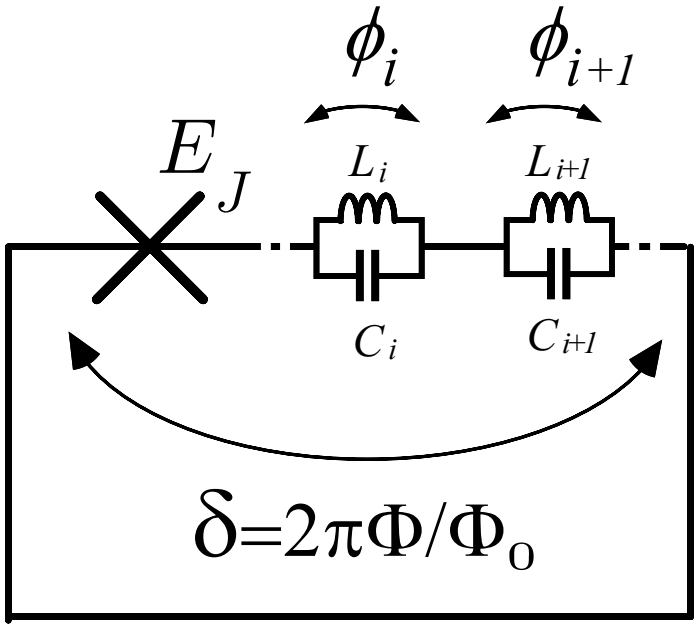

Figure 4.6. Equivalent circuit for a Josephson junction embedded in an electromagnetic environment. The impedance $Z(\omega)$ has been replaced by an infinite series of harmonic LC oscillators. The phase δ across the whole circuit is imposed by applying a magnetic flux Φ through the loop.

That a LC circuit is generally characterized by a purely imaginary impedance should not obscure the fact that an infinite series of these can result in a complex impedance[1]. By extending the definition of the impedance to complex frequencies and taking the limit, the expression of the impedance Z_m of a parallel LC circuit of elements L_m and C_m is given by:

$$Z_m(\omega) = \text{v.p.}\left(\frac{-i\omega}{C_m(\omega^2-\omega_m^2)}\right) + \frac{\pi}{2C_m}\left[\delta(\omega+\omega_m)+\delta(\omega-\omega_m)\right]. \tag{4.11}$$

The real part of Z_m is precisely located at the resonance frequency ω_m. Identifying 4.8 with

[1] This property is well known in the case of semi-infinite transmission lines, which have a real impedance and can be described by an infinite ladder of LC circuits.

the real part of 4.10, one obtains, using expression 4.11:

$$\frac{\pi}{2C_m} = \mathrm{Re}\left(Z(\omega_m)\right)\Delta\omega. \tag{4.12}$$

Even if this equation fixes only the real part of the impedance, the imaginary part of the impedance is also properly reconstructed by this identification. Indeed, due to the analyticity of Z, an equation linking the imaginary part of Z with the oscillator parameters can be obtained using Kramers-Krönig relations. The values of the elements L_m and C_m are then determined by the set of Equations: 4.9 and 4.12. It is often more convenient to characterize the LC circuit by its resonance frequency ω_m and its characteristic impedance $\mathcal{Z}_m$:

$$\mathcal{Z}_m = \sqrt{L_m/C_m} = \frac{2}{\pi}\,\mathrm{Re}\left(Z(\omega_m)\right)\frac{\Delta\omega}{\omega_m}. \tag{4.13}$$

The quantum states defined by tensorial products of single oscillator eigenstates:

$$|E\rangle = \bigotimes_m |N_m\rangle\,, \tag{4.14}$$

(where $|N_m\rangle$ is an eigenstate of the oscillator m with N_m quanta), form a complete basis for the quantum states of the environment. In this basis, the Hamiltonian of the environment $\mathcal{H}_{env}$ is straightforwardly written in correspondence to the classical limit. It has a diagonal form and writes as:

$$\mathcal{H}_{env} = \sum_m \left(\frac{\hat{\phi}_m^2}{2L_m} + \frac{\hat{Q}_m^2}{2C_m}\right) = \sum_m \left(N_m + \frac{1}{2}\right)\hbar\omega_m \quad , \tag{4.15}$$

where N_m is the number of excitation quanta in oscillator m and $\hat{Q}_m$ and $\hat{\phi}_m$ are respectively the charge and the flux operators. This latter operators are related to the charge number and phase through the relation

$$\begin{cases} \hat{Q}_m = -2e\ n_m \\ \hat{\phi}_m = \frac{\hbar}{2e}\ \varphi_m \end{cases} .$$

4.1.4 Total Hamiltonian of the system

The total Hamiltonian $\mathcal{H}$ describing this system is the sum of the Josephson Hamiltonian $\mathcal{H}_J$ and of the Hamiltonian of the electromagnetic environment $\mathcal{H}_{env}$.

A convenient basis to write the total Hamiltonian is the basis of vectors $|S\rangle$ consisting of the tensorial product of the kets of the Josephson junction $|n\rangle$ by the quantum states $|E\rangle$ of

the environment:

$$|S\rangle = |n\rangle \otimes |E\rangle = |n; N_1, N_2, .., N_k, ..\rangle \,. \tag{4.16}$$

In this basis $|S\rangle$, the Hamiltonian of the environment $\mathcal{H}_{env}$ is still diagonal but the Josephson Hamiltonian $\mathcal{H}_J$ is not because the transfer of a Cooper pair through the Josephson element induces the transfer of a charge $2e$ through the electromagnetic environment.

In the basis $|S\rangle$, the expression 4.2 of the bare Josephson Hamiltonian is replaced by:

$$\mathcal{H}_J = -\frac{E_J}{2} \sum_n \left(|n+1\rangle \langle n| \otimes \widehat{T}_{2e} + |n\rangle \langle n+1| \otimes \widehat{T}_{2e}^{\dagger} \right). \tag{4.17}$$

where the operator $\hat{T}_{2e}$ is the operator which translates by $2e$ the charge passed through the environment. As described in section 4.1.2, let us introduces the dual basis $|\Psi\rangle$ of $|S\rangle$ with respect to quantum number n:

$$|\Psi\rangle = |\delta\rangle \otimes |E\rangle = \sum_n e^{in\delta} |n\rangle \otimes |E\rangle \,. \tag{4.18}$$

In this basis, the Hamiltonian $\mathcal{H}_J$ writes:

$$\mathcal{H}_J = -\frac{E_J}{2} e^{i\hat{\delta}} \otimes \widehat{T}_{2e} + h.c. \tag{4.19}$$

The translation operator can be written in the dual basis by analogy with the bare Josephson Hamiltonian:

$$\widehat{T}_{2e} = \exp\left(i \frac{2e}{\hbar} \widehat{\Phi}' \right), \tag{4.20}$$

where $\widehat{\Phi}' = \sum_m \widehat{\phi}_m$ is the total flux operator of the environment. The Josephson Hamiltonian in presence of the environment rewrites as:

$$\mathcal{H}_J = -\frac{E_J}{2} \left[e^{i\left(\hat{\delta} + \frac{2e}{\hbar} \sum_m \widehat{\phi}_m \right)} + h.c. \right]. \tag{4.21}$$

And finally, the total Hamiltonian has the following expression:

$$\mathcal{H} = \mathcal{H}_J + \mathcal{H}_{env} = -\frac{E_J}{2} \left[e^{i\left(\hat{\delta} + \frac{2e}{\hbar} \sum_m \widehat{\phi}_m \right)} + h.c. \right] + \sum_k \left(\frac{\widehat{\phi}_k^2}{2L_k} + \frac{Q_k^2}{2C_k} \right). \tag{4.22}$$

Examining this latter expression, one can express several remarks:

• the oscillator fluxes $\widehat{\phi}_m$ are recoupled in the Josephson Hamiltonian through a non-linear term. Unlike for the bare Hamiltonian, the basis $|S\rangle$, composed of the tensorial product

of single oscillator eigenstates, does not diagonalize the total Hamiltonian. A Cooper pair transfer shifts the environment state, which leads to a coupling between states $|S\rangle$ with neighboring n and different environment states. (see Fig. 4.7).

• this structure of Hamiltonian is similar to many other types of Hamiltonians encountered in condensed matter physics [7]. In a more general way, our problem can be mapped on the problem of a particle in a periodic potential interacting with a dissipative bath of harmonic oscillators. The particular case of the restriction to two neighboring charge states, relevant for the previously considered superconducting box problem, leads to the well-known spin-boson Hamiltonian [8].

• the eigenvalues of the total Hamiltonian $\mathcal{H}$, which depend on the external phase δ, form energy bands that have to be calculated.

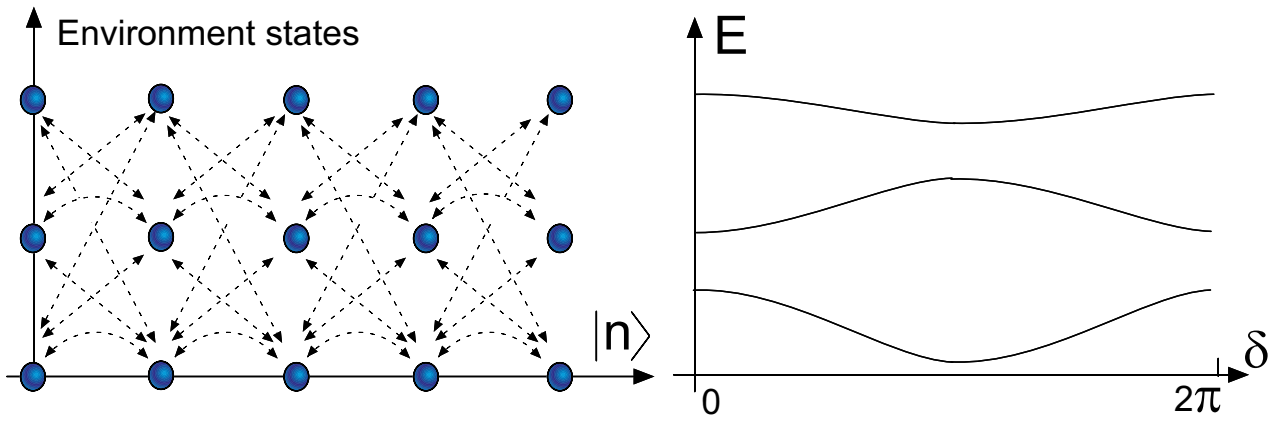

Figure 4.7. Left panel: schematic diagram of the quantum states for the system {Josephson junction + environment}. The Josephson Hamiltonian couples states differing by one Cooper pair transferred through the junction, as indicated by the arrows.
Right panel: sketch of the corresponding energy bands obtained in the phase space δ.

4.2 Perturbational calculation

As a first approach, we treat the effect of the Josephson Hamiltonian in a perturbational way by developing the translation operator $\hat{T}_{2e}$ on the oscillator basis up to the second order in the flux operators $\widehat{\phi}_m$:

$$\hat{T}_{2e} = e^{i\frac{2e\hat{\phi}}{\hbar}} \approx 1 + i\frac{2e}{\hbar}\sum_m \widehat{\phi}_m - \frac{1}{2}\left(\frac{2e}{\hbar}\right)^2 \left(\sum_m \widehat{\phi}_m^2 + \frac{1}{2}\sum_{\substack{l,m \\ l\neq m}} \widehat{\phi}_l\widehat{\phi}_m\right). \tag{4.23}$$

The corresponding perturbational expression $\mathcal{H}_J$ of the Josephson Hamiltonian rewrites as:

$$\mathcal{H}_J \approx -\frac{E_J}{2}e^{i\hat{\delta}} \otimes \left[1 + i\frac{2e}{\hbar}\sum_m \widehat{\phi}_m - \frac{1}{2}\left(\frac{2e}{\hbar}\right)^2 \left(\sum_m \widehat{\phi}_m^2 + \frac{1}{2}\sum_{\substack{l,m \\ l\neq m}} \widehat{\phi}_l\widehat{\phi}_m\right)\right] + h.c. \tag{4.24}$$

According to this latter expression, one can separate the action of the operator $\hat{\delta}$ from those of the operators $\widehat{\phi}_m$ and project $\mathcal{H}_J$ on the eigenvectors $|\delta\rangle$. This defines a perturbational Hamiltonian $\mathcal{H}_{pert}$ function of the eigenvalues δ, written in the residual basis of the environment quantum states $|E\rangle$:

$$\langle\Psi|\mathcal{H}_J|\Psi\rangle = \langle\delta,E|\mathcal{H}_J|\delta,E\rangle \approx \langle E|\mathcal{H}_{pert}(\delta)|E\rangle, \tag{4.25}$$

where

$$\mathcal{H}_{pert}(\delta) = -E_J\left[\cos\delta + i\frac{2e}{\hbar}\sin(\delta)\sum_m \widehat{\phi}_m - \frac{1}{2}\left(\frac{2e}{\hbar}\right)^2\cos(\delta)\left(\sum_m \widehat{\phi}_m^2 + \frac{1}{2}\sum_{\substack{l,m \\ l\neq m}} \widehat{\phi}_l\widehat{\phi}_m\right)\right].$$

The flux operator $\widehat{\phi}_m$ of each harmonic oscillator can be expressed as a function of bosonic creation and annihilation operators, respectively noted $a_m^\dagger$ and a_m :

$$\begin{aligned} \widehat{\phi}_m &= \sqrt{\frac{\hbar\mathcal{Z}_m}{2}}\left(a_m^\dagger + a_m\right) \\ \widehat{\phi}_m^2 &= \frac{\hbar\mathcal{Z}_m}{2}\left(1 + 2N_m + a_m^{\dagger\,2} + a_m^2\right). \end{aligned} \tag{4.26}$$

Neglecting all terms containing a product of two operators, the perturbational Hamiltonian

$\mathcal{H}_{pert}$ writes:

$$\mathcal{H}_{pert}(\delta)= -E_J\cos\delta\times\left[1-\frac{1}{4}\left(\frac{2e}{\hbar}\right)^2\sum_m(1+2N_m)\hbar\mathcal{Z}_m\right]-iE_J\frac{2e}{\hbar}\sin\delta\left[\sum_m\sqrt{\frac{\hbar\mathcal{Z}_m}{2}}\left(a_m^\dagger+a_m\right)\right]. \tag{4.27}$$

The Hamiltonian $\mathcal{H}_{pert}$ couples the ground state to excited states with only one excitation quantum in one mode.

4.2.1 First perturbational correction of the ground state energy

The diagonal part of the perturbational Hamiltonian in the basis $|E\rangle$ gives the energy including corrections of order $E_J\mathcal{Z}_m/R_K$:

$$\langle E|\,\mathcal{H}_{pert}\,(\delta)\,|E\rangle=\langle N_1,..N_m..|\,\mathcal{H}_{pert}\,(\delta)\,|N_1,..,N_m,...\rangle=-E_J\cos\delta\left[1-2\pi\sum_m(1+2N_m)\frac{\mathcal{Z}_m}{R_K}\right]. \tag{4.28}$$

The discrete sum over the oscillators can now be replaced by an integral over the frequency. The correspondence is obtained from Eq. 4.13:

$$\sum_m\mathcal{Z}_m\quad\Leftrightarrow\quad\frac{2}{\pi}\int_0^\infty\frac{\mathrm{Re}\,Z\,(\omega)}{\omega}d\omega. \tag{4.29}$$

Thus, the above expression for the energy writes:

$$\langle\Psi|\,\mathcal{H}_{pert}\,(\delta)\,|\Psi\rangle=-E_J\cos\delta\left[1-4\int_0^\infty\frac{\mathrm{Re}\,Z\,(\omega)}{R_K}(1+2N\,(\omega))\frac{d\omega}{\omega}\right]. \tag{4.30}$$

- For the ground state energy band, this expression reduces to:

$$E_0^{(1)}\,(\delta)=-E_J\left[1-4\frac{M_1}{R_K}\right]\cos\delta, \tag{4.31}$$

where M_1 is the average impedance defined as : $\quad M_1=\int_0^\infty\mathrm{Re}\,Z\,(\omega)\,\frac{d\omega}{\omega}.$ (4.32)

4.2.2 Second order correction

The perturbation theory up to second order for $\mathcal{H}_{pert}\,(\delta)$ provides the following correction of order $E_J^2\mathcal{Z}_m/R_K$ to the energy:

$$E_i^{(2)}\,(\delta)=\sum_{p\neq i}\frac{|\langle E|\,\mathcal{H}_{pert}\,(\delta)\,|E\rangle|^2}{E_i-E_p}. \tag{4.33}$$

• For the ground state energy band, the correction is:

$$\begin{aligned} E_0^{(2)}(\delta) &= -\sum_m \frac{|\langle 1_m| \mathcal{H}_{pert}(\delta) |0_m\rangle|^2}{\hbar\omega_m} \\ &= -8E_J^2 \sin^2\delta \frac{e^2}{h} \int_0^\infty \mathrm{Re}\, Z(\omega) \frac{d\omega}{\hbar\omega^2} \\ &= -8E_J^2 \sin^2\delta \times \frac{M_2}{\hbar R_K}, \end{aligned} \tag{4.34}$$

$$\text{where} \quad M_2 = \int_0^\infty \mathrm{Re}\, Z(\omega) \frac{d\omega}{\omega^2}. \tag{4.35}$$

The integral M_2 has the dimensions of an inductance and can physically be associated to the effective inductance of the environment "seen" by the Josephson junction. Taking this second order correction into account, one obtains for the ground state energy $E_0(\delta)$:

$$E_0(\delta) = E_0^{(1)}(\delta) + E_0^{(2)}(\delta) = -E_J\left(1 - 4\frac{M_1}{R_K}\right)\cos\delta - 8E_J^2\frac{M_2}{\hbar R_K}\sin^2\delta. \tag{4.36}$$

At zero temperature, the current flowing through the junction is obtained from the ground state energy band using the relation:

$$I(\delta) = \frac{1}{\Phi_0}\left(\frac{\partial E_0}{\partial\delta}\right), \tag{4.37}$$

which leads to:

$$I(\delta) = \frac{E_J}{\Phi_0}\left(1 - 4\frac{M_1}{R_K}\right)\sin\delta - 8E_J^2\frac{M_2}{\hbar R_K}\sin 2\delta. \tag{4.38}$$

The whole circuit behaves like an effective Josephson junction but with a modified current-phase relation.

In particular, the critical current (*i.e.* the maximum supercurrent), obtained at $\delta = \frac{\pi}{2}$, is reduced compared to the bare Josephson junction critical current $I_c^0 = E_J/\Phi_0$:

$$I_c = I_c^0\left(1 - 4\frac{M_1}{R_K}\right). \tag{4.39}$$

This reduction can be interpreted as a Coulomb blockade of the DC Josephson effect due to the electromagnetic environment. The latter formula, calculated at the order M_1/R_K, is quantitatively valid in the low-impedance limit defined by :

$$M_1 = \int_0^\infty \mathrm{Re}\left(Z(\omega)\right)\frac{d\omega}{\omega} \ll \frac{R_K}{4} = \frac{h}{(2e)^2}. \tag{4.40}$$

This perturbational approach can be compared with exact numerical calculations in the specific case of a single mode environment (see section 4 – A).

4.3 Variational calculation

The perturbational calculation shows that the electromagnetic environment modifies the current-phase relation of a Josephson junction, but its validity is limited to low series impedances. We propose here a variational approach valid for arbitrary series impedances.

4.3.1 Definition of trial functions

Let us start from the total Hamiltonian given by Expr. 4.22:

$$\mathcal{H} = \mathcal{H}_J + \mathcal{H}_{env} = -\frac{E_J}{2}\left[e^{i\widehat{\delta}}\prod_m e^{i\frac{2e}{\hbar}\widehat{\phi}_m} + h.c.\right] + \sum_p \left(n_p + \frac{1}{2}\right)\hbar\omega_p. \tag{4.41}$$

The first term in the Hamiltonian is a many-body term which is a product of single oscillator displacement operators $e^{i\frac{2e}{\hbar}\widehat{\phi}_m}$. This suggests to use trial functions of the type:

$$\left|\Xi\left(t_m,..\right)\right\rangle = \bigotimes_m \mathcal{D}(t_m)\left|0_m\right\rangle, \tag{4.42}$$

where $\left|0_m\right\rangle$ is the ground state of oscillator m and $\mathcal{D}(t_m)$ is the translation operator of constant t_m, defined by its action on bosonic operators:

$$\mathcal{D}^\dagger(t_m) a_m \mathcal{D}(t_m) = t_m + a_m. \tag{4.43}$$

The variational ground state energy is then obtained by solving the stationarity equations:

$$\frac{\partial\left\langle\Xi\left(t_m,..\right)\right|\mathcal{H}\left|\Xi\left(t_m,..\right)\right\rangle}{\partial t_m} = 0 \qquad \text{and} \qquad \frac{\partial\left\langle\Xi\left(t_m,..\right)\right|\mathcal{H}\left|\Xi\left(t_m,..\right)\right\rangle}{\partial t_m^*} = 0. \tag{4.44}$$

4.3.2 Calculation of $\left\langle\Xi\left(t_{1,..}t_m,..\right)\right|\mathcal{H}_J\left|\Xi\left(t_{1,..}t_m,..\right)\right\rangle$

One has to evaluate:

$$\left\langle\Xi\left(t_m,..\right)\right|\exp\left(\frac{2e}{\hbar}i\hat{\phi}_m\right)\left|\Xi\left(t_m,..\right)\right\rangle = \prod_m \left\langle 0_m\right|\mathcal{D}^\dagger(t_m)\exp\left(\frac{2e}{\hbar}i\hat{\phi}_m\right)\mathcal{D}(t_m)\left|0_m\right\rangle. \tag{4.45}$$

Using:

$$\mathcal{D}^\dagger(t_m)\hat{\phi}_m\mathcal{D}(t_m) = \hat{\phi}_m + \sqrt{\frac{\hbar\mathcal{Z}_m}{2}}\left(t_m^* + t_m\right), \tag{4.46}$$

one first gets:

$$\mathcal{D}^{\dagger}(t_m)\exp\left(\frac{2e}{\hbar}i\hat{\phi}_m\right)\mathcal{D}(t_m)=\exp\left(\frac{2e}{\hbar}i\sqrt{\frac{\hbar\mathcal{Z}_m}{2}}\left(t_m^*+t_m\right)\right)\exp\left(\frac{2e}{\hbar}i\hat{\phi}_m\right), \tag{4.47}$$

thus leading to:

$$\langle 0_m|\exp\left(i\frac{2e}{\hbar}\hat{\phi}_m\right)|0_m\rangle=\langle 0_m|\exp\left(i\frac{2e}{\hbar}\left(a_m^{\dagger}+a_m\right)\right)|0_m\rangle. \tag{4.48}$$

Using Glauber identity [16] : $\exp\left(\alpha a_m^{\dagger}-\alpha^* a_m\right)=\exp-\frac{1}{2}|\alpha|^2\exp\alpha a_m^{\dagger}\exp-\alpha^* a_m$, one finds:

$$\langle 0_m|\exp\left(i\frac{2e}{\hbar}\hat{\phi}_m\right)|0_m\rangle=\exp\left(-\frac{e^2\mathcal{Z}_m}{\hbar}\right)=\exp\left(-\frac{2\pi\mathcal{Z}_m}{R_K}\right). \tag{4.49}$$

The expression (4.45) reduces to:

$$\begin{aligned}\langle\Xi\left(t_m,..\right)|\mathcal{H}_J|\Xi\left(t_m,..\right)\rangle &= \exp\left(-\frac{2\pi}{R_K}\sum_m\mathcal{Z}_m\right)\exp\left(\frac{i2e}{\hbar}\sum_m\sqrt{\frac{\hbar\mathcal{Z}_m}{2}}\left(t_m^*+t_m\right)\right)\\ &= \rho\times e^{i\theta},\end{aligned} \tag{4.50}$$

$$\text{where } \rho \text{ and } \theta \text{ are defined as : } \begin{cases}\rho=\exp\left(-\frac{2\pi}{R_K}\sum_m\mathcal{Z}_m\right)\\ \theta=\frac{4e}{\hbar}\sum_m\sqrt{\frac{\hbar\mathcal{Z}_m}{2}}t_m\end{cases}. \tag{4.51}$$

4.3.3 Calculation of $\langle\Xi\left(t_{1,..}t_m,..\right)|\mathcal{H}_{env}|\Xi\left(t_{1,..}t_m,..\right)\rangle$

The environment energy is directly reduces to:

$$\langle\Xi\left(t_{1,..}t_m,..\right)|\mathcal{H}_{env}|\Xi\left(t_{1,..}t_m,..\right)\rangle = \sum_m\hbar\omega_m\langle 0_m|\mathcal{D}^{\dagger}(t_m)\left(\hat{n}_m+\frac{1}{2}\right)\mathcal{D}(t_m)|0_m\rangle \tag{4.52}$$

$$= \sum_m\hbar\omega_m t_m^* t_m. \tag{4.53}$$

4.3.4 Variational solutions

Associating Eqs. 4.50 and 4.53, we obtain the average value of the total Hamiltonian:

$$\langle \Xi(t_{1,..}t_m,..)|\,\mathcal{H}\,|\Xi(t_{1,..}t_m,..)\rangle = \sum_m \hbar\omega_m t_m^* t_m - E_J \exp\left(-\frac{2\pi}{R_K}\sum_m \mathcal{Z}_m\right)\times \cos\left[\delta + \frac{2e}{\hbar}\sum_m \sqrt{\frac{\hbar\mathcal{Z}_m}{2}}\,(t_m^* + t_m)\right] \quad (4.54)$$

$$= \sum_m \hbar\omega_m t_m^* t_m - E_J \rho\cos[\delta+\theta]\,. \quad (4.55)$$

The variational equations 4.44 lead to:

$$\begin{cases} t_m^* = t_m \qquad (t_m \text{ is a real variable}) \\ \hbar\omega_m t_m = -E_J\left(\frac{2e}{\hbar}\sqrt{\frac{\hbar\mathcal{Z}_m}{2}}\right)\exp\left(-\frac{2\pi}{R_K}\sum_n \mathcal{Z}_n\right)\sin\left(\delta + \frac{4e}{\hbar}\sum_n\sqrt{\frac{\hbar\mathcal{Z}_n}{2}}t_n\right). \end{cases} \quad (4.56)$$

Using Eq. 4.51, we find:

$$\forall m \quad \text{integer}, \qquad \hbar\omega_m t_m = -E_J\left(\frac{2e}{\hbar}\sum_n\sqrt{\frac{\hbar\mathcal{Z}_n}{2}}\right)\rho\sin(\delta+\theta)\,. \quad (4.57)$$

By summing over m, one finally obtains the self-consistency equation obeyed by θ :

$$\theta = -\frac{8\pi E_J}{R_K}\left(\sum_m \frac{\mathcal{Z}_m}{\hbar\omega_m}\right)\rho\sin(\delta+\theta)\,. \quad (4.58)$$

Passing to the limit $\Delta\omega \to 0$ using the transformation given in 4.29, one obtains :

$$\begin{cases} \theta = -\kappa\sin(\delta+\theta) \\ \text{with} \\ \kappa = \frac{16E_J}{\hbar R_K}\rho\left(\int_0^\infty \frac{\mathrm{Re}[Z(\omega)]}{\omega^2}d\omega\right) = \frac{16E_J}{\hbar R_K}M_2\exp\left(-4\frac{M_1}{R_K}\right), \end{cases} \quad (4.59)$$

where M_1 and M_2 are defined as in Eqs. 4.32 and 4.35.

The fundamental energy band $E_0(\delta)$ is finally obtained by rewriting the energy given by expression 4.54:

$$E_0(\delta) = -E_J\exp\left(-4\frac{M_1}{R_K}\right)\cos(\delta+\theta) + \frac{8E_J^2 M_2}{\hbar R_K}\exp\left(-8\frac{M_1}{R_K}\right)\sin^2(\delta+\theta)\,. \quad (4.60)$$

where θ satisfies the self-consistent equation (4.59).

4.3.5 Comparison with the perturbational theory

The energy band $E_0(\delta)$ has a similar structure as obtained in the perturbational case. However the expression 4.60 differs from the perturbational result 4.36:

- The renormalization factors are now exponential terms containing all powers of $\frac{M_1}{R_K}$.

• The phase arguments are now given by the sum $(\delta + \theta(\delta))$ in place of δ. Since $\theta(\delta)$ is a non-linear function of δ, the current-phase relation now contains all harmonics in δ.

More precisely, one can check that the perturbational approach corresponds to a limit case of the variational calculation, for a **low impedance environment**.

In this limit, both integrals M_1 and $\frac{E_J}{\hbar}M_2$ are small compared to the "superconducting" resistance quantum $h/(2e)^2 = R_K/4$:

$$\begin{cases} M_1 \ll R_K/4 \\ \frac{E_J}{\hbar}M_2 \ll R_K/4 \end{cases} . \tag{4.61}$$

Since the parameter κ is also small, the self-consistent equation (4.59) is straightforwardly solved:

$$\theta = -\kappa \sin\delta \ , \tag{4.62}$$

thus leading to the ground state energy:

$$E_0(\delta) \approx -E_J \exp\left(-4\frac{M_1}{R_K}\right)\cos\left[\delta - \kappa\sin\delta\right] + \frac{8E_J^2 M_2}{\hbar R_K}\exp\left(-8\frac{M_1}{R_K}\right)\sin^2\left[\delta - \kappa\sin\delta\right]. \tag{4.63}$$

We now perform an expansion of $E_0(\delta)$ retaining the lowest order terms in M_1 and M_2:

$$\begin{aligned} E_0(\delta) &\approx -E_J\left(1-4\frac{M_1}{R_K}\right)\cos\delta - E_J\left(1-4\frac{M_1}{R_K}\right)\kappa\sin^2\delta + \frac{8E_J^2}{\hbar R_K}M_2\left(1-8\frac{M_1}{R_K}\right)\sin^2\delta \\ &\approx -E_J\left(1-4\frac{M_1}{R_K}\right)\cos\delta - \frac{8E_J^2}{\hbar R_K}M_2\sin^2\delta. \end{aligned} \tag{4.64}$$

which coincides with Expression. 4.60 obtained using perturbation theory.

4.3.6 Comparison with the classical limit

It is instructive to compare the variational equations 4.59 to the equations one would obtain at equilibrium for the same Hamiltonian 4.22, but with the operators $\hat{\phi}_k$ replaced by classical variables ϕ_k.

The Hamilton-Jacobi equations $\frac{\partial\mathcal{H}}{\partial\phi_k} = 0$ write:

$$\phi_k = -4\pi e\frac{E_J}{h}\sin\left[\delta + \sum_m \frac{2e}{\hbar}\phi_m\right]L_k. \tag{4.65}$$

Summing over k this latter equation leads to:

$$\sum_k \frac{2e}{\hbar}\phi_k = -8\pi\frac{E_J}{R_K}\sin\left[\delta + \sum_m \frac{2e}{\hbar}\phi_m\right]\left(\sum_k L_k\right). \tag{4.66}$$

One thus obtains the self-consistent equation :

$$\begin{cases} \theta = -8\pi \frac{E_J}{R_K} L_{eff} \sin\left[\delta + \theta\right] \\ \text{with :} \quad L_{eff} = \sum_k L_k \\ \text{and :} \quad \theta = \sum_k \frac{2e}{\hbar} \phi_k \end{cases} \tag{4.67}$$

This equation is similar to the variational equation (Eq. 4.59) but with the restriction $\rho = 1$.

One can draw from this latter comparison several remarks:

• There is a perfect agreement between the classical and the variational treatment of the total Hamiltonian assuming that the reduced parameter ρ is set to 1.

• All quantum effects in the variational treatment are thus contained in the factor $\rho < 1$. The non-commutation of position-like and momentum-like variables leads to the factor ρ in the Glauber formula .

The variational method used here appears as a semi-classical method which takes into account single oscillator quantum correlations.

4.3.7 Solutions of the self-consistent equation

The self-consistent Equation 4.59 relating θ to the external phase δ can be numerically solved as a function of the parameter κ defined in Eq. 4.59. The value $\kappa = 1$ separates two domains for the solution $\theta(\delta)$:

• $\kappa < 1$

The resolution of the equation for $\kappa \ll 1$ has already been given in Eq. 4.62. In this regime, the phase $\theta = -\kappa \sin\delta$ is proportional to κ. As the parameter κ increases, the curve $\theta(\delta)$ progressively deviates from a sine function. In particular, the curvature $\frac{\partial^2\theta}{\partial\delta^2}$ at $\theta = \pi$ (mod. 2π) increases and diverges when κ reaches 1 (see Fig. 4.8, top panel). Correlatively, the fundamental energy band, which has an harmonic dependence in the perturbational case $\kappa \ll 1$, develops a cusp-like maximum at $\delta = \pi$ (see Fig. 4.8, bottom panel).

• $\kappa > 1$

$\theta(\delta)$ is no longer a continuous function. It has a saw-tooth dependence with periodic jumps at $\delta = \pi + 2p\pi$ (p integer). The ground state energy band presents cusps (see Fig. 4.8, bottom panel) where its derivative is discontinuous. The supercurrent through the junction

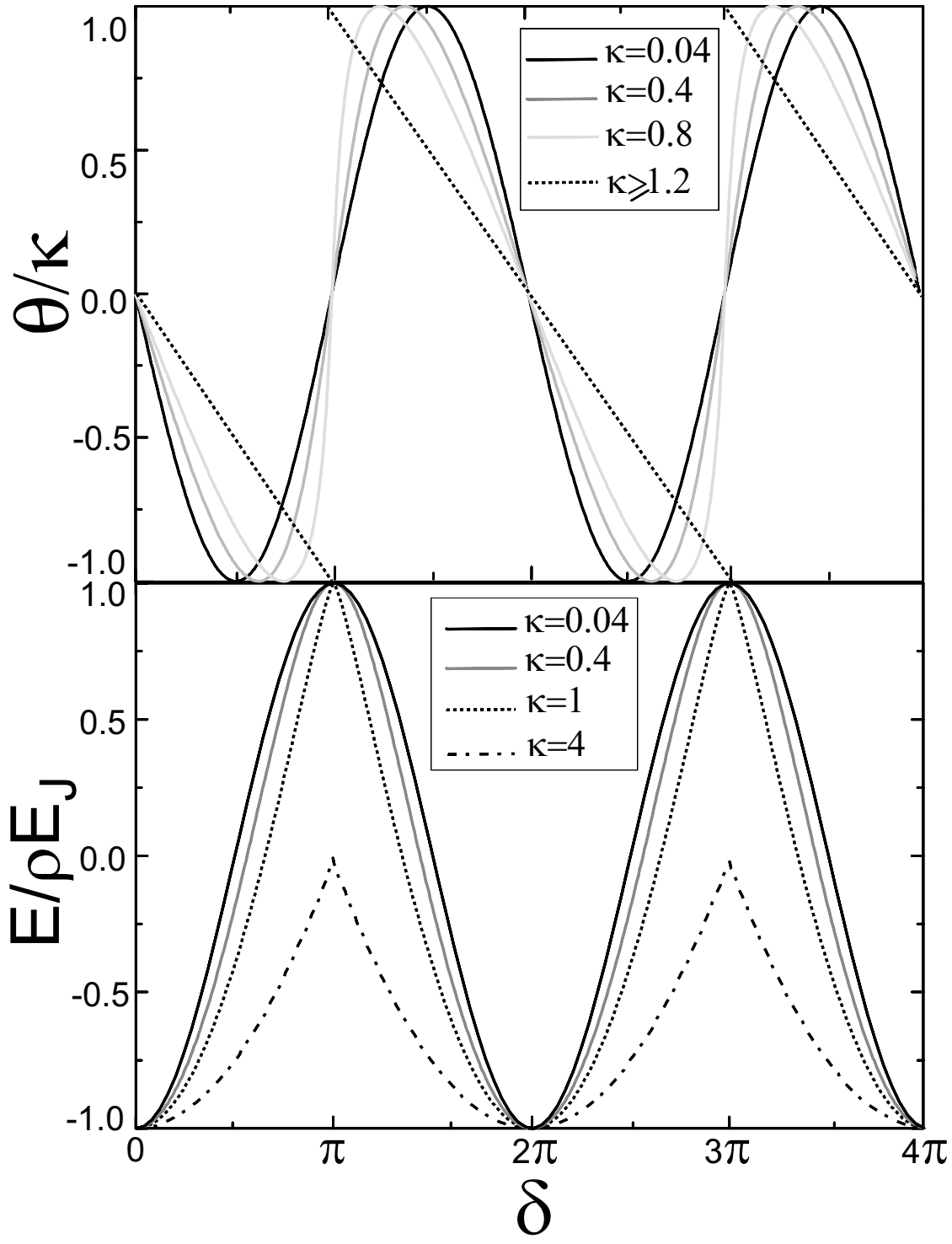

Figure 4.8. Top panel: solutions of the self consistent equation $\theta = -\kappa \sin(\theta + \delta)$ *for different values of the parameter* κ*. The value* $\kappa = 1$ *defines a threshold between a domain for which* $\theta(\delta)$ *is a continous funtion and a domain for which* $\theta(\delta)$ *switches at* $\delta = \pi \pmod{2\pi}$*. Bottom panel: reduced ground state energy* $E(\delta)/\rho E_J$ *for different values of the parameter* κ*.*

is thus also a discontinuous function of δ at these points.

The threshold $\kappa = 1$ defines a transition point between a domain in which the supercurrent $I(\delta)$ is continuous (for $\kappa < 1$), and a domain in which it is not (for $\kappa > 1$). The physical meaning of the transition will discussed in appendix 4−A, in the case of an impedance reduced to a single LC oscillator.

4.3.8 Expression of the supercurrent at zero temperature

At zero temperature, the expression 4.37 of the current, calculated using 4.59 and 4.60, leads to:

$$I_{(T=0)} = \frac{E_J^\star}{\Phi_0} \sin\left(\delta + \theta\left(\delta\right)\right), \tag{4.68}$$

where $E_J^\star = E_J \exp\left(-4\frac{M_1}{R_K}\right)$ can be interpreted as a renormalized Josephson coupling energy.

In the case $\kappa < 1$, the critical current is given by:

$$I_c = I_c^0 \exp\left(-4\frac{M_1}{R_K}\right). \tag{4.69}$$

Compared to the case of a bare junction, **the critical current is exponentially reduced by the flux quantum fluctuations of the environment modes**. This result extends the perturbational expansion (4.39) previously obtained. It predicts the existence of an environmental Coulomb blockade of the DC Josephson effect. This effect is the analogous for Josephson junctions to the Coulomb blockade of the conductance for normal-metal tunnel junctions.

In the case $\kappa > 1$, the critical current is given by $\lim_{\delta \to \pi^-} I_{(T=0)}$, where $I_{(T=0)}$ is given by expression 4.68.

4.3.9 Expression of the supercurrent at finite temperature

The variational method can be readily extended at finite temperatures in the case of an environment with a discrete spectrum. The different energy bands can then be indexed by an integer n, and the average supercurrent is given by a Boltzmann average of the supercurrents $I_n(\delta)$ carried by the excited states n:

$$\bar{I}(T,\delta) = \sum_n P_n I_n(\delta) = \sum_n \frac{P_n}{\Phi_0}\left(\frac{\partial E_n}{\partial \delta}\right), \tag{4.70}$$

where the P_n are normalized Boltzmann factors:

$$P_n = \frac{e^{-\frac{E_n}{k_B T}}}{\sum_m e^{-\frac{E_m}{k_B T}}}. \tag{4.71}$$

At temperatures such that $T \ll \min\left[E_1(\delta) - E_0(\delta)\right]/k_B$, the ground state contribution to the current is dominant. At higher temperatures, the contributions of the excited states contribute to the average current and tend to decrease it (see Fig. 4.9). Note that at a given phase δ, the signs of the currents carried by successive states can be different. This situation is reminiscent of the permanent currents carried by single electron states in small normal metal rings [10].

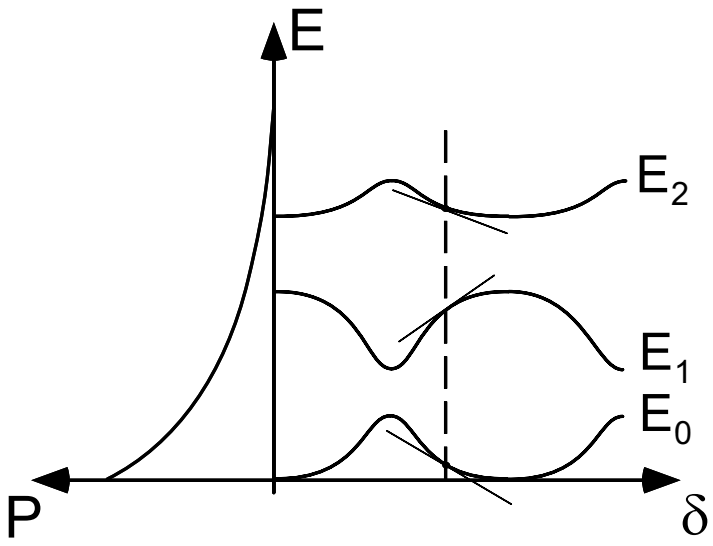

Figure 4.9. Left: Boltzmann statistics $P(E)$ at finite temperature T.
Right: schematic diagram of the energy bands participating to the global supercurrent through the Josephson junction. At finite temperature T, the average supercurrent through the junction results from the thermal average $\frac{1}{\Phi_0}\sum_i P(E_i)\,\partial E_i/\partial\delta$ of supercurrents $\frac{1}{\Phi_0}\partial E_i/\partial\delta$ associated to each band.

4.3.10 Comparison with the renormalization group approach

We have compared our predictions with those of Hekking *et al.* [11] derived using a renormalization group (RG) approach, for a particular environment.

They consider a Josephson junction connected to a thin superconducting loop. The electromagnetic environment states are plasmon modes propagating along the loop. The corresponding impedance spectrum consists of a series of Dirac peaks at harmonics of the fundamental

resonance frequency ω_0 with weight R/ω_0, up to a cut-off frequency Ω_M (see Fig. 4.10).

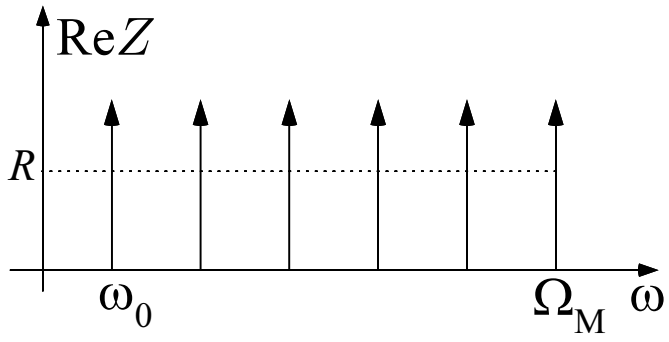

Figure 4.10. Real part of the environment impedance considered by Hekking et al. It consists of a series of Dirac peaks, beginning at frequency ω_0 up to a cut-off frequency Ω_M . The average effective value is $R_K/4g$.

They find that the junction still behaves as an effective Josephson junction. However, its associated Josephson energy $\widetilde{E}_J$ is renormalized by the electromagnetic environment with respect to the bare energy E_J^0. Two renormalization regimes occur depending on the value of the dimensionless parameter $g = R_K/4R$ with respect to 1:

- $g < 1$

$$\widetilde{E}_J = E_J^0 \left(\frac{\omega_0}{\Omega_M}\right)^{\frac{1}{g}} \tag{4.72}$$

- $g > 1$

$$\widetilde{E}_J = E_J^0 \left(\frac{E_J^0}{\Omega_M}\right)^{\frac{1}{g-1}} \tag{4.73}$$

Similar results can be also derived within the framework of our variational approach as discussed in the following.

We first calculate the renormalized Josephson energy $E_J^\star$ given by equation 4.68 in the case of the electromagnetic environment considered by Hekking *et al.* By replacing $\mathrm{Re}\left[Z\left(\omega\right)\right]$ by its average value $R_K/4g$, we obtain:

$$E_J^\star = E_J^0 \exp\left(-\frac{4}{R_K}\int_0^\infty \frac{\mathrm{Re}\left[Z\left(\omega\right)\right]}{\omega}d\omega\right) \approx E_J^0 \exp\left(-\frac{4}{R_K}\int_{\omega_0}^{\Omega_M} \frac{R_K/4g}{\omega}d\omega\right), \tag{4.74}$$

which leads to:

$$E_J^\star \approx E_J^0 \exp\left(-\frac{1}{g}\ln\left(\frac{\Omega_M}{\omega_0}\right)\right) = E_J^0 \left(\frac{\omega_0}{\Omega_M}\right)^{\frac{1}{g}}. \tag{4.75}$$

This result coincides with the prediction for $\widetilde{E}_J$ in the case $g < 1$.

If the renormalized energy $E_J^\star$ is larger than $\hbar\omega_0$, the expression 4.74 needs to be modified because the low frequency oscillators do not contribute in fact to the renormalization. This effect is similar to the "slave boson" effect in the spin-boson problem [12]. The low frequency cut-off ω_0 has to be replaced in this case by $E_J^\star/\hbar$. The renormalized Josephson energy $E_J^\star$ is then:

$$E_J^\star = E_J^0 \exp\left(-\frac{4}{R_K}\int_{E_J^\star/\hbar}^{\Omega_M} \frac{\mathrm{Re}\left[Z\left(\omega\right)\right]}{\omega} d\omega\right) \approx E_J^0 \left(\frac{E_J^\star}{\Omega_M}\right)^{\frac{1}{g}}, \tag{4.76}$$

which leads to:

$$E_J^\star = E_J^0 \left(\frac{E_J^0}{\Omega_M}\right)^{\frac{1}{g-1}}. \tag{4.77}$$

This result coincides with the prediction for $\widetilde{E}_J$ obtained by Hekking *et al.* in the case $g > 1$. Although both approaches lead to similar results, the value $g = 1$ does not appear as a transition point in our model.

4.4 Case of a Josephson junction coupled to a single mode oscillator

Our predictions obtained using both perturbational and variational approaches can be tested in a case in which an exact numerical calculation of the energy bands can be performed. For that purpose, we have considered an electromagnetic environment consisting of a single-mode oscillator. The system can be thus modeled as a bare Josephson junction in series with a single LC oscillator (see Fig. 4.11, right panel).

Let us mention that this basic circuit corresponds to the well defined experimental situation of RF-SQUIDs [13]. This circuit can represent a superconducting loop interrupted by a single Josephson junction. The loop plays the role of an inductor with effective inductance L, while the electrodes facing each other at the junction can be associated to an effective capacitance C (see Fig. 4.11, left panel). The externally applied magnetic flux Φ_{ext} provides the phase bias, and the observed variable is the inner magnetic flux Φ_{int}. The loop behaves then as a "**fluxon box**" since it can store and deliver flux quanta one by one. Such an experiment is strictly the **dual equivalent of the single Cooper pair box** experiment presented in

chapter 2, the charge being replaced by it conjugate variable. Quantum effects have indeed already been observed in RF-SQUIDs with large Josephson junctions [14] and in the case of YBaCuO superconducting rings presenting weak links [15].

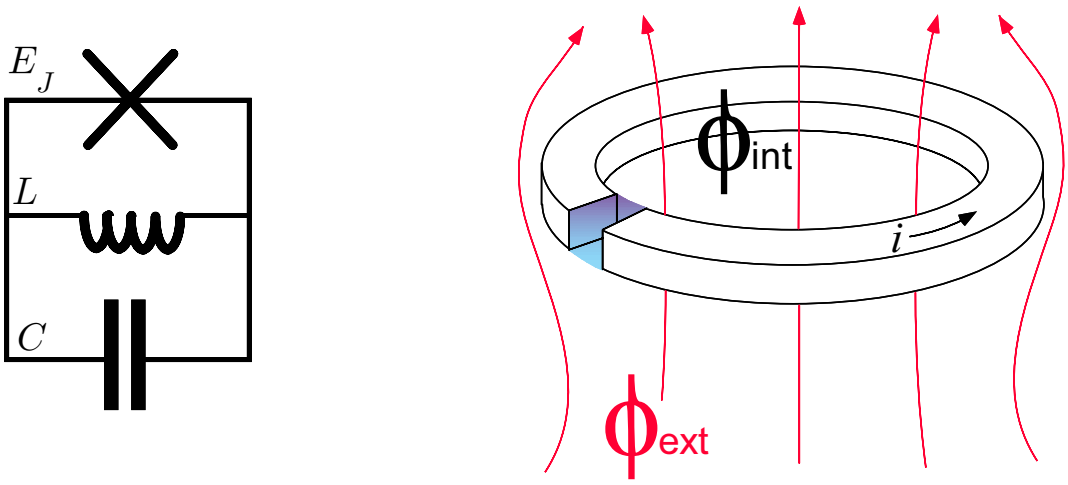

Figure 4.11. Left: schematic diagram of a phase biased Josephson junction coupled to a single-mode oscillator.
Right: sketch of the corresponding experimental circuit which consists of a superconducting loop interrupted by a Josephson junction. The phase bias is provided by an externally applied magnetic flux Φ_{ext}. The inner flux Φ_{int} differs from Φ_{ext} due to the superconducting screening current around the loop.

4.4.1 Hamiltonian description of a Josephson junction coupled to a LC oscillator

The Hamiltonian 4.22 reduces to:

$$H(\delta) = \frac{Q^2}{2C} + \frac{\Phi_{int}^2}{2L} - E_J \cos\left(\frac{2\pi\Phi_{int}}{\Phi_0} + \delta\right), \tag{4.78}$$

where $\delta = 2\pi\Phi_{ext}/\Phi_0$ is the phase bias imposed by an applied external flux Φ_{ext}.

This Hamiltonian involves three characteristic energies:

- the bare Josephson coupling energy E_J
- the inductive energy E_L characterizing the energy of a fluxon Φ_0 entering the loop:

$$E_L = \frac{\Phi_0^2}{2L} = \frac{h^2}{8Le^2} \tag{4.79}$$

- the charging energy E_c of the junction:

$$E_c = \frac{e^2}{2C} \tag{4.80}$$

According to these notations, the Hamiltonian writes:

$$H(\delta) = E_c \left(\frac{Q}{e}\right)^2 + E_L \left(\frac{\Phi_{int}}{\Phi_0}\right)^2 - E_J \cos\left(\frac{2\pi\Phi_{int}}{\Phi_0} + \delta\right). \tag{4.81}$$

Since Q and Φ are conjugated variables, this Hamiltonian can be interpreted as the Hamiltonian of a particle with position $2\pi\Phi_{int}/\Phi_0$ and mass $C\left(\Phi_0/2\pi\right)^2$ placed in a parabolic corrugated potential $\mathcal{V}\left(\Phi_{ext}, \Phi\right)$ (see Fig. 4.12) given by:

$$\mathcal{V}\left(\Phi_{ext}, \Phi_{int}\right) = E_L \left(\frac{\Phi_{int}}{\Phi_0}\right)^2 - E_J \cos\left(\frac{2\pi\left(\Phi_{int} + \Phi_{ext}\right)}{\Phi_0}\right). \tag{4.82}$$

This potential $\mathcal{V}\left(\Phi_{ext}, \Phi\right)$, plotted in two different cases, together with the position of its absolute minimum and the ground state wave function, is sketched in Fig. 4.12 for various values of Φ_{ext}.

4.4.2 Hamiltonian matrix elements in the harmonic oscillator basis

Expressed in the basis $|n\rangle$ of the harmonic oscillator, the matrix elements of the Hamiltonian are:

$$\begin{aligned} H_{nm}(\delta) &= \langle n| H(\delta) |m\rangle = (n + \frac{1}{2})\hbar\Omega_0\delta_{nm} - E_J \langle n| \cos\left(\frac{2\pi\Phi_{ext}}{\Phi_0} + \delta\right) |m\rangle \\ &= (n + \frac{1}{2})\hbar\Omega_0\delta_{nm} - \frac{E_J}{2} \langle n| e^{i\gamma\left(\hat{a}+\hat{a}^\dagger\right)+\delta} + h.c. |m\rangle, \end{aligned} \tag{4.83}$$

where $\gamma^2 = \frac{4\pi e^2}{h}\sqrt{\frac{L}{C}} = 4\pi Z/R_K$ and $\hat{a}$ (respectively. $\hat{a}^\dagger$) are the annihilation (respectively. creation) operators.

Using Glauber identity [16], one finds for the unitary translation operator $\hat{T}$:

$$\widehat{T} = e^{i\gamma\left(\hat{a}+\hat{a}^\dagger\right)} = e^{-\gamma^2/2} e^{-i\gamma\hat{a}^\dagger} e^{i\gamma\hat{a}}, \tag{4.84}$$

which implies for its matrix elements $\hat{T}_{nm}$:

$$\hat{T}_{nm} = \langle n| \widehat{T} |m\rangle = e^{-\gamma^2/2} \left\langle e^{-i\gamma\hat{a}} n\right| e^{i\gamma\hat{a}} m\rangle. \tag{4.85}$$

Each part of the bracket can be developed using a coherent state expansion [16] :

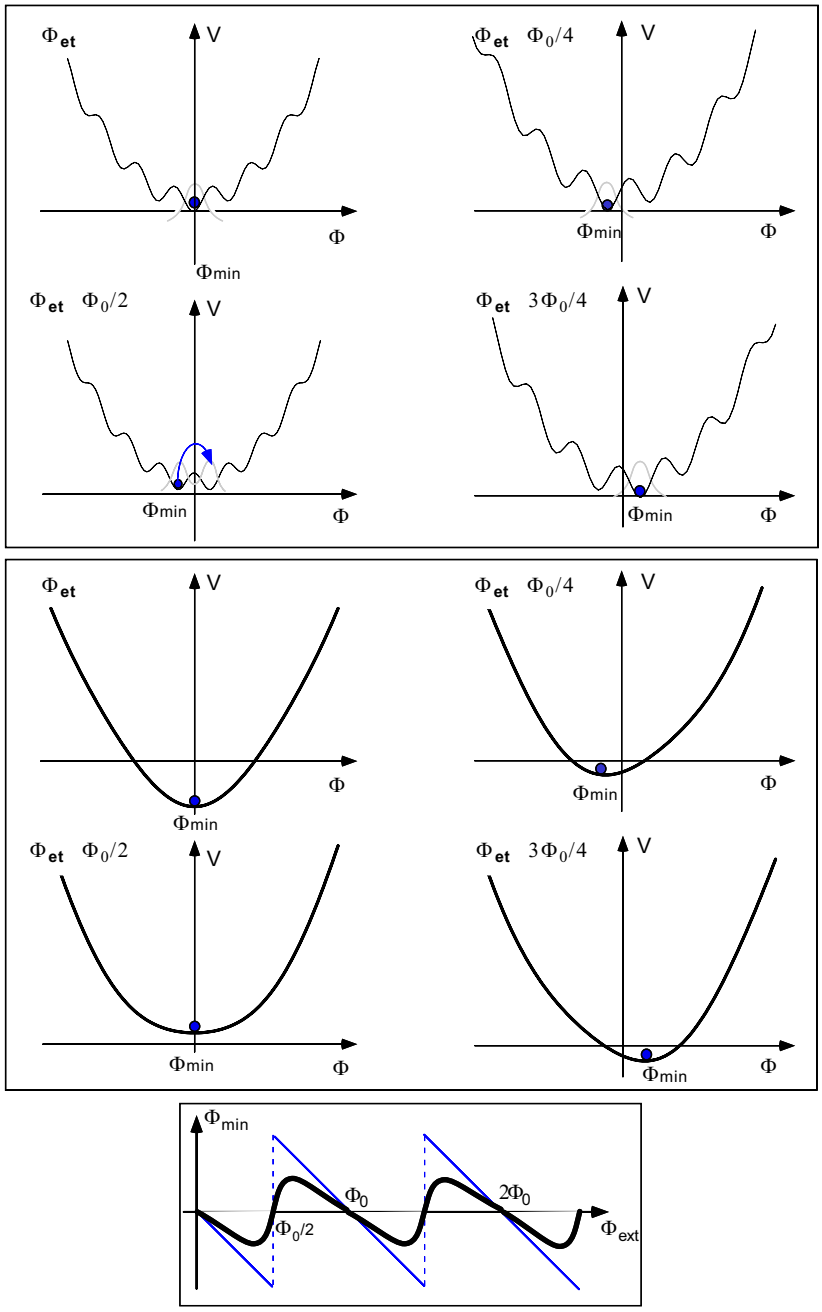

Figure 4.12. Potential $V(\Phi, \Phi_{ext})$ for different bias fluxes Φ_{ext} plotted for the domains $E_J > E_L/2\pi^2$ (top panel), and $E_J < E_L/2\pi^2$ (middle panel). Ground state quantum wave-functions are sketched by a gray curve whereas classical equilibrium solutions are symbolized by black dots. Its dependence with the bias flux $\Phi_{est.}$, (thin line for large E_J, thick line for small E_J) is represented in bottom panel.

$$\begin{cases} e^{i\gamma\hat{a}}\left|m\right\rangle = \sum_k \frac{(i\gamma)^k}{k!}\hat{a}^k\left|m\right\rangle \\ \text{where :} \\ \hat{a}^k\left|m\right\rangle = \sqrt{\frac{n!}{(n-k)!}}\left|m-k\right\rangle \end{cases} . \tag{4.86}$$

The element $\hat{T}_{nm}$ rewrites as:

$$\hat{T}_{nm} = e^{-4\pi Z/R_K} \sum_{k=0}^{Inf(m,n)} \frac{(-1)^k (i\gamma)^{n+m-2k}\sqrt{n!\,m!}}{k!\,(n-k)!\,(m-k)!}. \tag{4.87}$$

The matrix elements h_{mn} of the reduced Hamiltonian $\mathcal{H}/\hbar\Omega_0$ are then given by:

$$h_{nm}(\delta) = \frac{1}{\hbar\Omega_0}\left\langle n\right| H(\delta)\left|m\right\rangle = (n+\frac{1}{2})\delta_{mn} - \frac{e_J}{2}\left[\hat{T}_{nm}e^{i\delta} + \hat{T}^{\dagger}_{nm}e^{-i\delta}\right], \tag{4.88}$$

where e_J is the reduced Josephson energy: $E_J/\hbar\Omega_0$.

4.4.3 Computational procedures

We have numerically determined the eigenstates and eigenvalues of the restriction of the Hamiltonian to the subspace S_D of dimension D spanned by the states $(\left|n\right\rangle)_{n<D}$. This dimension D has to be chosen in order to give reliable results without leading to too time-consuming computations.

Actually, one can evaluate the minimum dimension required to obtain a correct description of the ground state energy band $\mathrm{E}_0(\delta)$: it is necessary that the linear combination of oscillators states for the shifted state $\hat{T}\left|0\right\rangle$ is a state of the subspace S_D up to a good accuracy. As can be seen in Fig. 4.13, the value of the modulus of $\hat{T}_{0n}$ is negligible for values of n larger than twice the value n_t for which the modulus is maximum. Therefore one should have:

$$D \gtrapprox 2 \times n_t. \tag{4.89}$$

One can obtain an estimate of n_t by noting that a Cooper pair which tunnels through the junction increases the environment energy by a quantity equal the charging energy of the junction $E_c = (2e)^2/2C$. The maximum value for $\left|\hat{T}_{0n}\right|^2$ is obtained when the energy of the oscillator state matches E_c. The value of n_t thus satisfies:

$$\left(n_t + \frac{1}{2}\right)\hbar\Omega_0 \approx (2e)^2/2C\ . \tag{4.90}$$

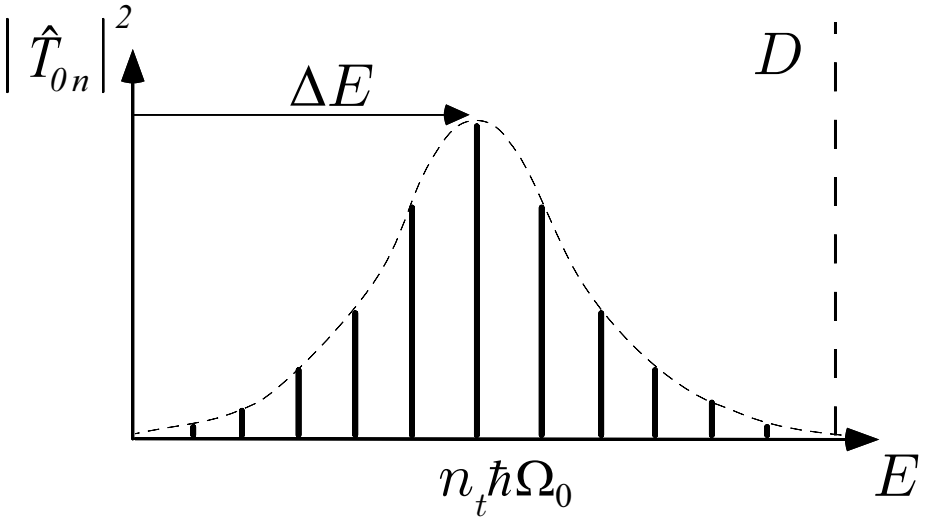

Figure 4.13. Square modulus of the components $\left|\widehat{T}_{0n}\right|^2$ *of the vector* $\widehat{T}\,|0\rangle$ *as a function of the associated oscillator energies* $n\hbar\Omega_0$

The two relations 4.89 and 4.90 determines the minimal dimension $D_{\min}$:

$$D_{\min} = \frac{8\pi}{R_K}\sqrt{\frac{L}{C}}\ . \tag{4.91}$$

We have checked that the numerically obtained eigenenergies remained unchanged when the dimension D was increased well above this limit.

4.4.4 Control of the results

We have checked that the numerical results obtained in the low-impedance limit are in agreement with the perturbational results. In the case of a single mode environment, both parameters M_1 and M_2 defined in Eqs. 4.32 and 4.35 can be exactly calculated :

$$\begin{cases} M_1 = \frac{\pi}{2}\sqrt{\frac{L}{C}} \\ \\ M_2 = \frac{\pi}{2}L \end{cases}\ . \tag{4.92}$$

The expression 4.36 of the ground state energy band reads:

$$\begin{aligned} E_0(\delta) &= E_0^{(1)}(\delta) + E_0^{(2)}(\delta) \\ \text{with}\quad E_0^{(1)}(\delta) &= -E_J\left(1 - \frac{2\pi}{R_K}\sqrt{\frac{L}{C}}\right)\cos\delta \\ \text{and}\quad E_0^{(2)}(\delta) &= -E_J^2\frac{4\pi L}{\hbar R_K}\sin^2\delta. \end{aligned} \tag{4.93}$$

Similarly, a generalization of the previous perturbational calculation gives for the energy $E_p(\delta)$ of the p^{th} excited state:

$$\begin{aligned} E_p(\delta) &= E_p^{(1)}(\delta) + E_p^{(2)}(\delta) \\ \text{with} \quad E_p^{(1)}(\delta) &= -E_J\left(1 - \frac{2\pi}{R_K}(1+2p)\sqrt{\frac{L}{C}}\right)\cos\delta \\ \text{and} \quad E_p^{(2)}(\delta) &= -E_J^2\frac{4\pi L}{\hbar R_K}\sin^2\delta, \end{aligned} \tag{4.94}$$

which leads to the reduced energy $E_p(\delta)/\hbar\Omega_0$:

$$E_p(\delta)/\hbar\Omega_0 = (p+\frac{1}{2}) - e_J\left[1 - 2\pi z(1+2p)\right]\cos\delta - 4\pi z e_J^2\sin^2\delta, \tag{4.95}$$

where $e_J = E_J/\hbar\Omega_0$ is the reduced Josephson energy and $z = \sqrt{\frac{L}{C}}/R_K$ the reduced environment impedance. The bands have a first order correction that preserves the harmonic dependence upon the phase and an anharmonic second order correction which does not depend on the band index p. This latter expression can be directly compared to the numerical results for a given set of environment variables. The comparison for the ground state and the first excited state energies is shown in Fig. 4.14 in a specific case. This comparison illustrates the good agreement obtained in the perturbational regime.

4.4.5 Comparison with the variational approach

In the case of a single mode environment, the variational prediction Eq. 4.60 for the ground state energy reduces to:

$$\begin{aligned} E_0(\delta) &= -E_J\exp\left(-\frac{2\pi}{R_K}\sqrt{\frac{L}{C}}\right)\cos(\theta+\delta) + \frac{8\pi E_J^2 L}{\hbar R_K}\exp\left(-\frac{4\pi}{R_K}\sqrt{\frac{L}{C}}\right)\sin^2(\theta+\delta), \\ \text{with} \quad &: \quad \theta = -\kappa\sin(\theta+\delta) \quad \text{and} \quad \kappa = \frac{8\pi E_J L}{\hbar R_K}\exp\left(-\frac{2\pi}{R_K}\sqrt{\frac{L}{C}}\right). \end{aligned} \tag{4.96}$$

We have checked that variational solutions are in good agreement with the numerical results for $\kappa < 1$ as well as for $\kappa > 1$. The comparison for the ground state and the first excited state energies is shown in Fig. 4.14 for the value $\kappa = 22$. A good agreement is obtained for all values of the parameters. Let us note however that the variational approach always predicts a zero gap level crossing at $\delta = \pi/2$ (mod. π) for $\kappa > 1$, whereas the exact numerical results show a residual gap.

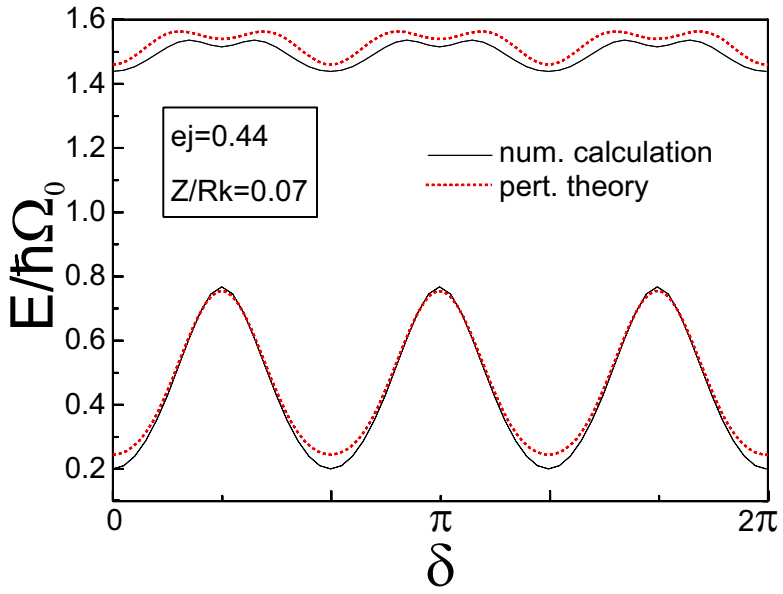

Figure 4.14. Comparison of ground state and first excited state energy bands obtained using the perturbational approach (dashed lines) and numerical calculations (solid lines) in the case of a Josephson junction with $E_J = 0.44\hbar\Omega_0$ connected to a low impedance environment $Z/R_K = 0.07$.

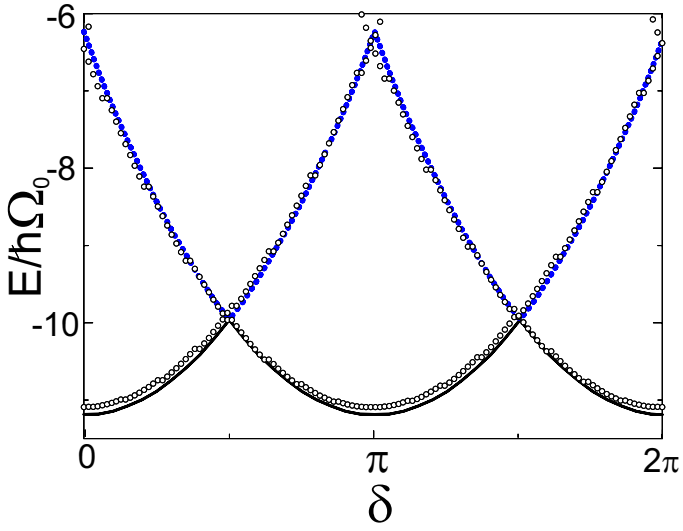

Figure 4.15. Comparison of ground state and first excited state energy bands obtained using the variational method (open dots) with the numerical calculations (black curve and solid dots). The parameters are: $E_J = 15\hbar\Omega_0$ and $Z = 4220\Omega = R_K/4$, leading to $\kappa = 22$.

4.4.6 Phase transition induced by quantum fluctuations

The discussion of the variational solutions has shown that the value $\kappa = 1$ separates solutions $\theta(\delta)$ with different behaviors. More precisely, the relation $\kappa = 1$ determines a transition line in the parameter space $(E_J/E_L,\ E_J/E_c)$, as seen in Fig. 4.17. The solution $\theta(\delta)$ of the self-consistent equation is either continuous (for $\kappa < 1$) or discontinuous (for $\kappa \geqslant 1$). This phenomenon is furthermore confirmed by the numerical calculation although the observed transition is not as sharp. Its has a clear physical interpretation in terms of the magnetic response of a RF-SQUID:

- For $\kappa > 1$, The variations of Φ_{int} with the external flux Φ_{ext} follow a discontinuous staircase-shaped curve with jumps. A single flux quantum enters the loop when the magnetic energy of the two configurations separated by one quantum are equal (see Fig. 4.16, top panel). The inner flux Φ_{int} follows then a "Faraday staircase" function (see Fig. 4.16, middle panel), which is the dual of the "Coulomb staircase" of the single Cooper pair box at small values of E_J/E_c (see previous chapter). In this regime, the circuit behaves as a "single fluxon box ". This perfect quantization is due to a screening supercurrent which follows a saw-tooth function (see Fig. 4.16, bottom panel). The jumps in the screening current occur when the current reaches the critical current. A map of iso-critical current lines (I_c/I_c^0) in the parameter space is shown in Fig. 4.18.

- For $\kappa < 1$, the Faraday staircase is not as sharp as in the previous case and Φ_{int} is a continuous function of Φ_{ext}. The staircase is rounded by the quantum fluctuations of the flux which tend to suppress the flux quantization. This rounding is analogous to the rounding of the Coulomb staircase of the single Cooper pair box when E_J/E_c is of order unity. However, the problem of the fluxon box involves three energies: E_J, E_c and E_L instead of two (E_J, E_c) in the single Cooper pair box. This explains why a transition between a discontinuous and continuous inner flux Φ_{int} can still be obtained in the classical limit ($E_c \to 0$, thick line on Fig. 4.17). In this limit, discontinuous solution vanishes for $E_J < E_L/2\pi^2$ and corresponds to the suppression of the metastable minima in the potential $\mathcal{V}(\Phi_{ext}, \Phi)$ (see Fig. 4.12, middle panel). The Josephson coupling is then too weak to maintain a sufficiently high screening current.

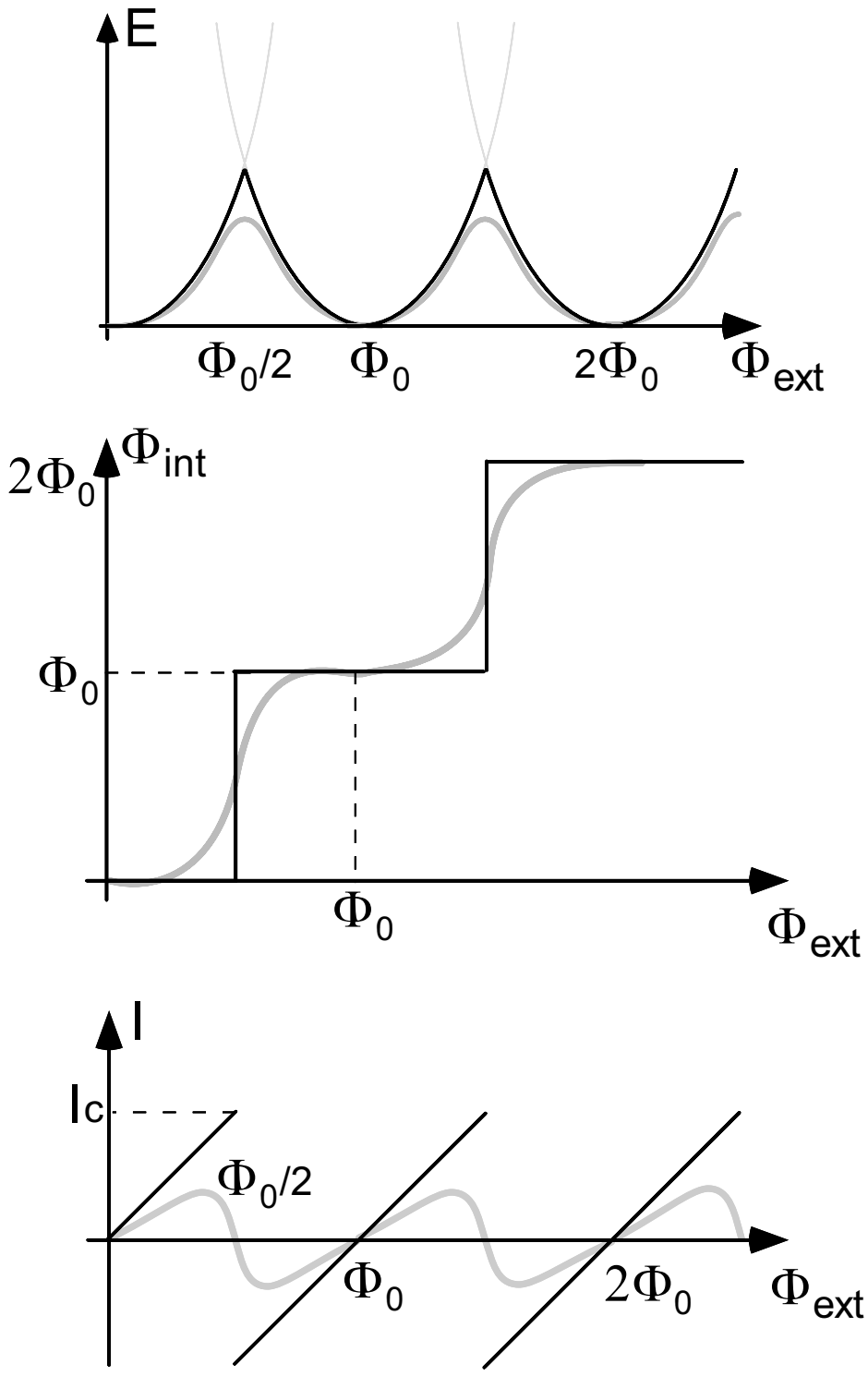

Figure 4.16. Flux dependence of physical variables of the superconducting loop ground state for both cases $\kappa > 1$ (black curves) and $\kappa < 1$ (gray curves)
top figure: ground state energy of the system $E(\Phi_{ext})$
middle figure: "Faraday staircase" of the inner flux $\Phi_{int}(\Phi_{ext})$
bottom figure: superconducting screening current.

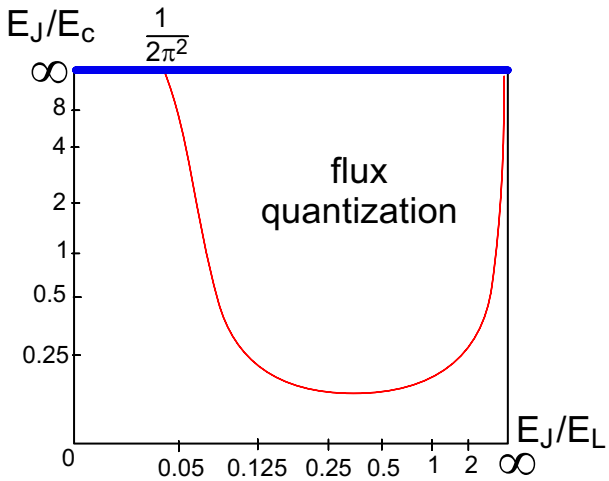

Figure 4.17. Transition line representing the solutions of the equation $\kappa = 1$ *in the parameter plane defined by the reduced coordinates* E_J/E_L *and* E_J/E_c*. The curve separates the space into two domains: in the upper-right* $(\kappa > 1)$ *domain, the flux inside the loop is an integer number of flux quanta; in the other* $(\kappa < 1)$ *domain, the flux inside the loop is a continuous function of the externally applied flux. The classical regime is obtained in the limit* $E_J/E_c \to \infty$ *(top thick line).*

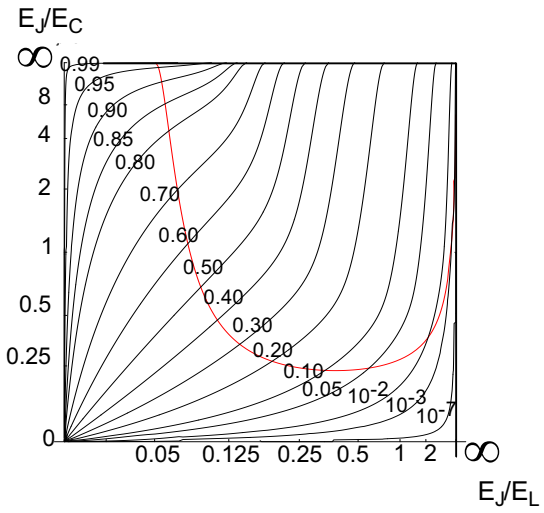

Figure 4.18. Map of iso-critical current lines in the parameter space $(E_J/E_L,\ E_J/E_c)$*. The values indicate to the reduction factor with respect to the fully developped critical current* $I_c^0 = E_J/\Phi_0$ *of the bare Josephson junction. The transition line* $\kappa = 1$ *shown in previous figure is also indicated.*

4.4.7 Effect of dissipation

We have investigated the effect of dissipation by reducing the quality factor of the LC circuit. This can be done by placing a resistive shunt in parallel with the LC oscillator (see Fig. 4.19). Firstly, we have calculated the two impedance integrals M_1 and M_2 as functions of the oscillator quality factor.

We have then determined the transition line $\kappa = 1$ in the parameter space for different values of the shunt resistance R (see Fig. 4.20). For resistances R small[2] compared to $R_K/4 \approx 6.4\,\mathrm{k}\Omega$, the continuous inner flux area (above the surface $\kappa = 1$) tends to occupy the whole parameter space except for $E_J/E_L < 1/(2\pi^2)$ which is the classical domain limit. We interpret this result by the suppression of quantum fluctuations by dissipation, which tends to restore the classical behavior of the system.

4.5 General expression of the renormalized Josephson energy

4.5.1 Starting from the tunneling Hamiltonian

We have assumed up to here that the superconducting gap Δ is much higher than the charging energy E_c, thus ensuring that the coupling Hamiltonian between superconducting electrodes across the tunnel junctions takes its usual Josephson form (Eqs. 4.2 and 4.3). This limit is actually not always experimentally fulfilled, in particular for Aluminum electrodes for which Δ is about 2 k_BK, while typical values of E_c are around 1 k_BK. In such a case, a more general approach starting from the tunneling Hamiltonian is required. The derivation of the effective Hamiltonian has been done by Joyez [6] using a time-representation formalism. By combining his result with the variational approach, we have obtained an expression of the renormalized Josephson energy $E_J^\star$ which extends the expression 4.68:

$$E_J^\star = E_J^0 \frac{4}{\pi^2} \int_0^{+\infty} d\tau \; K_0^2(\tau) \; e^{-2\int_0^\infty \frac{d\omega}{\omega} \frac{\mathrm{Re}[Z(\omega)]}{R_K} \left(1+e^{-\frac{\hbar\omega\tau}{\Delta}}\right)}, \tag{4.97}$$

where K_0 is the modified Bessel function of the second kind.

[2] This limit similarly involves the "superconducting" resistance quantum $R_K/4$ as in Eqs 4.61 which set the low impedance limit for the environment.

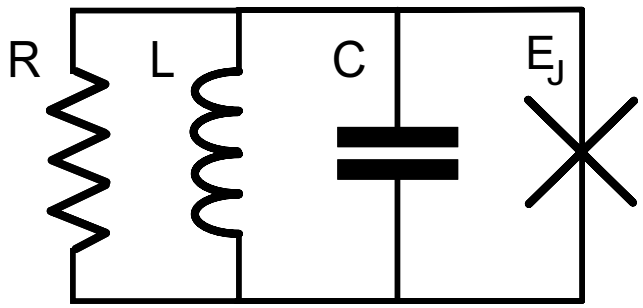

Figure 4.19. Schematics of a Josephson junction coupled to a single mode oscillator with a finite quality factor. The environment of the junction can then be modeled as a parallel RLC circuit.

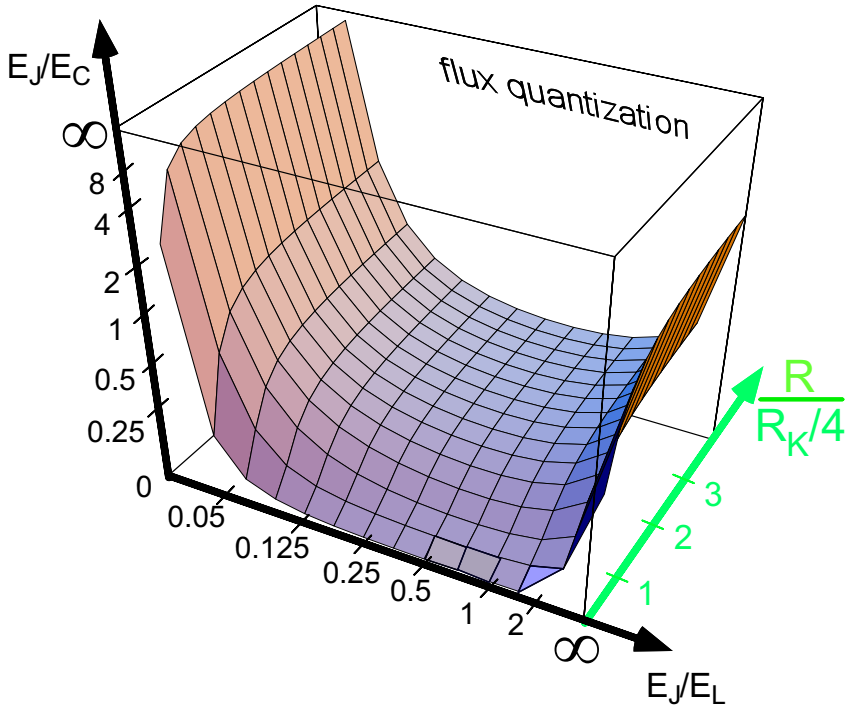

Figure 4.20. Transition surface ($\kappa = 1$) in the parameter space $(E_J/E_L, E_J/E_c, R/(R_K/4))$. For shunt resistances R small compared to $R_K/4$, the flux quantization is restored except in the classical regime $E_J/E_L < 1/2\pi^2$.

In this time representation, the Cooper pair tunneling is described by a sequence of two single electron tunneling processes, separated by a time delay τ. The time factor in the exponential: $\left(1+e^{-\frac{\hbar\omega\tau}{\Delta}}\right)$ has an interesting physical meaning: it describes the effect of the electromagnetic environment on the two consecutive tunneling processes. One can note that the larger this delay is, the lower the influence of the environment on the junction. Therefore, passing two electrons successively is "easier" than two electrons at a time.

One can check that this latter formula is in agreement with our calculation in the limit $\Delta \to +\infty$. Using the identity $\int_0^{+\infty} d\tau\ K_0^2(\tau) = \frac{\pi^2}{4}$, one finds:

$$\lim_{\Delta\to+\infty} E_J^\star = E_J^0\ e^{-4\int_0^\infty \frac{d\omega}{\omega}\frac{\mathrm{Re}[Z(\omega)]}{R_K}}, \tag{4.98}$$

which is exactly the renormalization factor obtained in Eq. 4.68.

4.5.2 Self-consistent expression of the renormalized Josephson energy

Finally, we propose to extend the result 4.97 in order to take into account the "slave-boson" effect as previously discussed in section 4.10. This is tentatively done by setting the low frequency cut-off of the impedance integral at $E_J^\star/\hbar$. This way of reasoning leads to the general, self-consistent expression of the renormalized Josephson energy:

$$E_J^\star = E_J^0\frac{4}{\pi^2}\int_0^{+\infty} d\tau\ K_0^2(\tau)\ \ e^{-2\int_{E_J^\star/\hbar}^\infty \frac{d\omega}{\omega}\frac{\mathrm{Re}[Z(\omega)]}{R_K}\left(1+e^{-\frac{\hbar\omega\tau}{\Delta}}\right)}. \tag{4.99}$$

This expression contains all previously obtained results in the appropriate limits.

Conclusion

Using perturbational and variational approaches, we have shown that a Josephson junction in series with an impedance behaves as an effective Josephson junction but with a different current-phase relation. The current-phase relation is no longer sinusoidal and the critical current is reduced compared to the bare junction critical current. In particular, a high-impedance environment strongly reduces its value. We interpret this effect as an environmental Coulomb blockade of the Josephson effect analogous to the blockade of the conductance observed in single normal metal tunnel junctions. Recent calculations based on the renormalization group agree with our interpretation. In the case of a Josephson junction in a superconducting loop placed in a magnetic field, the comparison with exact numerical calculations confirms the existence of a transition from a regime in which the inner flux is quantized in units of flux quantum Φ_0 to a regime in which it varies continuously with the applied field. The disappearance of quantization is due either to weak screening currents or large quantum fluctuations. Introducing dissipation in the system tends to suppress quantum fluctuations and therefore to restore flux quantization.

Finally, let us mention that our prediction of an environmental Coulomb blockade of the Josephson effect could be experimentally addressed by measuring the magnetic susceptibility of RF-SQUIDs with adequate parameters. The direct measurement of the maximum supercurrent in a current bias mode would not give the critical current but the switching current which is a stochastic quantity smaller than the critical current [17], as discussed in previous chapter.

References of chapter 4

[1] G. L. Ingold and Yu. V. Nazarov, in *Single Charge Tunneling,* edited by H. Grabert and M.H. Devoret (Plenum, New York,1992), chapter 2.

[2] V. Ambegaokar and A. Baratoff, Phys. Rev. Lett. **10**, 486 (1963).

[3] M.H. Devoret, in *Quantum Fluctuations*, edited by E. Giacobino, S. Reynaud and J. Zinn-Justin (Elsevier,1996), course 10.

[4] A.O. Caldeira and A. J. Leggett, Ann. Phys. **149**, 374 (1983).

[5] H. Pothier, Ph. D. Thesis, Université Paris 6, (1991).

[6] P. Joyez, Ph. D. Thesis, Université Paris 6, (1995).

[7] F. Guinea, V. Hakim, and A. Muramatsu, Phys. Rev. Lett. **54**, 4 (1985).

[8] S. Chakravarty and A.J. Leggett, Phys. Rev. Lett. **52**, 5 (1984).

[9] C. Cohen-Tannoudji, B. Diu, F. Laloë, *Mécanique Quantique*, Ed. Hermann, Paris (1973).

[10] M. Büttiker, Y. Imry, and R. Landauer, Phys. Lett. A**96,** 365 (1983).

[11] F.W.J. Hekking and L.I. Glazman, *Proceedings of LT 21*, Czech. J. Phys. **46,** 2323 (1996).

[12] H. Grabert, private communication.

[13] A. Barone and G. Paterno, *Physics and applications of the Josephson effect*, Wiley and sons, (1982).

[14] R. Rouse, Siyan Han, and J.E. Lukens, Phys. Rev. Lett. **75**, 1614 (1995).

[15] P. Bamas, R.Cabanel, B. Dessertenne, K. Bouzehouane, H. Bouchiat, B. Reulet and P. Monod, Physica C, 2042, (1994).

[16] J.R. Klauder and B.S. Skagerstam, *Coherent states,* World scientific, Singapore (1985).

[17] D. Vion, M. Götz, P. Joyez, D. Esteve, and M.H. Devoret, Phys. Rev. Lett. **77**, 3435 (1996).

Chapter 5

Charge detection and noise level in single electron transistors

Introduction

The appealing idea of using the charge quantization in small islands to represent logical bits emerged at the very early stages of the development of single electronics [1]. In a single electronics logical device, a single bit would be represented by two charge states differing by one electron, instead of two charge states of a capacitor differing by a macroscopic number of electrons as currently implemented nowadays. Although this ultimate coding scheme provides obvious advantages such as reduced dissipation, it suffers from serious drawbacks which have hindered its practical realization. Firstly, tunneling is a stochastic phenomenon and the evolution of a circuit is not fully deterministic. Secondly, the single electron charge state which represents the bit is presently not robust, due to the intrinsic sensitivity of single electron devices to their electromagnetic environment. In particular, island charge states which are normally determined by the control gate voltages are also affected by variations in the local electrostatic field. The electrostatic configuration of all trapped charges in the lattice impurities of the substrate, or in surface impurities in the vicinity of islands, thus has a direct influence on island charge states. The overall effect on an island of the extra electrostatic

field sources is equivalent to an "offset" charge on the gate capacitor. Such a dependence of single electron devices on offset charges actually ruins all the advantages that single electronics could bring to digital electronics, at least within the framework of present day technology. Indeed, offset charges are randomly distributed and subject to random changes in time. Even assuming that offset charges can be compensated by applying tedious gate voltage corrections, their unpredictably time dependence would definitely cause unrecoverable memory erasures and calculation errors for the proposed digital circuits. More generally, offset charges which affect all the single electron devices operated up to now appear as one of the main practical problems hindering the development of single electronics. For instance, offset charges limit the error-free operation time of single electron pumps or the charge sensitivity of single electron transistors (SETs) used as electrometers. These latter devices are actually perfectly suited to investigate the time evolution of the offset charge of a single island. The subject of this chapter is to give a closer view of SET characterization and of their use in high-sensitivity electrometry. We show experimental results that provide a reliable determination of the offset charge levels of SETs fabricated on different substrates. We discuss their origin and the localization of the field sources. Finally, we propose a possible application of the SET to the monitoring of the trajectory of charged particles.

5.1 The SET as an electrometer

The operating principle of the single electron transistor [3] has been previously described (see section 1.1). The relevant property for electrometry is the sensitivity of the output signal (the voltage or current depending on the bias mode) with respect to the charge electrostatically induced on the island. In the following,we consider only the case of a current biased although charge measurements using voltage-biased SETs are possible as well (an example is provided in the article reprinted in appendix 5-D).

For a given bias current I, the voltage V across the electrometer is periodically modulated by the induced charge q[1], the period being one electron on the island (see Fig. 5.4):

$$V(t) = V_0(I) + f\left(\frac{q(t)}{e}, I\right) \tag{5.1}$$

[1] The SET is the analogous for electrometry of the dc-SQUID for magnetometry [2]. Both devices have similar periodic response functions and provide a sub-quanta detection accuracy. This similarity is not accidental but arises from a deeper duality principle between charge and flux (see Chapter 4).

The bias current I is chosen in order to maximize the voltage modulation. The gate voltage V_g is adjusted to reach a working point where the function f has a maximum slope $\frac{\partial f}{\partial q}$. These two successive settings therefore ensure an optimal charge detection gain g. At this working point (for example, the point O represented in Fig. 5.4), the output signal directly reflects the sub-electronic variations of the charge polarized on the island, thus probing with a great sensitivity the local electric field (see Fig. 5.2). The measurement of the excess charge in the single electron box experiment described in chapter 2 clearly illustrates the usefulness of such a device.

As for any other electronic device, the detection limit and the accuracy of a SET are limited by its noise level. This noise can be separated into two components with different physical origins:

5.1.1 Shot noise

The first source of noise is intrinsic to the device: stochastic tunneling of discrete charges through the device results in current fluctuations, referred to "shot noise". This noise has a flat frequency spectrum (thus is commonly referred as a white noise). Compared to a purely Poissonian process through a single junction, the noise level in a SET can be reduced by up to a factor 2 due to the correlations between successive tunnel events through the two junctions in series. These predictions have been recently experimentally confirmed by Birk *et al.* [4].

At the optimal working point of the SET, the characteristic time τ of each tunnel process is $\tau \approx R_T C$ where R_T and C are respectively the resistance and the capacitance of the tunnel junctions. The shot noise is thus equivalent to a white noise in the charge to be measured with a spectral density S_q satisfying:

$$\sqrt{\frac{\tau}{2}}\, e/\sqrt{\mathrm{Hz}} \leqslant S_q \leqslant \sqrt{2\tau}\, e/\sqrt{\mathrm{Hz}}, \tag{5.2}$$

the maximum value being obtained for uncorrelated successive tunnel events. The shot noise, which sets an intrinsic accuracy limit for the charge detection (see paper reprinted in Appendix 5-D), is not however the dominant noise source at low frequency.

5.1.2 Background charge noise

The second kind of noise affecting SETs is extrinsic: it arises from the stochastic motion of

the already mentioned trapped charges. This motion induces on the island a time dependent offset charge $q_n(t)$. The precise relation between the distribution of trapped charges and q_n is established in Appendix 5-B.

Hence, to be detected by the SET, a charge will have "to speak louder" in the considered bandwidth than the background charges surrounding the SET island. We will see in the following that this background noise exceeds the shot noise at low frequency.

5.2 Charge noise measurements

The measurement of the background charge noise of a SET electrometer is above all a determination of its sensitivity. But beyond electrometry purposes, it also provides a measurement of the background noise level acting on the islands of any single electron device fabricated with the same process. The noise level is thus an important specification which characterizes a given fabrication process. Measuring the background charge noise is therefore necessary when one decides to dramatically change the fabrication methods in order to implement new features (see Chapter 6). More precisely, can the newly introduced substrates such as polyimide or silicon nitride be considered as "quiet" substrates with respect to the background noise?

5.2.1 Measurement principles

In order to address this question, we have carried out a test experiment on a SET fabricated on an oxidized silicon substrate covered with a plastic layer made of polyimide, using the multilayer fabrication technique described in chapter 6.

The electrometer was first designed to measure the charge of an electron box (see Fig. 5.1). The very long T-shaped island of typical size (10×0.1 μm^2) was not optimized for a low-noise charge detection. One should rather consider this sample as a typical device used in "real case" sub-electronic charge detection. $I-V$ measurements were performed at low temperature ($T = 20$ mK). Each line connecting the device to the apparatus at room temperature was carefully filtered using miniature cryogenic filters [5]. A magnetic field of about 0.15 Tesla was applied to suppress superconductivity in the aluminum electrodes.

From the I-V curves presenting respectively zero and maximum Coulomb gap (Fig.5.3),

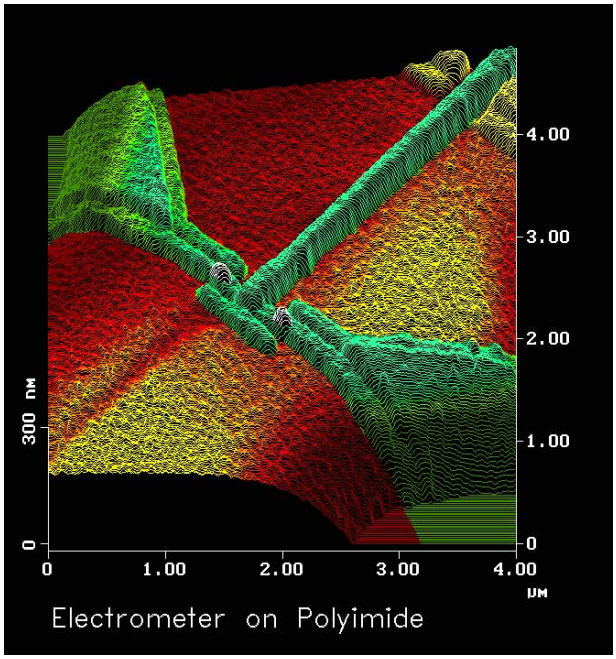

Figure 5.1. AFM image of a SET electrometer deposited on a polyimide substrate. The two bright dots are the tunnel junctions. The T-shaped island (in diagonal on the picture) probes the charge of an electron box (not in the picture). The gate electrode is buried below the polyimide substrate and leads to a small shadow on the resist (lower left) .

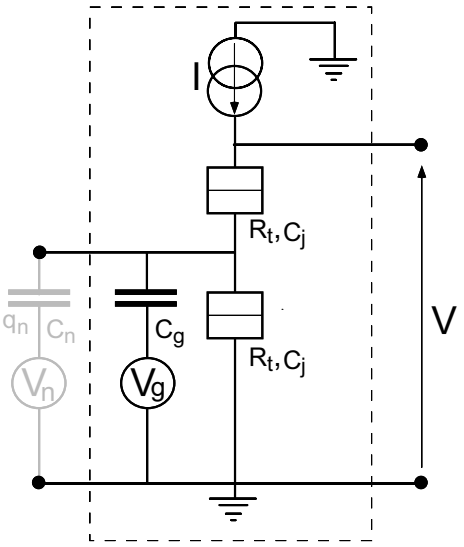

Figure 5.2. Schematic diagram of the device used in the experiment. It consists of a current biased SET whose voltage V is measured. The total charge induced on the island is the superposition of the gate charge $C_g V_g$ and of the so-called charge noise q_n. This charge noise can be considered as being equivalent to a noise source V_n connected to an effective capacitance C_n.

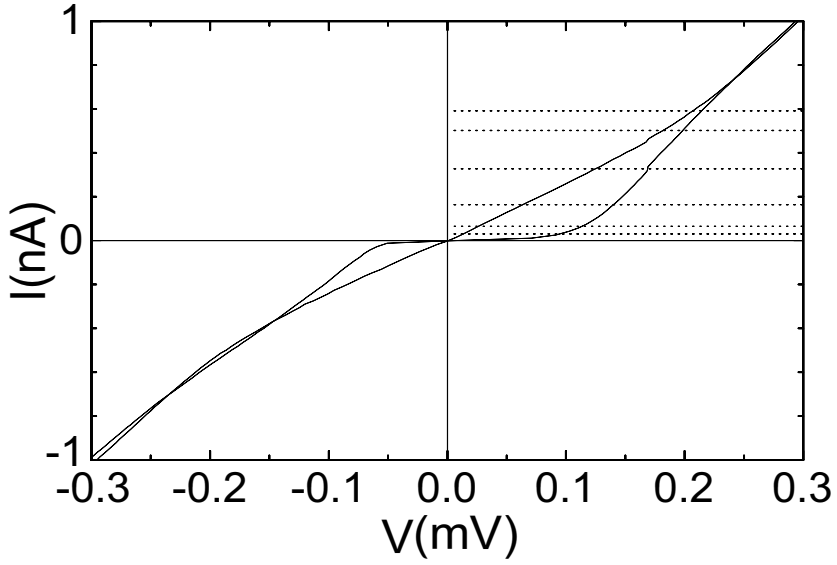

Figure 5.3. I-V characteristics of a SET electrometer fabricated on polyimide, measured at 20 mK for two gate voltages leading respectively to a zero and maximum Coulomb gap. The dashed lines indicate the currents at which the modulation curves in the next figure have been recorded.

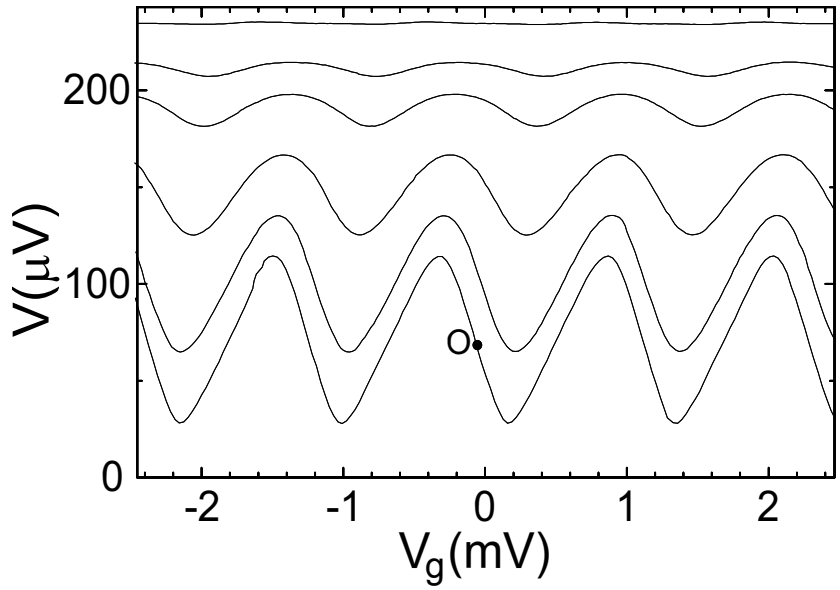

Figure 5.4. Modulation curves of the SET output voltage with the gate voltage V_g, at 20 mK. The bias currents are 5, 165, 327, 500 and 590 pA from bottom to top, respectively.

we deduce the tunnel resistance per junction (R_T = 63 kΩ), and the junction capacitance (Cj = 0.8 fF). Due to the specific geometry of the gate with has its electrode buried below the SET island, its capacitance to the island C_g is relatively large (C_g = 140 aF). The charging energy of the SET is then equal to $e^2/2\,(C_g + 2C_j) \approx 0.6\ k_B$K.

The total polarized charge q results from the superposition of the charge noise $q_n\,(t)$ and the charge of the gate capacitance $C_g V_g\,(t)$ (see Fig. 5.2):

$$q\,(t) = q_n\,(t) + C_g V_g\,(t)\,. \tag{5.3}$$

The direct measurement of the output voltage signal can be used to determine the frequency spectrum of the background charge noise in the frequency range where it dominates over the intrinsic shot noise and over the output amplifier $1/f$ noise. Characterizing the low frequency part of the background noise spectrum thus requires a careful rejection of the amplifier noise.

We have performed a specific "lock-in" detection by modulating the gate voltage. This indirect measurement method has the advantage of shifting the charge noise spectrum to frequencies for which the amplifier noise is orders of magnitude lower. Such a technique is detailed in Appendix 5-A. The other measurement circuitry is similar to those used for the superconducting box experiment (see Appendix 2-A).

The calibration factor which relates the output signal spectrum to the background noise spectrum can be determined through two independent ways. In the first method, we measure the mean value of the modulation slopes $\left(\frac{\partial V}{\partial q}\right)$ where the detection is performed in order to determine the overall gain and therefore the spectrum calibration. In the second method, a direct calibration is obtained by superposing onto the gate voltage a small harmonic marker signal, corresponding to a known fraction of electron. The marker peak integral found in the obtained spectrum then provides a second calibration of the spectrum, obtained "*in-situ*".

Finally, we check that the direct and indirect methods give the same results in the frequency range for which both of them can be used. Usually, the spectrum in the bandwidth $10^{-1}-10$ Hz is best measured around a carrier wave of frequency 70 Hz whereas for higher frequencies the direct measurement is sufficient.

5.2.2 Measured charge noise spectra

Noise power spectra obtained at T=20 mK with the direct and indirect methods are shown

in Fig. 5.5. Both methods are in good agreement in the intermediate common frequency range 3-20 Hz. The frequency dependence over the whole frequency range follows a $1/f$ noise law. The two marker peaks at 1 Hz and 10 Hz result from an extra gate charge modulation with amplitude $e/10$; their intense signatures in the spectra reflects the large signal-to-noise ratio provided by such an electrometer.

One has to note however that the $1/f$ dependence is not always observed as shown further below (see Fig. 5.9). We have found that spectra following a $1/f$ dependence are also temperature independent below a temperature of the order of 100 mK.

To make sure that the measured noise does originate from the SET background charge noise, we have repeated the measurements at a SET working point for which the charge gain is zero (see Fig. 5.14a in appendix 5-A). The resulting spectrum (curve a in Fig. 5.6) falls well below the first one obtained at full charge gain (curve b), thus ensuring that the measured noise at the optimal bias point cannot be attributed at frequencies below 100 Hz to the parasitic noise of the measurement set-up. The charge noise reference level of this SET is equal to $3\times10^{-4}e/\sqrt{\text{Hz}}$ at a frequency of 10 Hz. It is interesting to notice that charge noise spectra with similar $1/f$ dependence and similar levels have been obtained by other groups on metallic SET electrometers [9, 10] but also on semiconductor-based quantum dots [12, 13]. One can wonder whether this striking "universality" of measured charge noise levels has a physical signification.

5.2.3 Interpretation of the noise spectra

The $1/f$ dependence is compatible with the hypothesis that the noise is generated by a collection of fluctuating dipoles with distributed switching times, each one producing a two-level telegraphic noise. Indeed, the superposition of Lorentzian spectra originating from uncorrelated noise sources readily leads to a $1/f$ dependence (see a discussion of this property in the end of Appendix 5-C). Similar two level fluctuators have already been detected inside the oxide barrier of SQUID Josephson junctions by measuring the telegraphic noise they induce in the critical current [15].

Could the charge noise measured by the SET has the same physical origin? More specifically the question to be addressed now is: does the charge noise originate from dipoles which are more or less regularly distributed within the substrate or is the noise dominated by dipoles

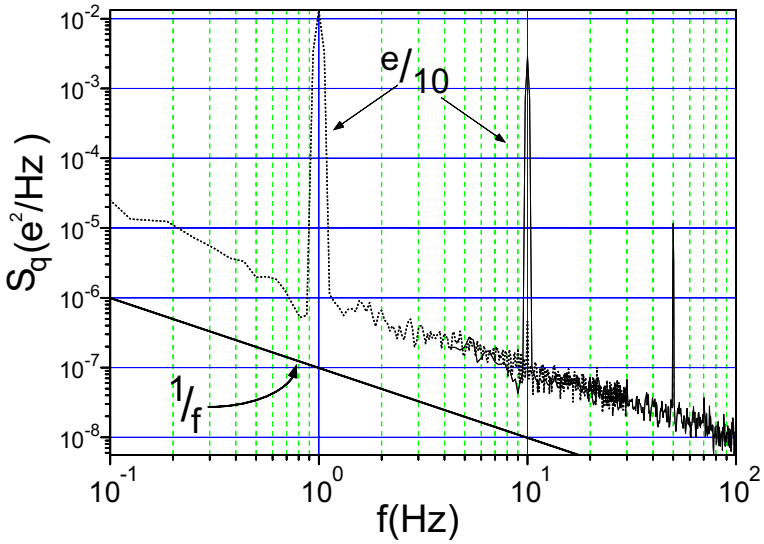

Figure 5.5. Background charge noise power spectra of the SET measured at $T = 20$ mK for a maximum gain and optimal bias current 65 pA. The dashed spectrum has been obtained using the specific lock-in technique whereas the other one results from a direct measurement. The two peaks at 1 Hz and 10 Hz correspond to sinusoidal markers of amplitude $\frac{e}{10}$. Parasitic noise at 50 Hz is equivalent to a sine signal with peak to peak amplitude : $5\times10^{-3}e$.

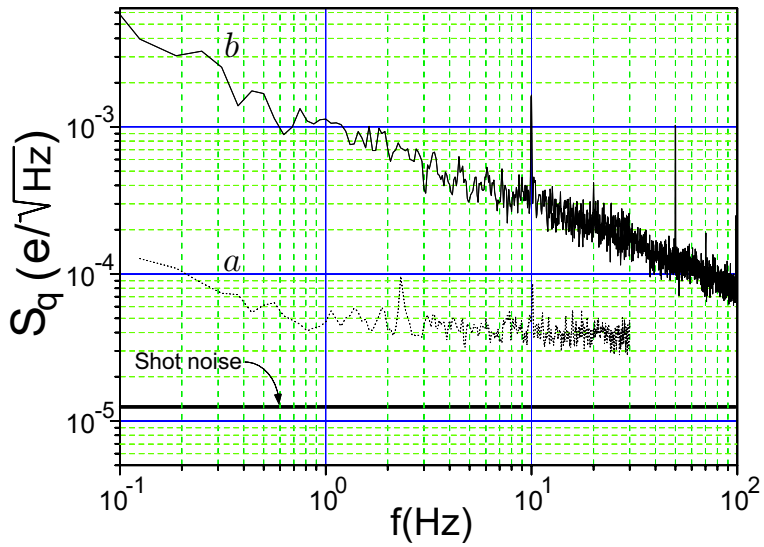

Figure 5.6. Noise spectra of the SET electrometer at $T = 20$ mK at an optimal bias current $I = 65$ pA. Curve a has been obtained at minimum charge gain and gives the residual noise of the measurement set-up. Curve b has been obtained at maximum charge gain. The thick line indicates the predicted shot-noise level.

which are concentrated in the vicinity of the island surface or even in the oxide barrier of the tunnel junctions like in the Josephson junction experiments?

In the case of a uniform distribution of dipoles, we have calculated that the charge noise scales with the self-capacitance of the island: see Eq. 5.20 in Appendix 5-B. Such a scaling law is in qualitative agreement with the island size dependence found by Verbrugh *et al.* [14] on SETs with different islands. In order to investigate the noise origin in SETs fabricated with our new fabrication process, we performed an experiment with three SETs deposited on the same chip but having different island sizes and deposited on two different bottom substrates.

5.3 Origin of the charge noise

5.3.1 A test experiment

In this second experiment, we simultaneously fabricated three SETs on the same chip. All of them have nominally identical tunnel junctions, in order to ensure similar charge modulation and detection gain. Their patterns are sketched in Fig. 5.7. SET n°1 has a small island ($0.1 \times 1\ \mu m^2$) and is deposited on top of a 0.5-μm-thick polyimide layer covering a grounded gold plane. SET n°2 has a large island size ($0.1 \times 10\ \mu m^2$) and same substrate as SET n°1. SET n°3 has an island similar to SET n°1, but is deposited on top of a 0.5-μm-thick polyimide layer covering oxidized silicon (silica thickness: 0.5 μm). Comparison of the noise levels of SET n°1 and SET n°2 will reflect the influence of island size while comparison between SET n°1 and SET n°3 will determine the influence of a silica substrate.

The noise measurements were performed using the same method as previously described. Values of the noise levels measured at different frequencies are given in table 5.8.

Noise levels measured for the three SETs are almost equal at very low frequencies (in the bandwidth 0.1-1 Hz), whereas differences appear in the frequency range 10-100 Hz. Differences of noise level between SET n°1 and SET n°3 remain small : the silica layer at 0.5 μm beneath the island has little influence on the noise level. On the other hand, the noise level for the large-island SET (SET n°2) is the double of that recorded for the small-island SET (SET n°1). A perfect capacitance scaling would have given a noise level (in units of $e/\sqrt{\text{Hz}}$) 3.2 times higher for the SET n°2. Although the noise level increases with the island size, it does not precisely scale with the island capacitance.

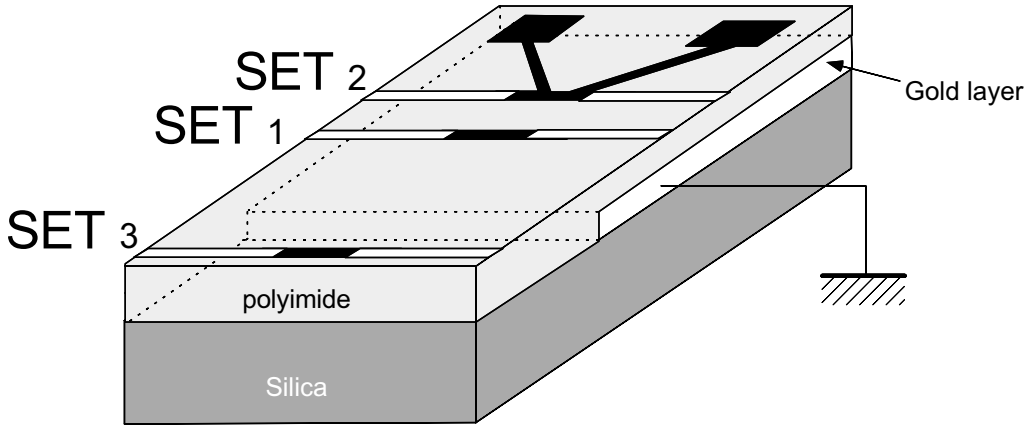

Figure 5.7. Layout of the chip with three SETs fabricated to test the influence of the substrate and of the island size on the charge noise. SET n° 1 has a small island ($\sim 1\mu m$) and is deposited on polyimide over a ground plane. SET n° 2 has a large island ($\sim 10\ \mu m$) and same substrate as SET n° 1. SET n° 3 has an island similar to SET n° 1 but is deposited on a substrate composed of 0.5 μm of polyimide on top of a 0.5 μm silica layer. Comparison of the noise levels between SET n° 1 and SET n° 2 test the influence of island size while comparison between SET n° 1 and SET n° 3 test the influence of the insulating layer composition.

Whatever its constitutive material, the substrate thus contributes to a large part of the observed charge noise with a rather constant noise level. However, participation of other sources are presently not excluded. Let us mention here that in all these noise measurements, we had difficulties to obtain precise estimate of the noise level, since it is subject to random changes in time even with keeping physical parameters constant.

We attribute these changes to the time dependence of two-level fluctuators.

Frequencies

Electrometer characteristics: Noise levels($e/\sqrt{Hz}$)	0.1 Hz	1 Hz	10 Hz	100 Hz
SET 1 island 1 μm on Polyimide/Gold	9.9×10^{-3}	2.6×10^{-3}	4.7×10^{-4}	1.4×10^{-4}
SET 2 island 10 μm on Polyimide/Gold	6.7×10^{-3}	2.5×10^{-3}	8.3×10^{-4}	2.6×10^{-4}
SET 3 island 1 μm on Polyimide/Silica	1.0×10^{-2}	2.5×10^{-3}	5.0×10^{-4}	2.0×10^{-4}

Figure 5.8. Average charge noise levels measured at different frequencies for each of the three measured SETs.

5.3.2 Observation of a single two-level fluctuator

The hypothesis of two level fluctuators is further confirmed by the occasional direct observation of the telegraphic noise due to a single large fluctuator. Examples of direct time recordings of the output voltage of a SET displaying two superimposed telegraphic noises are reproduced in Fig. 5.9c. We have observed fluctuators with amplitudes up to 0.4 e and with time constants up to 10 s. Each fluctuator is characterized by the two average life-time of each state τ_1 and τ_2, that can be of the same order of magnitude (see Fig. 5.9,b) or very different, as shown in Fig. 5.10.

Such large fluctuators can dominate the total observed noise as shown in Fig. 5.9,a. We have found that the amplitude of a given fluctuator is stable in time whereas life-times is subject to random changes in time (see Fig. 5.9,b). These variations lead to a shift in the

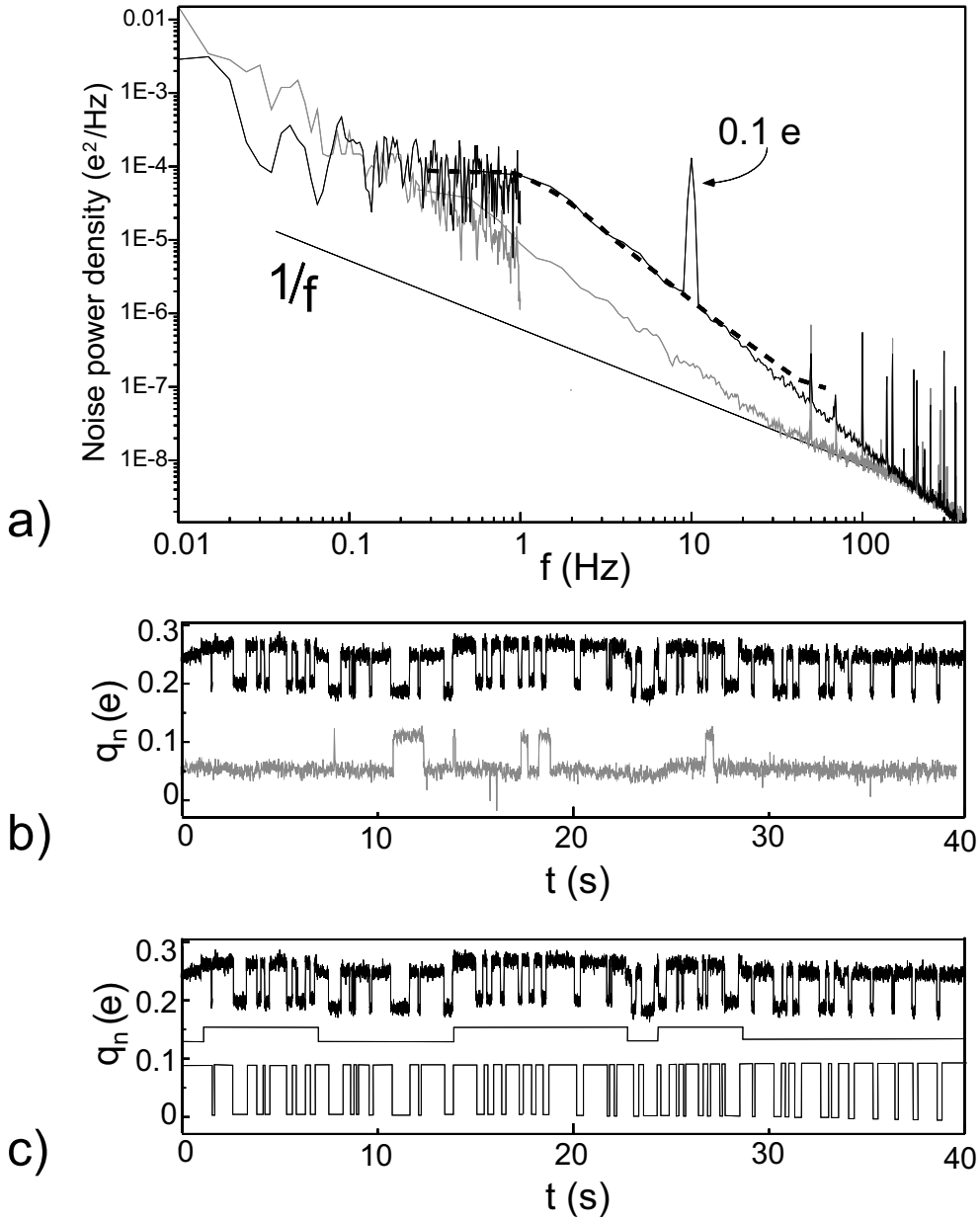

Figure 5.9.
a) Noise power spectra of SET n° 2 measured at 20 mK, at different moments, two days apart. Both spectra were recorded when a single two-level fluctuator dominated the noise, thus explaining the strong deviations from a $1/f$ dependence. The peak at 10 Hz in the upper spectra is a calibration marker. The dashed line is the direct Fourier transform of the time trace of the dominating two level fluctuator shown in the lower trace of panel (c). The characteristic switching frequency of this fluctuator is of the order of 1 Hz.
b) Time recordings of the output voltage of SET n°2 showing a single dominating two-level-fluctuator whose life-time in one state changes in time. Upper (resp. lower) time trace corresponds to the upper (resp. lower) spectrum shown in a).
c)Time trace of the fluctuator plotted in b) showing its decomposition into two superimposed fluctuators. The dominating fluctuator (lower trace) gives a lorentzian spectrum which fits well the associated noise spectrum (see panel a).

characteristic roll-off frequency $f = (\tau_1 + \tau_2) / (\tau_1 \tau_2)$ of the fluctuator spectra (see appendix 5-C), and explains the observed modifications of the noise level in time (Fig. 5.9a and b).

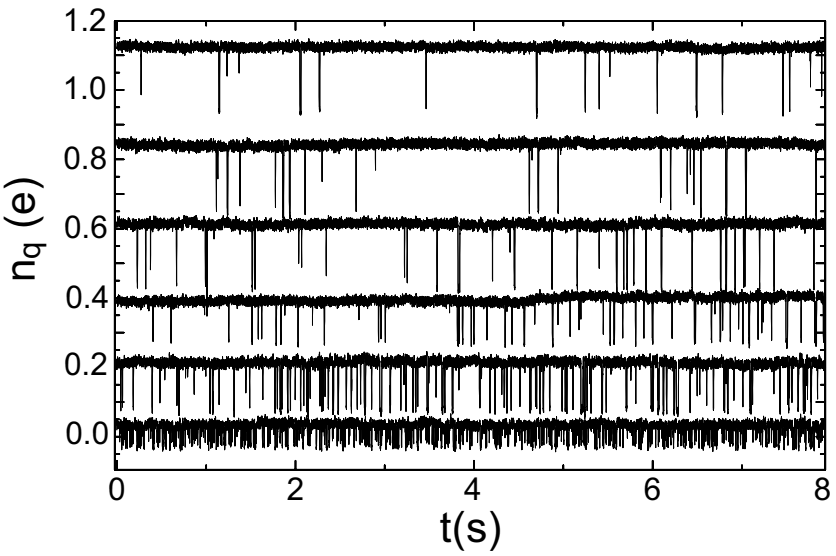

Figure 5.10. Time recordings of the voltage accross a SET showing a single two level fluctuator producing a 0.17e telegraphic noise. Unlike previous recordings, this fluctuator has very different life-times τ_1 and τ_2. Traces measured for increasing temperatures are shifted for sake of clarity. From top to bottom, temperatures are 25, 36, 77, 100, 144, 269 mK, respectively. The reduced amplitude of the lower traces is not due to a reduction in the noise but to a reduced sensitivity of the SET with increasing temperature.

We have measured the temperature behavior of a single two-level fluctuator which has a very short life-time in one of the two states, thus defining a single switching rate. As shown in Fig. 5.10, the switching frequency increases with temperature even at very low temperatures. We have checked that the switching process follows uncorrelated Poissonian statistics at all temperatures (An example is provided in Fig. 5.11). The temperature dependence of the corresponding "long" life-time τ_2 is shown in Fig. 5.12. Actually, this life-time does not follow a simple thermal activation law and its temperature dependence flattens at low temperature. Tunneling activated by unknown processes are then involved.

5.3.3 Localization of the large two level fluctuators

Assuming that a two level fluctuator inducing a charge δq for the offset charge corresponds

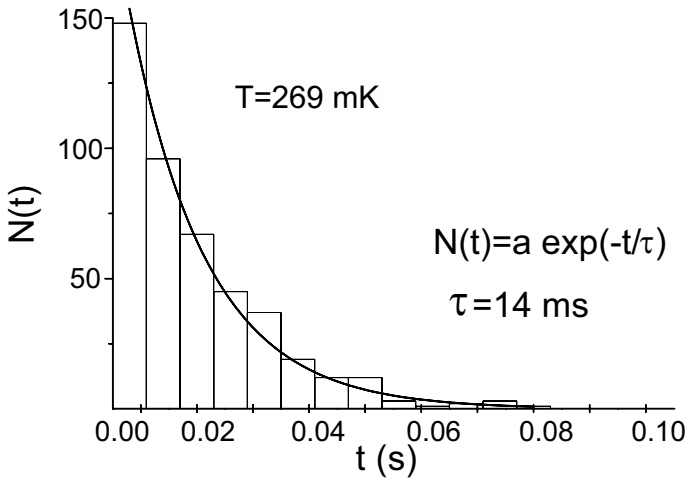

Figure 5.11. Distribution of the switching time of a two-level fluctuator, at 269 mK. This distribution was infered from the analysis of the largest switching time in a recording plotted in previous figure. The distribution obeys Poissonian statistics with a characteristic time $\tau \approx 14$ *ms.*

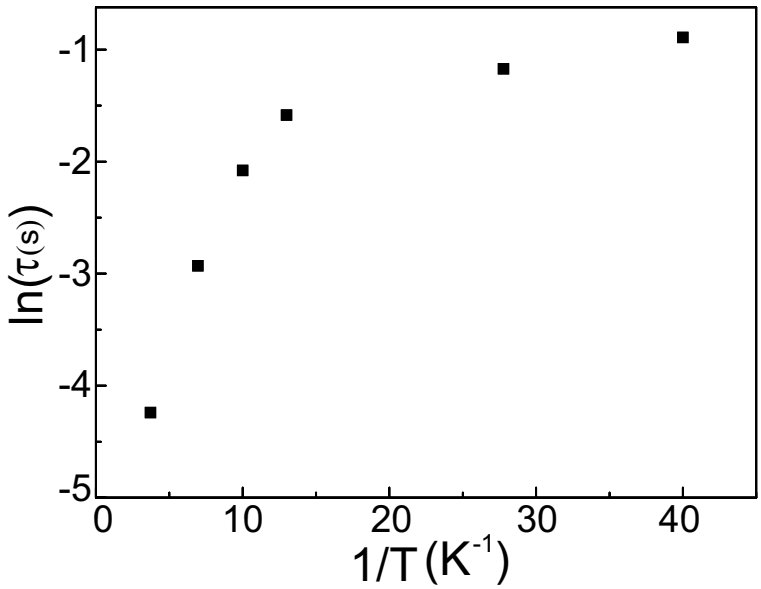

Figure 5.12. Temperature dependence of the characteristic time τ *of a single fluctuator obtained by fitting time distributions similar to the one shown in the previous figure. The two-level fluctuator does not follow a thermally activated behaviour.*

to a dipole P, one deduces from Eq. 5.16 the following inequality:

$$P > \delta q \times d_{\min} \ , \tag{5.4}$$

where $d_{\min}$ is the minimum distance between the island and any other electrode. The closest approach $d_{\min} \sim 1$ nm is obtained for dipoles lying in the tunnel barrier or extremely close to it. Large fluctuators with amplitude $\delta q \sim 0.4\ e$ thus result from dipoles larger than the product of e by an atomic distance. Zorin *et al.* have also observed similar large fluctuators [10]. These authors have localized them in the substrate because they could perform a "stereo" detection using two different SETs close to one another. The dipolar moment corresponding to such a fluctuator would then be larger than 10 $e \times$ nm. A reasonable explanation for the microscopic origin of fluctuators with such large amplitudes has not yet been proposed.

The last experiment tells us that that noise measurements in SETs actually depends on two independent factors:

- the nature of the sample (geometry, materials) which fixes a given set of trapped charges that can be activated
- the experimental set-up, and the physical parameter of operation (temperature..) that set a variable activation level for the trapped charges.

As pointed out by Zorin [6] , the time dependence of the noise level for a given sample can be therefore explained by a variable activation of the set of trapped charges. Among many possible causes of activation, three main causes have been observed:

- improper filtering, that let photons activate the noise
- large gate voltages, which causes locally high electric fields
- intensive thermal cycling, which thermally activate trapped charges

Further studies are necessary to see if substrates and tunnel barriers fabricated using other materials can possibly lead to a decrease of the noise level.

5.4 The SET as a position detector for charged particles

We have shown that a SET has the ability to detect single microscopic charge fluctuators. Could it also be able to detect the passage of moving charged particles in the vicinity of its island? We propose, in the paper reproduced in Appendix 5-D, to use SETs as position sensors

for low energy charged particles.

We show that SETs operated at high-frequency could, in principle, detect a single charged particle passing at a speed of 10 m/s within a distance of about 0.5 mm from the island. This sensitivity could be used for a delicate measurement in particle physics: the monitoring of the position of an antiproton released in a drift tube. Several SETs independently operated and placed along the trajectory would be required to monitor the particle position during it motion. A relative determination of the gravitational mass of the antiproton, an important issue in general physics, could be obtained from the time-of-flight recordings. We discuss in particular the back-action noise of the measuring SET on the moving particle.

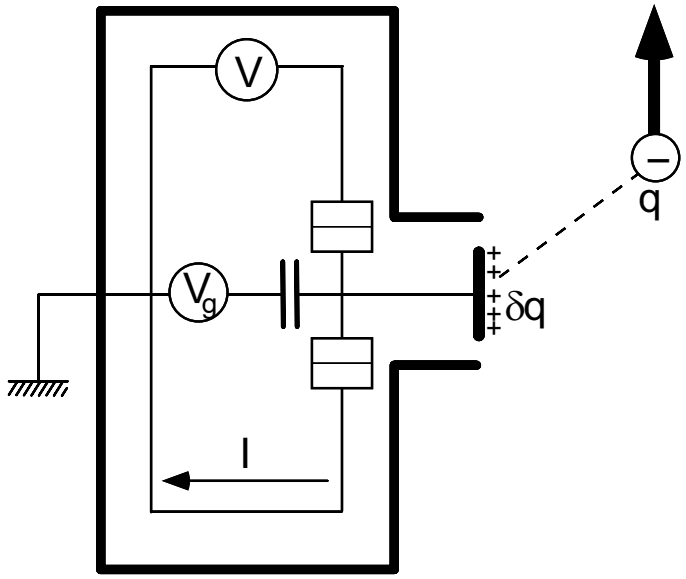

Figure 5.13. Schematics of the proposed position sensor for charged particles based on a SET electrometer. The SET measures the polarization charge δq induced by a charge q moving along the z axis.

Conclusion

In this chapter, some results concerning electrometry applications of single electron devices have been obtained:

• SET-based electrometers have a detection threshold determined at low frequencies by fluctuating background charges.

• The typical charge noise level of a SET electrometer with island size 0.1×10 μm, fabricated on a polyimide substrate is equal to $3{\times}10^{-4}e/\sqrt{\text{Hz}}$ at 10 Hz. This value appears somewhat universal and seems not to depend on the chemical nature of the substrate

• For a given configuration of fluctuating charges, the background charge noise of a SET is determined by a purely geometrical factor. In particular, in the case of uniformly distributed charges, we predict that the charge noise scales with the island capacitance.

• The charge noise of a SET is occasionally dominated by a very small number of two level charge fluctuators which produce a telegraphic noise. The noise power spectrum contains then Lorentzian spectra superimposed on the $1/f$ dependence.

• The location of such large fluctuators has not been determined but their strong influence on the SET suggests a position very close to the island or in the oxide barrier of the tunnel junctions. It is not excluded that fluctuating charges of different origin may contribute at the same time.

• These fluctuators do not follow a simple thermal activation law.

References of chapter 5

[1] D.V. Averin and K.K Likharev, in *Single Charge Tunneling*, NATO ASI series, eds. H. Grabert and M. H. Devoret (Plenum, New York, 1992), chapter 7.

[2] A. Barone and G. Paterno, *Physics and applications of the Josephson effect*, (Wiley & Sons, 1982).

[3] T. A. Fulton and G. J. Dolan, Phys. Rev. Lett., **59,** 109 (1987).

[4] H. Birk, M. J. M. de Jong, and C. Schönenberger, Phys. Rev. Lett., **75**, 1610 (1995).

[5] D. Vion, P.F. Orfila, P. Joyez, D. Esteve and M.H. Devoret, J. Appl. Phys. **77**, 2519 (1995).

[6] A. Zorin, SETTRON final meeting, Saclay, January 1997.

[7] J. Clarke, W. M. Goubau, and M. B. Ketchen, J. Low Temp. Phys., **25**, 99 (1976).

[8] E.H. Visscher, S.M. Verbrugh, J. Lindeman, and J. E. Mooij, Appl. Phys. Lett. **66**, 3 (1995).

[9] G. Zimmerli, T.M. Eiles, R.L. Kautz, and John M. Martinis, Appl. Phys. Lett. **61**, 2 (1992).

[10] A.B. Zorin, F.-J Ahlers, J. Niemeyer, T. Weimann, H. Wolf, V.A. Krupenin and S.V. Lotkhov, Phys. Rev. B, **53**, 13682 (1996), A.J Manninen and J.P. Pekola, Proceedings of LT 21, Czech. J. Phys. **46,** 2293 (1996).

[11] D. Song, A. Amar, C. J. Lobb and F.C. Wellstood, IEEE Trans. Appl. Superc. **5**, 2 (1995).

[12] L. Saminadayar, P. Grousset, A. Kumar and D.C. Glattli, submited to J. Appl. Phys.

[13] SETTRON/ESPRIT Project 9005 EC, Periodic Progress Reports 1994/95 and 1995/96

[14] S.M. Verbrugh, M.L. Benhamadi, E.H. Visscher, and J. E. Mooij, J. Appl. Phys. **78**, 4 (1995).

[15] C.T. Rogers, R.A. Burhman, W.J. Gallagher, S.I. Raider, A.W. Kleinsasser, and R.L. Sandstrom, IEEE Trans. Mag. **23**, 2 (1987).

[16] S. Machlup, J. Appl. Phys. **25**, 341 (1954).

[17] for a review of 1/f noise in condensed matter physics see M.B. Weissman, Rev. Mod. Phys. **60**, 537 (1988).

Appendix 5-A
Noise detection "lock-in" technique

We describe here the detection technique we have used to extract the background charge noise of a single electron transistor. This method is greatly inspired from the lock-in technique commonly used for DC-SQUID operation [7]. We apply on the gate capacitor a square signal Σ of frequency ν_0 and amplitude Σ_0 with an offset V_0:

$$V_g(t) = \Sigma(t) = V_0 + \Sigma_0 \times \Gamma_{\nu_0}(t), \tag{5.5}$$

where Γ_{ν_0} is a square wave of frequency ν_0 switching between the values ± 1.

In the absence of charge noise, the output voltage has the following ideal form:

$$V = \frac{(U_1 + U_2)}{2} + \frac{(U_2 - U_1)}{2} \times \Gamma_{\nu_0}(t), \tag{5.6}$$

$$\text{where } U_{\frac{2}{1}} = V(V_g = V_0 \pm \Sigma_0).$$

Small variations of the gate voltage around the two bias points induce changes in V determined by the dynamic gains $g_1 = \left(\frac{\partial V}{\partial V_g}\right)_{U_1}$ and $g_2 = \left(\frac{\partial V}{\partial V_g}\right)_{U_2}$. A charge gain $\left(\frac{\partial V}{\partial q}\right)_U = g/C_g$ is associated at each point.

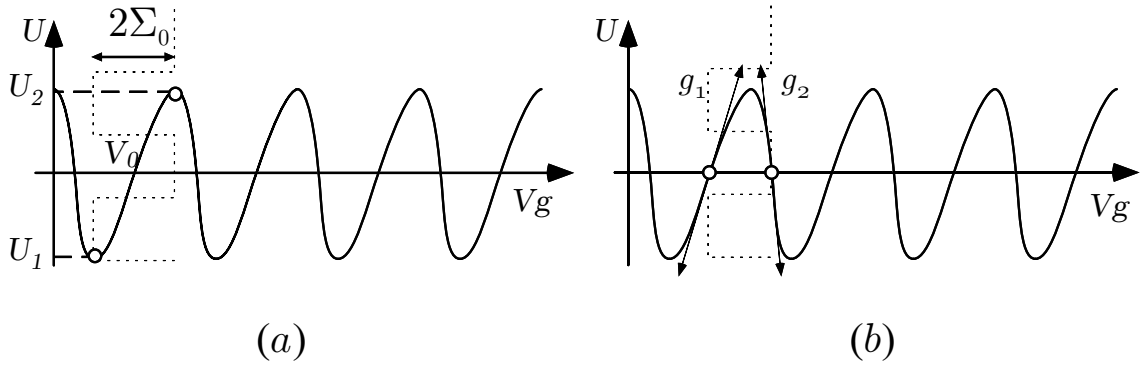

Figure 5.14. Noise detection technique.
As a square voltage signal Σ is applied on the gate capacitance, the output voltage V switches between two values U_1 and U_2. By adjusting offset and amplitude of Σ, the dynamic gain for small variations can be chosen either minimum (case a) for set-up noise checking or maximum (case b) for charge noise measurement.

In presence of a background charge noise q_n, the output voltage is given by the following expressions:

- during the first half-period :

$$V_1 \approx U_1 + \left(\frac{\partial V}{\partial q}\right)_{U_1} \times q_n(t) = U_1 + \frac{g_1}{C_g} \times q_n(t)\,. \tag{5.7}$$

- during the second half-period, a symmetric expression is obtained:

$$V_2 \approx U_2 + \frac{g_2}{C_g} \times q_n(t)\,. \tag{5.8}$$

The global expression of the output voltage in presence of noise is then:

$$V \approx \frac{1}{2}\left[(U_1+U_2) + \frac{(g_1+g_2)}{C_g} \times q_n(t)\right] + \frac{\Gamma_{\nu_0}(t)}{2} \times \left[(U_2-U_1) + \frac{(g_1-g_2)}{C_g} \times q_n(t)\right]. \tag{5.9}$$

If the gains are such that $g_1 + g_2 \ll g_1 - g_2$ (case b of Fig. 5.14), the first term has only a DC contribution whereas the second term corresponds to the charge noise chopped by the square signal.

The Fourier spectrum of the output voltage is therefore proportional to the convolution product of the charge noise spectrum with the Fourier spectrum $\tilde{\Gamma}_{\nu_0}(\nu)$ of the square wave:

$$\tilde{V}(\nu) \propto \tilde{q}_n(\nu) \star \tilde{\Gamma}_{\nu_0}(\nu)\ , \tag{5.10}$$

$$\text{with :} \qquad \tilde{\Gamma}_{\nu_0}(\nu) = \sum_{n=0}^{n=+\infty} \frac{2}{i(2n+1)\pi}\left[\delta(\nu-(2n+1)\nu_0) - \delta(\nu+(2n+1)\nu_0)\right]. \tag{5.11}$$

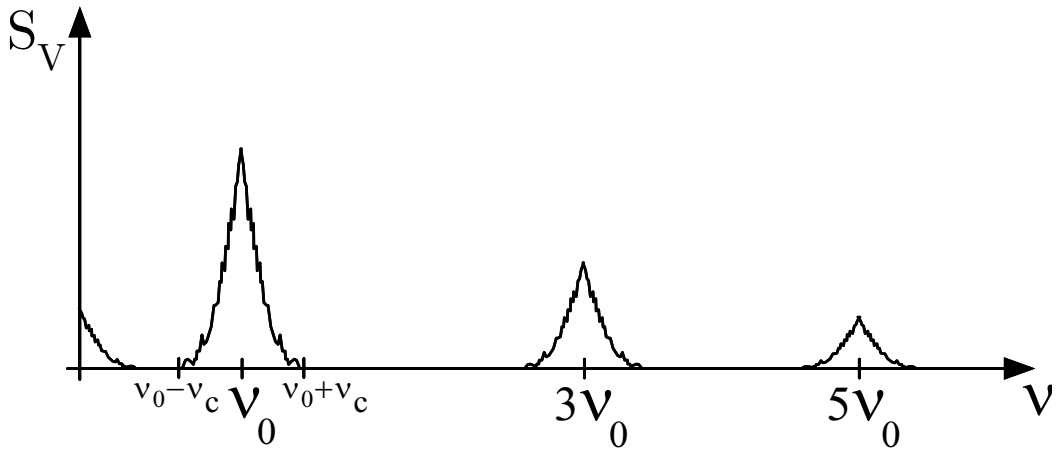

Figure 5.15. Schematic plot of the output voltage SET spectrum obtained using the lock-in method. The low-frequency noise is symetrically shifted around odd harmonics of the carrier wave with frequency ν_0.

The charge noise spectrum is then symmetrically shifted at regularly spaced frequencies

(2n+1)ν_0 (see Fig. 5.15). If the charge noise cut-off frequency ν_c satisfies the condition $\nu_c < \nu_0$, the shifted spectra do not overlap and the low frequency noise can be measured by zooming around the fundamental frequency ν_0.

Near the fundamental frequency ν_0, the power spectrum is obtained from a spectrum analyzer. For our measurements we used two different analyzers, a Scientific Atlanta SD-380 and a Hewlett Packard HP-35665A. The analyzer acquires time traces of the SET voltage $V(t)$ and it output gives the following power spectrum:

$$S_V(\nu) = \left|\tilde{V}(\nu)\right|^2 + \left|\tilde{V}(-\nu)\right|^2 = \left(\frac{g_1 - g_2}{\pi C_g}\right)^2 \left(S_q(\nu - \nu_0) + S_q(\nu_0 - \nu)\right), \tag{5.12}$$

where $S_q(\nu)$ is the charge noise power spectrum of $q_n(t)$ restricted to its positive part, ensuring the power conservation :

$$\lim_{\theta\to\infty} \frac{1}{\theta} \int_0^\theta (q_n(t))^2 \, dt = \int_0^\infty S_q(\nu) \, d\nu. \tag{5.13}$$

Depending on the offset of the carrier Σ, we can adjust the differential gain $(g_1 - g_2)$ either to its maximum value for the noise detection (Fig. 5.14, case b), or to nearly zero (Fig. 5.14, case a). In this last case, we can check that the noise level is orders of magnitude lower than the noise measured in the case b) thus ensuring that the measured noise does originate from the background charge noise.

Appendix 5-B
Charge noise of the electrometer induced by fluctuating dipoles

We first determine the polarized charge δq induced on the island by a charge q placed in the substrate at a distance $\vec{r}$ from the SET island. We use for that purpose a very general relation of reciprocity for a linear system composed of a collection of conductors i: Considering two states determined by of set of charges (q_i), (resp.(q_i')) and potentials (V_i), (resp.(V_i')) , they obey the following reciprocity relation:

$$\sum_i q_i' V_i = \sum_i \sum_j C_{ij} V_j' V_i = \sum_j \sum_i C_{ji} V_i V_j' = \sum_j q_j V_j', \tag{5.14}$$

where C_{ij} are the capacitance matrix elements.

We apply this reciprocity relation to the two different following states of the system consisting of the SET and of a point charge placed at $\vec{r}$:

- all SET electrodes at $V = 0$ and a point charge q at $\vec{r}$ inducing δq on the island.
- island at potential $V_i = V_0$, other SET electrodes at $V = 0$ and no charge ($q = 0$) at $\vec{r}$.

Eq. 5.14 then leads to: $qV(\vec{r}) + \delta q V_0 = 0$. The polarized charge δq on the island thus is:

$$\delta q = -q \frac{V(\vec{r})}{V_0}. \tag{5.15}$$

where V(r) is the potential at point $\vec{r}$ obtained when the island is at potential V_0 and the perturbing charge q is removed. The ratio $V(\vec{r})/V_0$ is a purely geometrical factor.

This result is easily extended to the case of a dipole $\vec{P}$:

$$\delta q = \frac{-\vec{P}.\vec{E}(\vec{r})}{V_0}, \tag{5.16}$$

where $\vec{E}(\vec{r})$ is the electric field at point $\vec{r}$ similarly obtained when the island is at potential V_0 and the perturbing dipole is removed. The influence of a dipole thus strongly depends on its position. Eq. 5.16 shows that dipoles have a stronger influence on the electrometer noise when they are located on short electric-field lines emerging from the island to the other electrodes. In particular, charge displacements in the oxide barrier of one of the junctions are the most effective.

The total polarized charge due to a distribution of dipoles around the island is:

$$\delta q(t) = \iiint d^3r \, \frac{\vec{P}(\vec{r},t).\vec{E}\,(\vec{r})}{V_0}. \tag{5.17}$$

The time autocorrelation function of the induced charge is thus given by:

$$\delta q(0)\delta q(t) = \iiint d^3r \, \frac{\vec{P}(\vec{r},0).\vec{E}\,(\vec{r}) \times \vec{P}(\vec{r},t).\vec{E}\,(\vec{r})}{V_0^2}. \tag{5.18}$$

Assuming that the distribution of dipoles is isotropic with a constant volumic density n_p, the autocorrelation function of δq is given by:

$$\begin{aligned} \langle \delta q(0)\delta q(t) \rangle &= \frac{n_p}{3} \left\langle \overrightarrow{P}\,(\vec{r},0).\overrightarrow{P}\,(\vec{r},t) \right\rangle \iiint d^3r \, \frac{\left|\vec{E}\,(\vec{r})\right|^2}{V_0} \\ &= n_p \frac{P(t)}{3} \left(\frac{C}{\epsilon_0 \epsilon_r} \right), \end{aligned} \tag{5.19}$$

where C is the total capacitance of the island with respect to the ground and $P(t)$ is the time autocorrelation function of the dipole distribution $\overrightarrow{P}\,(\vec{r},t)$ averaged on both time and space. Note that in real-cases, we rather face a planar geometry since single electron transistors are deposited on top of an insulating layer. With dipoles only distributed in the lower half-space, Eq. 5.19 becomes:

$$\langle \delta q(0)\delta q(t) \rangle = \gamma \times n_p \frac{P(t)}{3} \left(\frac{C}{\epsilon_0 \epsilon_r} \right). \tag{5.20}$$

where γ is a geometrical factor lying between 0.5 and 1 (see Fig. 5.16). In the case of a substrate with a uniform dipole distribution, the background charge noise thus almost scales with the island capacitance.

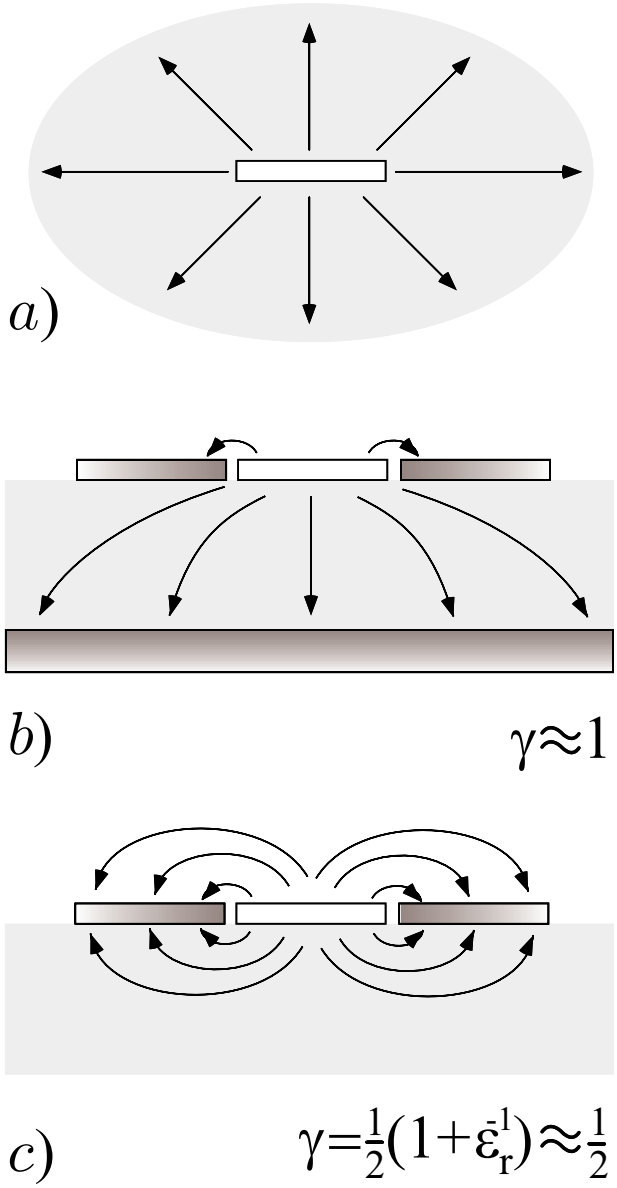

Figure 5.16.
a) Schematic layout of the electric field lines diverging from a charged island immersed in a dielectric material.
b) Cross section of a "real case" set-up for a SET deposited over a substrate with a bottom ground plane. Almost all electric field lines reach the substrate leading to a geometrical factor γ close to 1.
c) cross section of a "real case" set-up for an insulating substrate: electric field lines converge towards neighboring electrodes and the geometrical factor γ is almost equal to $\frac{1}{2}$.

Appendix 5-C
1/f noise induced by a collection of two-level fluctuators with distributed switching energies.

We calculate here the background charge noise spectrum in the particular case of a distribution of dipoles generating a telegraphic noise. By applying the Wiener-Khinchin theorem to Eq. 5.20, we obtain the relation between the charge noise spectrum density $S_q(f)$ and the Fourier transform $\tilde{P}(f)$ of the correlation function $P(t)$:

$$S_q(f) = \gamma n_p \frac{C}{3\epsilon_0 \epsilon_r} \tilde{P}(f) \tag{5.21}$$

Let us assume that each dipole randomly switches between two states and can be modeled as a two-level fluctuator emitting a telegraphic noise. Such an assumption has been experimentally proven to be well followed at least for dipoles strongly coupled to the island since such "trapping events" can be individually measured (see Fig. 5.9). The conditional probability p_i that the dipole i will stay in a given state, is then given by simple Poissonian statistics : $p_i(t) = e^{-t/\tau_i}$, where τ_i is the average life-time of the state. In such a case, the two-level fluctuator is supposed to be characterized by two times τ_1 and τ_2, which correspond respectively to the life-time of each state. Machlup [16] has shown that this telegraphic noise produces a Debye-Lorentzian noise spectrum of the following type :

$$S_T(f) = \frac{\tau_1 \tau_2}{\pi (\tau_1 + \tau_2)^2} \left[\frac{\tau_{eff}}{1 + (2\pi f)^2 \tau_{eff}^2} \right] \approx \frac{1}{\pi} \times \frac{\tau_{eff}}{1 + (2\pi f)^2 \tau_{eff}^2}, \tag{5.22}$$

where $1/\tau_{eff}$ is defined by the sum of the two attempt rates : $1/\tau_{eff} = 1/\tau_1 + 1/\tau_2$.

This spectrum has a roll-off frequency $1/\tau_{eff}$ and a $1/f^2$ dependence above it.

A collection of dipoles with similar moments but different roll-off frequencies results in a spectrum with rough $1/f$ dependence in the range of the roll-off frequencies. This trend is illustrated in Fig. 5.17 where only three fluctuators of that kind have been superimposed.

In the case of a normalized distribution $\Gamma(\tau_{eff})$ for the characteristic times, the total spectrum is:

$$\tilde{P}(f) \;=\; \int_0^\infty \Gamma(\tau_{eff}) S_T(\tau_{eff}) d\tau_{eff} \tag{5.23}$$

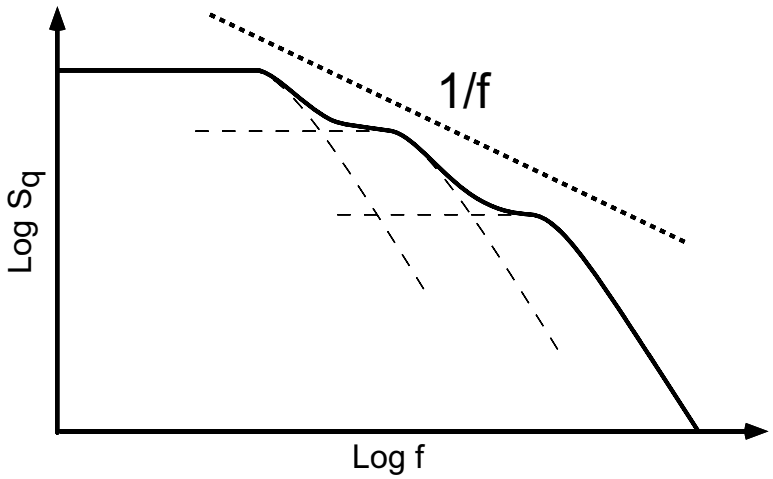

Figure 5.17. Noise spectrum obtained from the superposition of three two-level fluctuators with similar amplitudes but different roll-off frequencies. The spectrum, which is the sum of the three corresponding Debye-Lorentz spectra, displays a rough $1/f$ dependence in the roll-off frequency domain.

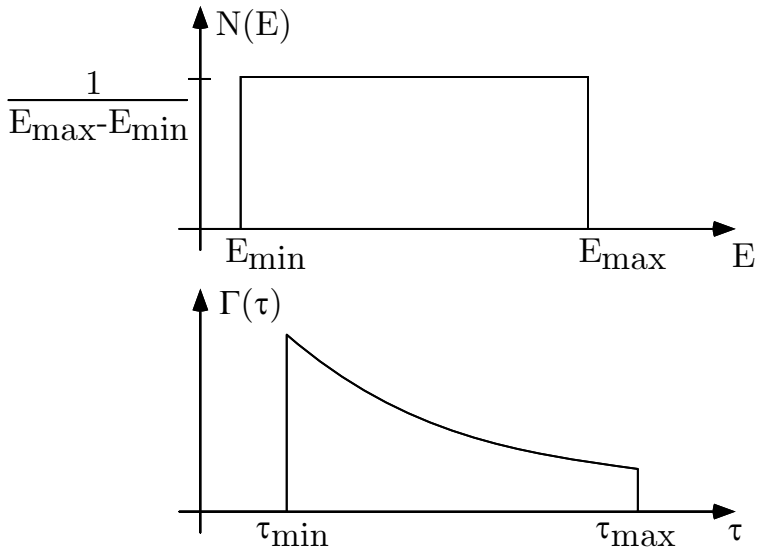

Figure 5.18. Distribution of trapping energies (top) and of the corresponding characteristic switching times (bottom) for a thermally activated process.

$$= \frac{1}{\pi}\int_0^\infty \Gamma(\tau_{eff})\frac{\tau_{eff}}{1+(2\pi f)^2\tau_{eff}^2}d\tau_{eff}$$

A $1/f$ spectrum is obtained in particular for a distribution $\Gamma(\tau_{eff}) \propto \frac{1}{\tau_{eff}}$ over a sufficiently large time interval $[\tau_{\min}, \tau_{\max}]$:

$$\begin{aligned}
\tilde{P}(f) &= \frac{1}{\pi \ln\left(\frac{\tau_{\max}}{\tau_{\min}}\right)}\int_{\tau_{\min}}^{\tau_{\max}}\frac{d\tau_{eff}}{1+(2\pi f)^2\tau_{eff}^2} \\
&= \frac{1}{2\pi^2 \ln\left(\frac{\tau_{\max}}{\tau_{\min}}\right)} \times \left[\tan^{-1}(2\pi f\tau_{\max}) - \tan^{-1}(2\pi f\tau_{\min})\right] \times \frac{1}{f} \\
&\approx \frac{1}{2\pi \ln\left(\frac{\tau_{\max}}{\tau_{\min}}\right)} \times \frac{1}{f}. \qquad (5.24)
\end{aligned}$$

Distributions $\Gamma(\tau_{eff})$ with a $\frac{1}{\tau_{eff}}$ dependence can originate from various physical phenomena.

Thermal activation over potential barriers with a flat barrier height distribution provides one example, as shown below.

More precisely, if one assumes thermally activated rates $\frac{1}{\tau} = \nu e^{-E/k_BT}$ with a constant density of barrier heights in the interval $[E_{\min}, E_{\max}]$, (see Fig. 5.18).

In the time interval $\left[\nu e^{-E_{\max}/k_BT}, \nu e^{-E_{\min}/k_BT}\right]$, the distribution of characteristic times is:

$$\Gamma(\tau_{eff}) = \frac{k_BT}{\tau_{eff}(E_{\max} - E_{\min})} \qquad (5.25)$$

The $\frac{1}{f}$ spectrum amplitude is in this simple case proportional to the temperature:

$$\tilde{P}(f) = \frac{k_BT}{(E_{\max} - E_{\min})} \times \frac{1}{2\pi f} \qquad (5.26)$$

Appendix 5-D

Instrumental application:

Measurement of the antiproton gravitational mass using a single electron transistor

Published in Hyperfine Interactions 109, 345, (1997).

Measurement Method of the Antiproton Gravitational Mass using the Single Electron Transistor.

V. Bouchiat*, G. Chardin†, M. H. Devoret*, D. Esteve*

**Service de Physique de l'Etat Condensé*

†*Service de Physique des Particules*

CEN - Saclay, F-91191 Gif-sur-Yvette Cedex, France

Abstract

We propose a non destructive method to measure the trajectory of a single antiproton in a drift tube using position sensors based on the Single Electron Transistor. We show that this recently developed device has sufficient sensitivity to detect the electric field of a moving charged particle. Comparison of the trajectories of individual antiprotons and H^- ions may allow a reliable determination of the gravitational mass of the antiproton.

Hyperfine Interactions **109**, 345, (1997).

INTRODUCTION

The measurement of the gravitational mass of an antiparticle has been the subject of interest and considerable experimental effort over the past thirty years [1–4], without success until now. Pioneering experiments on the electron by Witteborn and Fairbank [1,2] aimed at ultimately measuring the gravitational mass of the positron. However, the original result of Witteborn and Fairbank [1,2] has been partly retracted [5] and, for reasons which will be analyzed below, we are probably still very far from a measurement on the electron or the positron.

On the other hand, the Low Energy Antiproton Ring (LEAR) at CERN has been providing for the last ten years an intense beam of low-energy antiprotons. The PS-200 collaboration [6] has thus proposed to measure the gravitational mass of the antiproton using, similarly to Witteborn and Fairbank, a time-of-flight technique in a vertical drift tube where the antiprotons would be confined along the vertical axis using a strong magnetic field. The technical difficulties of such an experiment are enormous. Because of the large annihilation cross-section of an ultralow-energy antiproton, a vacuum of extremely high quality is required for the antiparticles to survive the cooling and measurement stages. But the main experimental problem probably resides in the stray electric fields [7] which easily overwhelm the tiny gravitational force on the antiproton. Whereas a differential measurement is in principle possible using a comparison with the time-of-flight of H^- ions, two conditions should be achieved for this comparison to be meaningful : firstly, the conditions of release of antiprotons and H^- ions in the drift tube should be kept identical to a high degree of accuracy and, secondly, the stray electric fields should be kept at a value constant in time and sufficiently small compared to the gravitational force.

We propose here to replace the time-of-flight measurement by the direct monitoring of a single trajectory. More precisely, we propose to use ultra-sensitive electrometers distributed along the drift tube to determine the passage times of a single particle trapped in the tube. Such non-destructive and repeated measurements would considerably relax the constraints

mentioned above. Electrometers approaching the requirements for single particle monitoring have recently been developed. They are based on the Single Electron Transistor (SET) first operated by Fulton and Dolan in 1987 [8].

II. DISCUSSION OF EXISTING AND PROPOSED EXPERIMENTS.

A. *Existing experiments.*

The measurement of the gravitational mass of individual particles has been achieved only on neutral particles, namely photons [9,10], neutrons [11] and atoms [12]. Although several techniques have been proposed [1,4,13,14], no measurement has been successfully carried out on charged particles. Only indirect determinations have been deduced from measurements on bulk matter [15]. As mentioned previously, the situation is even more dramatic for antiparticles since cooling them at ultra-low energies is made difficult by their large annihilation cross-sections. State-of-the-art developments on the antiproton include the Gabrielse trap [16] and the Holzscheiter trap [4]. These traps have been shown to capture and hold up to 10^6 particles for several months under optimum vacuum conditions using cryo-pumped cavities [17]. In the Gabrielse trap [16], the slowing down of individual antiprotons down to velocities of a few hundreds m/s, typical of the velocities we will consider in the following, has been achieved. On the other hand, the Holzscheiter group [18] has demonstrated the feasibility of extracting antiprotons from the trap and transferring them to other experiments.

B. *Residual electric field problems.*

It should be remembered that the action of gravity on a proton can be counterbalanced by an electric field $\mathcal{E} = m_p g/e \approx 10^{-7}$ V/m. For an electron, this field is of course approximately 2000 times smaller and of the order of 5×10^{-11} V/m. This gravitational force is so weak that the attraction force of an electron to the Earth is equivalent to the electrostatic force applied

by a single electron 5 meters away. For this reason, the measurement of the gravitational mass of the antiproton appears more realistic than that of the positron. Even in this case, however, all nongravitational forces must be suppressed with a high degree of accuracy.

The experimental problems raised by the gravitational mass measurement of individual charged particles have been reviewed by Darling *et al.* [20]. The main experimental difficulty appears to be due to the patch effect [7]. To reduce the ambient electrostatic forces, a metallic drift tube is used in all existing or proposed experiments. However, although textbooks state that the electric field is zero inside a conducting cavity, the non-uniformity of the dipole density at the surface of crystal domains induces a residual field. This effect, called patch effect, is due to variations of the work function from one domain to another by a fraction of eV. For some metallic surfaces with amorphous coatings, the variations of the surface voltage Φ_Σ integrated over the area of a Kelvin probe appear to be reduced close to its sensitivity [7] which lies in the mV range. The size of these patch domains is typically $l \approx 1\mu$m. The residual potential fluctuation along the axis of a cylinder with radius ρ has a root mean square value $\Phi_{rms} \approx 0.6\ \Phi_\Sigma l/\rho$. This would correspond to potential variations less than 10^{-5} V in a tube with $\rho = 0.1$ m. In order for the patch effect to be negligible with respect to the gravity force, a reduction of such variations by two orders of magnitude seems then required. Therefore, these stray electric fields which can very easily overwhelm the effect of gravity constitute the most stringent constraint on any measurement of gravity on a charged particle.

In these conditions, the measurement of the gravitational mass of a charged particle appears extremely problematic since existing and proposed experiments can only give access to a single quantity, i.e. time-of-flight or position of the particle, after which the particle is either irretrievably perturbed or even annihilated. Repeated weakly perturbative measurements thus appear necessary to disentangle the gravity and electric field contributions. We now discuss whether position sensors based on SETs could meet these two requirements.

III. THE SINGLE ELECTRON TRANSISTOR

A. *Description.*

Various single electron devices in which the current results from subsequent transfers of single electrons have been operated during the last ten years [24]. The SET is the basic active device of single electronics. It consists of two ultrasmall tunnel junctions in series, with a small intermediate electrode (island) capacitively coupled to a gate electrode (see Fig. 1). This device is characterized by the tunnel resistance R_t of each junction and by the total capacitance of the island C =$C_g + 2C_j$, where C_g and C_j act respectively for the gate and junction capacitances. In a voltage biased SET, the current is periodically modulated by the gate voltage V_g, the period corresponding to one electron charge induced in the island.

Two conditions are required for operating a SET :

1) The tunnel resistance R_t of each junction should be of the order of or larger than the resistance quantum $R_K = h/e^2 \approx 25.6$ kΩ.

2) The island capacitance C must be small enough and the temperature must be low enough so that the energy $E_c = e^2/2C$ required to add a single electron charge to the island exceeds by far the available energy of thermal fluctuations, i.e., $E_c \gg k_B T$. In practice, C≈1 fF, which requires sub-Kelvin temperatures.

When these conditions are satisfied, the island charge corresponds to an integer number of extra electrons and the current results from the sequential tunneling of electrons one by one through both junctions. Each tunnel event occurs at a rate which depends on the change in electrostatic energy that it induces. Since the electrostatic energy of the island depends on the gate voltage, the current through the device is modulated by the gate voltage.

B. *A highly sensitive electrometer.*

Current modulation curves of a typical SET with metallic tunnel junctions are shown in Fig. 2. A maximum modulation depth of the order of $e/(R_t C)$ is obtained for a bias

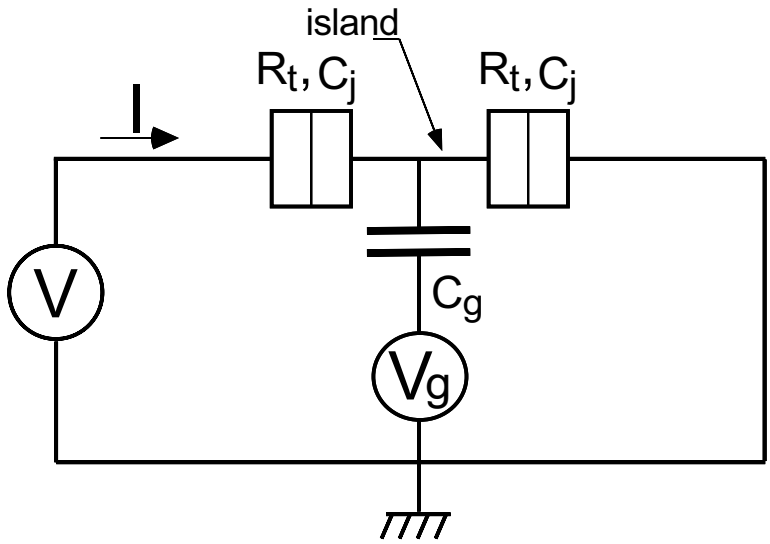

Figure 1: Schematic diagram of a voltage biased Single Electron Transistor. The intermediate electrode between the two tunnel junctions is an ''island'' whose charge is quantized in units of e. R_t and C_J are respectively the tunnel resistance and the capacitance of each junction. The gate voltage induces a polarization charge on the island which modulates the current.

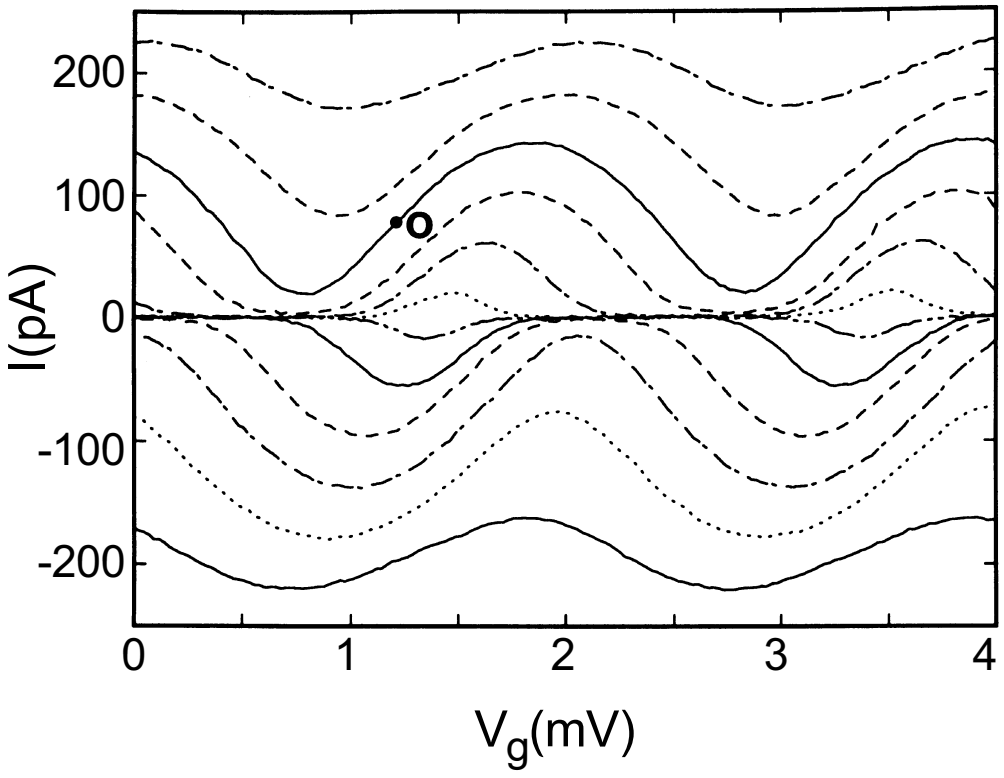

Figure 2 : Current modulation curves of a SET as a function of the gate voltage for a temperature of 20 mK. The different curves correspond to a set of values of the bias voltage V separated by 25 μV. The island capacitance is C=0.6 fF. The maximum charge sensitivity is obtained at the working point O.

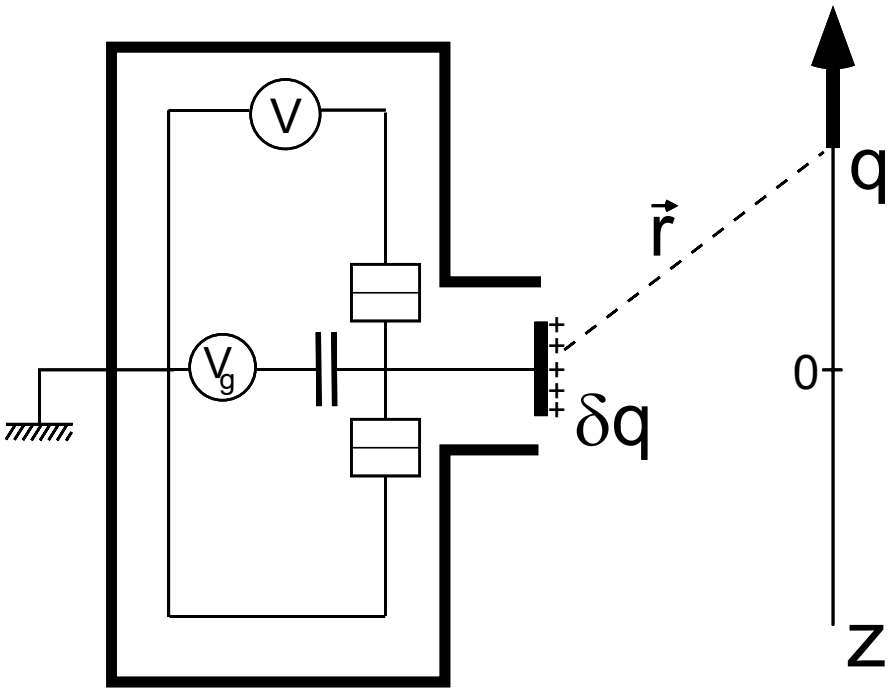

Figure 3 : Schematic diagram of a charged particle position sensor based on a SET. The SET measures the polarization charge dq induced by the charge q moving along the z axis.

voltage $V \approx e/C$. Any variation of the electric field near the island will induce in the island a polarization charge that will act in the very same way as a similar change of the gate charge $q = C_g V_g$. Since a SET is a sub-electron sensitivity electrometer for the induced polarization charge on the island, it is worth noticing that SETs can already provide an important improvement in the measurement of the residual electric field in a metallic drift tube as compared to Kelvin probes [7].

IV. SET AS A POSITION SENSOR FOR CHARGED PARTICLES

It is now clear that a SET can detect, at least in principle, the passage of a charged particle in the vicinity of its island. The operating principle of such a detector is sketched in Fig. 3. The island of the SET actually behaves like an antenna which probes locally the electric field in the drift tube. Its self-capacitance contributes to the total island capacitance C. The grounded electrode surrounding the SET shields the electric field due to the voltage sources. One should however take care to keep the interaction energy between the particle and this ground electrode sufficiently small to prevent trapping of the particle when passing in front of the detector.

The SET measures the polarization charge δq induced in the island by the charge q moving along the z axis of the drift tube. The Gauss reciprocity identity shows that $\delta q = -q\mathrm{V}(\vec{r})/\mathrm{V}_0$, where $\mathrm{V}(\vec{r})$ is the potential at point $\vec{r}$ when the island is at potential V_0. The coupling constant $\alpha(\vec{r}) = -\delta q/q = \mathrm{V}(\vec{r})/\mathrm{V}_0$ is a geometrical factor which depends on the position of the particle and on the shape of the electrodes. Expected variations of α when a charged particle follows the z axis of a drift tube are shown in Fig. 4a. The characteristic width w of this interaction curve is of the order of the minimal distance between the SET island and the particle. It is worth noticing such a position sensor could also be used to monitor the position of an antiproton in a trap.

The reciprocity theorem also implies that the measuring SET will have a back-action on the particle. As seen from the particle, the fluctuating electric field due to the variations of

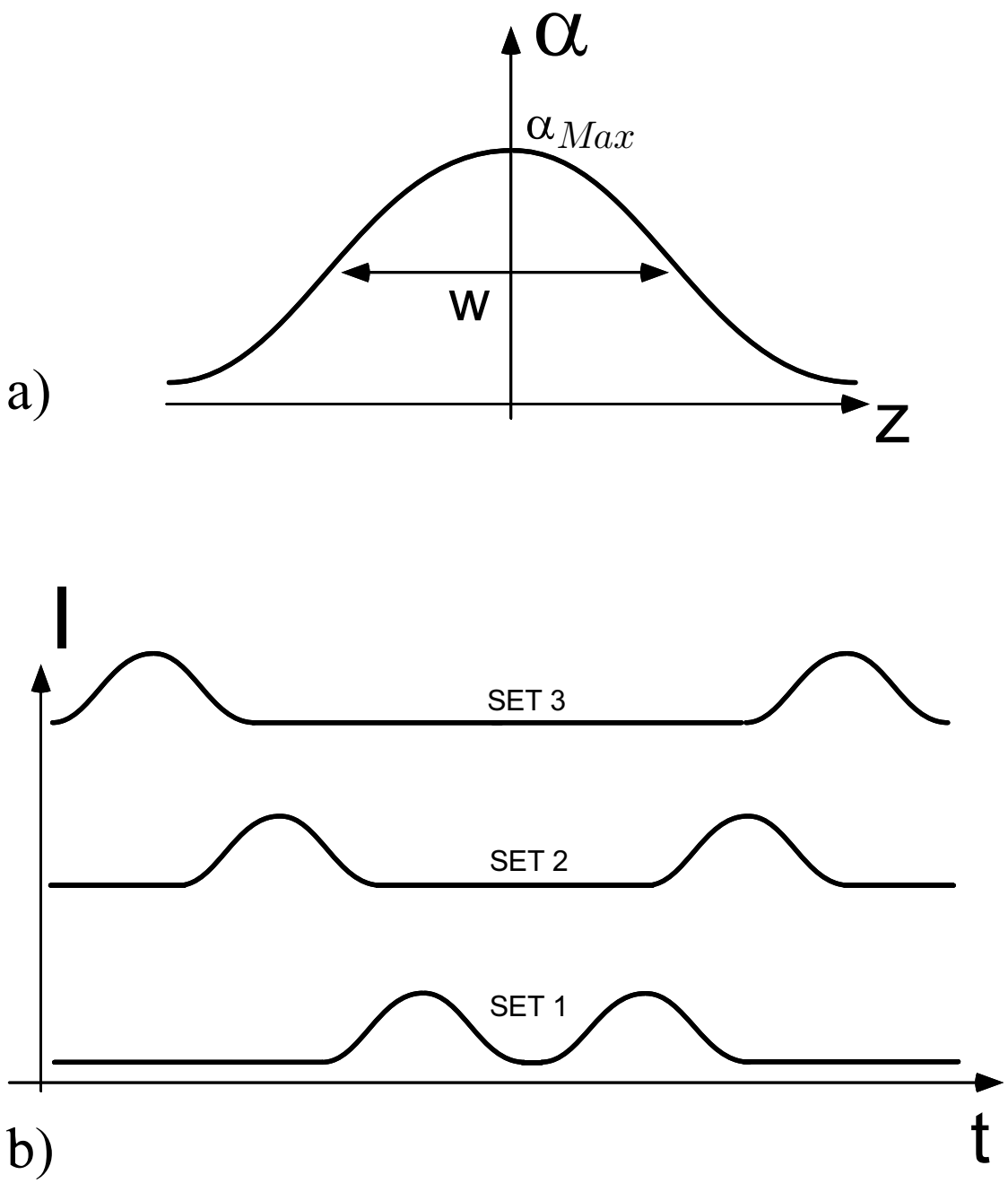

Figure 4: (a) Expected dependence of the electrostatic coupling constant a with the particle position z. The width w is of the order of the minimal distance between the particle and the island. (b) Expected time dependence of the current in three SETs distributed along a drift tube containing a trapped antiproton moving back and forth between two reflectors. The effect of gravity is deduced from the analysis of the passage times.

the number $n(t)$ of extra electrons on the island is given by :

$$\vec{\mathcal{E}}(\vec{r},t) = n(t)\,(e/C)\,\vec{\nabla}\alpha\,(\vec{r})\,. \tag{1}$$

The observation of the moving particle will thus induce a modification of the kinetic energy of the particle.

A. *Detection sensitivity of the SET electrometer.*

Two kinds of noise limit the accuracy of the SET as a charge detector.

1. Shot Noise.

The first source of noise is intrinsic to the device: the successive transfers of single electrons are uncorrelated and constitute a Poisson process. At the optimal working point of the SET, the characteristic time τ of this Poisson process is $\tau \approx R_t C$. The current noise is equivalent to a white noise in the charge to be measured with a spectral density $q_N \approx \sqrt{2\tau}\ e/\sqrt{\mathrm{Hz}}$. This noise figure is $q_N \approx 10^{-5}\ e/\sqrt{\mathrm{Hz}}$ for an optimized SET with a bias current of about 1 nA.

2. Background charge noise.

The second source of noise is extrinsic: since the SET measures the polarization charge induced on the island, any displacement of charges in the vicinity of the island results in a parasitic signal. It has been observed that this noise originates from a collection of charges randomly jumping between two positions. Each of them acts as a two-state fluctuator producing a telegraphic noise with a given characteristic switching time. The superposition of all these fluctuators results in a $1/f$ noise [21]. The amplitude of this $1/f$ charge noise currently observed in SET's regardless of the composition of the substrate is $q_N^{'} \approx 3 \times 10^{-4} e/\sqrt{\mathrm{Hz}}$ at 10 Hz. It dominates the intrinsic shot noise up to a crossover frequency

of the order of 10 kHz and result in a long time drift of the SET working point. A low-frequency feed-back on the gate voltage is necessary to maintain the working point at the optimal gain and to prevent the $1/f$ noise from acting on the moving charged particles. The determination of the passage time of the particles is then not affected by the $1/f$ noise provided that the measuring time is less than 10^{-4} s. In this case, the passage time of a particle with velocity v_0 and charge e can be determined with an accuracy w/v_0 provided that the following condition is satisfied :

$$\alpha_{Max}\sqrt{\frac{w}{v_0}} > \frac{q_N}{e} \tag{2}$$

B. *Operation of a SET at high frequencies.*

The measurement bandwidth of SETs is usually limited by the cut-off frequency of the filtering circuitry connecting the device to the room temperature amplifiers. Coupling the SET to a cryogenic amplifier that provides impedance matching is necessary to obtain a large bandwidth. One realization [22] has been achieved by bonding a SET to a InP High Electron Mobility Transistor (HEMT) thus leading to a cut-off frequency of 700 kHz at the expense of an increased noise of $3\times10^{-4}e/\sqrt{\text{Hz}}$. Direct fabrication of a SET directly on top of a HEMT is also promising [23].

C. *Back-action of the measurement on the particle.*

The electric field produced by the island charge at the particle position modifies its energy. The change δE of the particle kinetic energy E_0 after one measurement is $\delta E = e\int \mathcal{E}_z(z = v_o t, t)v_o dt$. Using the expression (1) of the electric field, we obtain :

$$\delta E = 2E_c \int n(t)\frac{\partial \alpha}{\partial z}(z = v_0 t)v_0 dt \tag{3}$$

The systematic part of δE cancels out because the temporal average of $n(t)$ only depends on the position of the particle through the coupling coefficient $\alpha(z)$:

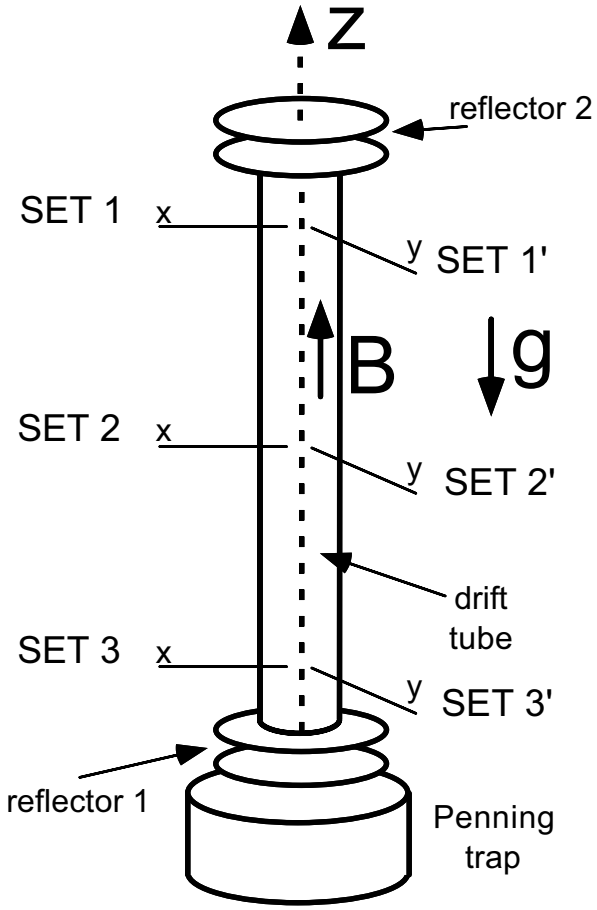

Figure 5 : Sketch of the antiproton gravitational mass measurement based on SETs. Antiprotons in a Penning trap are injected in a drift tube and move back and forth between two reflectors. X and Y position sensors based on SETs are distributed along the tube in order to monitor the trajectory.

$$\overline{\delta E} = 2E_c \int_{trajectory} \bar{n}(\alpha) \frac{\partial \alpha}{\partial z} dz = 0$$

The assumption that the velocity of the particle remains almost constant during the measurement requires, however, that:

$$2E_c \int_0^{\alpha_{Max}} \bar{n}(\alpha) d\alpha \approx E_c \alpha_{Max}^2 \ll E_0 \tag{4}$$

The standard deviation δE^* of the fluctuating part of δE is readily calculated assuming that $\tau \ll w/v_0$:

$$\delta E^* \approx E_c \sqrt{v_0 \tau \int_{trajectory} \left(\frac{\partial \alpha}{\partial z}\right)^2 dz} \approx E_c \alpha_{Max} \sqrt{\frac{v_0 \tau}{w}} \tag{5}$$

Ensuring that the effect of gravity on the particle trajectory is not washed out by the back-action thus implies the following constraint on the design parameters :

$$E_c \alpha_{Max} \sqrt{\frac{v_0 \tau}{w}} \ll m_p g L \tag{6}$$

This constraint limits the maximum coupling α_{Max} and thus prevents from benefiting of the full sensitivity of the SET. This constraint is not, however, a fundamental limitation imposed by quantum mechanics. In particular, the randomness in the charge-discharge cycles of the island could be avoided if the island state corresponded to a coherent quantum superposition of two charge states. SETs based on 2D electron gases could be, in principle, operated in this regime, but the issue of back-action noise has not yet been investigated. On the other hand, the large magnetic field in the drift tube forbids the use of superconducting single Cooper pair electrometers which might also present a smaller back-action noise.

V. DESIGN OF A SET-BASED $\bar{\mathrm{P}}$ GRAVITATIONAL MASS MEASUREMENT

A. *Description.*

The proposed geometry for the gravitational mass measurement of a charged particle is schematically represented on Fig. 5. The particle (proton, antiproton, H^- or ion) is released

from a Penning trap and confined along the vertical axis of a drift tube by a magnetic field of typically 1 T. For the velocities considered here, typically 100 m/s, the cyclotron radius $R = m_p v_0/(eB)$ of the trajectory is of the order of 1 μm so that the motion can be considered to be one dimensional.

After the particle has been released from the Penning trap in the measurement region, the potential at the electrode reflectors is increased so that the particle bounces back and forth and is confined in the central region where the potential is kept as constant as possible.

Since the measurement is non-destructive, several SETs can be placed along the drift tube to monitor the trajectory (see Fig. 5). In the configuration proposed, three measurement positions are used. Two SETs have been placed at each measurement position in order to estimate both the x and y transverse coordinates of the particle. Since obviously the gravitational mass measurement requires a very small residual electric field in the measurement region, the trajectory of the particle will slowly drift over a timescale of seconds. The measurement of this drift will provide a further estimate of stray electric fields together with the gravitational force. A differential measurement comparing the trajectories of antiprotons and H^- ions, with the same electric charge, could provide a determination of the difference of gravitational mass of these particles. In the case of H^- ions, the Stark effect in the residual electric field also contributes to modify the trajectory. However, this effect, compared to the effect of gravity, is negligible for the residual field amplitudes that have to be obtained in the experiment.

B. *Determination of the gravitational mass.*

The potential energy $U(z)$ of the particle in the tube is the sum of an electrostatic and of a gravitational contribution. Assuming that $U(z)$ is small compared to the total energy of the particles $E = \frac{1}{2}\mathfrak{m}v_0^2$, the velocity v is:

$$v = \sqrt{\frac{2}{\mathfrak{m}}\left(E - U\left(z\right)\right)} \approx v_0 \left(1 - \frac{U\left(z\right)}{\mathfrak{m}v_0^2}\right)$$

which gives for the passage time $t\left(z\right)$ at position z :

$$t\,(z) \approx \frac{z}{v_0} + \frac{\int_0^z U(z')dz'}{\mathfrak{m}v_0^3}$$

From the comparison of the passage times of antiprotons and of H^- particles at three heights z_i along the tube, it is possible to get rid of the common electrostatic contribution through the differences $\int_{z_i}^{z_f} U_{\bar{p}}(z')dz' - \int_{z_i}^{z_f} U_{H^-}(z')dz' = (m_{\bar{p}} - m_{H^-})g(z_f - z_i)$, where $m_{\bar{p}}$ and m_{H^-} are the gravitational masses to be compared. Repeated measurements would increase the accuracy by averaging the back-action of the measuring SETs on the particles.

C. *Operating parameters.*

From the previous discussion, we propose here a realistic set of parameters that make it possible to determine the gravitational mass of the antiproton :

- The PS196 experiment [16,17] has shown that antiprotons can be slowed down to velocities $v_0 \approx 100$ m/s (i.e. with an energy $E_0 \approx 50$ μeV).

- We assume that a $L \approx 1$ m long drift tube with sufficiently low residual electric field can be fabricated. A drift tube with a similar length is presently used by the PS200 experiment [19]. The corresponding gravitational energy change for a proton over this distance is $\delta E_G = m_p g L \approx 0.1$ μeV.

- The charging energy of each SET is chosen to be $E_c \approx 20$ μeV which corresponds to a total island capacitance $C \approx 5$ fF. This requires an operating temperature of 50 mK. The tunnel resistance is chosen such as $\tau \approx R_t C \approx 10^{-10}$ s.

- The chosen SET coupling parameters are $\alpha_{Max} \approx 0.05$ and $w \approx 500$ μm. These values appear to be consistent with the chosen island capacitance C. With this set of parameters, the characteristic energy change δE^*due to back-action given by (3) is of the order of 0.005 μeV, which corresponds to 5% of δE_G.

- Assuming that the SET sensitivity is only limited by the shot-noise $q_N \approx 10^{-5}$ e/$\sqrt{\text{Hz}}$ and that the bandwidth is 1 MHz, the signal to noise ratio obtained from Eq. (2)

is $e\alpha_{Max}/q_N\sqrt{w/v_0} \approx 10$. The expected time resolution is therefore better than the interaction time $w/v_0 \approx 5$ μs.

VI. CONCLUSIONS AND PERSPECTIVES

From the previous discussion, we conclude that SET based technology offers an alternative for charge sensing that could be used to monitor the trajectory of a charged antiproton in a trap or in a drift tube. The measurement of the gravitational mass of a single proton or antiproton appears to be feasible by placing state-of-the-art SETs in a 1 m long drift tube provided that residual electric fields are kept low enough.

Acknowledgments

Stimulating discussions with B. Bonin, P. Debu, M. Holzscheiter, Ph. Joyez, A. Mills and C. Urbina are gratefully acknowledged.

REFERENCES

[1] F. C. Witteborn and W. M. Fairbank, Nature 220 (1968) 436.

[2] F. C. Witteborn and W. M. Fairbank, Phys. Rev. Lett. 19 (1967) 1049.

[3] J. M. Lockhart, F. C. Witteborn and W. M. Fairbank, Phys. Rev. Lett. 38 (1977) 1220.

[4] M.H. Holzscheiter et al., Phys. Lett. A214 (1996) 279.

[5] J. M. Lockhart, F. C. Witteborn and W. M. Fairbank, Phys. Rev. Lett. 67 (1991) 283.

[6] N. Beverini et al., CERN proposal CERN/PSCC/86-26 and LANL Report LA-UR-86-260.

[7] J. B. Camp, T. W. Darling and R. E. Brown, J. Appl. Phys. 69 (1991) 7126.

[8] T. A. Fulton and G. J. Dolan, Phys. Rev. Lett. 59 (1987) 109.

[9] R.V. Pound and G.A. Rebka, Jr., Phys. Rev. Lett. 4 (1960) 337; R.V. Pound and J.L. Snider, Phys. Rev. 140 (1965) B788.

[10] R.F.C. Vessot and M.W. Levine, in: Proc. of the 2nd Frequency Standards and Metrology Symposium, ed. H. Hellwig, (1976) p.659.

[11] A.W. Overhauser and R. Colella, Phys. Rev. Lett. 33 (1974) 1237.

[12] M. Kasevich and S. Chu, Appl. Phys. B54 (1992) 321.

[13] G. Testera, these proceedings.

[14] A.P. Mills, these proceedings.

[15] M.M. Nieto and T. Goldman, Phys. Rep. 205 (1991) 221.

[16] G. Gabrielse et al., Phys. Rev. Lett. 57 (1989) 1360.

[17] G. Gabrielse et al., Phys. Rev. Lett. 65 (1990) 1317.

[18] X. Feng, M.H. Holzscheiter, R.A. Lewis, R. Newton, M.M. Schauer, Hyperfine. Int. (1996) in print.

[19] R.E. Brown, J.R. Camp and T.W. Darling, Nucl. Instr. Meth. B56/57 (1991) 480.

[20] T. W. Darling, F. Rossi, G. I. Opat, and G. F. Moorhead, Rev. Mod. Phys. 64 (1992) 237.

[21] C.T. Rogers, R.A. Burhman, W.J. Gallagher, S.T. Raider, A.W. Kleinsasser and R.L. Sandstrom. IEEE Trans. Magn., 23 (1987) 1658.

[22] J. Pettersson, P. Wahlgren, P. Delsing, N. Rorsman, D. B. Haviland, H. Zirath and T. Claeson, Göteborg University preprint (1996).

[23] E. H. Visscher, J. Lindeman, S. M. Verbrugh, P. Hadley, J.E. Mooij and W. van der Vleuten, Appl. Phys. Lett. 68 (1996) 2014.

[24] M. H. Devoret, D. Esteve and C. Urbina, Nature 360 (1992) 547; For a more complete review of this field see *Single Charge Tunneling*, NATO ASI series, eds. H. Grabert and M. H. Devoret (Plenum, New York, 1992).

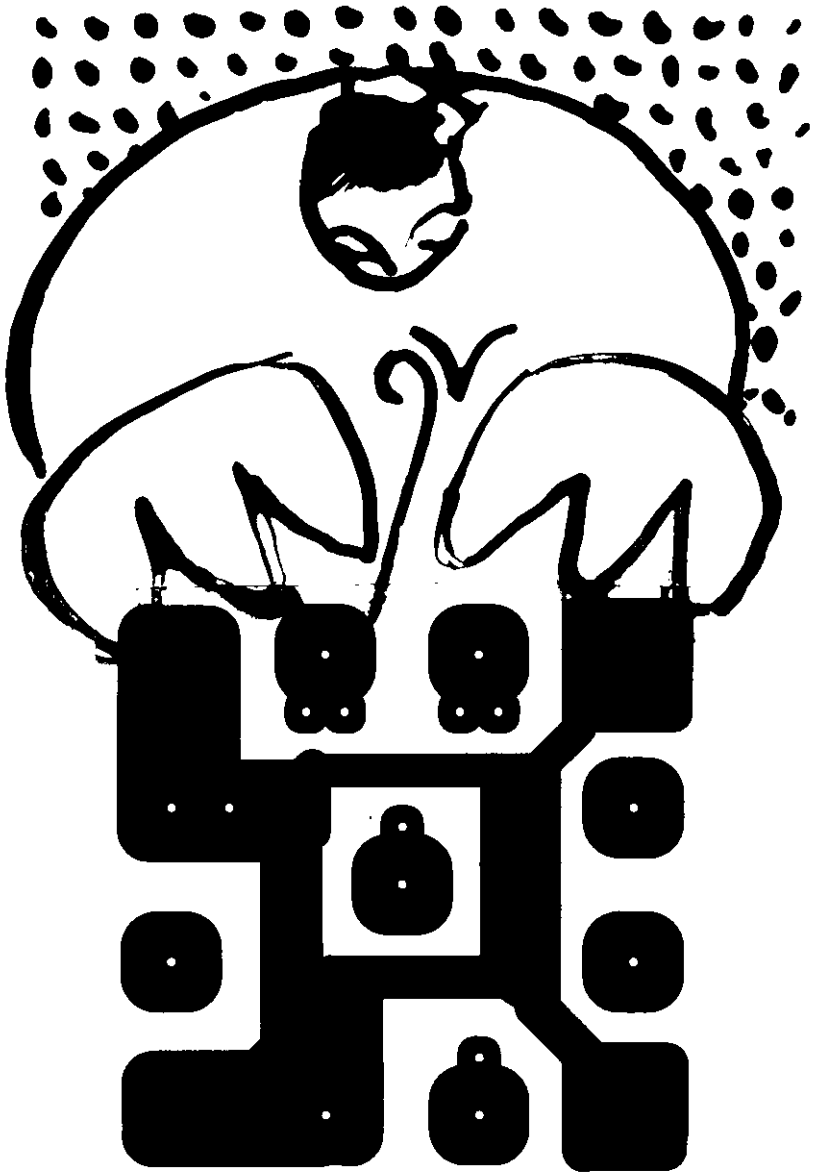

Chapter 6

Fabrication techniques

Introduction

The discovery of single electron charging effects and of other new phenomena in mesoscopic physics results from the advances obtained during the last 15 years in the fabrication of nanostructures. During that period, physical principles were selected and processes were optimized in order to reach smaller dimensions. These recently developed techniques keep sufficient versatility to allow the fabrication of a wide range of structures using a wide range of materials. Almost all the fabrication of nanostructures can be separated in two main steps which are respectively the patterning of the structure using a mask obtained by a writing technique, and the deposition of materials. Since the patterning technique limit the resolution, developments principally occurred in that field. The two writing techniques responsible for recent advances are the X-ray lithography and the electron beam lithography which both involve radiations with an associated wavelength so short that diffraction effects do not limit the resolution. We present in the following the technique of electron beam lithography and its adaptation to the fabrication of single electron (or single Cooper pair) devices.

Another recent trend of nanostructure fabrication was to take advantage of advances in microscopy to develop new patterning processes: The discovery of proximal probe microscopies composed by the scanning tunneling microscope [1] and followed by the atomic force micro-

scope (AFM) [2] that has shown that imaging at the atomic scale is possible, have inspired many new ways for fabricating nanostructures "from bottom to top", eventually leading to the direct manipulation of single atoms [3]. We present inthe following, a general fabrication technique using the atomic force microscope to fabricate structures with a resolution comparable with those currently obtained using electron beam lithography.

6.1 Electron beam lithography

In the technique of electron beam lithography (EBL), a focused electron beam, emitted from the gun of an electron microscope, locally alters a polymer resist. The beam position is monitored by a computer in such a way that a precise irradiation dose is delivered on the sample inside the designed pattern. Between two area exposures, the beam is shifted away from the sample using beam blanking. After exposure is completed, the sample is removed from the microscope and placed in a specific solvent with a great solubility difference between exposed and non-exposed areas. In the case of polymethylmethacrylate (PMMA) resist which is a positive resist, the exposed areas are completely removed by the solvent while the non-exposed ones remain unaffected. This structure forms a mask which can be used in different fabrication processes. Two kinds of processes are generally employed. In the first one, thin layers of insulating or metallic material are deposited on top of the mask prior its removal in a solvent (lift-off technique, see Fig. 6.1 left). In the second one, the pattern generated by the height contrast between exposed and non-exposed areas is transferred to a layer underneath using dry etching (etching technique, see Fig. 6.1 right). The resolution reached by EBL is not limited by the electron beam radius nor by diffraction but by the scattering of decelerating electrons inside the resist resulting in a partial exposure of the resist near the exposed pattern. This broadening effect is especially important near large exposed areas where all small details in the vicinity must consequently be underexposed according to a position-dependent exposure dose correction. Such a proximity effect makes EBL a non-straightforward technique for complex patterning. Since the scattering depends on the energy of accelerated electrons, the achieved resolution lies between 50 nm for the 40 keV beam emitted of a scanning electron microscope to around 10 nm for the high energy beam (around 300 keV) generated by a transmission electron microscope [4, 5] .

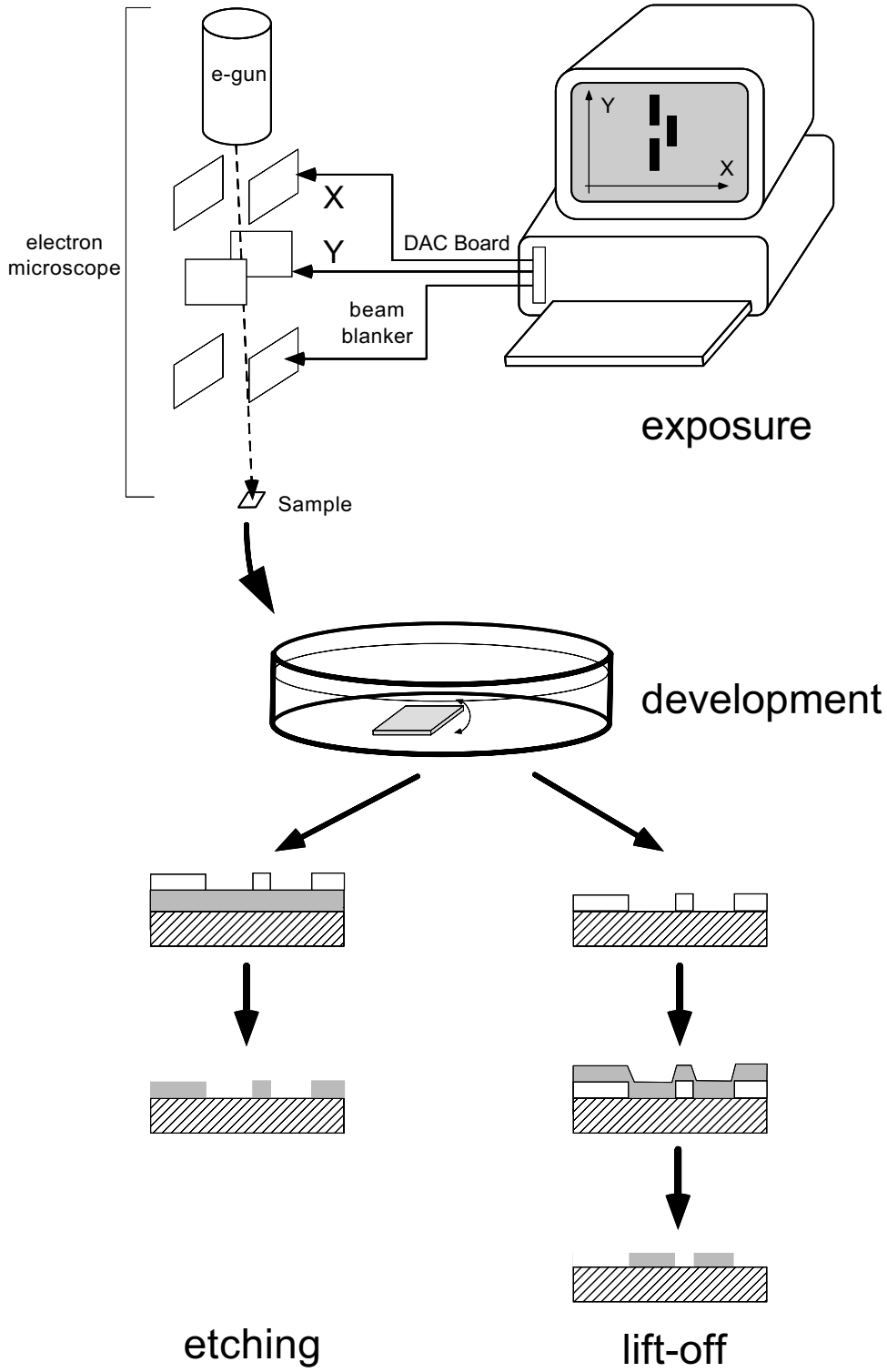

Figure 6.1 Electron beam lithography.
Top: the digital-to-analog convertor in a PC monitors the X/Y deflection of an electron microscope beam.
Bottom: the two main post-processing sequences of an resist mask (white parts).
Left column: The height contrast is transferred onto a bottom layer by dry-etching.
Right column: The developed resist is used as a mask through which the top layer is evaporated. Traces of resist are finally removed in a solvent during the lift-off process.

In our laboratory, we use a 35 keV electron beam generated by a customized commercial scanning electron microscope JEOL 840. With this apparatus it is routinely possible to accurately fabricate, using technology described in the following, lift-off masks with a resolution of the order of 60 nm.

6.2 Nanofabrication techniques for single electron devices.

The observation of single electron charging effects in metallic islands requires the fabrication of small electrodes connected through ultrasmall tunnel junctions. We have seen in previous chapters that the tunnel junction size directly sets an upper limit for the operating temperature of a single electron device. More precisely, the capacitance of an aluminum-oxide tunnel junction with typical a overlap area of 0.1×0.1 μm^2 is of the order of 1 fF, regardless of the junction tunnel resistance. The associated charging energy corresponds to a temperature of 1 K. Measuring single electron charging effects in such samples thus requires to cool the sample down to temperatures T $\leq$ 0.1 K which are routinely obtained in a ^{3}He - ^{4}He dilution refrigerator. Therefore, both design and fabrication of the tunnel junctions, even though they represent only tiny fractions of the whole structure, appear as critical.

Because we need, above all, devices with well-controlled parameters, the reliability of the fabrication processes is more important than the achieved resolution. The required reproducibility is obtained using a suspended mask, which ensures self-alignment of tunnel junction electrodes. In the first part of this chapter, we describe three different processes leading to a suspended mask: the well-known bilayer and trilayer processes, based on EBL, and a new one that uses atomic force microscopy.

On the other hand, the field of single charge tunneling has now reached a stage in which more complex structures must be fabricated to observe new properties. In order to meet this demand, we have developed techniques that implement features which were impossible to obtain with classical processes. As an example, we are going to show how to fabricate three dimensional structures implementing vias, crossings, shielded lines for microwave transmission, resistors and capacitors with overlapping electrodes.

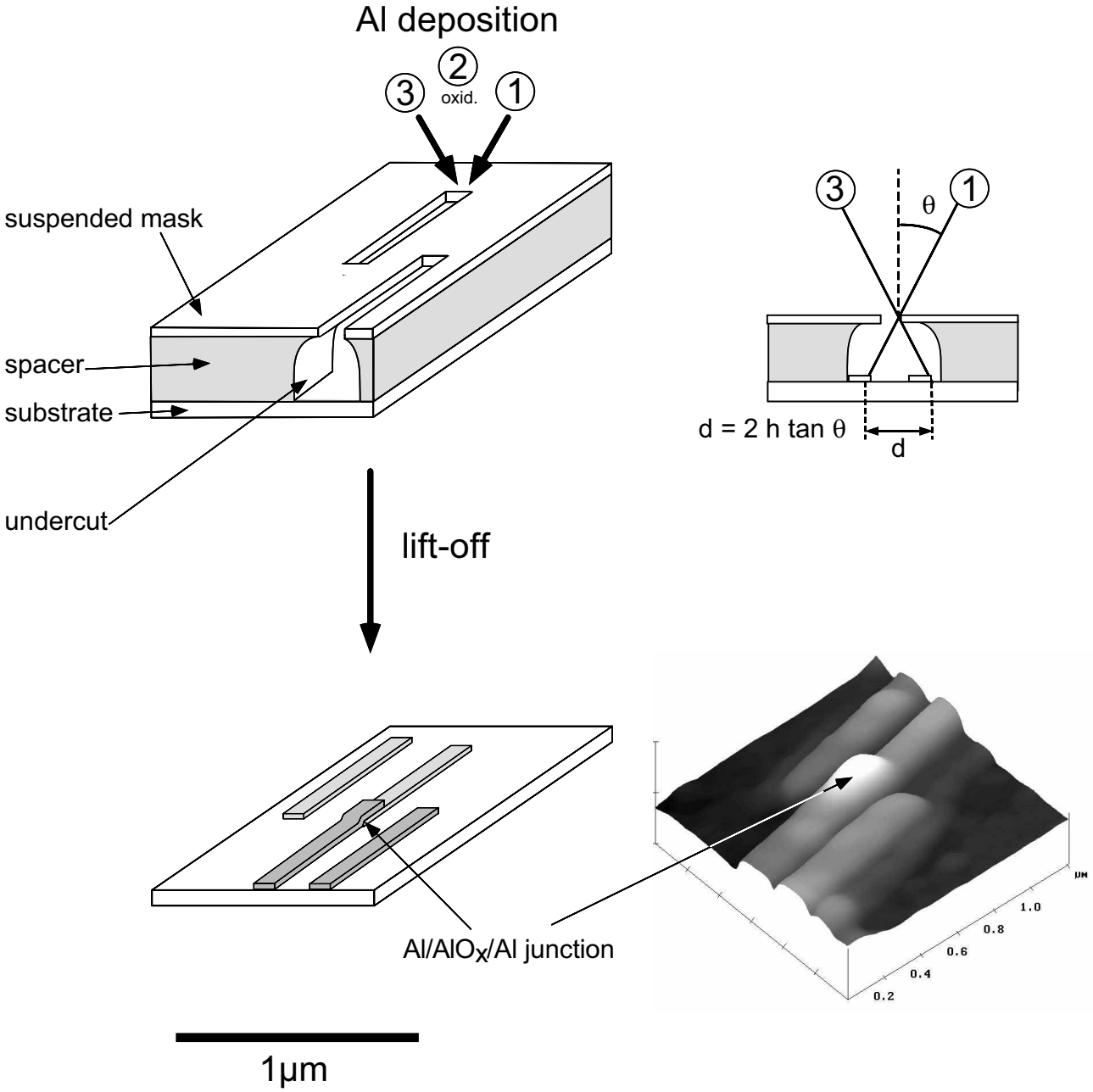

Figure 6.2 Top left: *Schematic diagram of a suspended "double-slit" shadow mask during a two angle deposition of Aluminum* (*steps 1 and 3*). *The first deposited Al layer is oxidized between the two depositions* (*Step 2*).
Top right: cross section of the mask showing the two shifted wires resulting from the two angle deposition through the same slit.
Bottom left: *After lift-off of the mask, the remaining metallic strips overlap on a small surface which forms the tunnel junction.*
Bottom right. Contact AFM image of a typical sample showing the topography height contrast due to both electrodes of the tunnel junction.

6.3 The suspended shadow mask technique.

The shadow mask technique is a widely spread method for fabricating sub-micron metallic tunnel junctions [6] which has been used since the beginning of single electronics [7] . This technique is directly adapted from the lift-off method presented in figure 6.1: the only difference from the basic lift-off is the existence below the mask of a spacer which is etched to provide an undercut (see Fig. 6.2). Thus the mask is suspended over the substrate. If the angle of evaporation is changed between two layer depositions, the mask edge shadows are shifted (see Fig. 6.2): a single slit in the mask leads to separate projected electrodes. The angles are adjusted in such a way that two deposited electrodes overlap over a small area. A tunnel junction is obtained by oxidizing the first aluminum layer prior to the evaporation of the counterelectrode. The junction capacitance and tunnel resistance can be controlled independently by varying the overlap area and oxidation parameters respectively (see appendix 6-F).

The three processes that we have used for fabricating suspended masks are pictured in Fig. 6.3. The first process is called "bilayer process" because it involves two layers of polymer resists [8] . The second is called "trilayer process" because it involves in addition a third intermediate germanium layer which forms the mask. This was the first method developed for fabricating suspended masks [6] . Even though these two processes (bilayer and trilayer) were designed for EBL, both can be adapted to any type of "writing" which generates a height contrast on the top layer. We show below how the atomic force microscope (AFM) can be used in a trilayer process instead of an electron microscope [9] .

6.3.1 The bilayer process

This is up to now the simplest process for fabricating suspended masks. Two layers of polymer resists are deposited using spin-coating on an oxidized silicon substrate (see appendix A-1 for all technical details). The top layer is made of PMMA whereas the bottom layer is made of PMMA/MAA[1] which has a greater solubility in the developer. This solubility contrast creates a cavity below the mask with an undercut profile, thus allowing angle evaporations.

PMMA masks have two features which make them ideal for the multilayer fabrication process presented in part 6.4.

[1] copolymer made of polymethyl methacrylate and methacrylic acid.

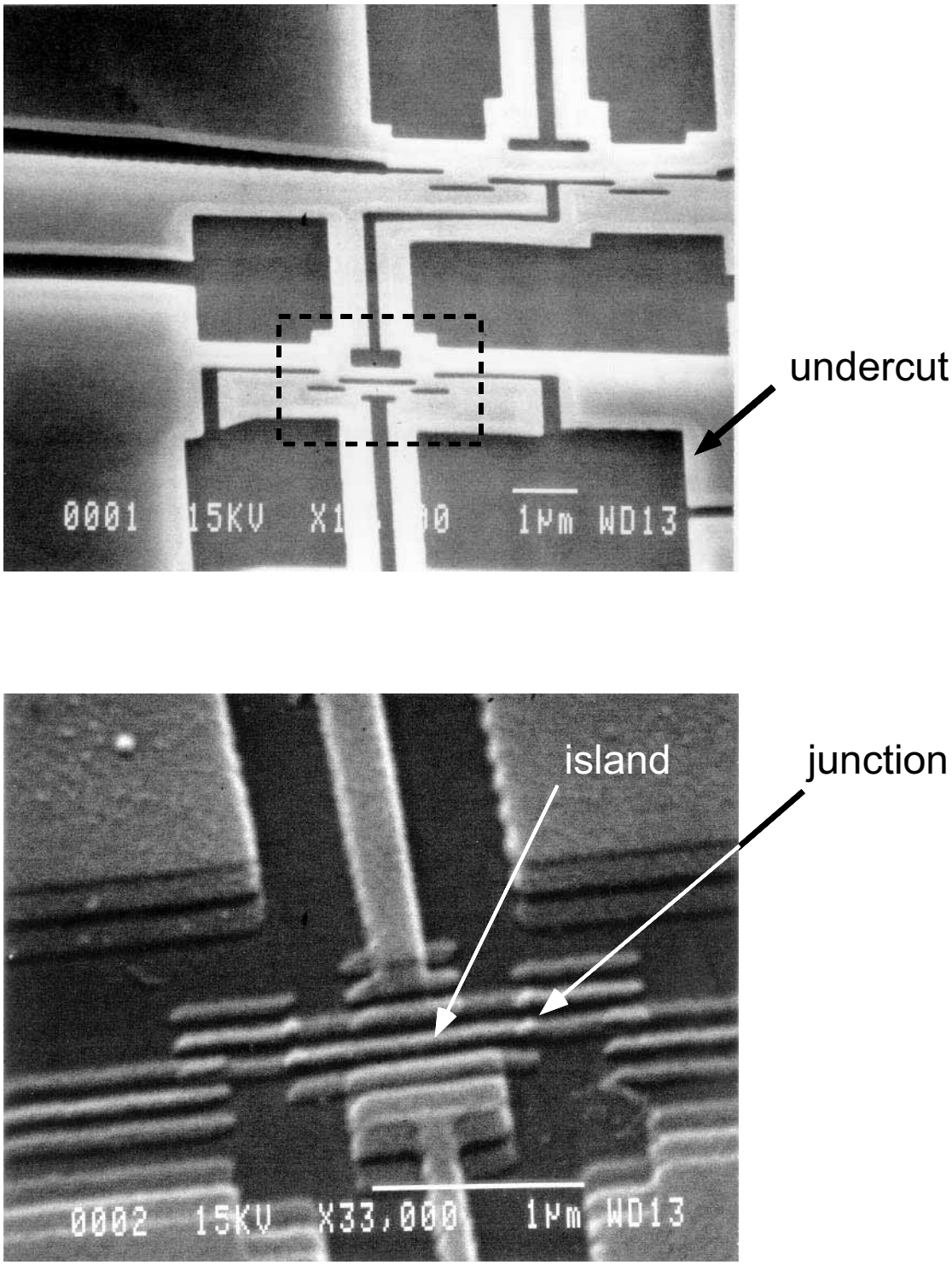

Figure 6.3: Scanning electron micrographs detailing the trilayer process used in early single Cooper pair device fabrication.

Top: *etched germanium mask before deposition. The bright zones surrounding the mask edges corresponds to the undercut in the copolymer ballast layer generated by an isotropic plasma etching.*
Bottom: *fully processed single Cooper pair box obtained after evaporation at three angles through the germanium mask and final lift-off (dashed frame shown above).*

Firstly, the two layers are almost completely transparent to scanning electron microscope electrons thus allowing alignment of the exposed pattern with respect to previously fabricated structures. Secondly, this lithography process can be performed over irregular surfaces because of the smoothing properties of the bottom resist: a 400 nm-thick bilayer resist deposited on a substrate with 500 nm deep holes and surface residual rugosity of typically 10 nm gave a sharp lithography without any noticeable distortion in the shape of the deposited layers (see picture 6.8 top panel).

6.3.2 The trilayer process

In this process (see appendix A-2), a germanium layer is intercalated between two polymer layers with composition and thicknesses similar to the bilayer case. The top PMMA layer is exposed as previously described but the developed pattern is transferred to the germanium mask using anisotropic plasma etching. The undercut which is not obtained during the development of the top resist (because of the protection provided by the germanium layer) is realized using isotropic plasma etching.

Since the suspended mask is now made of germanium, it has an increased robustness compared to PMMA masks. This is crucial for the fabrication of complex patterns with long suspended bridges (see figure 6.4). In particular, it has proven to be useful for fabricating structures requiring three angle evaporation such as our first single Cooper pair device described in chapter 2. Another advantage is that the mask thickness can be strongly reduced compared to PMMA masks: we have successfully used 10 nm-thick Ge masks whereas PMMA mask thicknesses exceed 50 nm. Since the evaporation angle is limited by the thickness of the shadow mask, thin masks allow depositions at larger angles and through narrower slits.

6.3.3 AFM-based lithography: an alternative to e-beam lithography

The basic idea that guided this work was to create a height contrast in a resist layer by scratching it with a sharp AFM tip. We tried several resists such as unbaked PMMA, photoresist, but the best results were obtained with ultra-thin layers of unbaked polyimide which has a soft, non-sticky surface.

Since the AFM tip allows imaging at the nanometer scale, the furrow generated by engraving

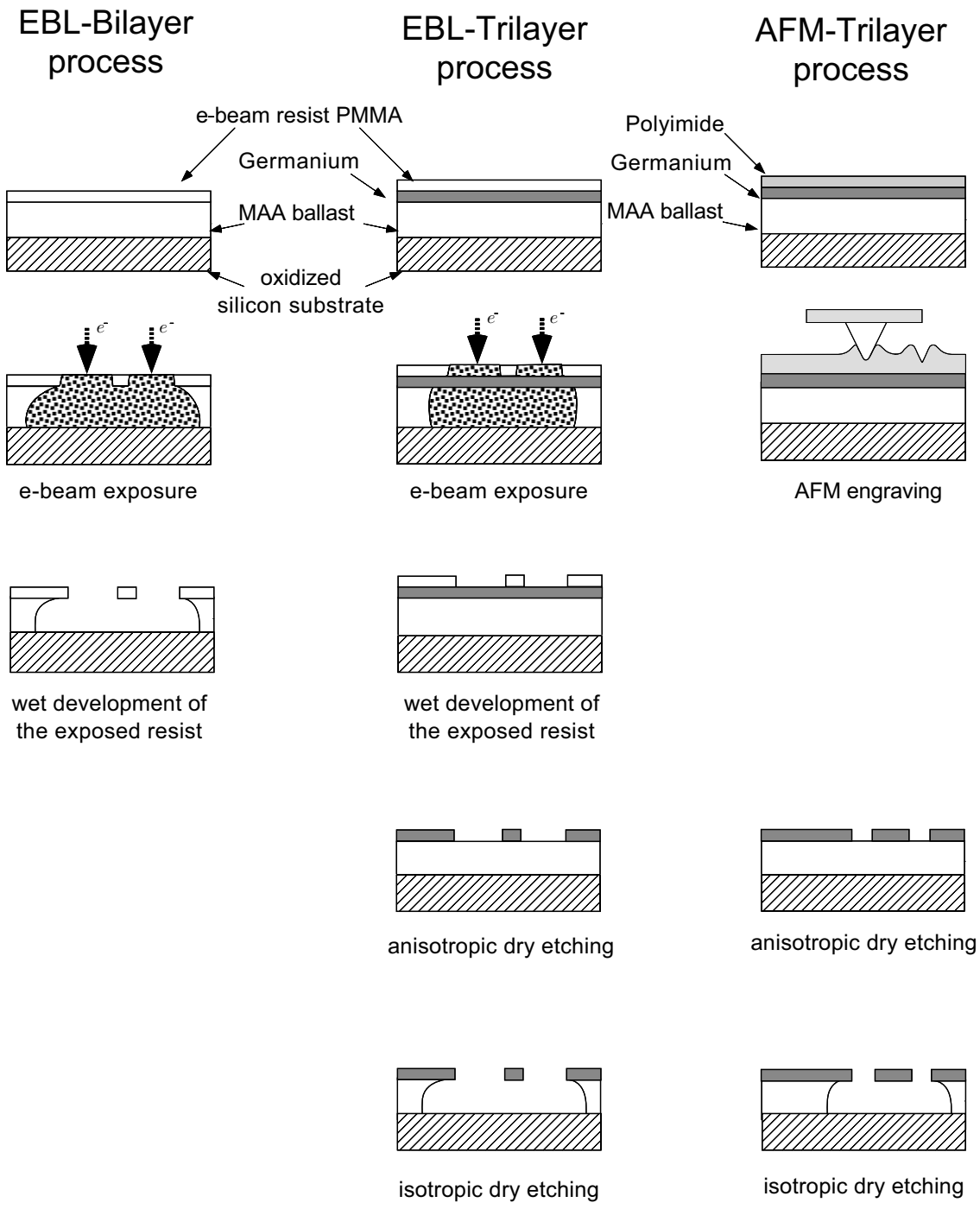

Figure 6.4: Comparison between three processes leading to a suspended shadow mask. EBL processes involve irradiation of the resist by an electron beam whereas the process depicted in right involves engraving with an atomic force microscope.

the polyimide layer is expected to have a width in the same range. This is actually the case but the achieved resolution (of the order of 40 nm) critically depends on the tip quality which is determined by the sharpness of its apex.

We have adapted the trilayer process described above and successfully fabricated single electron devices. These devices present the same characteristics as devices fabricated using conventional electron beam lithography. This process is described in the letter reprinted in appendix 6-B, which reports the fabrication of narrow lines and of single electron transistors. Compared to EBL, the AFM-lithography has two advantages: Firstly, it avoids damaging the underlying structure with high energy electrons. In particular, heterojunctions in semiconductors have been reported [11] to be sensitive to e-beam irradiation. Secondly, since AFM imaging is an intrinsically low-cost technology, AFM-lithography opens the realm of nanofabrication to a larger number of laboratories. The versatility of our process is further illustrated on figure 6.5 which shows lines with a variable width obtained by laterally sweeping the tip during engraving. Figure 6.6 shows the alignment of AFM-fabricated devices over a previously fabricated structure consisting of gold connecting wires. The alignment accuracy is about half a micron.

To conclude with this new fabrication method, we believe there is room for a gain in resolution since we have engraved only a few types of resists with commercially available tips. Since strongly sharpened tips such as those very recently obtained by Dai *et al.* [12] for which a single carbon nanotube is stuck on the apex, becomes available, one should expect to obtain narrower furrows. On the other hand, the understanding of the interaction between the tip and the surface and, more generally, of tribology at the nanometer scale might lead to significant improvements.

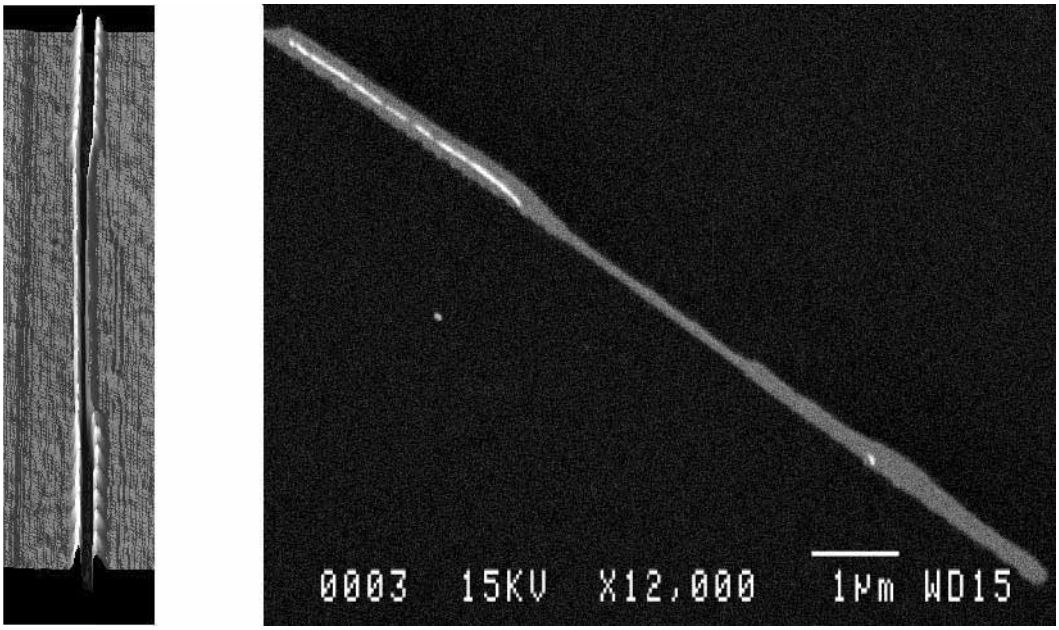

Figure 6.5 Left: AFM micrograph of a furrow engraved in soft polyimide. The broadened extremities were obtained by sweeping the tip lateraly during engraving.
Right: SEM micrograph of the Aluminum wire presenting a variable width. It was obtained after processing the sample which profile is shown in left.

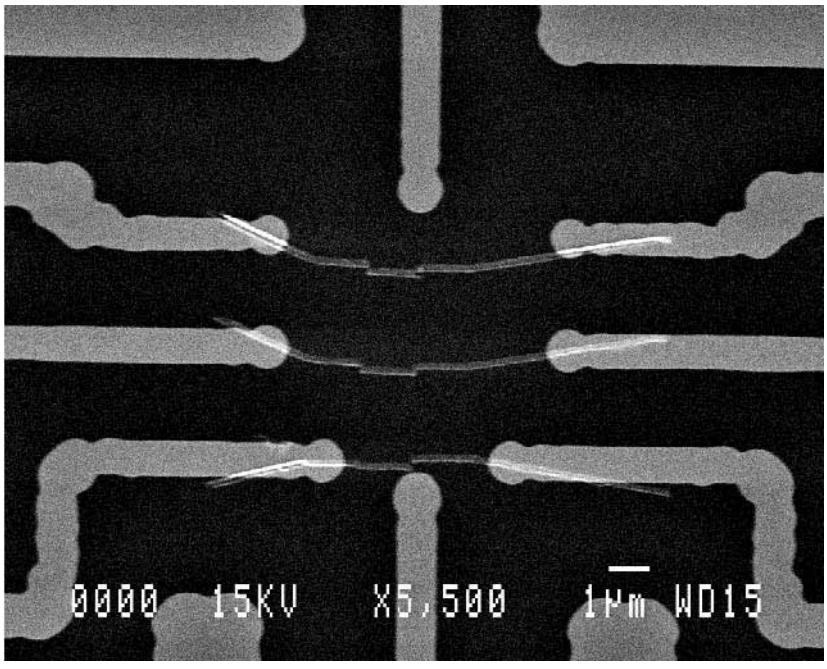

Figure 6.6: SEM micrograph of three single electron transistors fabricated by AFM lithography. These devices are aligned with respect to a pre-fabricated gold circuitry made by optical lithography. The picture shows the alignement accuracy (about half-a-micron) which is currently limited by the hysteresis of the piezo actuators monitoring the tip position.

6.3.4 Comparison between the three processes.

The following table provides a comparison between the three processes: EBL-bilayer, EBL-trilayer and AFM-trilayer, detailing for each process its respective pros and cons.

	Bilayer technique	Trilayer technique	AFM engraving
Advantages	-simplest technique -quick and versatile -allows easy and precise alignment above prefabricated samples -fabrication possible on top of corrugated surfaces	-very robust suspended mask -reduced proximity effect -allows very large undercut (up to several microns)	-no e-beam exposure -instant, non destructive AFM-imaging of the engraved structure.
Drawbacks	-fragile mask, not suitable for complex structures -proximity effect along with e-beam exposure -small undercut	-time consuming technique -substrate polluted during dry etching	-critical processing time during development -patterning of large surfaces is impossible

Table 6.7: Comparison between the three processes leading to a suspended shadow mask.

6.4 Multilayer fabrication

Until now, single electron devices are still mainly fabricated by directly depositing metallic layers on an insulating substrate through a shadow mask in a single pump down (see for example the first fabricated single Cooper pair box in Fig. 6.4 bottom panel). Except for the overlapping tunnel junctions, the resulting structure has a two dimensional topology: the electrostatic coupling between electrodes takes place through planar capacitors which have intrinsically small capacitances and relatively large cross-talk. On the other hand, wires cannot cross without contacting each other, which severely constrains the circuit design. Thus more complex designs require multilayered structures in which conductive layers are separated by insulating ones [10] . Restoring the third dimension has the great advantage to relax topological constraints. However, if one wants to recover all the features of a three dimensional network composed of tunnel junctions, capacitances and connections, contacts between conducting layers must be implemented by piercing vias through insulating layers (see Fig. 6.8).

We present here two methods for multilayer fabrication specially developed in our laboratory

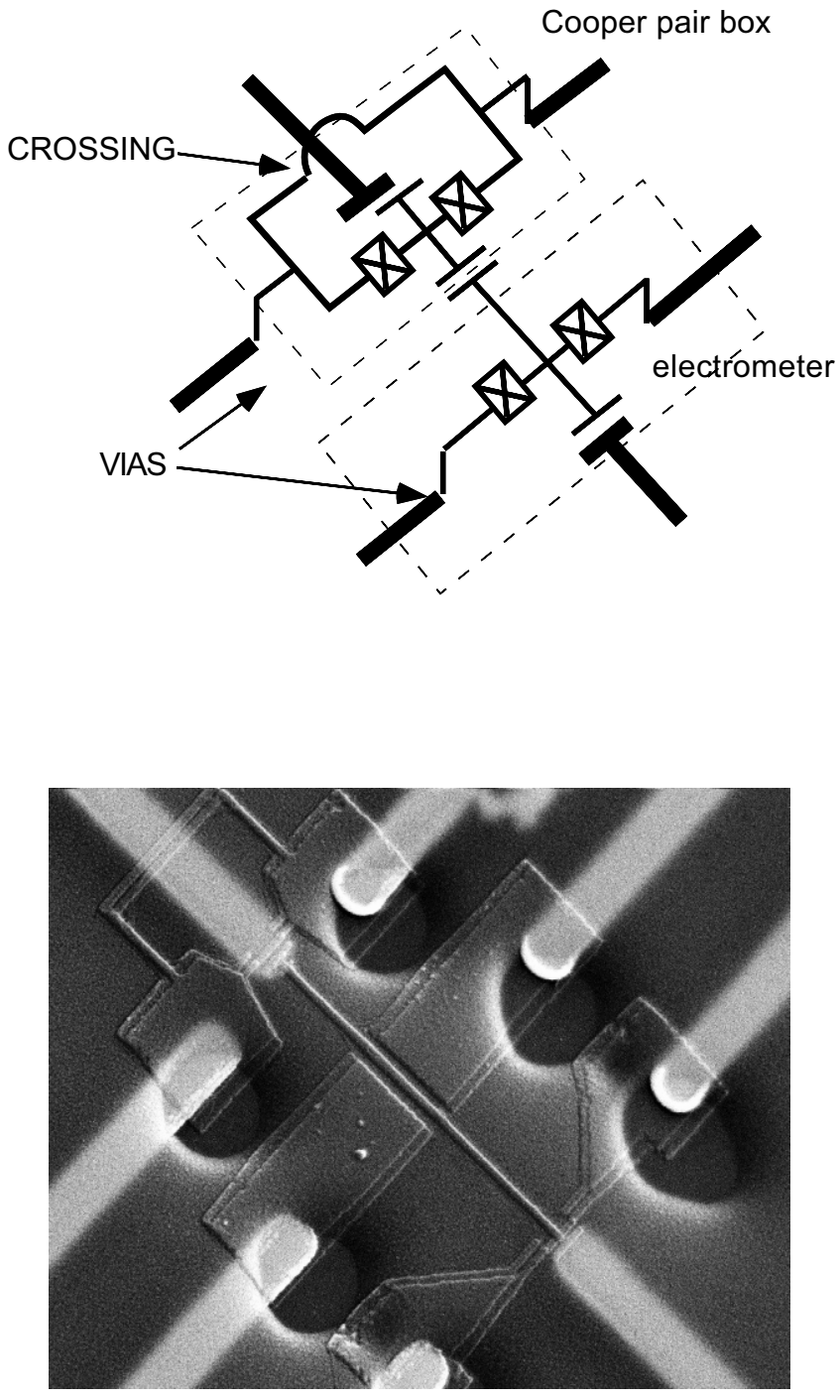

Figure 6.8: *Example of a multilayered device showing implementation of crossings and vias*: *schematic diagram showing the principles (top) and scanning electron micrograph of the ccrresponding fabricated sample (bottom). The device is a single Cooper pair box capacitively coupled to an electrometer measuring the island charge.*

for single Cooper pair devices (see Chapters 2 and 3). In these methods, the chosen insulator is respectively an organic material (polyimide polymer resist) or inorganic material (silicon nitride). In particular, the fabrication of smooth-edged vias requires a specific process.

6.4.1 Principles of the process

In a single electron device, only tunnel junctions and islands require sub-micron fabrication. Our idea was to separate these components requiring the best resolution provided by e-beam lithography from others which have less critical resolution requirements such as gate capacitances and connecting circuitry. We therefore decided to fabricate the latter components on a separate layer using standard ultra-violet optical lithography which has the great advantage to process many samples on a single silicon wafer "in parallel". Electron beam lithography is on the contrary basically a "serial" fabrication technique, since the beam scans all the exposed zones line after line. For the exposure of large areas such as connecting pads, EBL is a time consuming method, which motivated our decision to replace it by an optical lithography step.

The main steps of our hybrid Optical/EBL multilayer process, described in the following, are sketched in Fig. 6.9. The corresponding technical procedures are detailed in appendix 6–C. We first pattern on a whole 2-inches silicon oxidized wafer and using lift-off optical lithography, a circuitry consisting of gold leads (step 1). We cover the sample with an insulating resist (step 2) which will separate the upper conductive layer from the lower one and provides a planar layer of typical rugosity less than 10nm for the following metal depositions. The vias to the gold circuitry are fabricated according to the following sequence: we optically pattern small windows aligned over the gold wires (step 3). The resulting photoresist mask is etched and holes are opened in the insulator with diameter 1 μm (step 4). We thus uncover the gold lead extremities except for the gate capacitances (see Fig. 6.10a). We then perform an electron-beam lithography using a standard bilayer process (steps 5 and 6). The top level which consists of electrodes and tunnel junctions is fabricated using double-angle evaporation of aluminum through a shadow mask (step 7, Fig 6.10c). Junctions with typical size 0.1×0.1 μm^2 are obtained (see final aspect in Fig 6.10c and Fig. 6.12 bottom panel).

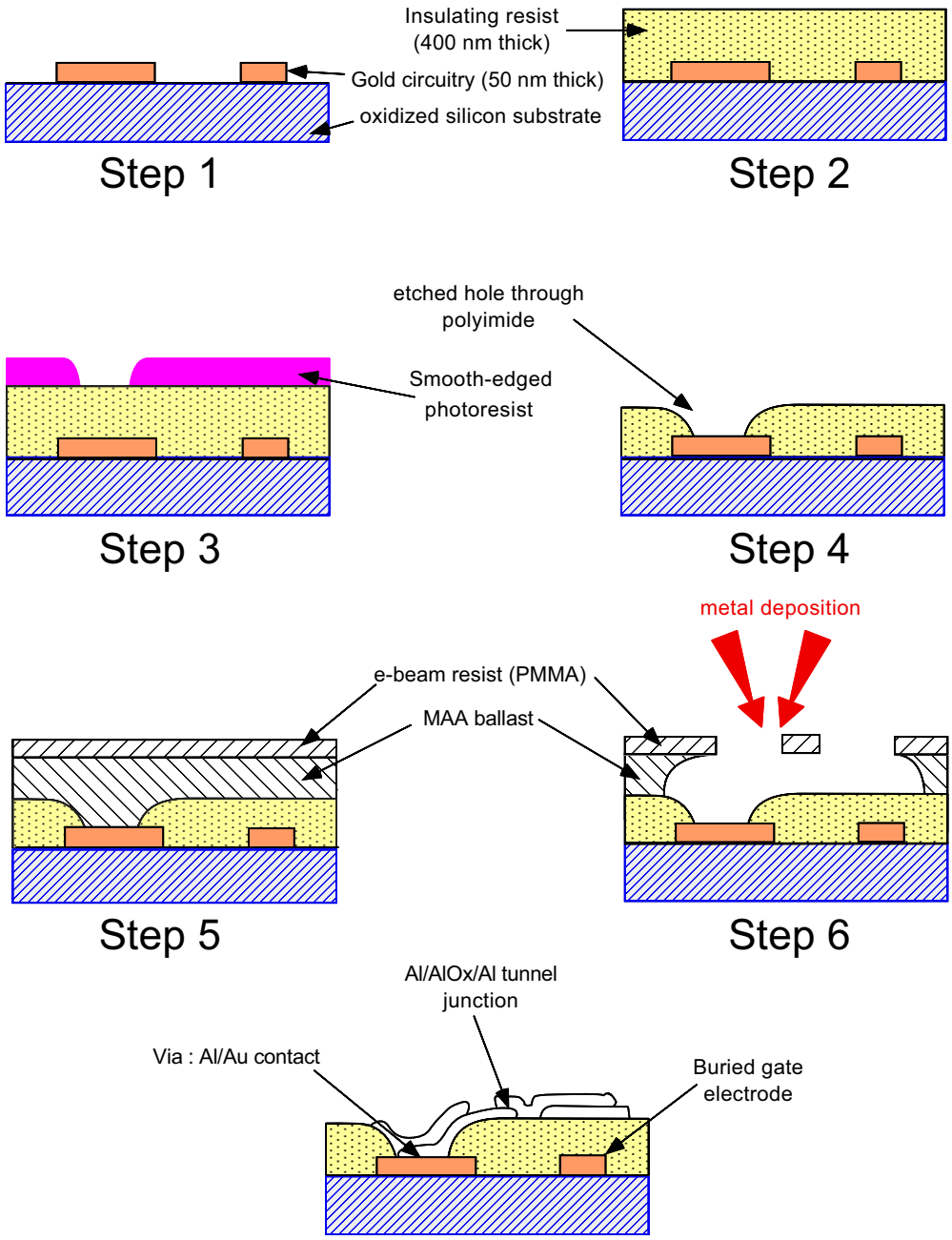

Figure 6.9: Processing sequence for the multilayer technique.
Step 1) *pre-fabrication of the connecting circuitry and capacitor bottom electrodes on a oxidized silicon wafer: UV lithography, gold deposition and lift-off.*
Step 2) *deposition of the insulating layer (polyimide or silicon nitride).*
Step 3) *aligned UV lithography of the via pattern.*
Step 4) *holes etching in the insulating layer for fabrication of vias.*
Step 5) *Bilayer resists spin coating and baking for EBL.*
Step 6) *EBL step: electron beam exposure and development of the suspended mask.*
Step 7) *Deposition of the islands, tunnel junction and gate capacitor counterelectrodes.*

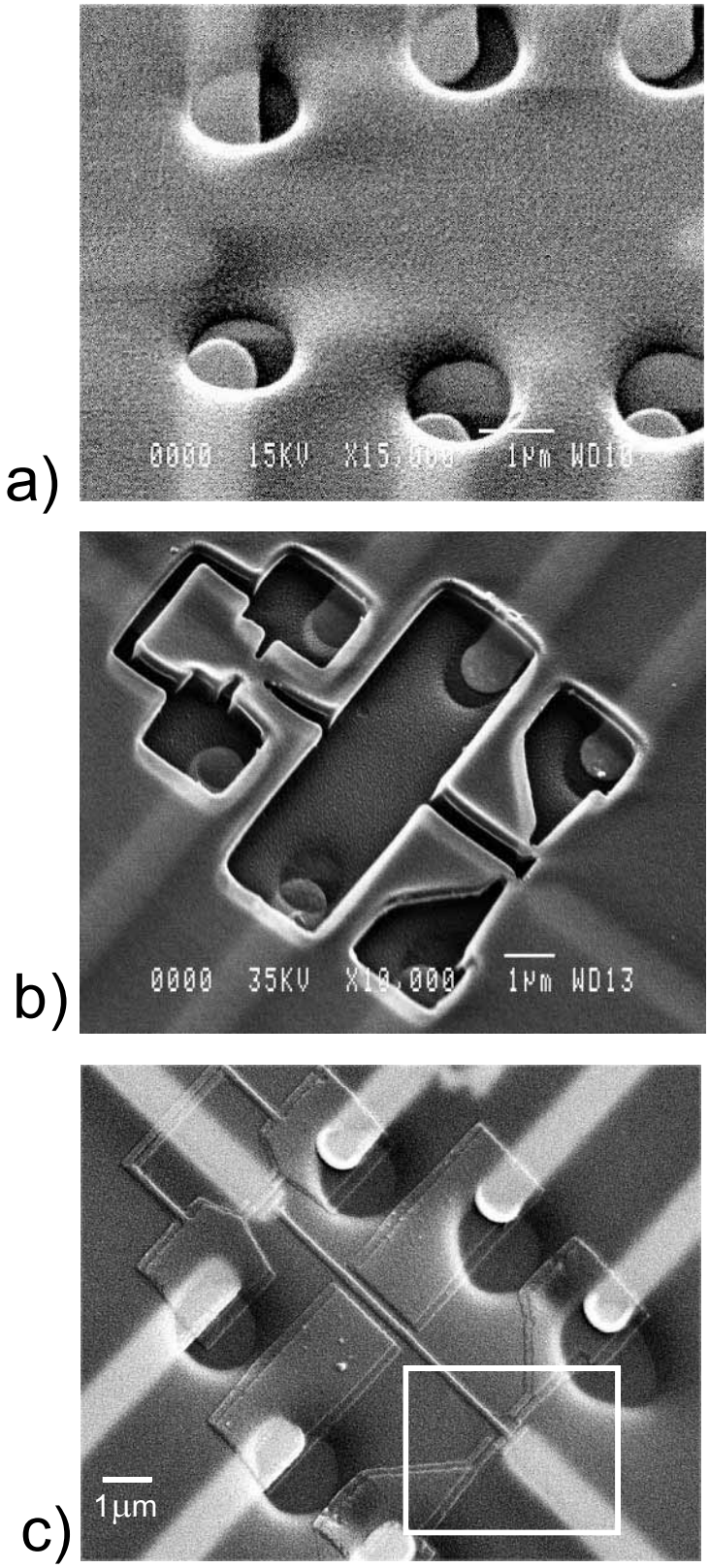

Figure 6.10: Scanning electron micrographs of a typical multilayered sample fabricated using polyimide as the insulating layer, and observed at different fabrication steps.
a) Sample at step 4 showing the smooth edged holes pierced through the insulator uncovering gold leads for vias fabrication.
b) Sample at step 6 showing the aligned bilayer mask suspended over the polymide (partly damaged during the SEM observation).
c) Fully processed sample. The device at bottom right (enlarged in figure 6.13) is a single electron transistor measuring the charge of a single Cooper pair box (top left) with its long, "T"-shaped island.

a)

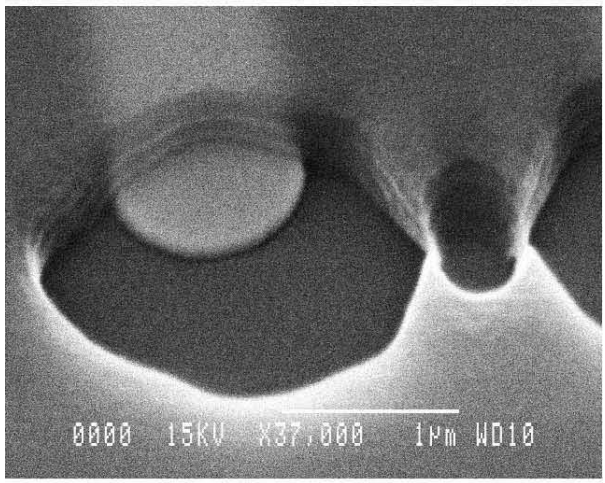

b)

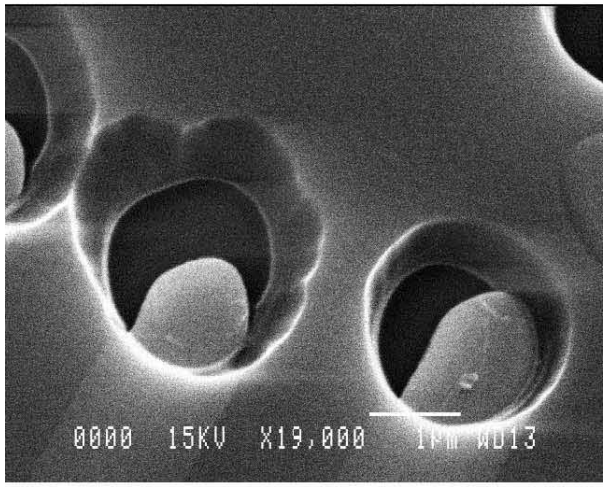

c)

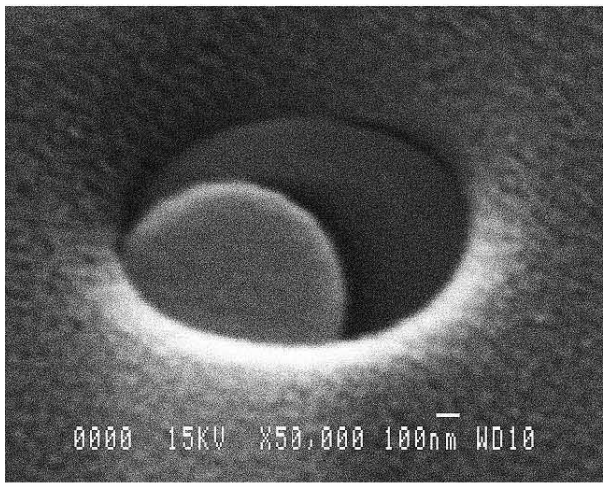

Figure 6.11: Scanning electron micrographs of holes pierced through the insulating layer showing the problems encountered for via fabrication.

a) Dry-etched hole in silicon nitride. the vertical edges obtained even using isotropic etching in a high pressure plasma will not preserve the electrical continuity of further metalic layer deposited on top.

b) Holes of the previous sample after exposure in a diluted solution of fluoridric acid. The profile is less steep but the remaining sharp edges make this technique not suitable for via fabrication.

c) Dry–etched hole in polyimide. The smooth profile of the photoresist is transferred during the dry-etching thus preserving the electrical contact of the layer deposited on top.

6.4.2 Deposition of insulating layers

As previously mentioned, we have tried two kinds of insulating layers selected for their good insulating properties: polyimide and silicon nitride. Deposition of these layers requires completely different processes that are detailed in appendix 6−C. Both materials have the same dielectric constant $\varepsilon_r \approx 3.6$ and the deposited layers lead to high breakdown voltages: polarization with voltages up to several volts across half-micron-thick layer does not lead to any damage for the device. Furthermore, half-micron thicknesses of polyimide are sufficient to planarize the surface, thus erasing the height contrast generated by the bottom conductive layer (see Fig. 6.14 top panel). Such a good planarization cannot be obtained with silicon nitride deposited either using a chemical vapor deposition process[2] or by plasma sputtering (see Fig. 6.14 bottom panel).

A key point when one introduces new insulators in single electron device fabrication is to check that the charge noise generated by these marerials is low enough. We have found that polyimide and silicon nitride are "quiet" insulators in the sense that they do not increase the noise level of an electrometer when compared to conventionally fabricated samples on silica: a complete discussion of this issue is given in Chapter 5.

6.4.3 Fabrication of vias

Via fabrication implies the piercing of the insulating layer in precisely located places in order to connect the two conductive layers. Since contacts between conductive layers are made by thin evaporated metalic strips through holes of 1-μm radius, the electrical connection is not straightforward. To ensure electric continuity between layers, the holes must have smooth edges and be clean in the bottom. Such smooth edged holes were only obtained using polyimide layers (see Fig. 6.11 bottom panel and process details in appendix 6-C) despite numerous trials of silicon nitride etching processes (see Fig. 6.11 top and middle panels). One-micron-wide holes are pierced through polyimide thus uncovering the bottom gold connecting circuitry. This gold surface is then cleaned by argon ion-milling prior to deposition of the bilayer resist for subsequent electron beam lithography.

[2] Technical support from Balzers is gratefully acknowledged for providing us the CVD deposited silicon nitride samples

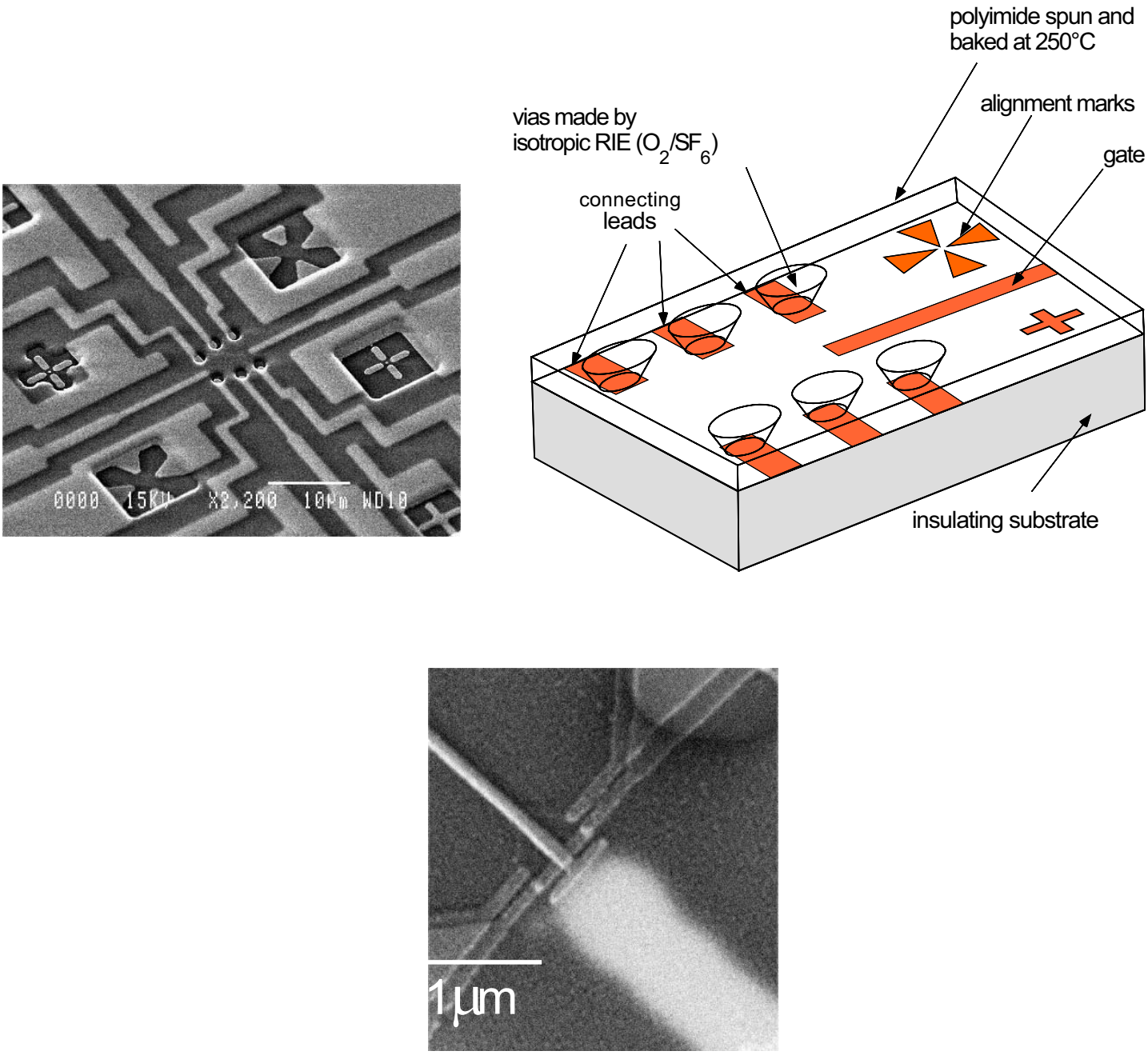

Figure 6.12: Pictures showing alignments results performed at both optical lithography and electron beam lithography stages.
Top: UV lithography alignment. scanning electron micrograph of a sample for multilayer fabrication shown at step 4 (left) and its corresponding schematic drawing (right). the alignment accuracy of the patterned hole with respect to the lead is about half a micron. Notice the alignment marks which are used for this alignment and also during EBL to position the SET device with respect to the structure underneath.
Bottom: EBL alignment. Scanning electron micrograph of a multilayered single electron transistor after full process. Tunnel junctions are shown the two bright dots. The alignment accuracy of the top structure (island in the center of the picture) with respect to the bottom gold layer (blurred bright finger) is better than 0.2 μm).

The respective advantages and drawbacks of the two kinds of insulators are summarized in the following table:

Insulating layer	Silicon nitride (Si_3N_4)	Polyimide
Advantages	• hard insulator with high breakdown field • low residual rugosity • suitable for ultrasonic bonding	• easy to spin • provides good planarization • isotropic dry-etching gives smooth edges suitable for vias.
Drawbacks	• no planarization • sharp edges when etched (not suitable for via fabrication)	• must be annealed at 350°C • too soft for enabling ultrasonic bonding.

Table 6.13: Comparison between the two materials tested as insulating layers.

6.4.4 Alignments of layers

Multilayer fabrication requires accurate alignment of layers with respect to each other at each deposition step. The accuracy depends on the device parts: half-micron accuracy is sufficient for aligning via holes over the gold circuitry (see Fig 6.14 top right). Therefore this alignment can be performed using the micrometric screw of the UV lithography mask aligner (see Fig 6.12 top panel). For the top layer however, one must align the single electron device above the gate electrode with the best resolution available. This last layer being fabricated using electron beam lithography, the alignment procedure is not straightforward since one cannot image the sample without exposing the resist. This alignment is performed in two steps. First, a coarse mechanical alignment is provided: the sample is shifted away from the center of the electron beam column and the center position is calculated after measurements of the coordinates of pre-alignment crosses at the sample edges. The average accuracy of this alignment step is about 3 μm. The second step consists in imaging alignment crosses by scanning small areas at the edges of the exposure field[3]. Since the sample has been pre-aligned, crosses are found inside the imaging field (with about 3 μm misalignment). The relative

[3] This precise alignment is performed using the Proxy-writer alignment procedure developped by Raith GmbH.

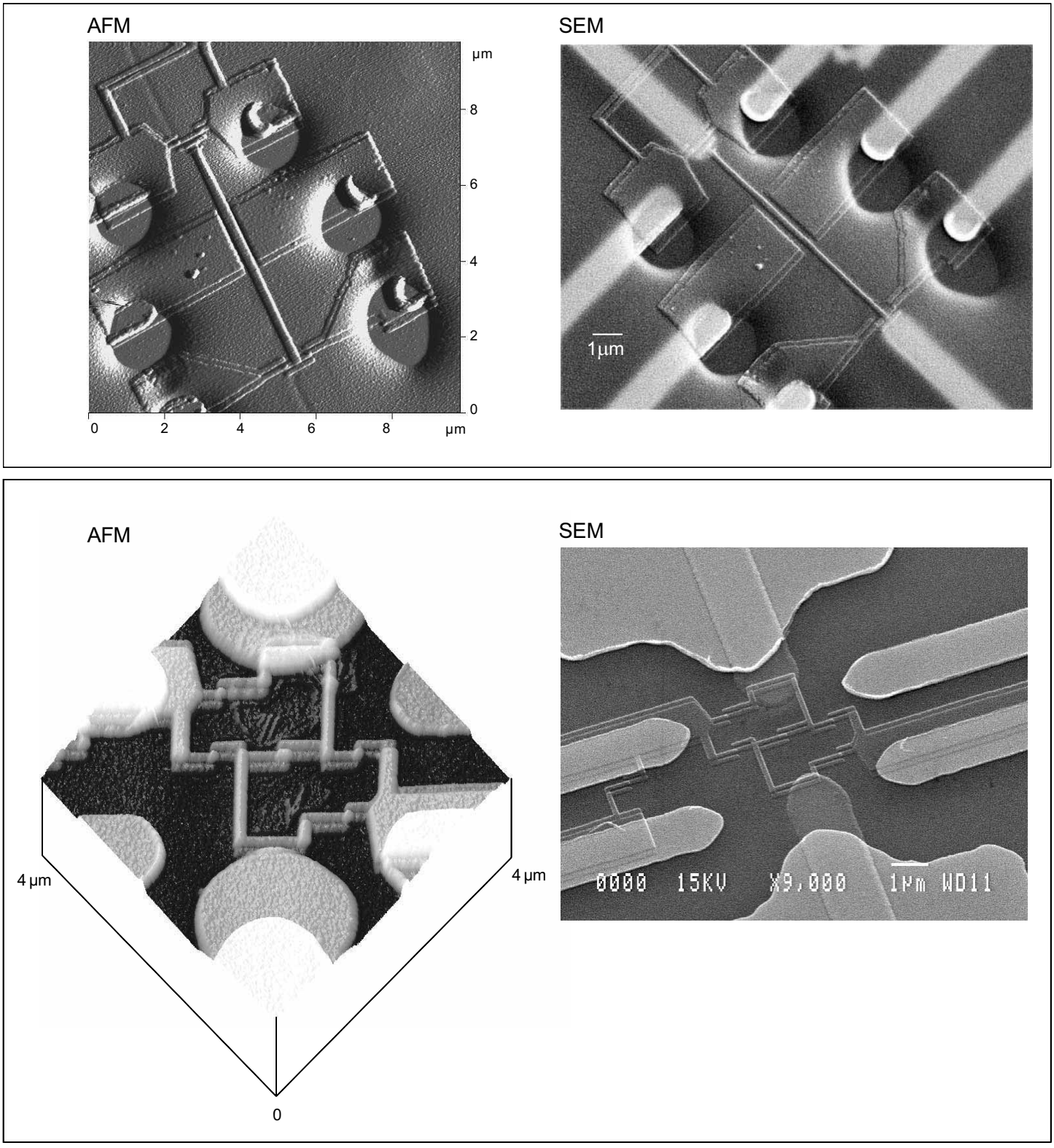

Figure 6.14 *AFM* (*left column*) *and SEM* (*right column*) *micrographs of two fully processed multilayer single electron devices using respectively polyimide* (*top panel*) *and silicon nitride* (*bottom panel*) *as insulating layers.*

Vias with smooth edges could be only implemented using polyimide whereas "buried" gates electrodes (*diagonal fingers*) *have been fabricated using both techniques. These* 50*nm-thick electrodes have almost completly dissapeared on the AFM image* (*top left*) *for the polyimide sample thus showing the perfect planarization provided by spin-coating of a half-micron-thick polyimide layer. For the same thickness of sputtered silicon nitride, no planarization effect is observed, as showed in bottom left picture.*

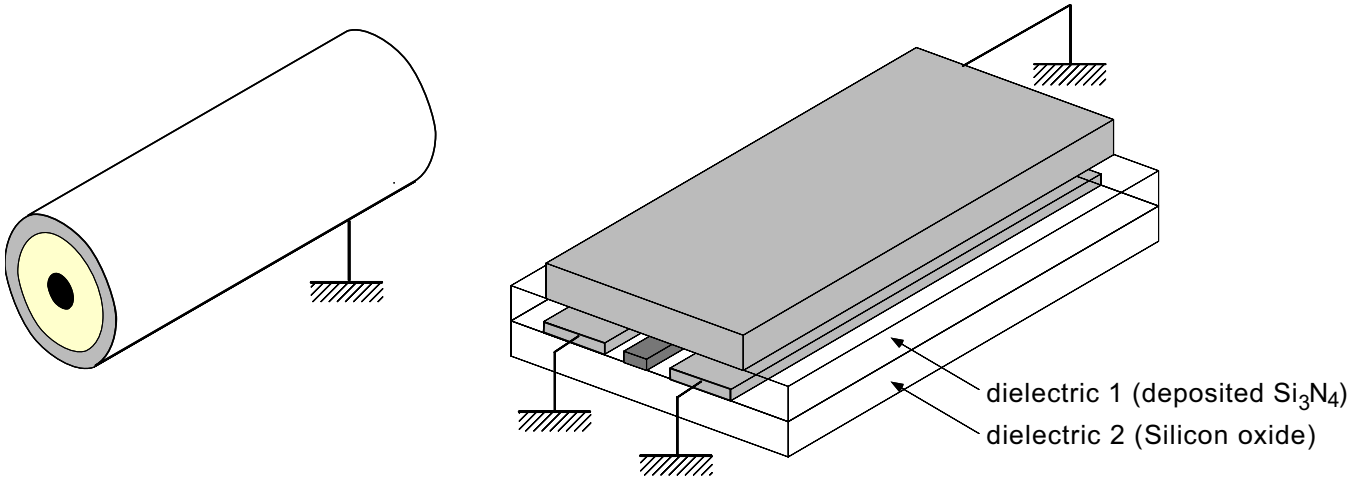

Figure 6.15. Drawings showing the integration of shielded lines on-chip approximating a coaxial line, (schematics in left). The insulator above the strip-line is the insulating layer whereas the oxidized silicon substrate plays the role of the bottom insulator.

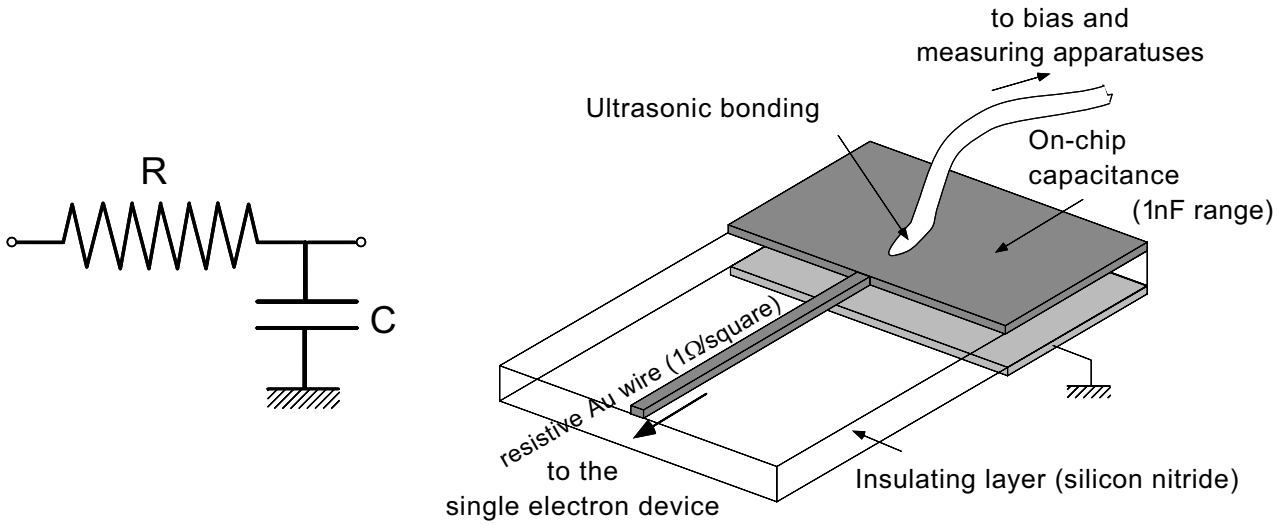

Figure 6.16. Controling the electromagnetic environment of single electron devices requires implementing dissipative elements very near the tunnel juntions. The picture shows how can overlap capacitors and strip line resistors can be integrated on-chip.

misalignment is measured for the four crosses and the beam-monitor computer calculates both translation and rotation corrections in order to properly shift the electron beam during exposure. Such a fine geometric compensation performed by the digital to analog board is efficient only if one images the alignment marks with the same current as for the exposure since the electron beam shifts with the current. The overall alignment accuracy is then of the order of 100 nm (see Fig. 6.12 bottom panel).

6.4.5 Customizing the electromagnetic environment

Multilayer fabrication also provides the opportunity to integrate on-chip components such as overlap capacitors and resistances very close to tunnel junctions. Such components allow the control of the electromagnetic environment of single electron devices. Capacitors with up to 5 mm^2 area yielding to a capacitance of ~ 100 pF have been realized. On the other hand, resistors in the range 1-1000 Ω, very close to islands have been obtained. As an example, RC circuits (see Fig. 6.16) were used to obtain large switching currents in small Josephson junctions (see Chapter 4). Drawings of Fig. 6.15 also illustrate the fabrication of shielded lines consisting of a strip line surrounded by ground electrodes. Such lines have been used to apply microwave signals on gate electrodes (see Chapter 4).

6.4.6 Future possible applications of multilayer fabrication

This multilayer layer technique is also promising for the fabrication of complex structures requiring coupling overlap capacitors. Among them, one can mention the multijunction single Cooper pair pumps with gate capacitors addressing one column at a time (see Figure 6.17).

In all the multilayer processes mentioned above, the tunnel junctions sit on the top level: An improvement of this multilayer technique would be to implement tunnel fabrication on different levels. Such a project raises several problems: It is well known that metal oxide tunnel junction cannot be exposed to the electron beam of a SEM without risking severe damages[4] (such as shorts). Therefore, it seems difficult to perform a new electron beam lithography step without destroying the junctions of the previously fabricated layers. The AFM-based lithography, which circumvents this problem, might allow fabrication of multi tunnel junction layers.

[4] AFM imaging, on the contrary, does not lead to any noticable junction damage

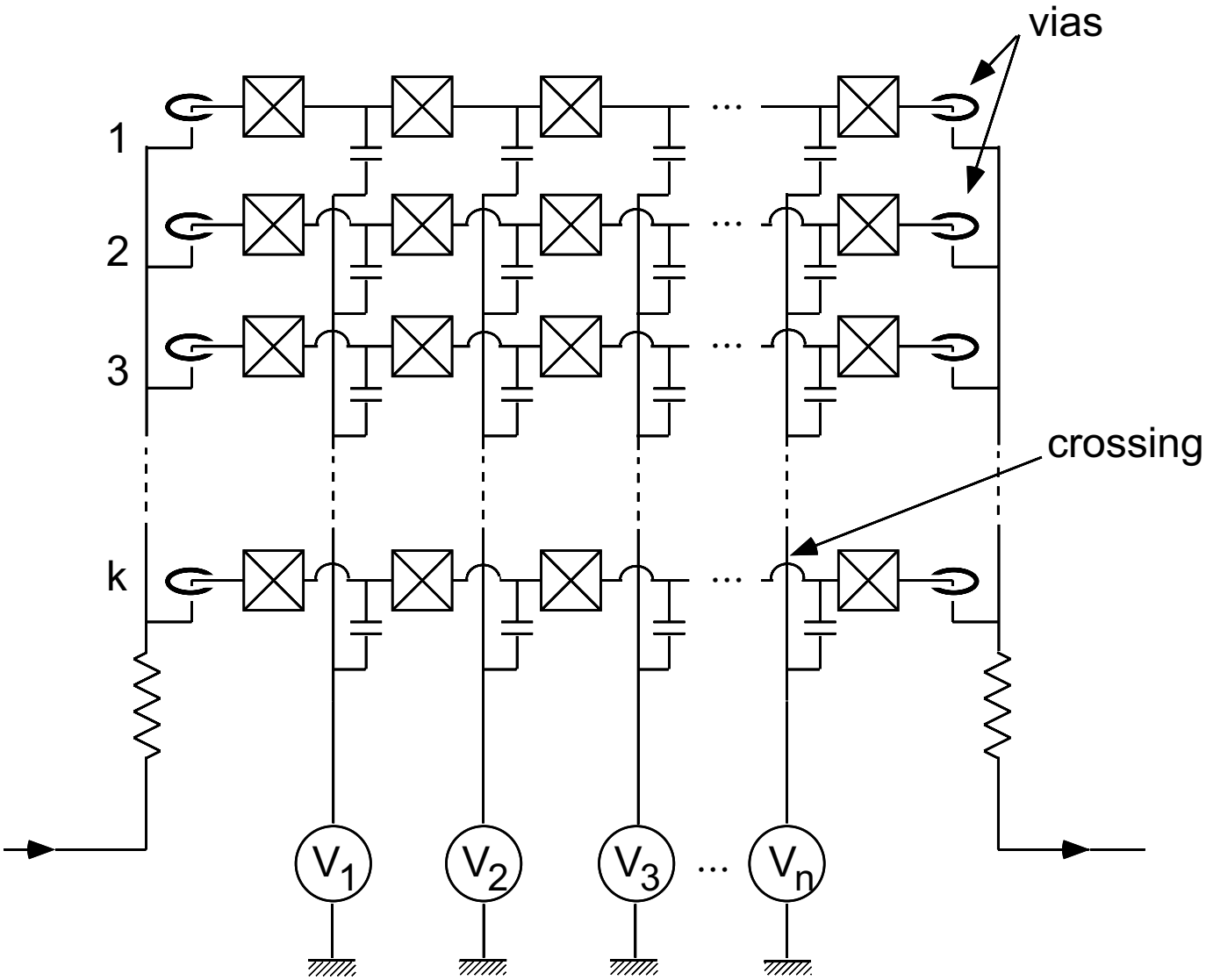

Figure 6.17. *Schematic diagram of a superconducting pump composed of a series of k single-Cooper pair pump in parallel, each pump being composed by n ultrasmall Josephson junction in series. If the circuit is operated with gate voltages* V_i *clocked at frequency f with relative phase* $2\pi/i$ *(where* $0 \leqslant i \leqslant n$*), then the net supercurrent flowing through the whole device is expected to be equal to* : $I=k(2e)f$.

Conclusion
New contributions to nanostructure fabrication

We have presented here all the processes involved in the fabrication of the nanostructures discussed in this thesis. Apart from the state-of-the-art techniques that have been modified to fulfill our specific needs, some new results have been obtained:

• Single electron devices have been successfully fabricated using a new fabrication technique based on the AFM, thus avoiding the use of electron beam lithography. The present lateral resolution obtained is 40 nm.

• Multilayer single electron devices have been obtained using organic and inorganic insulating layers.

• Vias and crossings have been successfully incorporated, thus providing a large design flexibility. The implementation of overlap capacitors increases the coupling capacitance by typically a factor 10 with respect to a planar geometry and leads to a crosstalk reduced to less than 10 %.

• The multilayer single electron transistors have shown no significant increase of the charge noise level (see Chapter 5).

• Samples with shielded gates for microwave excitation have been realized.

• A controlled electromagnetic environment for the single electron devices have been implemented using customized capacitors and resistors very close to the device.

References of chapter 6

[1] G. Binnig, H. Rorher, Ch. Gerber, E. Weibel, Appl. Phys. Lett. **40**, 178 (1982), see also G. Binnig, H. Rorher, Ch. Gerber, E. Weibel, Phys. Rev. Lett. **49**, 57 (1982)

[2] G. Binnig, C.F.Quate and Ch. Gerber, Phys. Rev. Lett. **56**, 930 (1986).

[3] D.M. Eigler and L.K. Schweizer, Nature, 344, 524 (1990).

[4] W. Chen and H. Ahmed, Appl. Phys. Lett. **62**, 1499 (1993).

[5] C. Vieu, M. Mejias, F. Carcenac, G. Faini and H. Launois, Microelectronic Engineering, **30**, 403 (1996).

[6] G.J. Dolan and J.H. Dunsmuir, Physica B **152**, 7 (1988), J. Romijn and E. Van der Drift, Physica B **152**, 14 (1988).

[7] T.A. Fulton and G.J. Dolan, Phys. Rev. Lett. **59**, 109 (1987).

[8] H. Courtois, Ph. D. Thesis; Université J. Fourier Grenoble, (1995).

[9] V. Bouchiat and D. Esteve, Appl. Phys. Lett. **69**, 3098 (1996).

[10] E.H. Visscher, S.M. Verbrugh, J. Lindeman, and J. E. Mooij, Appl. Phys. Lett. **66**, 3 (1995).

[11] D.C. Glattli, private communication.

[12] H. Dai, J.H. Hafner, A.G. Rinzler, D.T. Colbert, R.E. Smalley, Nature, **384**, 147 (1996).

APPENDIX 6−A
Technical data for shadow mask fabrication

1-Preparation of Bilayer resist samples

- Resist deposition
  - bottom layer: copolymer polymethyl-meta-acrylate/meta-acrylate acid (PMMA/MAA) diluted at 90 g.l^{-1} in 2-ethoxyethanol, filtered with 0.2 μm teflon filters
    - A spin at 2000 rpm during 40 s gives a 400 nm thick ballast. dry at 156°C for 1 minute.
  - top layer: poly-methyl-meta-acrylate PMMA (molecular weight 950K) 15g.l^{-1} in MIBK, 0.2 μm filtered with teflon filters.
    spin at 1000 rpm during 40 s bake at 156°C for 15 minutes.
- Electron beam exposure
  - Electrons accelerated by a voltage of 35 kV, standard dose 2 pC/μm^2
- development
  - develop for 35 s in a solution of MIBK(methyl-isobutyl-butyl-ketone) diluted at 25% vol. in propanol-2.
  - rinse in propanol-2.

2-Preparation of trilayer resist samples

- ballast deposition
  - copolymer PMMA/MAA 90 g.l^{-1} in 2-ethoxyethanol, 0.2 μm filtered with teflon filters.
  - A spin at 2000 rpm during 40s gives a 400nm thick ballast.
    bake on hot plate at 156°C for 15 minutes.
- germanium deposition
  - 30-50 nm of germanium are thermally evaporated on top (rate 0.2 nm/s).
- top layer electron sensitive deposition
  - PMMA (molecular weight 950K) 15 g.l^{-1} in MIBK, filtered.
    spin at 1000 rpm during 40 s bake on hot plate at 150°C for 15 minutes.
- electron beam exposure
  - almost the same dose as for the bilayer resist.
- wet development
  - develop for 10 s in a solution of cellosolve (commercial name of glycol-ethyl-monoethyl-ether) diluted at 30% vol. in methanol
  - rinse in propanol-2.
- dry etching
  - plasma etching of the germanium: SF6 5 sccm 2×10^{-3} mbar 10W during approx. 40-60 s.
  - plasma etching of the copolymer layer: O_2 10 sccm 2×10^{-3} mbar 100 W during 8-10 min.
- underetch: 2 possibilities depending in the desired undercut:
  - dry underetch (classical): isotropic oxygen plasma 0.11 mbar 15 W during 10 min.
  - wet underetch (for large undercut): 20-80 s in MIBK-propanol-2 at 20°C. A 80 s treatment gives a 1.2 μm edge to edge undercut. This wet underetch must be followed by a dry-etching in order to clean the remaining polymer sticking to the edges of the mask.
    - Etching parameters: O_2 10sccm 2×10^{-3} mbar 100 W during 5 min.

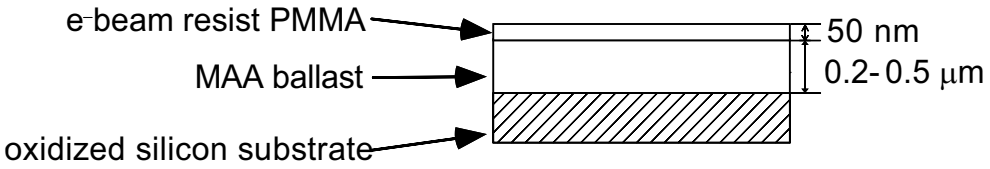

Schematic cross section of a bilayer for e-beam lithography

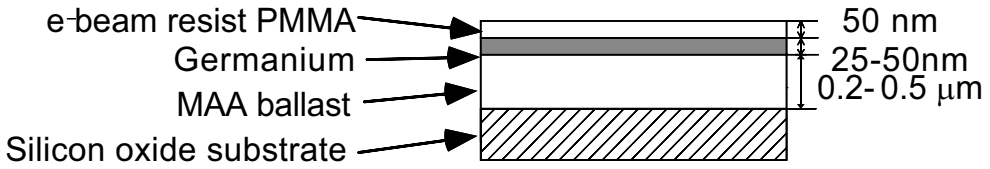

Schematic cross section of a bilayer for e-beam lithography

Important notice: The trilayer process is somewhat more difficult to realize than the bilayer. One should pay attention to the following recommendations that can avoid frequent problems:
1) DO NOT bake the wafer at two high temperature because internal stresses between layers might occur, leading to typical circular breaks in the thin germanium layer. A safe method is to bake the sample using decreasing temperatures (150°C the second time).
2) The first dry-etching step in SF_6 must be long enough to clean all germanium deposits on the substrate. It is extremely helpful to monitor the etching rate by laser interferometry.
3) Deposits remaining from the copolymer etch might lead to a pollution of the bottom silicon substrate. We suspect these deposits (probably carbon particles) to contaminate the tunnel junction barrier and make it more fragile.

3-Preparation of AFM-etched samples

• See the article "Lift-off lithography with an Atomic Force Microscope" reprinted in the following (appendix 6-B).

Appendix of chapter 6

APPENDIX 6–B

Lift-off lithography technique with an Atomic Force Microscope

published in Applied Physics Letters **69**, 3098, 1996.

Lift-off lithography using an atomic force microscope.

V. Bouchiat and D. Esteve

Service de Physique de l'Etat Condensé, Commissariat à l'Energie Atomique, 91191 Gif-sur-Yvette Cedex, France

Abstract

We present a technique to fabricate nanostructures with an atomic force microscope (AFM). By taking advantage of the AFM tip sharpness, we engrave a narrow furrow in a soft polyimide layer. The furrow is then transfered using dry-etching to a thin germanium layer which forms a suspended mask. Metallic layers are then evaporated through this mask. Metallic lines with a 40 nm linewidth and single-electron transistors have been fabricated. This lift-off technique can be used on any substrate and allows easy alignment with previously fabricated structures.

PACS# 7335, 7340G, 6116P, 8160

published in Applied Physics Letters (Nov. 96).

The observation of conductance quantization [1,2], the controlled transfer of single electrons [3] and the realization of almost perfect 2-dimensional atoms [4] are recent examples of experiments involving nanostructures. Such results could be obtained because electron-beam lithography (EBL) has made sub-100 nm scale fabrication easily accessible. Although high energy EBL reaches a resolution better than 10 nm [5], there is a need for simple fabrication techniques in the sub-50 nm range. The atomic resolution imaging achieved by proximal probe microscopy has risen hopes that such alternatives to EBL do exist. Indeed, a variety of techniques have been developed [6], culminating with the direct manipulation of atoms [7] and molecules [8]. Most of these techniques take advantage of the spatial resolution of the electronic emission from a tip to locally expose ultra-thin electron resists [9], such as self-assembled molecular monolayers [10] or Langmuir-Blodgett films [11], or to directly modify the structure of the superficial layer [12], such as the oxidation of hydrogenated silicon [13]. A few methods based on mechanically engraving a soft layer with a sharp atomic force microscope (AFM) tip have also been proposed [14]. In particular the PMMA resist bilayer process, commonly used in EBL, has been directly adapted [15]. We demonstrate in this paper the adaptation of the (PMMA/MAA [16]-Ge-PMMA) trilayer process [17], in which the intermediate germanium layer forms a suspended mask. The main advantage of this process is to provide a rigid mask allowing large free-standing areas. The combination of multiple angle evaporations of various metals required to fabricate nanostructures combining narrow wires, small contacts, tunnel junctions or other elements, is then possible. We illustrate the versatility of the technique by fabricating a single-electron transistor (SET) aligned with previously deposited contacts. We have operated at low temperature and characterized this basic circuit of single electronics.

In the usual trilayer process, the pattern, created by e-beam exposure in the top PMMA layer, is transferred using dry-etching to the intermediate metallic layer to form a suspended mask; further dry-etching of the bottom layer provides the necessary undercut for proper lift-off after evaporation of metallic layers through the mask apertures. In the present process, depicted in FIG. 1, the top resist is replaced by a soft polyimide layer in which an AFM tip

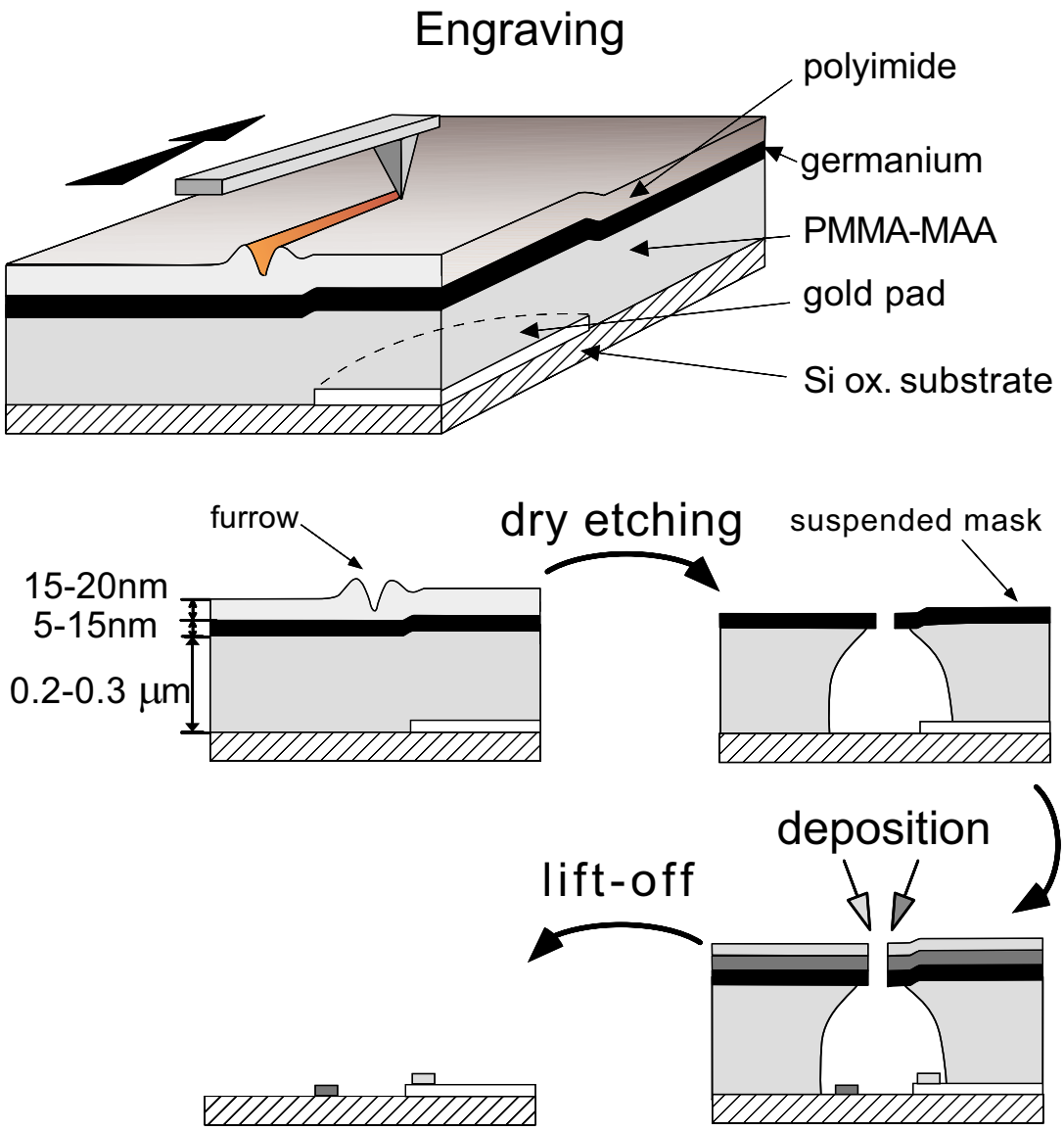

Figure 1: Main steps of the AFM-based trilayer process.

engraves a pattern of narrow furrows. Subsequent dry-etching steps are similar.

We first pattern on an oxidized silicon wafer the gold contacting circuitry by optical lithography. A gold thickness larger than 10 nm ensures that the contacting pattern is observable by scanning the sample surface with the AFM prior to engraving it, thus allowing easy alignment. This thickness should however be less than 50 nm in order to avoid large steps and ripples on the sample surface. A PMMA-MAA copolymer buffer layer with a thickness equal to the desired height for the suspended mask (200-300 nm) is then spun and baked. A germanium layer with a thickness in the 5-15 nm range is then thermally evaporated on top. At this stage, the wafer is diced, after which each chip is processed separately. Prior to engraving a chip, a thin polyimide layer with a thickness in the 15-20 nm range is deposited. Such a thickness insures that the furrows are deep enough to transfer the pattern properly during the subsequent dry-etching steps. Thin polyimide layers are obtained by spinning a highly diluted solution of polyimide (Dupont PI-2610) in N-methyl-2-pyrrolidinone (NMP). The solvent is removed by drying the chip on a hot plate at 60°C. The chip is then placed in an AFM equipped with a rigid and sharp silicon tip (L=125 μm, $k \approx 5$ N.m^{-1} from Nanoprobe). The top surface is imaged to allow a precise alignment with the underlying pattern. Engraving is done by pushing the tip (see FIG. 1) at a velocity in the $0.2 - 2$ μm.s^{-1} range with an applied vertical force in the 1.5-3 μN range, higher speeds requiring larger forces.

One should take care not to scratch the solid Ge mask in order to preserve the tip sharpness. An AFM image of a typical 50 nm wide furrow taken with the same tip as for engraving is shown in FIG. 2a. It displays a constant profile without any irregularity in the edges: polyimide appears to be a well suited material for engraving. Such a regularity is however not found if the tip is pulled, or pushed at angles exceeding 40° with respect to the cantilever axis, due to cantilever torsion by the asymmetric drag force. The obtained furrow profile is determined by the tip sharpness close to its apex, which is the main present limitation to the final line width. Fine control of the gap between two furrow ends (see FIG. 3a) is required to fabricate tunnel junctions by evaporating at two angles through the

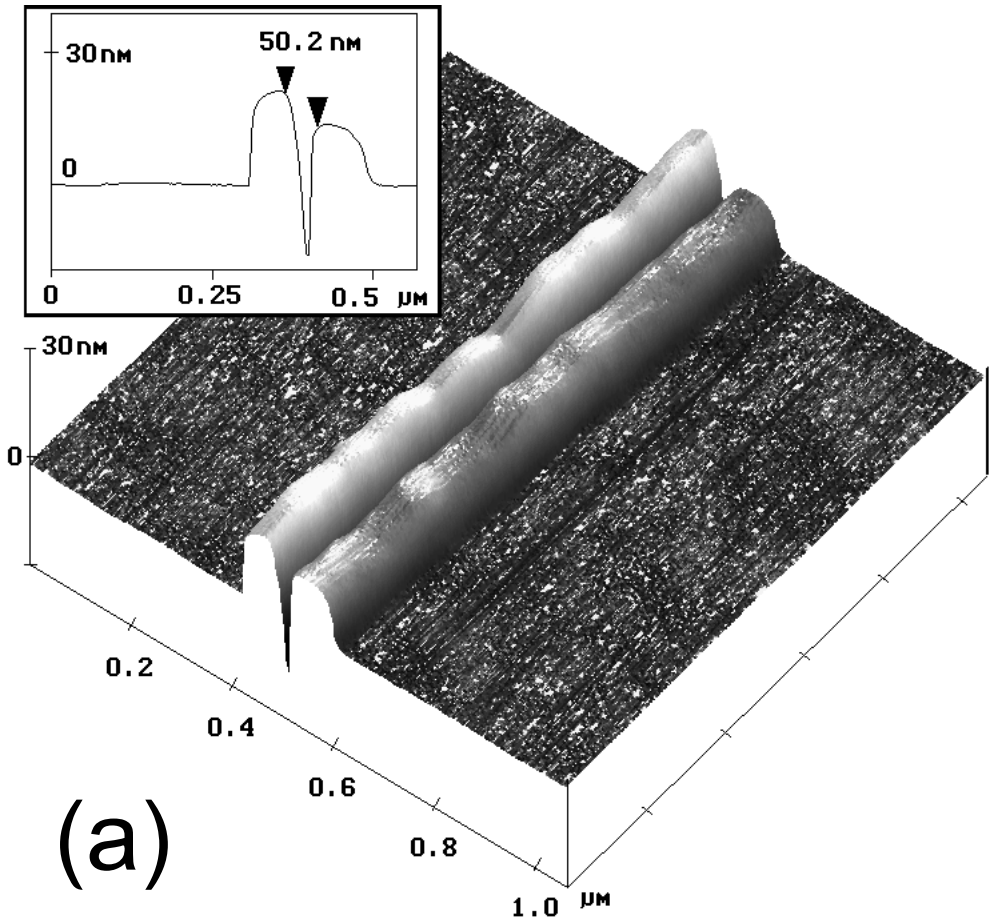

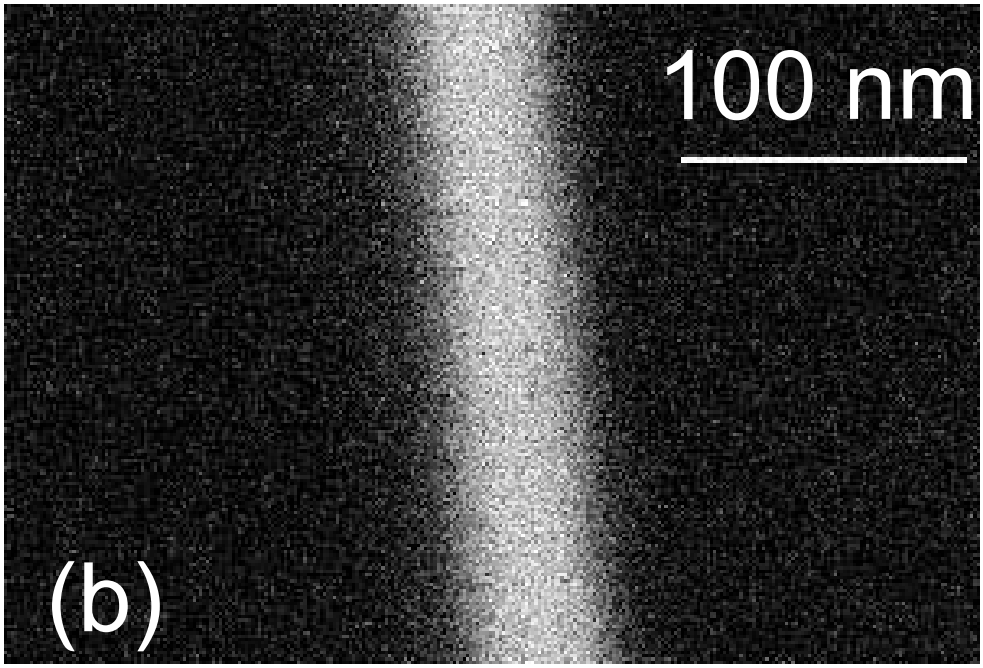

Figure 2 (a): AFM image of a furrow engraved in polyimide. Note that the profile shown in inset, obtained by scanning with the scribing tip is somewhat broadened by the finite tip radius.
(b): Scanning electron micrograph after deposition of 30nm of Gold through the corresponding mask.

suspended mask. Small positioning corrections need to be applied in this case in order to compensate the cantilever flection under the effect of the applied force and of the drag force. Furrows up to 500 nm-wide can be obtained by laterally sweeping the tip while pushing it.

The reactive ion etching (RIE) of the engraved chip is then done in three steps. A first etching is performed in a low pressure (0.002 mb) SF_6 plasma in order to transfer the furrow to the Ge layer. The etching rate ratio between PI and Ge measured by laser interferometry is equal to 0.3, which allows a reasonable latitude in the adjustment of the etching time. The second and third RIE steps are done in an O_2 plasma, at respectively low (0.002 mb) and high (0.11 mb) pressures. The low pressure RIE leads to anisotropic etching of the PMMA-MAA ballast down to the substrate. The high pressure RIE provides isotropic etching and creates the undercut required for the angle evaporations. It is worth noticing that the transfer of the furrow pattern onto the Ge mask is realized without significant broadening.

We then proceed to the angle evaporation of one or several metallic layers through the suspended mask in an electron-gun evaporator. Tunnel junctions are obtained by *in-situ* oxidation of an aluminum electrode prior to the deposition at a different angle of a counter-electrode. The height-width aspect ratio of the deposited lines is only limited by the obstruction of the mask due to the evaporated materials sticking on the mask edges. Finally, the Ge mask and the ballast are lifted-off in hot acetone.

FIG. 2b displays a scanning electron micrograph of a gold line deposited after etching the furrow shown in FIG. 2a. The line is very regular with a 40 nm line width. Electrical continuity has been checked on 50 μm-long Al lines connected to 50 nm-thick gold pads.

Combination of evaporations at different angles allows one to fabricate various types of devices. In order to illustrate the versatility of the technique, we have fabricated Single Electron Transistors (SET) which are the basic circuits of single electronics. A SET consists of two non-superconducting tunnel junctions in series, with a small intermediate electrode (island) capacitively coupled to a gate electrode [3]. At temperatures such that $k_B T \ll E_c = \frac{e^2}{2C}$, where e is the electron charge and C the total island capacitance, the current flowing through the device is periodically modulated by the gate voltage V_g. The period corresponds

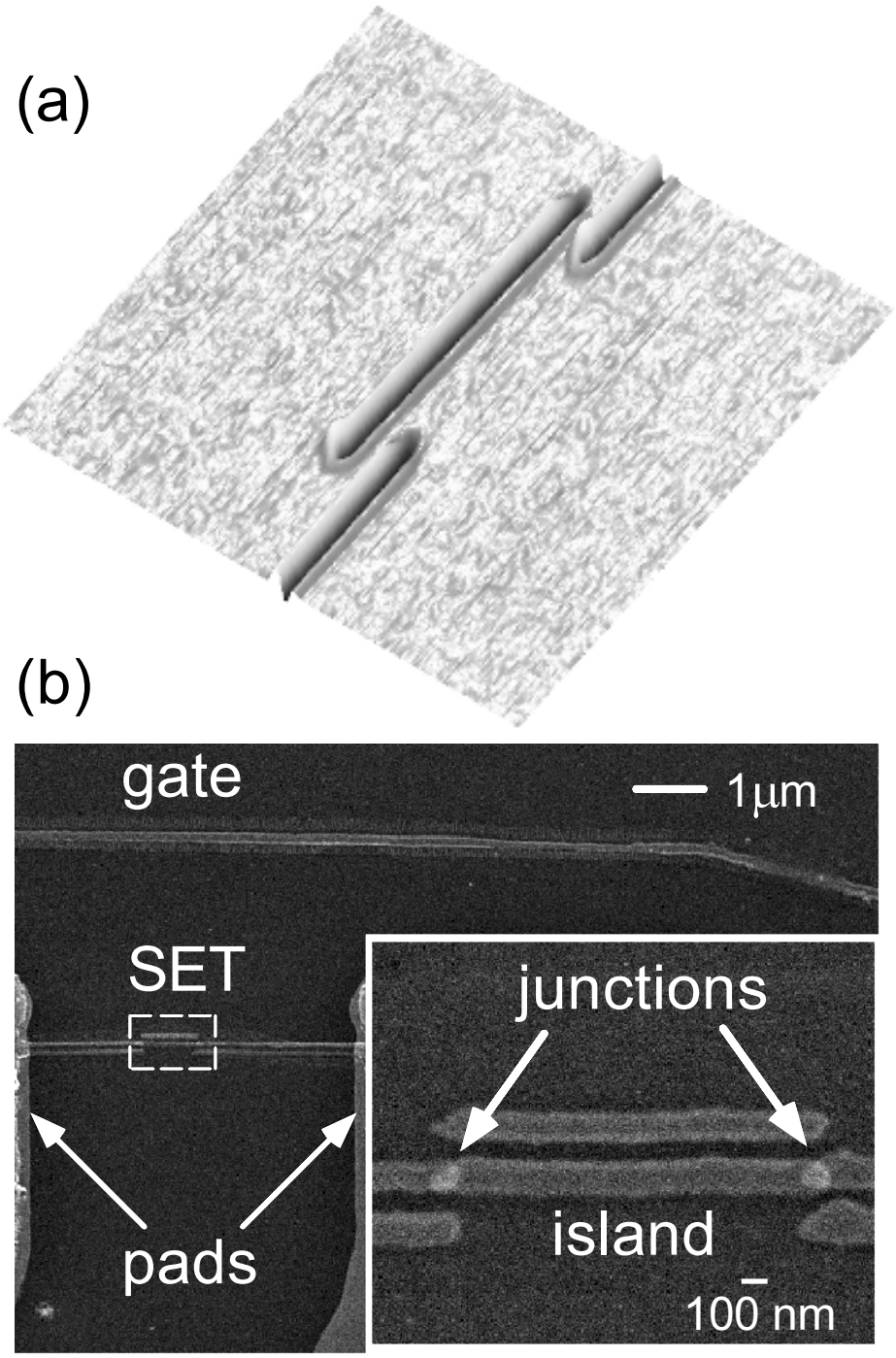

Figure 3 (a): AFM image of the pattern engraved in polyimide for fabricating a SET. (b): Scanning electron micrograph of the SET device after fabrication.

to one extra electron charge induced on the island by V_g.

Both the device and the gate electrode have been fabricated using AFM lithography. The AFM image of an engraved pattern and the Scanning electron micrograph of the resulting SET are shown in FIG. 3. The two overlapping Al/AlO_x/Cu tunnel junctions have been obtained by two angle ($\pm 15^\circ$) evaporations of Al and Cu. A series of V-V_g modulation curves obtained at 30mK are shown in FIG. 4. The charging energy E_c/k_B deduced from the I-V is equal to 0.7 K. The device characteristics are completely similar to those of SETs fabricated using EBL [3]. AFM lithography has the advantage of avoiding deterioration of fragile underlying structures by e-beam exposure. In particular, defects in 2D electron gases have been reported to be a consequence of the EBL exposure.

In conclusion, the AFM-based trilayer lift-off technique presented in this work is a general purpose nanofabrication technique with alignment capability. It already offers an alternative to standard electron beam lithography in specific cases. Further progress in the tip sharpness could bring the linewidth under the presently achieved value of 40 nm.

We thank G. Faini and C. Vieu for SEM imaging.

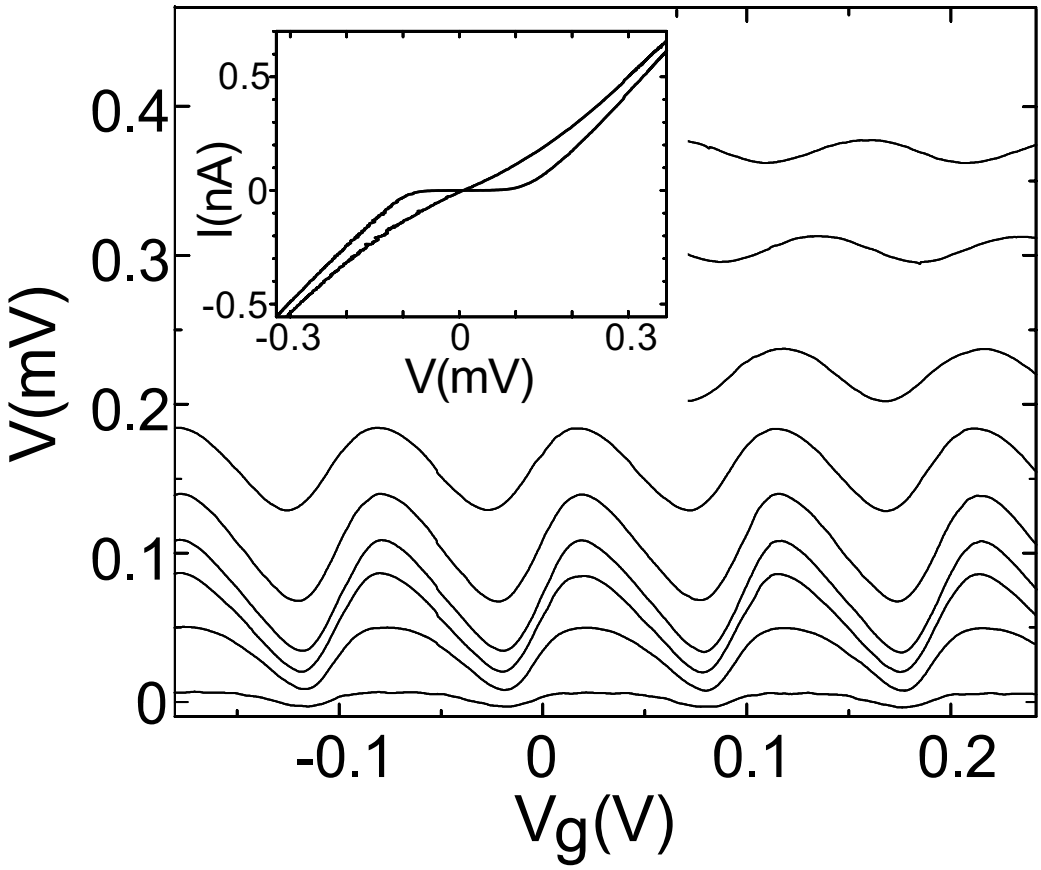

Figure 4: Modulation curves of the output voltage V of the SET at 20 mK as a function of the gate voltage V_g for different bias currents.

Inset: Extremal I-V characteristics of the SET.

REFERENCES

[1] B. J. Van Wees, H. van Houten, C.W.J. Beenaker and J.G. Williamson, Phys. Rev. Lett. **60**, 848 (1988)

[2] D. A. Wharam, T.J. Thornton, R. Newbury, M. Pepper, H. Ahmed, J.E.F frost, D.G. Hasko, D.C. Peakcock, D.A. Ritchie, G.A.C. Jones, J. Phys. **C21**, L209 (1988)

[3] for a review see *Single Charge Tunneling, Coulomb Blockade Phenomena in Nanostructures,* ed. by H. Grabert and M. H. Devoret, NATO ASI Series **294** (Plenum, 1992)

[4] L. P. Kowenhouven, private communication.

[5] W. Chen and H. Ahmed, Appl. Phys. Lett. **62**, 1499 (1993)

[6] *Technology of proximal probe lithography,* ed. by C.R.K. Marrian (SPIE 1993)

[7] D. M. Eigler and L. K. Schweizer, Nature **344**,524 (1990); C. Lebreton and Z. Z. Wang, Scanning Micr. J., **8**, 441 (1994)

[8] P. H. Beton, A. W. Dunn, and P. Moriarty, Appl. Phys. Lett. **67**, 1075 (1995)

[9] C. R. K Marrian and E. A. Dobisz, J. Vac. Sci. Technol. B**10**, 2877 (1992); A. Majumdar, P.I. Oden, J. P.Carrejo, L.A. Nagahara, J.J. Graham and J. Alexander, Appl. Phys. Lett. **61**, 2293 (1992); S. W. Park, H.T. Soh, C.F. Quate and S.I. Park, Appl. Phys. Lett. **67**, 2415 (1995); K. Kragler, L.E. Günther, R. Leuschner, G. Falk, A. Hammerschmidt, H. von Seggern and G. Saemann-Ischenko, Appl. Phys. Lett. **67**, 1163 (1995)

[10] C. R. K. Marrian, F.K. Perkins, S.L. Brandow, T.S. Koloski, E.A. Dobisz and J.M. Calvert, Appl. Phys. Lett. **64**, 390 (1994); A. Kumar, H.A. Biebuyck, N.L. Abbott and G. M. Whitesides, J. Am. Chem. Soc. **114**, 9188 (1992)

[11] L. Stockman, G. Neuttiens, C. Van Haesendonck and Y. Bruynseraede, Appl. Phys. Lett. **62**, 2935 (1993)

[12] T. Thundat, L.A. Nagahara, P.I. Oden, S.M. Lindsay, M.A. George, W.S. Glaunsinger,

J. Vac. Sci. Technol. A**8**,3537 (1990) ; ; S. C. Minne, H.T. Soh, P. Flueckiger and C.F. Quate, Appl. Phys. Lett. **66**, 703 (1995) ; T. Hattori, Y. Ejiri, K.Saito, M. Yasutake, J. Vac. Sci. Technol. **A12**, 2586 (1994)

[13] J. A. Dagata, J. Schnier, H. H. Harary, C. J. Evans, M. T. Postek and J. Bennet, Appl. Phys. Lett. **56**, 2001 (1990) ; N. Kramer, H. Birk, J. Jorritsm, C. Schönenberger, Appl. Phys. Lett. **66**, 1325 (1995)

[14] N.B. Larsen, T. Bjornholm, J. Ganaes, J. Larsen and K. Schaumburg, *Ultimate Limits of Fabrication and Measurement,* ed. M. E. Welland and J. K. Gimzewski, Kulwer Acad. Publ. (1995)

[15] L. L. Sohn and R.L. Willet Appl. Phys. Lett. **67**,1552 (1995)

[16] PMMA/MAA is a copolymer polymethyl methacrylate/ methacrylic acid

[17] J. Romijn and E.Van der Drift, physica B **152**,14 (1988)

APPENDIX 6−C
Technical data of multilayer fabrication (p. 253)

Multilayer fabrication process involves 7 steps: Step 2 to 4 depend on the nature of the insulating material (organic or inorganic).

- STEP 1 *Patterning gold leads using UV-lithography*
  On a 2-inches silicon oxidized wafer,we spin photoresist Hoechst AZ-5206 at 7000 rpm and hard-bake 5 minutes at 97°C. A chromium mask patterned on quartz is used on a Karl Suss mask aligner. We develop in AZ351 during 15-20 seconds. We then evaporate 2 nm of titanium (sticking layer for gold) and then 50 nm of gold in a Joule evaporator. The resist is lifted-off in acetone.

A- Polyimide resist as the insulating layer

- STEP A-2 *Spin-coating of the polyimide resist*
  We use Dupont PI-2610 polyimide resist whose viscosity is reduced by dilution in N-methyl-2-pyrrolidinone (3 kg of PI per liter of NMP). (parameters of spin are 5000 rpm, 30s, 0.5 μm thick). We carefully perform a heating process using hot-plates: We first gently hard-bake the wafer 2 minutes at 100°C and then bake it in vacuum during one hour at 350°C.
- STEP A-3 *Patterning holes over the polyimide*
  We spin photoresist AZ-5206 over the polyimide (7000 rpm for 1minute, $\sim$0.4 μm thick) and hard-bake 5 minutes at 97°C. Aligning the mask with small windows over the extremities of the gold leads is a critical step in this process: the allowed misalignment is about 0.5 μm. We then under-expose the resist (16-17 seconds). Some photoresist still subsists at the bottom of the patterned holes after development in AZ-351. The developed resist is then hard-baked 15 minutes at 160°C in order to form a smooth profile for the edges.
- STEP A-4 *Etching the polyimide resist*
  The smooth patterned profile in the photoresist is transferred to polyimide using reactive ion etching (R.I.E.). The plasma consists of a mixture gas SF_6/O_2 with respective proportions 5 sccm/50 sccm at total pressure 0.3 mbar. The RF parameters are 50 W, 67 V.
  We monitor the etching by measuring the interference fringes of a reflected laser beam focused in a etched hole (about 3 to 4 minutes of etching). The sample is then washed in acetone using ultrasonics. Gold leads appearing at the bottom of the holes are cleaned during 10 seconds under a low energy Argon ion milling .

B- Silicon nitride as the insulating layer

- STEP B-2 *Deposition of Si_3N_4 layer*
  The layer is deposited by reactive magnetron sputtering using a silicon nitride target in a Ar/N_2 plasma. The deposition parameters are:
  - distance target-sample: 10 cm
  - pressure 2×10^{-4} mbar N_2+ 8×10^{-4} mbar Ar.
  - Autopolarization voltage: 650 V
  - Temperature of the sample: 240°C.
  - deposition rate: $1\mu m$ per hour.
- STEP B-3 *Patterning holes:* see step A3 above.

- STEP B-4 *Etching the Si_3N_4 layer.*
  The silicon nitride layer is pierced using two steps of reactive ion etching (RIE):
  First, 80 % of the total thickness is etched at a high etching rate (40 nm/min) using a CHF_3/O_2 plasma and a large autopolarization voltage (typically 240 V) of the sample.
  Then the remaining thickness is removed at a lower etching rate in order to prevent physical sputtering of the gold layer which is uncovered at the end ; a SF_6 plasma and a low autopolarization voltage (below 30 V) are used.
- STEP 5 *Preparing the e-beam resist*
  A standard bilayer resist is used: The bottom ballast layer is made of copolymer (90 $g.l^{-1}$ MAA). We spin it at 2000 rpm for 30 seconds. This layer is hard-baked 10 minutes at 155°C in order to stretch the film and avoid thickness variations near the connecting holes.
  The top layer is then prepared. We use PMMA(polymethyl-metacrylate) diluted in MIBK (methyl-isobutyl-butyl-ketone) (15 $g.l^{-1}$ PMMA) spun at 1000rpm. We finally hard-bake the wafer at 155°C for 15 minutes.
- STEP 6 *E-beam lithography*
  The sample is exposed to 35 keV electrons in an scanning electron microscope which beam position is controlled by a PC connected to a DAC board (Raith Proxy-Writer system). The typical exposure dose is around 2 $pC/\mu m^2$.
- STEP 7 *Shadow mask evaporation*
  The sample is developed in MIBK/propanol in proportions 1:3 during 35 seconds at 20°C.
  An undercut is obtained. We finally proceed to an evaporation at two angles (-9/+9 degrees) of aluminum. An oxidation process is performed between the two evaporations with a controlled pressure of a mixture gas oxygen/argon (20% O_2) (typically 3 mbar, 5 minutes). Final lift-off of the bilayer is performed in acetone at 40°C.

APPENDIX 6–D
Novel Fabrication technique of Single Electron Devices

CPEM'96 proceedings

Novel Fabrication Technique for Single Electron Devices

V. Bouchiat, D. Vion, D. Esteve and M. H. Devoret

Service de Physique de l'Etat Condense, Commissariat à l'Energie Atomique,

91191 Gif-sur-Yvette Cedex, France

proceedings of the Conference of Precise Electromagnetic Measurements

(CPEM'96), Braünschweig June 1996

ABSTRACT

We present a new method for fabricating multilayer single-electronic circuits with vias, crossings and reduced cross-capacitances. A single electron transistor (SET) was fabricated with this method and successfully operated. Its intrinsic charge noise, 3×10^{-4} e/$\sqrt{\text{Hz}}$ at 10 Hz, matches that of other SETs.

INTRODUCTION

When single electron devices are fabricated using a single lithography step, the electrostatic coupling takes place through coplanar capacitors which are weak, subject to cross-talk and not compatible with a general network topology. These drawbacks have motivated the fabrication of multilayered circuits with overlapping capacitors [1]. Moreover, implementing with only two conductive layers all the features of a three dimensional network (composed of tunnel junctions and capacitances), necessitates an insulating spacer pierced in some points for connections (i.e. vias).

We present here a method for fabricating single electronic devices enabling crossings and vias. In our process, insulating layers are made of polyimide films.

FABRICATION

In the first step, we perform an optical lithography of the connecting circuitry and of the gate electrodes. In our case, we evaporate 50nm of gold onto an oxidized silicon wafer.

In a second step, we spin a polyimide resist over the sample. Its final thickness after a 1 hour vacuum hardbake at 350°C is 0.4μm. We then open by reactive ion etching 1μm^2 large windows through the resist, thus uncovering the connecting leads. The etching parameters are chosen in order to obtain smooth enough window edges thereby enabling electrical continuity when the upper layer is evaporated.

The third step is a standard (MAA/PMMA bilayer) electron-beam lithography of the tunnel junctions defining the core of the device. This step requires an alignment

with 0.1μm accuracy before exposure to ensure a correct positioning of the contacts and of the islands between junctions with respect to the windows and the buried gates. Finally, $0.1\times0.1\mu\text{m}^2$ Al/AlO_x/Al tunnel junctions are fabricated by evaporation at two angles through a shadow mask (see Fig. 1).

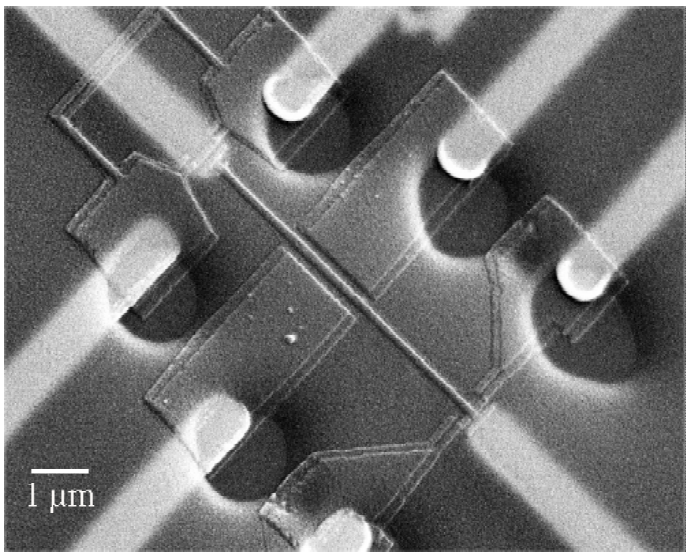

FIG. 1. Scanning electron micrograph of a typical sample. The bright fingers are gold leads and gates under the polyimide film. Windows through the polyimide appear as circular black holes. Junctions and parts of the island lie over the two gates. The device consists of an electrometer (bottom right) which measures by its long thin strip shaped island the charge of an electron box (upper left).

NOISE CHARACTERIZATION

We have tested our process by fabricating and operating a single electron transistor (Fig. 1). This device is known to be the most sensitive electrometer [2] (see Fig. 2). Any variation in the electrostatic field near the island of the electrometer due to the motion of charges in the lower layers [3,4], induces a polarization charge q_n, the so-called charge noise of the electrometer. The noise q_n determines the de-

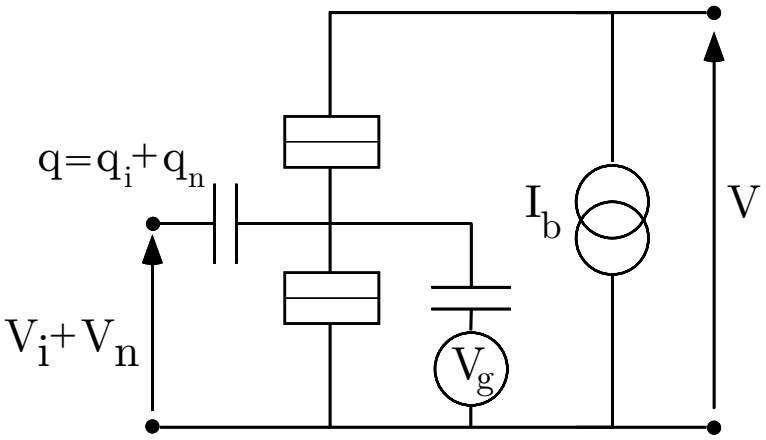

FIG. 2. Schematic diagram of a SET electrometer. For a given gate voltage V_g, the output voltage V is a periodic function of the input charge q_i. The sensitivity $\partial V/\partial q$ depends on both V_g and the current bias I_b. The detection limit is determined by the superimposed input charge noise q_n.

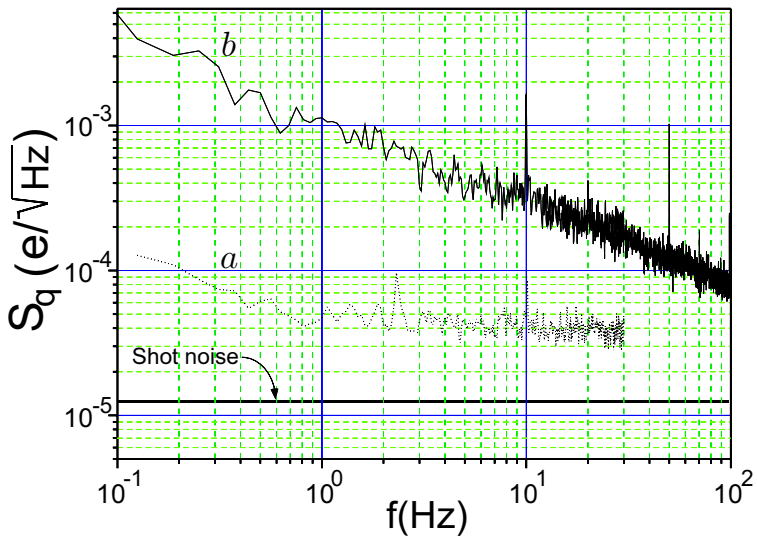

FIG. 3. Noise spectral densities of the SET electrometer. a) noise at zero sensitivity : it includes noise of the whole setup. b) Charge noise at maximum sensitivity. The bottom line corresponds to the shot-noise of the SET.

tection limit of the electrometer. Therefore, a question about our new device arises : Is an organic film such as the polyimide a sufficiently "quiet" substrate for single electronics ?

To answer this question, we have measured the noise power spectrum of the electrometer designed to measure the charge in an electron box. Noise measurements were made in a dilution refrigerator at 20mK at a constant current bias I_b maximizing the sensitivity $\partial V/\partial q$ of the electrometer. Each line connecting the device to the apparatus at room temperature was carefully filtered using miniature cryogenic filters [5]. Since we wanted to characterize the low frequency part of the noise we had to reject the 1/f noise generated by the amplifiers. Using a lock-in technique, the charge noise was shifted to higher frequencies at which the amplifier noise is orders of magnitude lower.

The charge noise spectrum S_q shown on Fig. 3 displays a 1/f dependence. This is in agreement with the fact that the noise is generated by a collection of charge traps in the substrate, each trap emitting a telegraphic noise with distributed switching times [6].

The noise level at 10Hz is equal to $3\times10^{-4}e/\sqrt{\text{Hz}}$. Despite the large area of the electrometer island ($10 \times 0.1\mu m^2$), this value is of the same order of magnitude as those currently reported for electrometers fabricated on various kinds of inorganic substrates.

In conclusion, we have developed a new method for fabricating multilayer single electron devices enabling full 3D features without increasing the noise level. It enables the fabrication of more complex circuits such as Cooper pair pump arrays.

REFERENCES

[1] E.H. Visscher, S. M. Verbrugh, J. Lindeman, P. Hadley, and J. E. Mooij. Appl. Phys. Lett., Vol. 66, p. 305, 1995.

[2] T. A. Fulton, and G.J. Dolan Phys. Rev. Lett., Vol. 59, p. 109, 1987.

[3] A.B. Zorin, F.J. Ahlers, J. Niemeyer, T. Weinmann, and H. Wolf. to be published,

1995.

[4]S.M. Verbrugh, M. L. Benhamadi, E. H. Visscher, and J. E. Mooij J. Appl. Phys., Vol. 78, p. 2830, 1995.

[5] D.Vion, P. F. Orfila, P. Joyez, D. Esteve, and M. H. Devoret. J. Appl. Phys., Vol. 77, p. 2519, 1994.

[6] C. T. Rogers, R. A. Buhrman, W.J. Gallagher, S. T. Raider, A.W. Kleinsasser, and R. L. Sandstrom. IEEE Trans. Magn., Vol. 23, p. 1658, 1987.

Appendix of chapter 6

APPENDIX 6-E
Fabrication diagram of the processing sequence

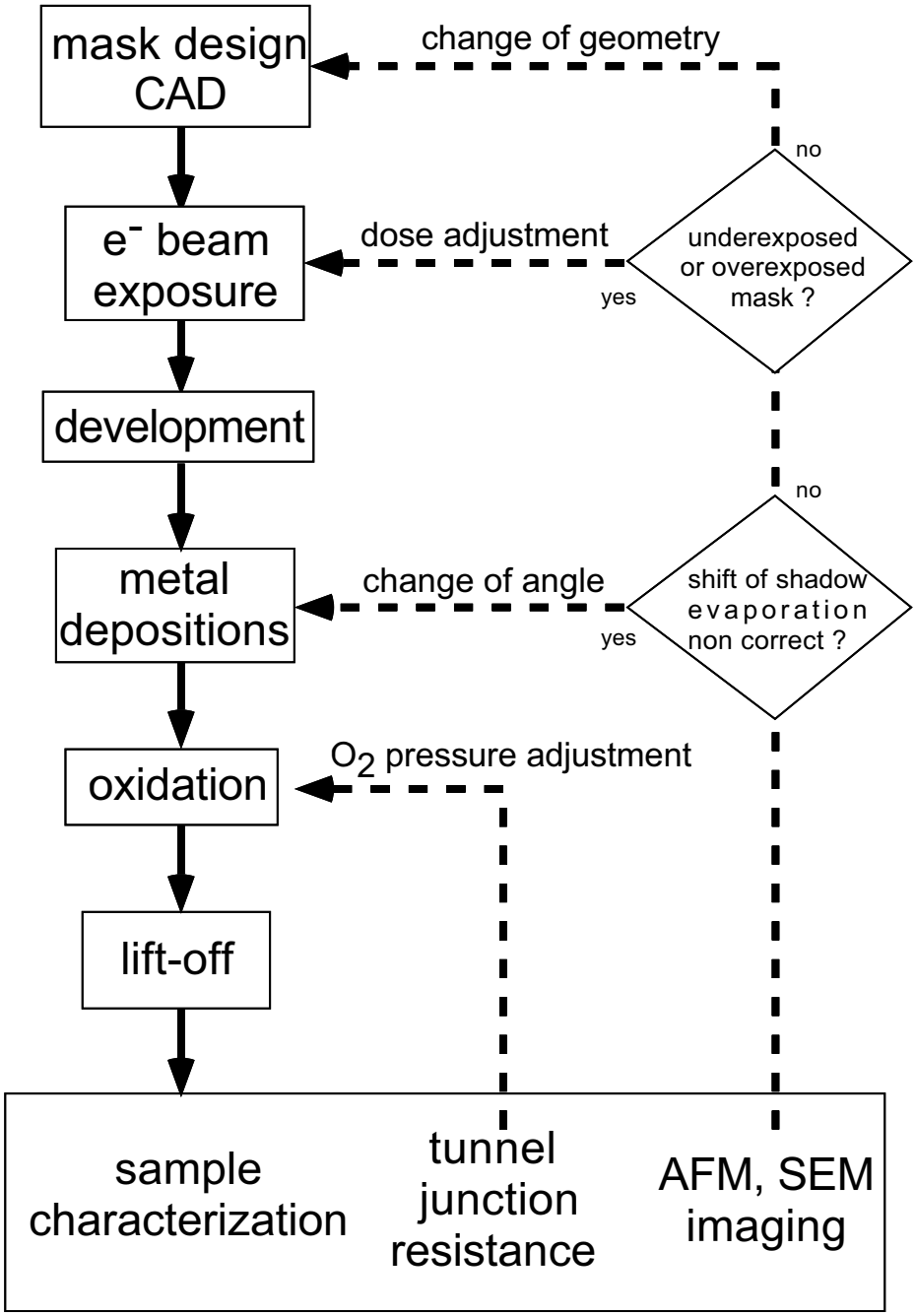

Figure 6.18: Diagram showing the fabrication process and feedback corrections after sample characterization.

APPENDIX 6-F
Tunnel junction resistivity data

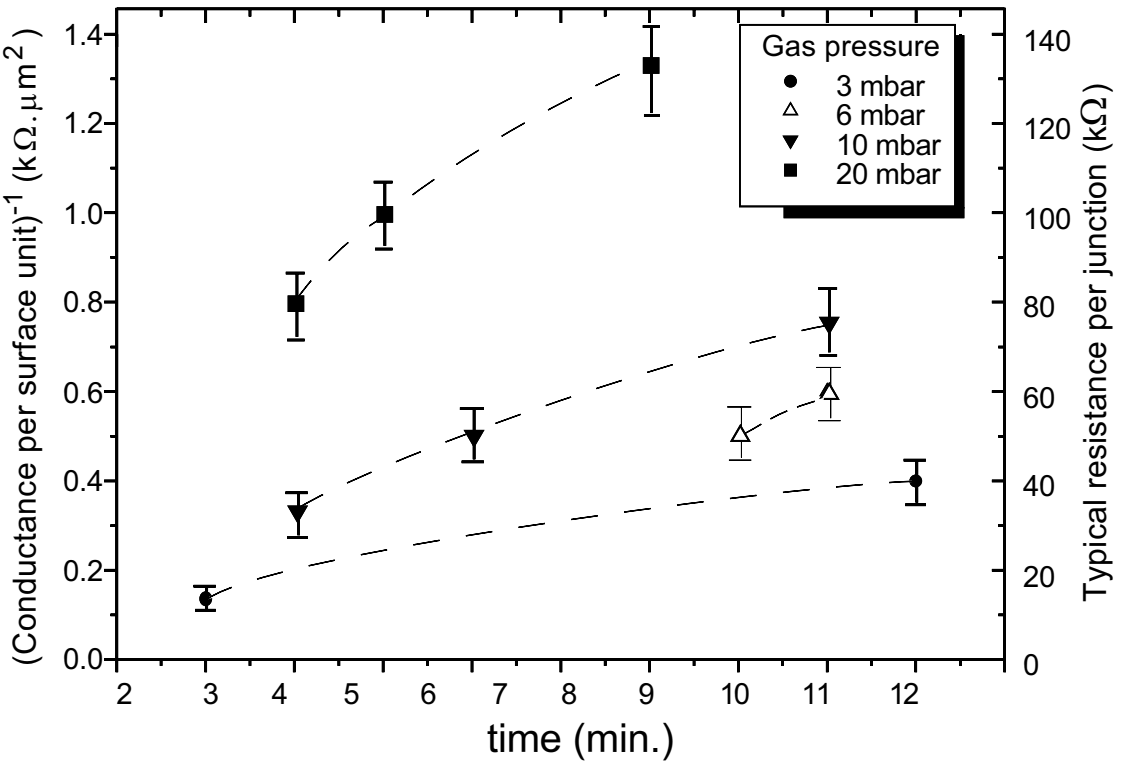

Figure 6.19: Resistances measured at room temperature of Al/AlOx/Al tunnel junctions fabricated using in-situ oxidation with a gas mixture O_2/Ar (15% O_2). The obtained resistances are plotted as a function of the time of oxidation for increasing gas pressures. Left axis labels indicates the measured resistance normalized to the junction area (Error bars correspond to the area uncertainty). Right axis labels gives the resistance for a typical junction (0.09x0.11μm^2). *Dashes are just guidelines for clarity.*

General conclusion

In this thesis work, we have presented an experimental approach of charge quantum fluctuations in single electron and Cooper pair circuits. For single electron devices, quantum fluctuations of the charge are governed by the ratio of the tunnel junction conductance to the conductance quantum e^2/h. By measuring extremal conductances of a series of SETs, we have observed that Coulomb blockade is progressively washed out and shifted to lower temperatures when the tunnel junction conductance is increased. Our experimental results show in particular that the renormalization of the effective charging energy of an island increases with the strength of tunneling.

In single Cooper pair devices, quantum fluctuations of the charge are determined by the ratio of the Josephson energy to the electrostatic energy. When both these energies are of the same order of magnitude, two charge states differing by one Cooper pair can coexist quantum mechanically. In the superconducting box experiment, the ground state is a macroscopic coherent superposition of charge states differing by one Cooper pair. However, such a coherent state which was observed at low temperature is somewhat fragile and can be "poisoned" by out-of-equilibrium quasiparticle excitations. We have found that quantization of the island charge in multiples of Cooper pairs is suppressed for substantial Josephson couplings.

We have then shown that this interplay between Josephson and charging energies can be extended to more complex single Cooper pair devices involving several superconducting islands, in which one could hope to probe excited states. Quantum states in this more elaborate systems are expected to be more robust with respect to decoherence since they are not directly coupled to dissipation in the environment.

In the course of this research, we have developed new fabrication techniques that are now sufficiently advanced to allow the design of complex multilayered circuits. In particular, these techniques lead to the optimization of electrostatic couplings between electrodes. They could be applied to the fabrication of single Cooper pair arrays which would be operated as "pumps". One can conjecture that the quantum delocalization of Cooper pairs in complex arrays could be used to circumvent the random gate voltage shifts due to offset charges. This would open the possibility to increase substantially the current delivered by the current standard based on the single electron pump.

Index of variables and acronyms

a_m : annihilation operator of the harmonic oscillator of index m $a_m^\dagger$: creation operator of the harmonic oscillator of index m

$c_{\sigma l}$: fermionic annihilation operator for a quasiparticle of spin σ in the eigenstate l

$c_{\sigma l}^\dagger$: fermionic creation operator for a quasiparticle of spin σ in the eigenstate l

e : charge of the bare electron

f_L, f_R : superconducting density of state on the left (resp. right) side of the junction

g : tunneling strength parameter: $R_K/4\pi^2 R_T$

h : Planck constant

h.c. : hermitic conjugate

$\hbar$: $h/2\pi$

h_{mn} : reduced hamiltonian matrix element

k_B : Boltzmann constant

n : excess charge number in the island (in units of Cooper pairs except in chapter 1: in units of electrons)

$|n\rangle$: quantum charge state of the bare Josephson junction

$\langle n \rangle$: average excess charge number in the island

n_g : gate charge number

n_0 : reduced gate voltage for single electron devices: $C_g U/e$ representing the effective number of induced electrons on the gate

n_c : reduced gate voltage for single Cooper pair devices: $C_g U/2e$ representing the effective number of induced Cooper pair on the gate

n_1, n_2 : excess charge number in the island number 1 (resp. 2)

p_+, p_- : switching probability from the higher (resp. lower supercurrent)

p_n : Boltzmann probability of having n excess electrons on the island

r : ratio of the junction areas

$\overrightarrow{r}$: displacement vector

q : excess charge of the island

q_n : charge of the SET island induced by background charge noise

q_i : electrostatic charge of electrode i

$\overrightarrow{s}$: spin $\frac{1}{2}$ vector

t : tunneling matrix element

t_m : translation vector for operator $\mathcal{D}(t_m)$

$\mathfrak{z}$: partition function of the normal metal single electron box

AFM : atomic force microscope

BCS : Bardeen-Cooper-Schriffer theory of superconductivity

C : generic capacitance

C_g : gate electrode capacitance

C_{ij} : capacitance matrix element of indexes i;j

C_j : tunnel junction capacitance

C_m : capacitance of the harmonic oscillator of index m

C_Σ : total island capacitance

CVD : chemical vapor deposition

DC : direct current

$\mathcal{D}(t_m)$: translation operator of vector t_m acting on oscillator m

EBL : electron beam lithography

$\overrightarrow{E}\left(\overrightarrow{r}\right)$: local electric field at $\overrightarrow{r}$ from the origin

$(|E\rangle)$: quantum basis of the environment

$E(n,p)$: electrostatic energy of the transistor in the state (n,p)

E_c : charging energy of one electron in an island: $e^2/2C_\Sigma$

E_g : energy gap between neighboring charge states

E_c^0 : bare charging energy

E_c^s : charging energy obtained from the resonances in the superconducting state

$E_c^\star$: renormalized charging energy

$\widetilde{E}_c$: effective charging energy

$\widetilde{E}_g$: effective energy gap

E_J : Josephson coupling energy

E_J^0 : bare Josephson coupling energy

$E_J^\star$: renormalized Josephson coupling energy

$E_n(\delta)$: energy band of index n of the Josephson junction

$E(n)$: electrostatic energy with n excess electron in the island

$E_J^\star$: renormalized Josephson coupling energy

E_n : electrostatic energy with n excess electron in the island

G : generic conductance

$G_{//}$: parallel conductance of the two tunnel junctions

$G_{\min}$: minimum SET zero bias conductance

$G_{\max}$: maximum SET zero bias conductance

G_0 : series tunnel conductance of two junctions in series

$G_0^\star$: renormalized series tunnel conductance

$\mathcal{H}$: total Hamiltonian of the system

H_{el} : electrostatic Hamiltonian

H_J : Josephson coupling Hamiltonian of a bare junction

$\mathcal{H}_{env}$: Hamiltonian of the environment

$\mathcal{H}_J$: Josephson coupling Hamiltonian of the junction embedded in the environment

$\mathcal{H}_{pert}$: perturbative Hamiltonian

I : generic current

I_c : critical current of the Josephson junction embedded in the environment

I_c^0 : critical current of the bare Jospehson junction

$I_n(\delta)$: supercurrent at $T = 0$ of the Josephson junction in excited state n

$\overline{I}(T, \delta)$: average supercurrent at finite temperature

L : generic inductance

L_{eff} : effective inductance of the environment

L_m : inductance of the harmonic oscillator of index m

M_1, M_2 : moment of order -1 (resp. -2) of the environmnent impedance Z

N_m : number of excitation quanta in the oscillator of index m

$\widehat{N}$: operator of the number of transferred Cooper pairs through the junction

$|N_m\rangle$: eigenstate of the harmonic oscillator m with N quanta)

$\overrightarrow{P}(\overrightarrow{r}, t)$: electric polarization vector at time t and at position $\overrightarrow{r}$

$P_n(T)$: normalized Boltzmann factor of energy band $E(n)$ at temperature T

R : generic resistance

RF: radio-frequency

RG: renormalization group theory.

RIE: reactive ion etching.

R_K : resistance quantum $h/e^2 \approx 25.8\,k\Omega$

R_T : resistance of the tunnel barrier in the normal state

R_{Ti} : resistance of the tunnel junction number i

$(|S\rangle)$: environment quantum basis composed of tensorial product of harmonic oscillator eigenstates

SEM : scanning electron microscope

SET : single electron transistor

SM : sequential tunneling model

S_q : spectral density of the SET charge noise

SQUID : superconducting quantum interference device

STM : scanning tunneling microscope

T : temperature

$\widehat{T}_{2e}$: translation operator of one Cooper pair in the environment

$\widehat{T}_{mn}$: matrix element of $\widehat{T}$

U : gate voltage

U_1, U_2 : gate voltage of gate electrode number 1 (resp. 2)

UV: ultra-violet

$\mathcal{V}$: particle classical potential

V : generic bias voltage

$V\left(\overrightarrow{r}\right)$: electrostatic potential at distance $\overrightarrow{r}$

V_i : electrostatic potential of electrode i

V_g : gate voltage

$Z(\omega)$: electromagnetic environment impedance

$Z_m(\omega)$: impedance of the harmonic oscillator of index m

$\mathcal{Z}_m$: characteristic impedance of the harmonic oscillator m, $\mathcal{Z}_m = \sqrt{L_m/C_m}$

α : tunneling strength parameter $G_{//}/G_K$

$\alpha^\star$: RG renormalized tunneling strength parameter

β : reduced temperature parameter $\beta = (k_B T)^{-1}$

γ : reduced environment impedance $\sqrt{4\pi Z/R_K}$

γ^+, γ^- : switching rate from the lowest (resp. highest) supercurrent

δ : phase difference across the considered system

$\delta(x)$: Dirac distribution

δ_{mn} : Kronecker symbol

ϵ_0 : dielectric permitivity of vaccum

ϵ_r : relative dielectric permitivity

ε : generic infinitly small number

ζ : Riemann Zeta function

θ : phase difference across the environment, solution of the variational method

κ : parameter of the self consistent equation

ν : generic frequency

π : $Pi = 3.14159...$

ρ : renormalization factor for the Josephson energy

ρ_L, ρ_R : density of state at the Fermi level on left side, (resp right side) of the junction

$\sigma_x, \sigma_y, \sigma_z$: Pauli matrices for the spin $\frac{1}{2}$ representation

τ : characteristic time of a tunneling process $\tau = R_T C$

ϕ : generic magnetic flux variable

φ_0 : generalized magnetic flux quantum $\Phi_0/2\pi$

$\widehat{\phi}_m$: flux operator of the fot the harmonic oscillator number m

ω : generic circular frequency

ω_n : resonance frequency of the harmonic oscillator of index n

Γ : generic variable for tunneling rate

$\Gamma^+(n), \Gamma^-(n)$: tunneling rates through the junction $\#i$ with n extra electrons on the island leading to increase (resp. decrease) the current .

Δ : superconducting gap, $\Delta = 180\,\mu eV$ for Aluminum

$\widetilde{\Delta}$: even-odd free energy of the superconducting island

ΔE : free energy difference before and after a tunneling event

$\Delta\omega$: frequency width for which the environment impedance $Z(\omega)$ is modeled by a single oscillator

$|\Xi(t_1, ..t_m..)\rangle$: trial wave function of parameters $t_1, ..t_m$

$\widehat{\Phi}'$: total flux operator of the environment

Φ_0 : magnetic flux quantum $h/2e$

Φ_{int} : magnetic flux inside the loop

Φ_{ext} : bias magnetic flux

$|\psi\rangle$: generic eigenfunction

Ω_0 : single oscillator resonance frequency